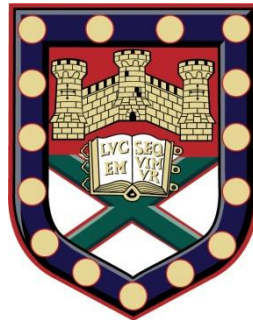


# Mathematical Modelling of Inter- and Intracellular Signal Transduction: The Regulatory Role of Multisite Interactions



Submitted by **Ildar Sadreev** to the University of Exeter  
as a thesis for the degree of  
Doctor of Philosophy in Mathematics  
In June 2015

This thesis is available for Library use on the understanding that it is copyright material and that no quotation from the thesis may be published without proper acknowledgement.

I certify that all material in this thesis which is not my own work has been identified and that no material has previously been submitted and approved for the award of a degree by this or any other University.

Signature: .....

## Abstract

Signalling processes regulate various aspects of living cells via modulation of protein activity. The interactions between the signalling proteins can occur at single or multiple sites. Although single site protein interactions are relatively easy to understand, these rarely occur in living systems. It is therefore important to investigate multisite interactions. Despite the recent progress in experimental studies, the underlying molecular mechanisms and molecular functions of the multisite interactions are still not clear and therefore require systems approaches for deeper understanding, for example to understand how the system will react to perturbation of one of its components. The examples of the molecular functions that are studied in this thesis are: kinetics of multisite calcium binding to proteins such as calmodulin (CaM), multisite phosphorylation of interferon regulatory factor 5 (IRF-5) and signal transducers and activators of transcription (STATs). We also study the role of STATs in the overall immune response and in T cell phenotype switching as well as multisite phosphorylation of high osmolarity glycerol factor 1 (Hog1) in mitogen activated protein kinase (MAPK) cascade during the adaptation of *Candida glabrata* to osmotic stress. In this thesis, these examples are studied using the systems approach in the context of human diseases: cancer, candidiasis, immunity-related pathologies such as rheumatoid arthritis, inflammatory bowel disease and systemic lupus erythematosus. We discuss potential therapeutic implications of the proposed models in these diseases. The predictions of the models developed in this thesis are supported by the experimental data and propose possible mechanisms of the multisite interactions involved in the cellular regulation.

## **Acknowledgements**

I wish to express my special appreciation and thanks to everyone who supported me throughout my studies. It is my great pleasure to acknowledge people who have given me guidance, help and encouragement.

Firstly, I would like to express my deepest gratitude to Professor Vadim Biktashev for his patient guidance, suggestions and endless encouragement, invaluable constructive criticism and friendly advice during the project work. Your advice on both research as well as on my career have been priceless.

I would like to thank Professor Ken Haynes for his aspiring guidance and support, introduction to biological community and enormous valuable discussions.

My sincere thanks also go to Professor Peter Ashwin for his support and important suggestions and remarks during my studies.

My special appreciation and thanks also go to Dr Najl Valeyev who introduced me to research community, for his support, mentoring, collaboration and valuable comments.

I would also like to express my gratitude to Professor Nikolay Kotov, for the continuous support, collaboration and invaluable discussions.

I thank the University of Exeter for financial support and for offering me an opportunity to do an exciting research in Exeter.

I would like to thank Emily Cook for experimental data and valuable discussions.

In addition, I would like to thank Dr Claudia Kemper for collaboration, invaluable discussions and important comments.

It has been my pleasure to work with my fellow students and colleagues: Tomas Sary, Burhan Bezekci, Abdullah Aldurayhim, Saad Almuaddi, Pierre Aumjaud and George Efstathiou. They made my years at the University of Exeter the most memorable period in my life.

I wish to thank my parents Ilshat Sadreev and Svetlana Sadreeva for their unconditional love, support and encouragement. Without you I would never have the opportunities that lie before me.

Finally, I would like to thank my wife Ilmira Sadreeva. Words cannot express how much you mean to me. I am thankful to you for believing in me and giving me your endless support over the last three years. Without your love and support I would not have achieved this.

*Dedicated to Ilmira Sadreeva for her kindness, care and endless support.*



# List of contents

<b>Abstract .....</b>	<b>2</b>
<b>Acknowledgements .....</b>	<b>3</b>
<b>List of figures.....</b>	<b>9</b>
<b>List of tables .....</b>	<b>14</b>
<b>Abbreviations.....</b>	<b>15</b>
<b>Publications and conferences attended .....</b>	<b>16</b>
<b>1 Introduction.....</b>	<b>17</b>
<b>2 Kinetic regulation of multi-ligand binding proteins .....</b>	<b>23</b>
2.1 Literature review .....	23
2.1.1 Biological review .....	23
2.1.2 Modelling review.....	24
2.2 Aims and objectives of this chapter .....	26
2.3 The model for abundant ligand concentration .....	26
2.3.1 Multisite protein with independent ligand binding sites.....	27
2.3.2 Multisite proteins with four identical ligand binding sites .....	42
2.3.3 Multisite proteins with four different ligand binding sites .....	45
2.3.4 The effects of cooperativity .....	48
2.4 The model for comparable ligand and protein concentrations .....	54
2.5 Conclusions .....	63
<b>3 A systems model of phosphorylation for inflammatory signalling events .....</b>	<b>66</b>
3.1 Literature review .....	66
3.1.1 Biological review .....	66
3.1.2 Modelling review.....	68
3.2 Aims and objectives of this chapter .....	69
3.3 A new model for phosphorylation .....	70
3.3.1 Single site phosphorylation .....	73
3.3.2 Multisite phosphorylation.....	79
3.4 Applications of the developed models (Equations 3.11, 3.22 and 3.27) to the regulation of the proteins activity.....	80
3.4.1 STAT3 phosphorylation .....	80
3.4.2 IRF-5 phosphorylation .....	84

3.4.3	Phosphorylation in the control of aggregation and deformability of erythrocytes	89
3.5	Sequential multisite phosphorylation .....	96
3.6	Conclusions .....	104
<b>4</b>	<b>The competitive nature of STAT complex formation drives phenotype switching of T cells</b>	<b>107</b>
4.1	Literature review .....	107
4.1.1	Biological review .....	107
4.1.2	Modelling review.....	109
4.2	Aims and objectives of this chapter .....	110
4.3	Model assumptions.....	110
4.3.1	The model for coupled STAT3-STAT5 signal transduction .....	114
4.4	Model parameters.....	124
4.5	Model predictions .....	126
4.5.1	STAT switching.....	126
4.5.2	Parameter sensitivity analysis.....	131
4.5.3	Comparative analysis of STAT3-STAT4 versus STAT3-STAT5 machinery.....	144
4.5.4	The role of individual cytokines in STAT dimer redistribution .....	149
4.6	Conclusions .....	151
<b>5</b>	<b>The interplay between MAPK signalling and biophysical regulation in <i>Candida glabrata</i> adaptation to osmotic stress</b>	<b>156</b>
5.1	Literature review .....	156
5.1.1	Biological review .....	156
5.1.2	Modelling review.....	160
5.2	Gennemark model.....	162
5.3	Aims and objectives of this chapter .....	168
5.4	A new systems model for <i>C. glabrata</i> adaptation to osmotic stress .....	169
5.4.1	Modification 1 of the biophysical part .....	169
5.4.2	Modification 2 of the glycerol metabolism module.....	176
5.4.3	Modification 3 of the Hog1 activation module .....	183
5.4.4	Modification 4 of receptor activation .....	200
5.5	Quantitative analysis of the developed model .....	203
5.5.1	Obtaining the set of parameters .....	205
5.5.2	Identifiability of the parameters .....	205
5.5.3	Parameter sensitivity analysis.....	207
5.6	Model predictions .....	209

5.6.1	The model predictions for Sho1 deletion and overexpression .....	213
5.6.2	Potential therapeutical application of the model .....	215
5.7	Conclusions .....	218
<b>6</b>	<b>Conclusions and further work .....</b>	<b>221</b>
6.1	Conclusions .....	221
6.2	Further work.....	226
<b>7</b>	<b>Appendix .....</b>	<b>229</b>
7.1	Appendix A .....	229
7.1.1	Biochemical kinetics .....	229
7.1.2	Molecular binding .....	231
7.1.3	Enzyme kinetics .....	235
7.2	Appendix B .....	237
7.2.1	Derivation of Equation (2.6) .....	237
7.2.2	Derivation of Equation (2.45) .....	238
7.2.3	Derivation of Equation (2.46) .....	239
7.2.4	Derivation of Equation (2.57) .....	240
7.2.5	Derivation of Equation (2.59) .....	243
7.2.6	Derivation of Equation (2.60) .....	244
7.3	Appendix C .....	244
7.4	Model for the STAT3-STAT5 circuit .....	247
7.4.1	Cytokine-receptor interactions .....	248
7.4.2	STAT phosphorylation and dimerisation .....	252
7.4.3	Cytokine production .....	258
7.5	Model for the STAT3-STAT4 circuit .....	265
7.5.1	Cytokine-receptor interactions .....	267
7.5.2	STAT phosphorylation and subsequent dimerisation .....	268
7.5.3	IFN- $\gamma$ and IL-10 production.....	274
7.6	Combined STAT3-STAT4-STAT5 model.....	275
7.6.1	Cytokine-receptor interactions .....	278
7.6.2	STAT phosphorylation and dimerisation .....	279
7.6.3	IFN- $\gamma$ and IL-10 production.....	288
7.7	Parametric analysis .....	289
7.8	Appendix D .....	292
7.8.1	Gennemark model.....	292
7.8.2	Modification 1 of the biophysical part .....	294

7.8.3	Modification 2 of the glycerol metabolism module.....	297
7.8.4	Modification 3 of the Hog1 activation module .....	298
7.8.5	Modification 4 of the receptor activation.....	299
7.8.6	Other quantitative predictions.....	302
7.9	Appendix E.....	306
7.9.1	The permission to use the experimental data in this thesis .....	306
<b>Bibliography .....</b>		<b>307</b>

## List of figures

<i>Figure 1.1. Schematic diagram of possible representations of cellular systems.</i>	21
<i>Figure 2.1. The schematic diagram for the transient responses of ligand-activated multisite proteins.</i>	25
<i>Figure 2.2. The effect of the number of binding sites on maximum concentrations of intermediate conformations.</i>	33
<i>Figure 2.3. Model predictions for the half-maximal effective ligand concentrations as a function of the number of binding sites and ligand concentration.</i>	35
<i>Figure 2.4. Temporal characteristics of the apo- and fully bound species in response to a ligand jump.</i>	40
<i>Figure 2.5. The characteristic times for apo- and fully bound forms as a function of the final ligand concentrations.</i>	42
<i>Figure 2.6. Characteristic time required for intermediate conformations to reach their maximum levels as a function of the step change magnitude.</i>	45
<i>Figure 2.7. Kinetics predictions for multisite protein species with marginally different association constants.</i>	46
<i>Figure 2.8. Kinetics of multisite protein species alterations for a protein with significantly different association constants.</i>	48
<i>Figure 2.9. Comparative analysis of cooperative versus non-cooperative <math>Ca^{2+}</math> binding to CaM.</i>	53
<i>Figure 2.10. The kinetics of free ligand concentration for high and low protein concentrations.</i>	59
<i>Figure 2.11. The comparison between the cases where the free ligand concentration is barely affected by interactions and exhausted as a result of binding.</i>	60
<i>Figure 2.12. Model predictions for the time required for multisite protein conformations to reach their maximal concentrations.</i>	62
<i>Figure 2.13. Model predictions for the time required for multisite protein conformations to reach their maximal and half growth concentrations.</i>	63
<i>Figure 3.1. A schematic diagram for the dependence of T cell differentiation on intracellular phosphorylation signalling.</i>	72

<i>Figure 3.2. Check of the feasibility of the solutions for the kinase-protein complexes concentrations.....</i>	<i>78</i>
<i>Figure 3.3. Model predictions for the concentration of STAT3<sub>p</sub> phosphorylated by JAK and dephosphorylated by SHP-1. ....</i>	<i>82</i>
<i>Figure 3.4. Multisite phosphorylation enables switching between multiple T cell phenotypes.....</i>	<i>86</i>
<i>Figure 3.5. Theoretical investigation of the regulation of IRF-5 multisite phosphorylation.....</i>	<i>88</i>
<i>Figure 3.6. Phosphorylation of EF1 and EF2 proteins controls the aggregation and deformability of erythrocytes.....</i>	<i>90</i>
<i>Figure 3.7. Check of the feasibility of the model assumptions, where the concentrations of enzyme-substrate complexes are neglected.....</i>	<i>96</i>
<i>Figure 3.8. Model predictions for the sequential phosphorylation of IRF-5.....</i>	<i>102</i>
<i>Figure 3.9. Theoretical investigation of the sequential IRF-5 phosphorylation. ....</i>	<i>103</i>
<i>Figure 4.1. The map of interleukins involved in induction of IFN-<math>\gamma</math> and IL-10 production via the STAT-activating mechanisms.....</i>	<i>112</i>
<i>Figure 4.2. Schematic diagram for IFN-<math>\gamma</math> and IL-10 production in Th1/Tr1 switching.....</i>	<i>114</i>
<i>Figure 4.3. Schematic diagram for IFN-<math>\gamma</math> and IL-10 production in response to IL-6, IL-2 and IL-21 as input signals, via signal processing by STAT3 and STAT5.....</i>	<i>117</i>
<i>Figure 4.4. The regulation of IL-2-dependent IFN-<math>\gamma</math> and IL-10 production in Th1/Tr1 switching.....</i>	<i>124</i>
<i>Figure 4.5. Model predictions for STAT3 and STAT5 activation in response to IL-2.....</i>	<i>126</i>
<i>Figure 4.6. Model predictions demonstrate cross-interaction effects between STAT3 and STAT5 signalling pathways. ....</i>	<i>128</i>
<i>Figure 4.7. Model predictions for low IL-2 reveal selectivity of the immune response.....</i>	<i>130</i>
<i>Figure 4.8. The probability of cases when the switching occurs.....</i>	<i>133</i>
<i>Figure 4.9. Parameter sensitivity analysis performed by eFAST.....</i>	<i>135</i>
<i>Figure 4.10. Parameter sensitivity analysis performed by eFAST.....</i>	<i>137</i>
<i>Figure 4.11. Parameter sensitivity analysis performed by eFAST.....</i>	<i>138</i>

<i>Figure 4.12. Systems model predictions for the produced IFN-<math>\gamma</math> and IL-10 dependence on the change in intracellular regulation. ....</i>	139
<i>Figure 4.13. The effects of change in extracellular IL-6 concentration. ....</i>	142
<i>Figure 4.14. The model predictions for STAT3-STAT4 circuit. ....</i>	145
<i>Figure 4.15. The model predictions for the combined STAT3-STAT4-STAT5 circuit. ....</i>	147
<i>Figure 4.16. The competition between STAT3-STAT4 and STAT3-STAT5 modules in the combined model depends on IL-21 concentration. ....</i>	149
<i>Figure 5.1. Functional diagram for the yeast adaptation to osmotic stress. ....</i>	159
<i>Figure 5.2. Schematic diagram for the model developed by Gennemark. ....</i>	162
<i>Figure 5.3. Hyper-osmotic NaCl signal as a function of time. ....</i>	165
<i>Figure 5.4. Schematic representation of the yeast cell adaptation to osmotic stress by the Gennemark model. ....</i>	168
<i>Figure 5.5. Functional link between the biophysical and biochemical parts of the proposed model. ....</i>	173
<i>Figure 5.6. Schematic representation of the yeast cell adaptation to osmotic stress after the introduction of modified biophysical part of the Gennemark model. ....</i>	175
<i>Figure 5.7. The structure of the new model after the introduction of the modified glycerol metabolism module. ....</i>	176
<i>Figure 5.8. Schematic representation of the yeast cell adaptation to osmotic stress after the introduction of the modified glycerol metabolism module. ....</i>	182
<i>Figure 5.9. The structure of the new model after the introduction of the modified Hog1 activation module. ....</i>	184
<i>Figure 5.10. Schematic representation of the yeast cell adaptation to osmotic stress after the introduction of the modified Hog1 activation module. ....</i>	197
<i>Figure 5.11. The comparison of the model predictions for Hog1 phosphorylation in C. glabrata BG2 and 2001 strains response to the different hyper-osmotic NaCl concentrations. ....</i>	199
<i>Figure 5.12. The comparison of the model predictions for C. glabrata 2001 and BG2 strains response to the hyper-osmotic stress. ....</i>	202
<i>Figure 5.13. Distribution of the optimised parameters. ....</i>	206
<i>Figure 5.14. The comparison of the model predictions with the experimental data. ....</i>	207

<i>Figure 5.15. Sensitivity indices for Hog1 phosphorylation obtained by eFAST.</i>	208
<i>Figure 5.16. The effects of the perturbations of the most sensitive parameters on Hog1 phosphorylation.</i>	209
<i>Figure 5.17. The model predictions for biophysical changes and Hog1 phosphorylation in BG2 strains adaptation to hyper-osmotic stress.</i>	210
<i>Figure 5.18. The model predictions for the change in concentrations of the osmotically active compounds inside the cell in BG2 strains under hyper-osmotic stress.</i>	211
<i>Figure 5.19. Theoretical investigation of the adaptation of C. glabrata BG2 strains to the modest hyper- and the hypo-osmotic stress conditions.</i>	212
<i>Figure 5.20. The model predictions for C. glabrata Sho1 deletion and overexpression.</i>	214
<i>Figure 5.21. Double hyper-and-hypo-osmotic NaCl signal as a function of time.</i>	216
<i>Figure 5.22. The model predictions for the double hyper-and-hypo-osmotic stress.</i>	217
<i>Figure 7.1. The model predictions for the swapped parameters.</i>	289
<i>Figure 7.2. The distribution of the optimised parameters.</i>	290
<i>Figure 7.3. The model predictions for the produced IFN-<math>\gamma</math> and IL-10 dependence on the changes in the STAT3 pathway.</i>	291
<i>Figure 7.4. The predictions of the Gennemark model in response to the strong hyper-osmotic stress 1M.</i>	292
<i>Figure 7.5. The predictions of the Gennemark model in response to the mild hyper-osmotic stress 0.3M.</i>	293
<i>Figure 7.6. The predictions of the Gennemark model in response to the hypo-osmotic stress 0.05M.</i>	293
<i>Figure 7.7. The model predictions after the introduction of the modified biophysical part in response to the strong hyper-osmotic stress 1.5M.</i>	294
<i>Figure 7.8. The model predictions after the introduction of the modified biophysical part in response to the mild hyper-osmotic stress 0.3M.</i>	295
<i>Figure 7.9. The model predictions after the introduction of the modified biophysical part in response to the hypo-osmotic stress 0.05M.</i>	296
<i>Figure 7.10. The model predictions after the introduction of the modified glycerol metabolism module in response to the strong hyper-osmotic stress 1.5M.</i>	297



<i>Figure 7.11. The model predictions after the introduction of the modified glycerol metabolism module in response to the mild hyper-osmotic stress 0.3M. ....</i>	297
<i>Figure 7.12. The model predictions after the introduction of the modified glycerol metabolism module in response to the hypo-osmotic stress 0.05M. ....</i>	298
<i>Figure 7.13. The model predictions after the introduction of the modified Hog1 activation module in response to the strong hyper-osmotic stress 2.5M. ....</i>	298
<i>Figure 7.14. The model predictions after the introduction of the modified Hog1 activation module in response to the mild hyper-osmotic stress 1M.....</i>	299
<i>Figure 7.15. The model predictions after the introduction of the modified Hog1 activation module in response to the hypo-osmotic stress 0.05M. ....</i>	299
<i>Figure 7.16. The model predictions after the introduction of the modified receptor activation module in response to the strong hyper-osmotic stress 2.5M. ....</i>	300
<i>Figure 7.17. The model predictions after the introduction of the modified receptor activation module in response to the mild hyper-osmotic stress 1M.</i>	300
<i>Figure 7.18. The model predictions after the introduction of the modified receptor activation module in response to the hypo-osmotic stress 0.05M. ...</i>	301
<i>Figure 7.19. The comparison of Hog1 phosphorylation for BG2 and 2001 strains of C. glabrata.....</i>	303
<i>Figure 7.20. The model predictions for the overexpression of Sho1 in 2001 strain of C. glabrata. ....</i>	303
<i>Figure 7.21. Model predictions for the double hyper-and-hypo-osmotic stress. ....</i>	304
<i>Figure 7.22. Model predictions for the double hyper-and-hypo-osmotic stress when the concentration of extracellular glucose in equilibrium is increased... </i>	304
<i>Figure 7.23. Model predictions for the single hyper-osmotic stress when the concentration of extracellular glucose in equilibrium is decreased. ....</i>	305

## List of tables

<i>Table 2.1. Molecular forms of the molecule with 4 binding sites.....</i>	<i>28</i>
<i>Table 2.2. The difference between ligand concentrations for the saturated multisite protein conformations when the protein species are equal to 90% and 10% of the total concentration. ....</i>	<i>36</i>
<i>Table 4.1. The effects of the parametric changes on the concentration of produced IFN-<math>\gamma</math> and IL-10 shown in Figure 4.12. ....</i>	<i>141</i>
<i>Table 5.1. The total number of moles of the kinases in MAPK pathways. ....</i>	<i>195</i>
<i>Table 7.1. Abbreviations used in the STAT phosphorylation model. ....</i>	<i>244</i>
<i>Table 7.2. Nominal, optimised parameters and squared error SM. ....</i>	<i>289</i>
<i>Table 7.3. The percentage of cases when the switching of both cytokine and STAT (C+S+), cytokine and not STAT (C+S-), not cytokine and STAT (C-S+), neither cytokine not STAT (C-S-) occurs for 1-10 fold change of the optimised parameters. ....</i>	<i>290</i>
<i>Table 7.4. Parameters in the STAT3-STAT4 subsystem and their correspondence to the parameters in the STAT3-STAT5 subsystem. ....</i>	<i>291</i>
<i>Table 7.5. Nominal and optimised parameters. ....</i>	<i>302</i>

## Abbreviations

**ODE** - Ordinary Differential Equation

**QSSA** - Quasi-Steady-State Assumption

**Ca<sup>2+</sup>** - Calcium ion

**CaM** - Calmodulin

**CaN** - Calcineurin

**TnC** - Troponin C

**JAK** - Janus Kinase

**STAT** - Signal Transducer and Activator of Transcription

**IRF** - Interferon Regulatory Factor

**IL** - Interleukin

**IFN** - Interferon

**Th** - T Helper cells

**Treg** - Regulatory T cells

***S. cerevisiae*** - *Saccharomyces cerevisiae*

***C. glabrata*** - *Candida glabrata*

**MAPK** - Mitogen-Activated Protein Kinase

**AQP** - Aquaporin

## Publications and conferences attended

Some results in this thesis have been presented in the following publications and conferences.

### Publications

- 1) **I.I. Sadreev**, M.Z.Q. Chen, G.I. Welsh, Y. Umezawa, N.V. Kotov, N.V. Valeyev, *A Systems Model of Phosphorylation for Inflammatory Signaling Events*, PLOS One, 2014.
- 2) A.N. Bazanovas, A.I. Evstifeev, S.F. Khaiboullina, **I.I. Sadreev**, A.I. Skorinkin, N.V. Kotov, *Erythrocyte: A systems model of the control of aggregation and deformability*, Biosystems, 2015.

### Conferences

- 1) *University of Exeter College of Engineering, Mathematics and Physical Sciences PGR conference*, 2013 (talk)
- 2) *The British Society for Immunology annual congress*, 2013, Liverpool
- 3) *The British Society for Immunology annual congress*, 2014, Brighton (poster presentation)

# 1 Introduction

This thesis describes a study related to mathematical modelling of molecular interactions in biochemical circuits. The research area of this thesis can be classified as Systems Biology. Compared to Physics, Biology and Mathematics, it is a relatively new discipline, which is extensively developing nowadays. Systems Biology studies biological systems as a whole and aims to analyse them by using techniques developed in Engineering, Mathematics and Physics [1]. The developed Systems Biology models then can be used to suggest strategies to control the system under malfunctions caused by various factors, for example genetic factors, infection and ageing. In order to analyse biological systems both qualitatively and quantitatively, experimental data along with mathematical modelling are essential parts of Systems Biology, where insight gained in experiments informs the models and vice-versa [2]. The most basic mathematical models used in Systems Biology are reviewed in Appendix A of this thesis.

In biochemical circuits, intracellular signal transduction is performed by molecular interactions such as phosphorylation, methylation, acetylation and ligand binding to proteins [3]. In this thesis, we apply a Systems Biology approach studying protein binding [4] and phosphorylation [5]. These molecular interactions can occur at one single or multiple sites of proteins. Single site interactions are relatively rare, and proteins frequently contain multiple interaction sites [6]. Protein functions that regulate cellular signal transduction depend on the state of sites of proteins (for example, occupied or non-occupied phosphorylated or non-phosphorylated). Thus, in comparison to single site interactions, multisite interactions allow more possibilities to control protein function [7,8], which we refer as multifunctionality. While single site interactions are relatively easy to understand, multisite interactions require systems approaches for deeper elucidation of multisite protein functions. For example it is important to understand how the system will react to perturbation of one of its components.

The steady-state of ligand binding to proteins was extensively studied in the previous modelling works [9-13] that became classical (briefly described in Appendix A). However, in these works only apo- and fully saturated protein conformations were studied as inactive and active protein conformations respectively, whereas there is experimental evidence that intermediate protein conformations also demonstrate activity [14,15]. In the modelling study [7] the steady-states of intermediate conformations were analysed. Nevertheless, intracellular concentrations of ligand are often subject to rapid change [16-18] so steady-state description is not always sufficient. An example of a relatively recent modelling study of ligand-receptor binding kinetics can be found in [19]. However in that work authors used a description of sequential calcium binding whereas calcium binding to EF-hand proteins is non-sequential [20]. Therefore the dynamics of ligand-dependent regulation of multisite proteins require further elucidation. In Chapter 2 of this thesis we will study the multisite ligand-receptor binding using calmodulin (CaM) as a data-rich example of a molecule with four binding sites for calcium [21,22]. We will investigate the dynamics of the multisite protein conformations with different number of occupied sites for different amount of available ligand.

The second basic biochemical reaction involved in intracellular signal transduction that we study in this thesis is phosphorylation. Phosphorylation alters enzymatic properties of proteins and modulates protein activity in cells [5]. A number of mathematical studies attempted to build a model of protein phosphorylation. One of the most well-known models of phosphorylation/dephosphorylation cycle for a single site protein was proposed in [23]. It used Michaelis-Menten kinetics to describe these enzymatic reactions. In the model [23] it was assumed that the total concentration of protein significantly exceeds the concentrations of kinase and phosphatase and therefore the concentrations of the Michaelis complexes can be neglected. The approach proposed in [23] was used in a number of modelling studies [24-26] and extended to multisite phosphorylation [27,28]. However, in real biological systems the concentrations of kinases, phosphatases and substrates are not always comparable [29]. Therefore it is important to investigate the role of the concentrations of enzyme-substrate complexes in protein activity. In Chapter 3

we will build a model for single- and multisite phosphorylation including enzyme-substrate complexes into the consideration. We will compare the predictions of the developed model with the previous model [23] studying activation of Signal Transducer and Activator of Transcription 3 (STAT3) and Interferon Regulatory Factor 5 (IRF-5) [30] as well as the regulation of erythrocyte aggregation and deformability [31].

Protein binding and phosphorylation studied in Chapters 2 and 3 are very common elements in intracellular signal chains of real biological systems. In the following Chapters 4 and 5 we will perform a higher-level analysis and study two examples of real biological signalling systems investigating such cell processes as T cell plasticity [32] and yeast adaptation to osmotic stress [33] respectively. These biological questions have been chosen due to the available experimental data and scientific interests of our research group.

The first example of high-level analysis presented in this thesis is performed in Chapter 4. In contrast to Chapter 3, where we focus on one single STAT protein, in Chapter 4 we will analyse the system of interacting STAT proteins in T cell plasticity [32]. STATs are key molecular determinants of the T cell fate and effector function [34,35]. Several inflammatory autoimmune diseases such as rheumatoid arthritis (RA) [36], systemic lupus erythematosus (SLE) [37] and diabetes [38] are characterised by an altered balance of T cell phenotypes and cytokine secretion [39]. However, it is still not clear how the same STAT proteins regulate the development of T cell phenotypes and their plasticity during changes in extracellular conditions. In previous modelling works [40-43] only single STAT pathways were studied at a time. However in T cell phenotype development and plasticity more than one STAT pathway is involved [39,44]. Thus the systems integrated approach is required to study the role of STAT proteins in T cell plasticity. In Chapter 4, we will investigate the STAT-mediated regulation of T cell phenotype formation and plasticity using mathematical modelling and experimental data for intracellular STAT signalling proteins.

Another example of high-level analysis is demonstrated in Chapter 5. The multisite protein phosphorylation controls the biochemical processes involved in the regulation of yeast adaptation to osmotic stress [33]. This is a very good example to demonstrate the power of the developed framework since intracellular signalling and overall cellular behaviour have been extensively studied for the well-known model organism, *Saccharomyces cerevisiae*. In Chapter 5 we focus on the yeast adaptation to osmotic stress using an example of pathogenic *Candida glabrata*. These fungi are close genetic relatives to *S. cerevisiae* and are one of the less studied pathogenic yeast [45]. Understanding of *C. glabrata* adaptation to osmotic stress has a clinical significance [46]. The previous models of yeast adaptation to osmotic stress [47-57] as well as their comparison with the developed model will be discussed in more detail in Chapter 5.

When studying the two examples of real biological signalling systems in Chapters 4 and 5, it is important to consider these objects using the systems approach due to their complexity. In Systems Biology cellular signalling systems can be represented in four various ways according to [1], as schematically illustrated in Figure 1.1. The top-level representation of the cellular signalling system may be done in terms of the core cellular processes such as the reproduction, survival, growth, reproduction, proliferation and differentiation, movement and sensitivity to external stresses and stimuli. These core processes define the cell behaviour. In order to understand and explain the cell behaviour it is important to understand the underlying molecular mechanisms of biological processes. In the approach proposed in [1], the mechanisms can be viewed as a complex of three components: functional, morphological and substrate (Figure 1.1). The functional representation allows considering the system as a complex of functional blocks. The morphological representation of the system considers the system as a complex of individual elements that have been identified by Molecular Biology, for example proteins, and links between them. The lowest level representation of the cellular system is substrate representation, which concerns individual elements of the morphological scheme and their properties. The link between these levels of representation of cellular signalling systems is provided by mathematical modelling. For example,



mathematical modelling of highly conserved MAPK cascade, which consists of multistep phosphorylation of MAPKKK, MAPKK and MAPK kinases, revealed such features of the cascade as signal amplification and noise attenuation [58,59]. It should be noted that these features arise only when considering the functional block consisting of these three kinase phosphorylation steps and not when considering phosphorylation of each kinase separately.

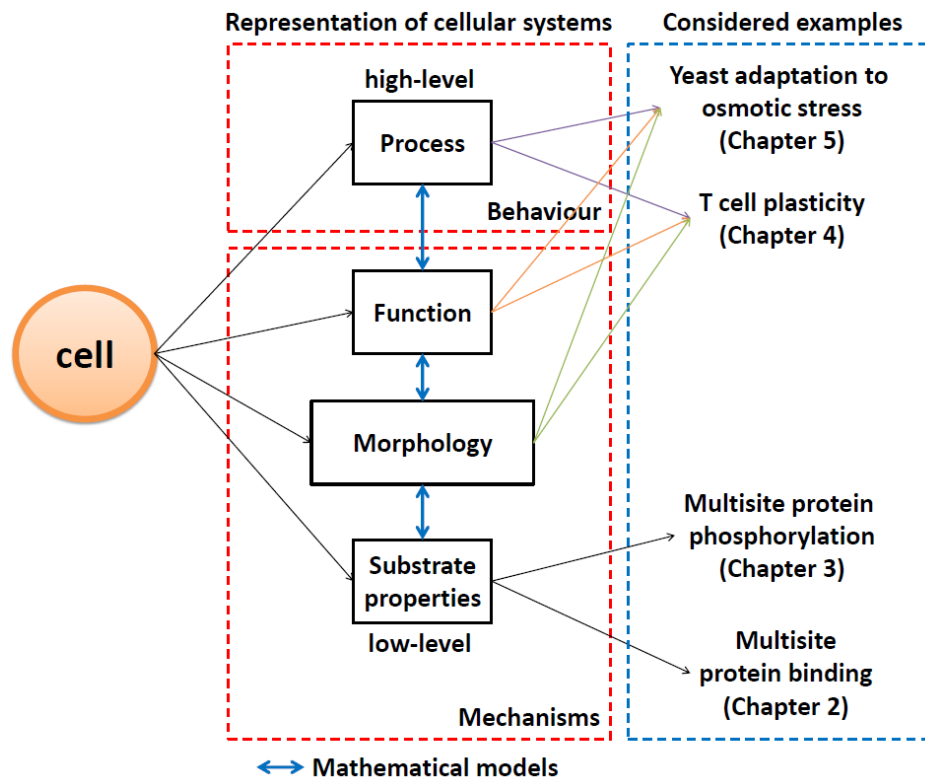


Figure 1.1. Schematic diagram of possible representations of cellular systems. The structure of the scheme is adopted from [1]. The cellular systems can be considered from different levels, from the low to high: substrate, morphological, functional and process. The first three levels can be viewed as "mechanisms" and the top level defines the behaviour of the cell. Mathematical modelling allows one to link all these levels. In this thesis we consider two examples of substrate properties analysis of multisite protein interactions in Chapters 2 and 3 as well as two examples of high-level analysis of cellular processes in Chapters 4 and 5.

Referring to Figure 1.1, in this thesis we will start our analysis with the low-level consideration of substrate properties in Chapters 2 and 3, where we investigate multisite protein binding and phosphorylation respectively. Then we perform a higher level analysis of signalling systems in Chapters 4 and 5 investigating

such cell processes as T cell plasticity and yeast adaptation to osmotic stress respectively. In each chapter we will focus on the areas that have been unexplored yet (this will be discussed further in corresponding chapters) due to the lack of understanding of the underlying mechanisms (Figure 1.1).

## **Aims and objectives of this thesis**

The main aims of this thesis are as follows:

1. Study the properties of two examples of multisite interactions:
  - ligand binding to multisite proteins,
  - multisite phosphorylation.
2. Propose potential mechanisms (in terms of Figure 1.1) of the two real examples of cellular processes in signalling systems:
  - T cell plasticity,
  - *C. glabrata* adaptation to osmotic stress.

The specific aims are described in more detail in the corresponding chapters of this thesis.

## **Methods**

In this thesis, we use the systems approach schematically illustrated in Figure 1.1. The mathematical methods used in this thesis are described in Appendix A. Briefly, we use the law of mass-action [60,61], and more complicated descriptions resulting from it, such as Michaelis-Menten kinetics, to describe the rates of biochemical reactions, and Ordinary Differential Equations (ODEs) to predict the time course of biochemical reactions resulting from these laws. We study dynamics or steady state of the systems depending on the research problems and available experimental data. For simplification we use, where appropriate, the Quasi Steady State Assumption (QSSA) [62] to describe the rate of enzymatic reactions. We use available experimental data to validate our models of real systems proposed in Chapters 4 and 5.

## 2 Kinetic regulation of multi-ligand binding proteins

### 2.1 Literature review

#### 2.1.1 Biological review

A wide variety of intracellular events are initiated via temporal change in ligand concentrations. One of the most important ligands in many cells is calcium ( $\text{Ca}^{2+}$ ). Calcium interacts with and regulates the activities of a large number of calcium-binding proteins as well as numerous effectors, for example calmodulin (CaM), calcineurin (CaN) and troponin (TnC) [63,64]. The number of functional calcium binding sites within the calcium-binding proteins can range from one or two to ten or more [65-67]. The most common number of calcium binding sites is four: as observed in the most ubiquitous protein, calmodulin (CaM) as well as troponin C (TnC) and other EF-hand containing proteins [21,22]. Temporal elevation of intracellular free  $\text{Ca}^{2+}$  is the key regulatory factor of the  $\text{Ca}^{2+}$ -dependent protein activity [68-72]. The characteristics of the induced calcium signal (duration, frequency, magnitude), which control cellular responses, are not fully understood: it remains to be determined how a single ligand is able to govern numerous intracellular properties such as cell proliferation, differentiation, apoptosis, secretion, fertilization and transcription factor activation [73].

Whilst the multisite ligand binding is not limited to  $\text{Ca}^{2+}$  signalling,  $\text{Ca}^{2+}$  is probably one of the most versatile ions in living cells regulating the activities of a large number of the effector proteins [74,75]. Several  $\text{Ca}^{2+}$ -binding proteins can be considered as examples of multisite ligand-protein interactions. Structural biology investigations of calcium binding proteins in complexes with target protein peptides suggested that the specificity in  $\text{Ca}^{2+}$ -CaM binding protein-dependent target activation arises from the diversity of interaction interfaces, that mediate these interactions [76], between the  $\text{Ca}^{2+}$ -regulated protein and its target proteins [14,22,63,77-85]. The most ubiquitous protein, CaM, consists of two globular domains, each domain containing a pair of helix-loop-helix  $\text{Ca}^{2+}$ -binding motifs called EF-hands [22,65,67,81,82]. It was demonstrated in [7,20,86] studying steady-state conditions, that in addition to the diversity of

CaM-target interfaces, the CaM selectivity emerges from its target specific  $\text{Ca}^{2+}$ -affinity, the number of  $\text{Ca}^{2+}$  ions bound and the target specific cooperativity.

Another major factor that contributes to the selectivity of seemingly simultaneous regulation of several multisite  $\text{Ca}^{2+}$  binding proteins and  $\text{Ca}^{2+}$ -mediated processes is the temporal alterations of  $\text{Ca}^{2+}$  [16-18]. The remarkable variety of  $\text{Ca}^{2+}$  signals in cells, ranging from infrequent spikes to sustained oscillations and plateaus, requires an understanding of how fast intracellular calcium changes regulate the kinetics of multiple multisite  $\text{Ca}^{2+}$  binding proteins. For example, mediator secretion in the synapse defines the delay of the signal [87], calcium kinetics defines the properties of muscle contraction [88]. It is important to know the limits of these systems in relation to calcium kinetics.

In [78,89,90] protein-ligand binding was studied by the pressure-jump technique, more precisely, transient kinetics of proteins in response to rapid changes in pressure. However the dynamics of intermediate protein conformations, the mechanism (for example, sequential or independent) as well as the influence of cooperativity on the kinetics of multisite binding proteins still remains unclear. Therefore, mathematical modelling of  $\text{Ca}^{2+}$  jump-induced responses could be useful in the interpretation of transient kinetic experiments.

### **2.1.2 Modelling review**

The review of previously published models of multisite protein binding for steady states [9-13] is presented in Appendix A. In these works only fully saturated protein conformations were considered as active molecular forms, whereas intermediate protein conformations can also activate a protein [7,14,15]. The quantitative determination of the dynamic properties of multisite cooperative binding can be found [19]. In this work the authors emphasized the significance of the cooperativity by studying the fast dynamics of  $\text{Ca}^{2+}$  binding to calretinin (CR), which has one independent and four cooperative binding sites. The investigation of cooperative effects of  $\text{Ca}^{2+}$  binding to CR was performed both experimentally and using mathematical modelling. The authors employed the simplified version of the Adair-Klotz model (Equations (7.17) and (7.19) in Appendix A) [91,92] to describe the dynamics of the interactions involved in

$\text{Ca}^{2+}$  binding to CR. This approach was then extended to the binding of  $\text{Ca}^{2+}$  to CaM [93]. The models proposed in these studies [19,93] demonstrated excellent fitting results to the experimental data, in comparison with the previously published models. However, the described approach is rather limited, as it describes fitting instead of providing a mechanistic description. An alternative methodology offered by [19,93] is not directly applicable from the physical and chemical point of view because the Adair-Klotz model (Equations (7.17) and (7.19) in Appendix A) for sequential ligand binding was utilized [91,92], whereas binding of  $\text{Ca}^{2+}$  to EF-hand proteins [94-97] is non-sequential [20].

The majority of studies of the activation of multisite proteins consider only the ligand concentration-dependent profiles, for example [9-13]. The shape of distribution of multisite proteins in complex with variable numbers of bound ligand is known or can be experimentally elucidated in many cases [7,20-22,81,86,98-100]. However, the role of temporal transitions caused by fast alteration of ligand concentration on multisite proteins and on multisite protein-regulated target proteins remains unclear. One of the interesting questions about these multisite proteins is how rapid temporal alterations of ligand concentration (Figure 2.1) contribute to their function.

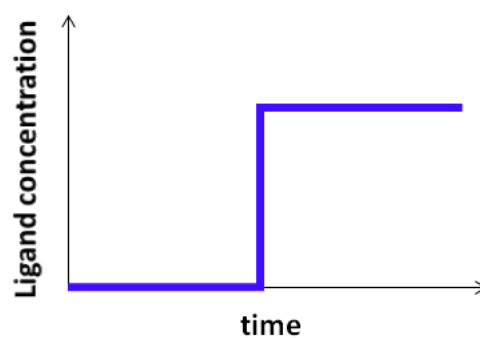


*Figure 2.1. The schematic diagram for the transient responses of ligand-activated multisite proteins.*

*The ligand concentration-dependent profiles are frequently investigated in the ligand-multisite protein interaction studies [9-13]. However, understanding the dynamics of protein activation in response to rapid change of ligand concentration allows more possible regulatory opportunities.*

## 2.2 Aims and objectives of this chapter

In this chapter we investigate multisite ligand-binding protein kinetics in response to rapid changes in ligand concentration. Mathematical models presented in this chapter aim to provide new insights into the conformational kinetics of multisite proteins in complex with variable number of bound ligands for the two distinct physiological situations that will be described:

- i) When the ligand concentration significantly exceeds protein concentration,
- ii) When the total amount of ligand is comparable with the protein concentration.

In the first case, one can neglect the variations in the free ligand concentration, i.e. consider it approximately constant, whereas in the latter, the ligand-protein interactions have a significant impact on the amount of available ligand and the binding kinetics. In this chapter, for each of the above mentioned cases we aim to do the following:

- build mathematical models to describe these cases,
- study the dynamics of the concentrations of individual conformations with certain number of bound ligands as a function of the ligand concentration, the number of binding sites and the binding affinities,
- investigate the impact of the number of binding sites, cooperativity, temporal effects on conformations, and regulation by multisite proteins of their effector proteins,
- derive and analyse the characteristic times when the concentration of the intermediate protein conformations is maximal and the characteristic times required for the apo- and fully saturated forms to reach their half growth level.

## 2.3 The model for abundant ligand concentration

In this section we assume that the ligand concentration significantly exceeds the multisite protein concentration and that the ligand binding to each site of the protein is an independent event, which is consistent with [20].

### 2.3.1 Multisite protein with independent ligand binding sites

The kinetic scheme for such interaction can be represented as follows:



where  $L_i^0$  is the  $i$ -th binding site of the multisite protein in unbound state,  $U$  is a ligand molecule,  $L_i^1$  is the  $i$ -th binding site of the multisite protein being occupied,  $k_i^+$  and  $k_i^-$  are the association and dissociation rates respectively.

There are two possible states of a binding site: occupied or not occupied. Since the number of sites in the molecule is  $n$ , there are  $2^n$  possible molecular forms, i.e. the states characterised by combinations of bound and free sites.

The probabilities for the  $i$ -th binding site to be not occupied or occupied as a function of ligand concentration  $U$  are given by:

$$p_i^0(U) = \frac{K_i}{K_i + U},$$

$$p_i^1(U) = \frac{U}{K_i + U}, \quad (2.2)$$

where  $K_i = \frac{k_i^-}{k_i^+}$  [7,20].

The probability for a multisite protein with independent binding sites to be in a particular molecular form is given by multiplication of probabilities of ligand binding to each site:

$$P_j(U) = \prod_{i=0}^{n-1} p_i^{c_i(j)}(U), \quad j = 0, \dots, 2^n - 1, \quad (2.3)$$

where  $j = \sum_{i=0}^{n-1} 2^i c_i(j)$  is the number of possible molecular forms,  $c_i(j) = 0$  or  $c_i(j) = 1$  for free or occupied binding site, respectively. For example, Table 2.1 shows possible molecular forms of a molecule with 4 binding sites (CaM). In total  $2^4 = 16$  combinations are possible. Using Table 2.1 we can write Equation (2.3) for the 16 molecular forms shown in the table. As an example, consider the molecular forms  $j = 1, 5, 14$ :

$$P_1(U) = p_0^1 p_1^0 p_2^0 p_3^0,$$

$$P_5(U) = p_0^1 p_1^0 p_2^1 p_3^0,$$

$$P_{14}(U) = p_0^0 p_1^1 p_2^1 p_3^1.$$

Table 2.1. Molecular forms of the molecule with 4 binding sites.

$j \setminus i$	3	2	1	0
0	0	0	0	0
1	0	0	0	1
2	0	0	1	0
3	0	0	1	1
4	0	1	0	0
5	0	1	0	1
6	0	1	1	0
7	0	1	1	1
8	1	0	0	0
9	1	0	0	1
10	1	0	1	0
11	1	0	1	1
12	1	1	0	0
13	1	1	0	1
14	1	1	1	0
15	1	1	1	1

To investigate the kinetics of the multisite protein ligand interactions, the presented model extends Equations (2.2) and (2.3) to consider the ligand concentration as a function of time. In this case we assume that the ligand concentration changes only at a given time point ( $t=0$ ) in a step fashion from  $U_0$  to  $U_1$  and remains constant otherwise.

The time-dependence of the probability of a multisite protein being occupied by ligand molecules, as it was shown in Equation (2.3), can be reformulated as follows:

$$P_j(U, t) = \prod_{i=0}^{n-1} p_i^{c_i(j)}(U, t), \quad j = 0, \dots, 2^n - 1. \quad (2.4)$$



The probability  $p_i^{c_i(j)}(U, t)$  can be determined by considering the original set of ordinary differential equations for single site interaction of a protein with a ligand according to Equation (2.1) [7]:

$$\begin{aligned}\frac{dL_i^0(U, t)}{dt} &= -k_i^+ \cdot L_i^0(U, t) \cdot U_1 + k_i^- \cdot L_i^1(U, t), \\ \frac{dL_i^1(U, t)}{dt} &= k_i^+ \cdot L_i^0(U, t) \cdot U_1 - k_i^- \cdot L_i^1(U, t), \\ L_i^0(U, t) + L_i^1(U, t) &= L_T,\end{aligned}\tag{2.5}$$

where  $L_i^0(U, t)$  is the concentration of a free binding site,  $L_i^1(U, t)$  is the concentration of bound ligand molecules and  $L_T$  is the total number of the protein molecules.

Now we need to obtain the solutions for the individual sites to be in a particular state for those cases where ligands are subject to rapid changes between steady-states. We use steady-state solutions  $L_i^0(U) = L_T \frac{K_i}{K_i + U}$  and  $L_i^1(U) = L_T \frac{U}{K_i + U}$  as initial conditions for the ligand concentration jump from  $U_0$  to  $U_1$ .

A particular solution for the system of differential Equations (2.5) in response to the ligand concentration shift from  $U_0$  to  $U_1$  is given by:

$$\begin{aligned}L_i^0(U, t) &= L_T \cdot \left( \frac{K_i}{K_i + U_1} - \left( \frac{K_i}{K_i + U_1} - \frac{K_i}{K_i + U_0} \right) \cdot \exp\left(-\frac{t}{\tau(U_1)}\right) \right), \\ L_i^1(U, t) &= L_T \cdot \left( \frac{U_1}{K_i + U_1} - \left( \frac{U_1}{K_i + U_1} - \frac{U_0}{K_i + U_0} \right) \cdot \exp\left(-\frac{t}{\tau(U_1)}\right) \right).\end{aligned}\tag{2.6}$$

(please see Appendix B for the derivation)

The normalisation of the solution (2.6) by the total protein concentration allows the definition of probability of the  $i$ -th binding site to be in an occupied  $p_i^1(U, t)$  or unoccupied  $p_i^0(U, t)$  state, respectively, at a given ligand concentration:

$$\begin{aligned}
p_i^0(U, t) &= p_i^0(U_1) - (p_i^0(U_1) - p_i^0(U_0)) \cdot \exp\left(-\frac{t}{\tau(U_1)}\right), \\
p_i^1(U, t) &= p_i^1(U_1) - (p_i^1(U_1) - p_i^1(U_0)) \cdot \exp\left(-\frac{t}{\tau(U_1)}\right).
\end{aligned}
\tag{2.7}$$

At any given time the total concentration of the protein,  $L_T$ , is conserved and the sum of the probabilities (2.7) equals 1:

$$\begin{aligned}
L_i^0(U, t) + L_i^1(U, t) &= L_T, \\
p_i^0(U, t) + p_i^1(U, t) &= 1.
\end{aligned}
\tag{2.8}$$

In the most general case, the concentration of the  $j$ -th molecular form,  $M_j(U, t)$ , of a molecule with  $n$  different binding sites in response to a step in ligand concentration is given by the product of probabilities (2.7) according to Equation (2.4):

$$M_j(U, t) = L_T \cdot \prod_{i=0}^{n-1} p_i^{c_i(j)}(U, t), \quad j = 0, \dots, 2^n - 1,
\tag{2.9}$$

where  $c_i(j) = 0$  or  $c_i(j) = 1$  for free or occupied  $i$ -th binding site respectively.

The probabilities for individual molecular forms in steady-state can be obtained from Equation (2.9) by setting  $t \rightarrow \infty$ :

$$M_j(U) = L_T \cdot \prod_{i=0}^{n-1} p_i^{c_i(j)}(U), \quad j = 0, \dots, 2^n - 1,
\tag{2.10}$$

In the case of multiple sites involved, knowledge of the state probability distribution for individual binding sites allows accurate estimation of the dynamics of the total concentration of bound ligand in response to a jump in free ligand concentration. The kinetics of the amount of ligand bound to a multisite protein with  $n$  binding sites can be written as follows:

$$S(U, t) = \sum_{j=0}^{2^n-1} M_j(U, t) \sum_{i=0}^{n-1} c_i(j),
\tag{2.11}$$

where  $S$  is the concentration of the bound ligand.

Equation (2.11) can be written in the following way:

$$S(U, t) = 1 \sum_{j \in J(1)} M_j(U, t) + 2 \sum_{j \in J(2)} M_j(U, t) + 3 \sum_{j \in J(3)} M_j(U, t) + \dots + n M_{2^n-1}(U, t), \quad (2.12)$$

where  $J(i)$  is the set of molecular forms with  $i$  bound ligands ( $i = 1, \dots, n$ ).

Equation (2.12) can be applied for Table 2.1:

$$S(U, t) = 1 \cdot (M_1 + M_2 + M_4 + M_8) + 2 \cdot (M_3 + M_5 + M_6 + M_9 + M_{10} + M_{12}) + \quad (2.13) \\ + 3 \cdot (M_7 + M_{11} + M_{13} + M_{14}) + 4 \cdot M_{15}$$

Equation (2.13) can be written in the following way:

$$S(U, t) = 1 \cdot M_1 + 1 \cdot M_2 + 2 \cdot M_3 + 1 \cdot M_4 + 2 \cdot M_5 + 2 \cdot M_6 + 3 \cdot M_7 + 1 \cdot M_8 + \quad (2.14) \\ + 2 \cdot M_9 + 2 \cdot M_{10} + 3 \cdot M_{11} + 2 M_{12} + 3 M_{13} + 3 M_{14} + 4 M_{15}$$

In order to gain more insights into the dependence of the intermediate protein conformations (complexes with variable number of bound ions) on the ligand concentrations and their evolution in time, we investigate the case of a multisite protein with identical binding sites. Further on, we refer to these dependencies as "distribution". While this case is a relatively rare occurrence in living cells, it enables insight into the role that the number of binding sites plays in cellular signalling. There are several examples of protein families that have variable number of ligand binding sites either due to their structural properties or by them forming large tertiary complexes. For example members of the  $\text{Ca}^{2+}$  family of binding proteins can differ in the number of ligand binding sites [101,102]. The most ubiquitous  $\text{Ca}^{2+}$ -binding protein, calmodulin (CaM), contains four  $\text{Ca}^{2+}$  binding sites as does troponin (TnC) [63] and calcineurin phosphatase (CaN) [64]. However the number of functional  $\text{Ca}^{2+}$  binding sites can vary from two to ten as in the protease, calpain [65] or even more in other cases [66]. To investigate the role that the number of ligand binding sites plays in multisite kinetics, the ligand concentrations, at which the concentrations of intermediate conformations reach their maximum values, and the corresponding magnitudes for those concentrations of intermediate conformations will be estimated.

In previously published studies [7,20] the authors analysed the steady-state of the ligand-receptor binding and derived the equation for the steady-state concentration of one of the molecular forms of multisite protein, where  $m$  out of  $n$  identical sites are bound and equilibrium dissociation constant equal  $K = \frac{k^-}{k^+}$ ,

as a function of ligand concentration:

$$N_m(U) = L_T \cdot \frac{U^m \cdot K^{n-m}}{(K+U)^n}, \quad m=0,1,\dots,n. \quad (2.15)$$

It was shown in [7,20] that the steady-state concentrations of the intermediate forms  $N_1(U), \dots, N_{n-1}(U)$  as a function of ligand concentration represent bell shapes reaching maximums at a particular ligand concentration  $U_m^{max}$ . Here we derive equations for these ligand concentrations  $U_m^{max}$  and the corresponding maximum protein concentrations  $N_m^{max}$ .

Differentiating Equation (2.15) with respect to  $U$  and solving  $dN/dU = 0$  for  $U$  gives:

$$U_m^{max} = \frac{K \cdot m}{n - m}, \quad m=1,2,\dots,n-1. \quad (2.16)$$

The magnitudes  $N_m^{max}$  of the intermediate conformations  $N_m$  corresponding to  $U_m^{max}$  values are:

$$N_m^{max} = L_T \cdot \frac{m^m}{n^n} (n-m)^{n-m}, \quad m=1,2,\dots,n-1. \quad (2.17)$$

Figure 2.2 shows the maximum protein conformations in complex with one, two and three ligands as a function of the total number of binding sites. Figure 2.2 demonstrates that the magnitude of individual intermediate conformations decreases as the number of binding sites increases. This in turn results in the regulation of the activity of the proteins with larger number of binding sites become subtler. As it will be shown later in Equation (2.28), the maximum

magnitudes of intermediate conformations  $N_m^{max}$ , obtained in Equation (2.17) for steady-states, are similar to the ones obtained for the kinetics.

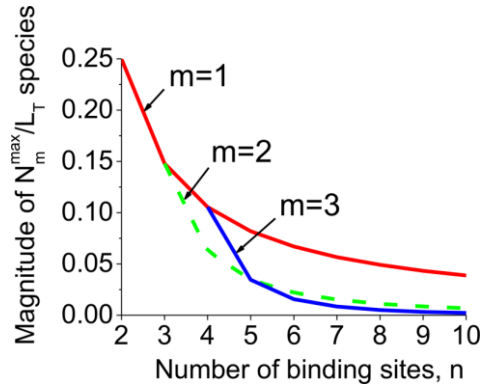


Figure 2.2. The effect of the number of binding sites on maximum concentrations of intermediate conformations.

The maximum magnitude of the concentrations of protein conformations in complex with one, two and three ligand molecules (y-axis) are shown as a function of the total number of binding sites (x-axis). The relative amount of ligand binding by conformations bound to a specific number of sites clearly diminishes as the number of sites grows. See Equation (2.17).

According to Equation (2.15), the multisite protein conformations in the apo-,  $N_0$ , and in the fully saturated states,  $N_n$ , would reach their maximum that equal to the total multisite protein concentration  $L_T$  under conditions of very low and very high ligand concentrations, respectively:

$$\lim_{U \rightarrow 0} N_0(U) = L_T \left( \frac{K}{K+U} \right)^n = L_T,$$

$$\lim_{U \rightarrow \infty} N_n(U) = L_T \left( \frac{U}{K+U} \right)^n = L_T.$$

Equation (2.15) can be used to estimate the half maximal effective ligand concentration ( $EC_{50}$ ),  $U_0^{0.5}$  and  $U_n^{0.5}$ , for the apo- and saturated multisite protein conformations respectively, when the protein species equal 50% of the total concentration  $L_T$ :

$$\begin{aligned}
U_0^{0.5} &= K \cdot \frac{1 - \sqrt[n]{0.5}}{\sqrt[n]{0.5}}, \\
U_n^{0.5} &= K \cdot \frac{\sqrt[n]{0.5}}{1 - \sqrt[n]{0.5}}.
\end{aligned}
\tag{2.18}$$

This solution shows that the ligand concentration for the half maximal protein activity, known as  $EC_{50}$ , would be equal to the equilibrium dissociation constant  $K$  ( $EC_{50} = K$ ) for proteins with one binding site only ( $n=1$ ). Equation (2.18) can be resolved with respect to the number of binding sites  $n$  as a function of the  $U_n^{0.5}$  and  $K$ :

$$n = 0.693 \cdot \left( \ln \left( \frac{K + U_n^{0.5}}{U_n^{0.5}} \right) \right)^{-1}.
\tag{2.19}$$

Figure 2.3A shows the dependence of  $U_0^{0.5}/K$  and  $U_n^{0.5}/K$  on the number of binding sites. The model predicts that there is a significant change in the ligand concentration  $U_n^{0.5}/K$  for the fully bound conformation compared to  $U_0^{0.5}/K$ .

In [7,20] the authors reported on the regulatory importance of the distribution of intermediate multisite protein conformations. It was suggested by the authors in these papers that the molecular forms with variable numbers of bound ligands (not only fully saturated forms) can selectively activate a protein. Here calculations are presented (Figure 2.3B) for the half-width between the half-maximal effective ligand concentrations  $U_0^{0.5}/K$  and  $U_n^{0.5}/K$  as a function of the ligand concentration for the intermediate conformations with one bound ligand for the molecules with different number of binding sites. Figure 2.3B shows that the relative magnitudes of the intermediate conformations with one bound ligand decrease for proteins with large number of binding sites.

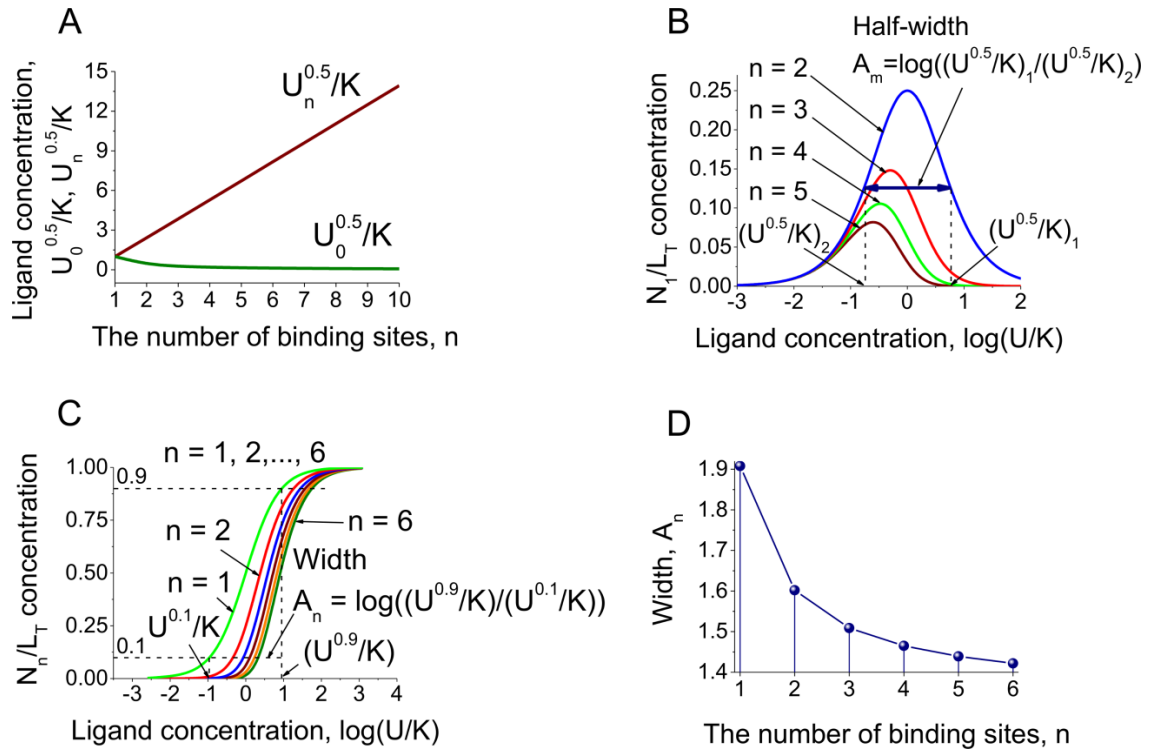


Figure 2.3. Model predictions for the half-maximal effective ligand concentrations as a function of the number of binding sites and ligand concentration.

A. The dependence of the half-maximal effective ligand concentration,  $U_0^{0.5}/K$  and  $U_n^{0.5}/K$ , for the apo- and saturated multisite protein conformations respectively, on the number of binding sites. The effect of the increasing of the amount of binding sites is negligible for the fully bound conformation. See Equation (2.18). B. Calculations for the half-width between the half-maximal effective ligand concentrations as a function of the ligand concentration for proteins with two, three, four and five binding sites (Equation (2.15) for  $m=1$  and  $n=2,3,4,5$ ). C. The difference between ligand concentrations for the saturated multisite protein conformations when the protein species equal to 90% and 10% of the total concentration as a function of the ligand concentration for the proteins with one to six binding sites. (Equation (2.15) for  $m=n$  and  $n=1,2,\dots,6$ ). D. The difference between ligand concentrations for the saturated multisite protein conformations when the protein species equal to 90% and 10% of the total concentration as a function of the number of binding sites up to six (Table 2.2).

The difference  $A_n$  between ligand concentrations  $U^{0.9}/K$  and  $U^{0.1}/K$  for the saturated multisite protein conformations, when the protein species are equal to 90% and 10% of the total concentration (Table 2.2), as a function of the ligand

concentration for proteins with different number of binding sites is shown in Figures 2.3C and 2.3D respectively.

*Table 2.2. The difference between ligand concentrations for the saturated multisite protein conformations when the protein species are equal to 90% and 10% of the total concentration.*

$n$	1	2	3	4	5	6
$A_n$	1.908	1.602	1.509	1.465	1.439	1.422

Equation (2.11) for the total amount of bound ligand, adapted for the case of multisite protein with identical binding sites, can be used to estimate the amount of bound ligand when the ligand concentration is equal to the equilibrium dissociation constant ( $U = K$ ) as shown in Equation (2.25). Our model predicts that the ligand concentration for the half maximal protein activation,  $EC_{50}$ , is equal to the equilibrium dissociation constant  $K$  for any number of bound sites for a multisite protein with identical binding sites.

According to Equations (2.2), (2.7) and (2.9) when the amount of ligand  $U = K$  we can write:

$$\begin{aligned}
 p^0(U) &= \frac{1}{2}, \\
 p^1(U) &= \frac{1}{2}, \\
 M_j(K, t) &= L_T \cdot \left(\frac{1}{2}\right)^n.
 \end{aligned} \tag{2.20}$$

And substitute it to Equation (2.11):

$$S(K, t) = \frac{L_T}{2^n} \sum_{j=0}^{2^n-1} \sum_{i=0}^{n-1} c_i(j). \tag{2.21}$$

In Equation (2.21)  $\sum_{j=0}^{2^n-1} \sum_{i=0}^{n-1} c_i(j) = \frac{1}{2} \cdot n \cdot 2^{n-1}$  since the double sum is equal to the number of bound sites multiplied by the number of molecular forms with the same amount of bound sites, and all this multiplied by 1/2 because of the



symmetry between the two states (1 and 0) in combinations. Thus we can write Equation (2.21) in the following way:

$$S(k, t) = L_T \cdot \frac{n}{4}. \quad (2.22)$$

For the case when the ligand concentration is equal to the saturating ligand concentration (when all binding sites are occupied),  $U = U^{sat}$ , we can write according to Equations (2.2), (2.7) and (2.9):

$$\begin{aligned} p^0(U) &= 0, \\ p^1(U) &= 1, \\ M_j(U^{sat}, t) &= L_T. \end{aligned} \quad (2.23)$$

Then substitute it to Equation (2.11):

$$S(U^{sat}, t) = L_T \sum_{i=0}^{n-1} c_i(j) = L_T \cdot n. \quad (2.24)$$

Comparing Equations (2.22) and (2.24) it can be written:

$$S(K, t) = \frac{1}{4} \cdot S(U^{sat}, t) \quad (2.25)$$

The dynamic alterations of intermediate conformation  $N_m(U, t)$  in response to ligand concentration jump from  $U_0$  to  $U_1$  according to Equations (2.6) and (2.7) are given by:

$$\begin{aligned} N_m(U, t) &= L_T \cdot (p^1(U, t))^m \cdot (p^0(U, t))^{n-m}, \\ p^0(U, t) &= \frac{K}{K+U_1} - \left( \frac{K}{K+U_1} - \frac{K}{K+U_0} \right) \cdot \exp\left( -\frac{t}{\tau(U_1)} \right), \\ p^1(U, t) &= \frac{U_1}{K+U_1} - \left( \frac{U_1}{K+U_1} - \frac{U_0}{K+U_0} \right) \cdot \exp\left( -\frac{t}{\tau(U_1)} \right), \\ \tau(U_1) &= \frac{K}{k^- \cdot (U_1 + K)}. \end{aligned} \quad (2.26)$$

The probabilities for a binding site to be occupied in response to the fast ligand concentration change enables the characteristic time  $\tau_m^{max}$ , when the intermediate conformations reach their maximal values, to be determined.

Differentiating Equation (2.26) with respect to  $t$  and solving for  $dN_m/dt = 0$  yields the time  $\tau_m^{max}$  when the multisite protein forms  $N_m$  with  $m$  bound molecules of ligand reach their maximal values  $N_m^{max}$ :

$$\tau_m^{max} = \tau(U_1) \cdot \ln \left( \frac{n \cdot K \cdot (U_1 - U_0)}{(K + U_0) \cdot ((n - m) \cdot U_1 - m \cdot K)} \right), \quad m = 1, 2, \dots, n - 1. \quad (2.27)$$

The substitution of  $\tau_m^{max}$  into Equation (2.26) gives the maximal values of intermediate multisite protein conformations reached at  $\tau_m^{max}$ :

$$N_m^{max} = L_T \cdot \frac{m^m}{n^n} (n - m)^{n - m}, \quad m = 1, 2, \dots, n - 1 \quad (2.28)$$

Comparison of Equations (2.17) and (2.28) suggests that the steady-state maximum values of intermediate multisite protein conformations are the same to those transiently reached during the dynamic response to the step in ligand concentration.

According to Equation (2.26)  $N_m(U, t)$  for the apo- and fully saturated forms when  $t = 0$ :

$$\begin{aligned} N_0(U, 0) &= L_T \cdot \left( \frac{K}{K + U_0} \right)^n, \\ N_n(U, 0) &= L_T \cdot \left( \frac{U_0}{K + U_0} \right)^n. \end{aligned} \quad (2.29)$$

According to Equation (2.15) steady state levels for the apo- and fully saturated forms when  $t \rightarrow \infty$ :

$$\begin{aligned}
N_0(U, \infty) &= L_T \cdot \left( \frac{K}{K + U_1} \right)^n, \\
N_n(U, \infty) &= L_T \cdot \left( \frac{U_1}{K + U_1} \right)^n.
\end{aligned} \tag{2.30}$$

Equation (2.26) is further used to define the time,  $\tau_0^{0.5}$ , required for the apo-form,  $N_0$ , to reach half of the growth concentration  $\frac{N_0(U, \infty) + N_0(U, 0)}{2}$  and the time period,  $\tau_n^{0.5}$ , required for the fully saturated protein species to gain half of the growth concentration  $\frac{N_n(U, \infty) + N_n(U, 0)}{2}$  (Figure 2.4):

$$\begin{aligned}
\tau_0^{0.5} &= \tau(U_1) \cdot \ln \left[ K \cdot \frac{U_1 - U_0}{(K + U_0) \cdot \left( (K + U_1) \cdot \left( 0.5 \cdot \left( \left( \frac{K}{K + U_0} \right)^n + \left( \frac{K}{K + U_1} \right)^n \right) \right)^{\frac{1}{n}} - K} \right]}, \\
\tau_n^{0.5} &= \tau(U_1) \cdot \ln \left[ K \cdot \frac{U_1 - U_0}{(K + U_0) \cdot \left( U_1 - (K + U_1) \cdot \left( 0.5 \cdot \left( \left( \frac{U_0}{K + U_0} \right)^n + \left( \frac{U_1}{K + U_1} \right)^n \right) \right)^{\frac{1}{n}} \right)}.
\end{aligned} \tag{2.31}$$

Figure 2.4 represents the calculations for the temporal characteristics of the apo- and fully bound species. Figures 2.4A and 2.4B show that the temporal shapes of the apo- and fully bound conformations in response to a ligand change are similar to the steady-state dependence of the same conformations on ligand concentration, which corresponds to Figure 1B in [7] reproduced here as Figure 2.4C.

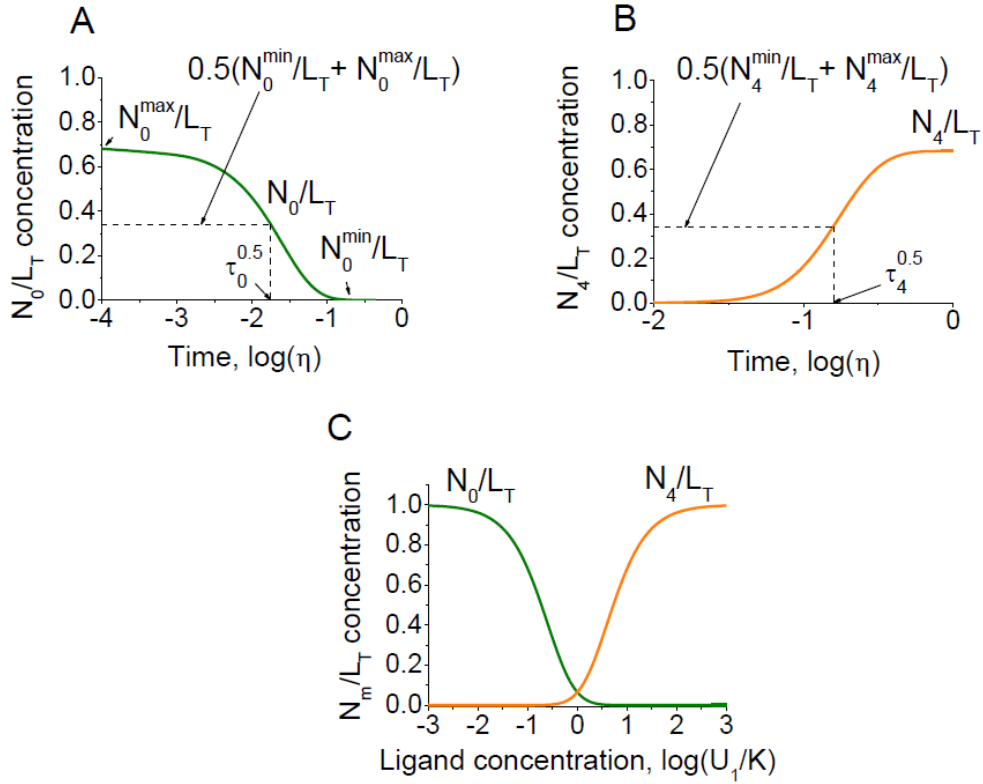


Figure 2.4. Temporal characteristics of the apo- and fully bound species in response to a ligand jump.

The dynamics of the concentration of proteins is investigated for apo- (A) and fully bound (B) forms in response to the ligand concentration change from  $U_0/K = 0.1$  to  $U_1/K = 10$ . The dotted lines indicate the time,  $\tau_0^{0.5}$ , required for the apo- conformation,  $N_0/L_T$ , to reach half of the fall in concentration and the period of time,  $\tau_4^{0.5}$ , that takes for the fully saturated protein species,  $N_4/L_T$ , to gain half of the growth in concentration. See Equations (2.26). The shapes of the temporal characteristics of the apo- and fully bound species in response to a ligand jump shown in (A) and (B) are similar to the corresponding shapes for the steady-state dependence obtained in [7] and reproduced here in (C).

The kinetic parameters,  $\tau_0^{0.5}$  and  $\tau_4^{0.5}$  can be estimated as the time required to reach 50% of the total concentration (Figures 2.4A and 2.4B). These kinetic parameters are investigated as a function of the initial and final ligand concentrations (Figures 2.5A and 2.5B). Our analysis reveals an inhibition shape and a reduction of the time constant  $\tau_0^{0.5}$  for the apo- conformation with the reduction of the initial ligand concentration  $U_0/K$  and the increase of the final ligand concentration  $U_1/K$  (Figure 2.5). However, the dependence of the

characteristic time  $\tau_4^{0.5}$  shows a non-trivial bell shape on the final ligand concentration compared to the simpler monotonic dependence for  $\tau_0^{0.5}$  shown in Figure 2.5A.

The bell shaped dependence of  $\tau_4^{0.5}$  on final ligand concentration shown in Figure 2.5B appears to be related to the presence of intermediate conformations. When  $n=1$ , that is in the absence of intermediate forms,  $\tau_4^{0.5}$  depends on  $U_1/K$  monotonically, i.e. there is no bell shaped dependence, as is evident from Equation (2.31). In multisite proteins ( $n>1$ ), the activation of intermediate conformations takes extra time, which affects  $\tau_4^{0.5}$ . This activation precedes the activation of the saturated form in time, and also as  $U_1/K$  increases, i.e. the intermediate conformations are more prevalent for smaller values of  $U_1/K$ , and the stationary distribution shifts towards the saturated form for larger  $U_1/K$ . As a result, an increase of  $U_1/K$  leads to an increase of the contribution of the kinetics of the intermediate complexes to the overall dynamics, and hence to an increase of  $\tau_4^{0.5}$ . Mathematically, the extra time associated with activation of intermediate forms is represented by the second factor in Equation (2.31). The dependence of the first factor,  $\tau(U_1)$ , on  $U_1/K$  is monotonically decreasing, which corresponds to the fact that all individual kinetic rates monotonically increase with  $U_1/K$ . Thus, in the dependence of  $\tau_4^{0.5}$  on  $U_1/K$ , there are two competing tendencies: the first factor is monotonically decreasing, and the second factor is monotonically increasing. As follows from the mathematical model, the dependence of this second factor on  $U_1/K$  is with saturation. As a result, the role of intermediate conformations is more pronounced for smaller  $U_1/K$ , so  $\tau_4^{0.5}$  increases, whereas for larger  $U_1/K$ , this role is less important and overall speed-up dominates, hence  $\tau_4^{0.5}$  decreases. Thus the model predicts that there is an intermediate ligand concentration, at which the kinetics of the fully saturated form, represented by  $\tau_4^{0.5}$ , is the slowest. Note that although Figures 2.4 and 2.5 show an example of four sites,

the results are more general than that, as Equations (2.26) and (2.31) are valid for arbitrary number  $n$  of binding sites.

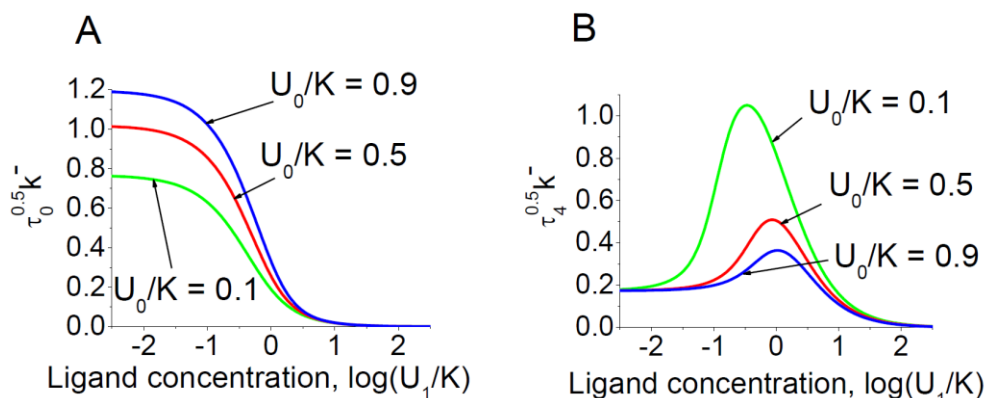


*Figure 2.5. The characteristic times for apo- and fully bound forms as a function of the final ligand concentrations.*

*The time  $\tau_0^{0.5}$ , required for the apo- conformation,  $N_0 / L_T$ , to reach half of the fall in concentration (A) and the time,  $\tau_4^{0.5}$ , that takes for the fully saturated protein species,  $N_4 / L_T$ , to gain half of the growth in concentration (B), are subject to the investigation as a function of the initial and final ligand concentrations. The presented analysis clearly demonstrates the bell shaped dependence of  $\tau_4^{0.5}$  on the final ligand concentration (B). See Equations (2.31).*

The proposed model will be employed to investigate the ligand jump-dependent kinetics of both saturated and non-saturated conformations. Initially, an idealized model of a multisite protein with identical binding sites will be used to investigate the impact of ligand concentrations on the multisite protein kinetics. However, in living cells there are very few proteins (if any) that have identical ligand binding sites. Therefore the model will be next extended to examine the implications of variations in binding site affinities on the predicted concentration-response profiles.

### **2.3.2 Multisite proteins with four identical ligand binding sites**

This model next considers the kinetic properties of a protein with four binding sites. This allows  $2^4 = 16$  molecular forms, each with potentially unique biochemical properties. There are four possible combinations of protein species

bound to one or to three ligands, and six possible distinct molecular forms with two sites occupied. In [7,20,86] the authors described the steady-state dependence of the individual multisite conformations on ligand concentration. Here we analyse the kinetic transition of the individual species concentrations in response to the step in ligand concentration.

The dynamical alterations of intermediate conformation  $N_m(U, t)$  in response to a step in ligand concentration from  $U_0$  to  $U_1$  according to Equation (2.26) are given by:

$$N_m(u, \eta) = L_T \cdot (p^1(u, \eta))^m \cdot (p^0(u, \eta))^{4-m},$$

$$p^0(u, \eta) = \frac{1}{1+u_1} - \left( \frac{1}{1+u_1} - \frac{1}{1+u_0} \right) \cdot \exp(-\eta \cdot (u_1 + 1)),$$

$$p^1(u, \eta) = \frac{u_1}{1+u_1} - \left( \frac{u_1}{1+u_1} - \frac{u_0}{1+u_0} \right) \cdot \exp(-\eta \cdot (u_1 + 1)),$$
(2.32)

where:  $u_0 = \frac{U_0}{K}$ ,  $u_1 = \frac{U_1}{K}$  are non dimensional ligand concentrations, and  $\eta = t \cdot k^-$  is non dimensional time. The parameters  $k^-$  and  $K = \frac{k^-}{k^+}$  are the dissociation and equilibrium dissociation constants for ligand binding, respectively.

The maximum values of  $N_m^{max}$  are reached at the following ligand concentrations:  $u_1^{max} = \frac{K}{3}$ ,  $u_2^{max} = K$ ,  $u_3^{max} = 3K$ , for the multisite protein species with one, two and three bound ions respectively, according to Equation (2.16) and equal  $N_1^{max} = 0.105L_T$ ,  $N_2^{max} = 0.063L_T$ ,  $N_3^{max} = 0.105L_T$  according to Equation (2.17).

Differentiating Equation (2.32) with respect to  $\eta$  and solving  $dN_m/d\eta = 0$  for  $\eta$  gives the non dimensional time  $\eta_m^{max} = \tau_m^{max} k^-$  when the intermediate species reach their maximum:

$$\begin{aligned}
\eta_1^{max} = \tau_1^{max} k^- &= \frac{1}{u_1 + 1} \ln \left( \frac{4 \cdot (u_1 - u_0)}{(1 + u_0) \cdot (3u_1 - 1)} \right), \\
\eta_2^{max} = \tau_2^{max} k^- &= \frac{1}{u_1 + 1} \ln \left( \frac{2 \cdot (u_1 - u_0)}{(1 + u_0) \cdot (u_1 - 1)} \right), \\
\eta_3^{max} = \tau_3^{max} k^- &= \frac{1}{u_1 + 1} \ln \left( \frac{4 \cdot (u_1 - u_0)}{(1 + u_0) \cdot (u_1 - 3)} \right).
\end{aligned} \tag{2.33}$$

Equations (2.33) suggest that  $\eta_1^{max}$ ,  $\eta_2^{max}$  and  $\eta_3^{max}$  are undefined when  $u_1 < \frac{1}{3}$ ,  $u_1 < 1$  and  $u_1 < 3$ , respectively ( $q_1$ ,  $q_2$  and  $q_3$  asymptotes). Under these conditions, the intermediate species do not reach the maximum in response to ligand step, instead their relative number increase in a monotonous manner.

Figure 2.6 shows the dependence of the time point  $\tau_m^{max} k^-$  when the intermediate protein conformations reach the maximum as a function of magnitude of ligand jump. It can be seen from Equations (2.33) that  $\tau_1^{max} k^-$ ,  $\tau_2^{max} k^-$  and  $\tau_3^{max} k^-$  do not exist for  $U_1/K < \frac{1}{3}$ ,  $U_1/K < 1$  and  $U_1/K < 3$  respectively. Under these special cases, the concentrations of the intermediate conformations do not reach their maximal values, instead, they monotonously grow to their respective steady-state levels.



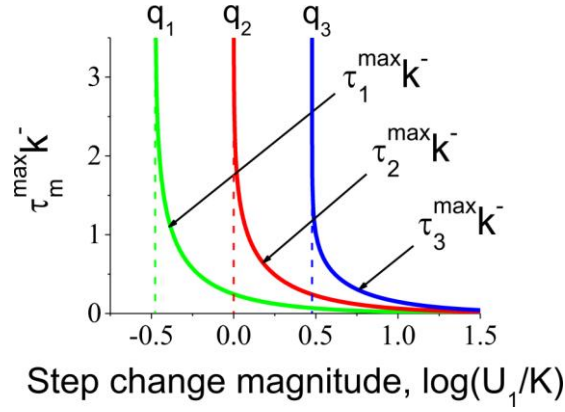


Figure 2.6. Characteristic time required for intermediate conformations to reach their maximum levels as a function of the step change magnitude. The analysis shows that the time required for reaching the maximum level of the intermediate species is inversely proportional to the concentration of the applied ligand (Equations (2.33) for the initial ligand concentration  $U_0/K = 0.1$ ). This effect is due to the growing abundance of the free ligand concentration available for faster interaction with the multisite protein.

### 2.3.3 Multisite proteins with four different ligand binding sites

In the previous subsection we analysed the ligand-binding kinetics of a protein with four identical binding sites. In this subsection we assume that these four sites are different and analyse the kinetic properties of the multisite protein. The steady-state analysis can be found in the previously published investigation [7,20].

We assume that all association  $k_1^+$ ,  $k_2^+$ ,  $k_3^+$ ,  $k_4^+$  and dissociation  $k_1^-$ ,  $k_2^-$ ,  $k_3^-$ ,  $k_4^-$  rates are unique for each binding centre. Then, assuming for example that  $k_1^+ > k_2^+ > k_3^+ > k_4^+$  and  $k_1^- = k_2^- = k_3^- = k_4^-$ , the non dimensional concentration  $u = \frac{U}{K}$

and non dimensional constants  $h_1 = 1$ ,  $h_2 = \frac{k_2^+}{k_1^+}$ ,  $h_3 = \frac{k_3^+}{k_1^+}$ ,  $h_4 = \frac{k_4^+}{k_1^+}$ ,  $h_1^- = 1$ ,

$h_2^- = \frac{k_2^-}{k_1^-} = 1$ ,  $h_3^- = \frac{k_3^-}{k_1^-} = 1$ ,  $h_4^- = \frac{k_4^-}{k_1^-} = 1$  can be introduced.

The set of Equations (2.32) can then be employed to calculate the dynamics of the multisite protein conformations bound to a different number of ligand molecules.

To investigate the impact of the dissociation constants of individual binding sites we employ the multisite protein model with marginally (Figure 2.7) and significantly different association constants (Figure 2.8).

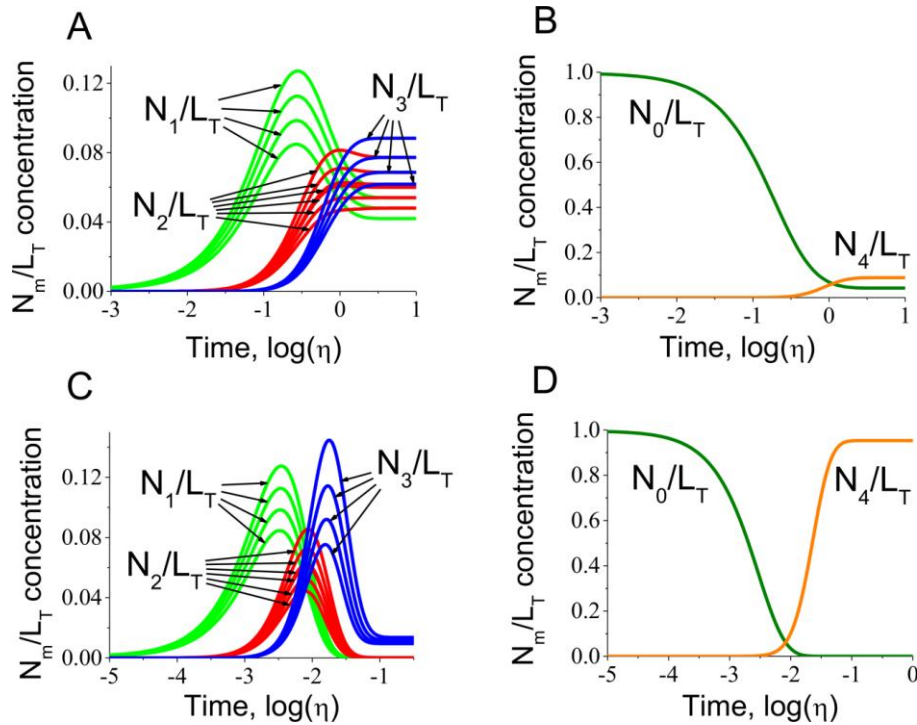


Figure 2.7. Kinetics predictions for multisite protein species with marginally different association constants.

The kinetics of multisite protein species (Equations (2.32)) is investigated for the intermediate (A) as well as for apo- and fully bound conformations (B) in response to step change of ligand from  $U_0/K = 0.001$  to  $U_1/K = 1.43$  for slightly different association constants  $h_1 = 1, h_2 = 0.9, h_3 = 0.8, h_4 = 0.7$  and equal dissociation constants  $h_1^- = h_2^- = h_3^- = h_4^- = 1$ . Similar analysis is also performed when step change is  $U_0/K = 0.001, U_1/K = 100$  for the intermediate (C) as well as for apo- and fully bound forms (D). The calculations show that the final level of the multisite protein species is defined by the ligand concentration after the step change. It is clear that the fully bound species are not saturated and most of the ligand is distributed among species bound to fewer ligands. However, step change application of ligand with much higher concentration from  $U_0/K = 0.001$  to  $U_1/K = 100$  for apo- (C) and fully bound (D) species demonstrate that the application of higher concentrations of ligand causes full saturation of the protein.

In previous studies [7,20] the authors suggested that intermediate protein conformations can selectively activate a protein. In these works steady-state analysis of the concentration of the intermediate, apo- and fully- saturated forms was presented. It was shown in [7,20] that the distribution of the intermediate forms has the bell shape in steady-state. However it has been remained unclear whether the temporal distribution of the intermediate forms is also bell-shaped. In previously published modelling papers, where the kinetics of multi ligand-receptor binding was studied [19,93], only fully saturated forms of multisite proteins were analysed.

The main result that follows from the analysis of the intermediate conformation curves presented in this section is that the temporal distribution of the intermediate conformations of multisite proteins is bell-shaped and the affinities of the different binding sites mainly affect the magnitudes of corresponding protein conformation. For example, the conformation of a multisite protein corresponding to the one ligand bound state is present in lower concentration if the affinity of the binding centre is lower (Figures 2.7 and 2.8). However the overall shape of the concentration dependent profile is not changed. This property is similar to the case of steady-state dependence on the ligand concentration. The only difference is that the bell shape dependence on time during the kinetic response is partially skewed.

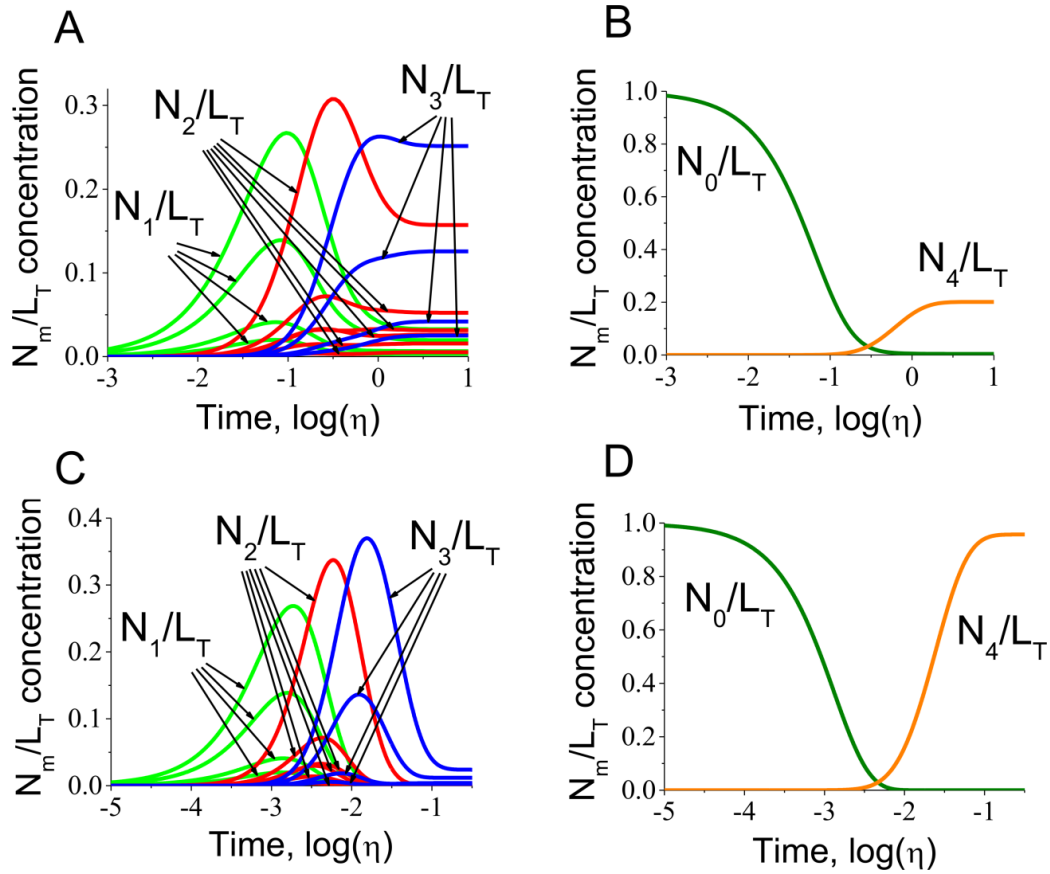


Figure 2.8. Kinetics of multisite protein species alterations for a protein with significantly different association constants.

The kinetics of multisite protein species (Equations (2.32)) is investigated in response to step change of ligand from  $U_0/K=0.001$  to  $U_1/K=8$  and to  $U_1/K=400$  for the intermediate (A), (C) as well as for apo- and fully bound conformations (B), (D), respectively, in the case of significantly different association  $h_1=1$ ,  $h_2=0.6$ ,  $h_3=0.2$ ,  $h_4=0.1$  and the same dissociation constants  $h_1^- = h_2^- = h_3^- = h_4^- = 1$ . The comparison with the kinetics of the protein with slightly different association constants suggest that in this case the species acquire a degree of asynchronous dynamics.

### 2.3.4 The effects of cooperativity

In order to investigate the influence of cooperativity, we chose a well-characterised protein, CaM, as the model object. The CaM protein contains two independent EF-hand globular domains, with two binding sites [22,65,67,81,82]. The sites within each of the domains cooperatively influence each other. It was reported that cooperative binding occurs between two neighbouring sites within the N- and C- terminal domains of CaM [20,103,104].

The molecule contains two independent domains  $A$  and  $B$ , with two identical cooperative binding sites. The association/dissociation kinetics at the domain  $A$  is described as follows:



The ODEs for the scheme (2.34) are given by:

$$\begin{aligned}
 \frac{dA_{00}(U,t)}{dt} &= -2k_1^+ \cdot A_{00}(U,t) \cdot U + k_1^- \cdot A_{10}(U,t) + k_1^- \cdot A_{01}(U,t), \\
 \frac{dA_{10}(U,t)}{dt} &= k_1^+ \cdot A_{00}(U,t) \cdot U - k_1^- \cdot A_{10}(U,t) - kc_1^+ \cdot A_{10}(U,t) \cdot U + kc_1^- \cdot A_{11}(U,t), \\
 \frac{dA_{01}(U,t)}{dt} &= k_1^+ \cdot A_{00}(U,t) \cdot U - k_1^- \cdot A_{01}(U,t) - kc_1^+ \cdot A_{01}(U,t) \cdot U + kc_1^- \cdot A_{11}(U,t), \\
 \frac{dA_{11}(U,t)}{dt} &= kc_1^+ \cdot A_{01}(U,t) \cdot U + kc_1^+ \cdot A_{10}(U,t) \cdot U - 2kc_1^- \cdot A_{11}(U,t),
 \end{aligned} \tag{2.35}$$

The total number of species that follows from Equations (2.35) is given by:

$$A_{00}(U,t) + A_{10}(U,t) + A_{01}(U,t) + A_{11}(U,t) = A_T. \tag{2.36}$$

The steady-state solutions of the system (2.35) are given by:

$$\begin{aligned}
A_{00}(U) &= A_r \cdot \frac{K_1 \cdot K_1^c}{U^2 + 2 \cdot K_1^c \cdot U + K_1 \cdot K_1^c}, \\
A_{10}(U) &= A_r \cdot \frac{U \cdot K_1^c}{U^2 + 2 \cdot K_1^c \cdot U + K_1 \cdot K_1^c}, \\
A_{01}(U) &= A_r \cdot \frac{U \cdot K_1^c}{U^2 + 2 \cdot K_1^c \cdot U + K_1 \cdot K_1^c}, \\
A_{11}(U) &= A_r \cdot \frac{U^2}{U^2 + 2 \cdot K_1^c \cdot U + K_1 \cdot K_1^c},
\end{aligned} \tag{2.37}$$

where  $K_1 = \frac{k_1^-}{k_1^+}$  and  $K_1^c = \frac{kc_1^-}{kc_1^+}$ .

One can re-write Equations (2.37) as follows:

$$\begin{aligned}
a_0(U) &= \frac{K_1 \cdot K_1^c}{U^2 + 2 \cdot K_1^c \cdot U + K_1 \cdot K_1^c}, \\
a_1(U) &= \frac{U \cdot K_1^c}{U^2 + 2 \cdot K_1^c \cdot U + K_1 \cdot K_1^c}, \\
a_2(U) &= \frac{U^2}{U^2 + 2 \cdot K_1^c \cdot U + K_1 \cdot K_1^c},
\end{aligned} \tag{2.38}$$

where  $a_0(U) = \frac{A_{00}(U)}{A_r}$ ,  $a_1(U) = \frac{A_{10}(U)}{A_r} = \frac{A_{01}(U)}{A_r}$ ,  $a_2(U) = \frac{A_{11}(U)}{A_r}$  are the

probabilities for the domain to be in a particular conformation due to the bound ligand molecules.

The probabilities for the other domain, which also contains a pair of cooperative binding sites, are given by:

$$\begin{aligned}
b_0(U) &= \frac{K_2 \cdot K_2^c}{U^2 + 2 \cdot K_2^c \cdot U + K_2 \cdot K_2^c}, \\
b_1(U) &= \frac{U \cdot K_2^c}{U^2 + 2 \cdot K_2^c \cdot U + K_2 \cdot K_2^c}, \\
b_2(U) &= \frac{U^2}{U^2 + 2 \cdot K_2^c \cdot U + K_2 \cdot K_2^c}.
\end{aligned} \tag{2.39}$$

These probabilities were derived for the two domains of the molecule (Equations (2.38) and (2.39) respectively). The probabilities of the molecule to be in a certain conformation with 0, 1 or 2 bound ligands in each of the domains, are as follows:

$$\begin{aligned}
p_{0,0}(U) &= a_0(U) \cdot b_0(U), \\
p_{0,1}(U) &= a_0(U) \cdot 2b_1(U), \\
p_{0,2}(U) &= a_0(U) \cdot b_2(U), \\
p_{1,0}(U) &= 2a_1(U) \cdot b_0(U), \\
p_{1,1}(U) &= 2a_1(U) \cdot 2b_1(U), \\
p_{1,2}(U) &= 2a_1(U) \cdot b_2(U), \\
p_{2,0}(U) &= a_2(U) \cdot b_0(U), \\
p_{2,1}(U) &= a_2(U) \cdot 2b_1(U), \\
p_{2,2}(U) &= a_2(U) \cdot b_2(U),
\end{aligned} \tag{2.40}$$

where  $p_{i,j}(U)$  is the probability of the protein conformation with  $i$  bound sites in one domain and  $j$  bound sites in the other. We use the sum of probabilities for the case of one bound site in a domain since we assume that in either domain, all its sites are identical.

The concentrations of the molecular forms of the protein with certain number of bound sites are given by:

$$\begin{aligned}
N_0(U) &= L_T \cdot p_{0,0}(U), \\
N_1(U) &= L_T \cdot (p_{0,1}(U) + p_{1,0}(U)), \\
N_2(U) &= L_T \cdot (p_{0,2}(U) + p_{1,1}(U) + p_{2,0}(U)), \\
N_3(U) &= L_T \cdot (p_{1,2}(U) + p_{2,1}(U)), \\
N_4(U) &= L_T \cdot p_{2,2}(U),
\end{aligned} \tag{2.41}$$

One can rewrite Equation (2.41) as follows:

$$\begin{aligned}
\frac{N_0(U)}{L_T} &= a_0(U) \cdot b_0(U), \\
\frac{N_1(U)}{L_T} &= 2 \cdot (a_0(U) \cdot b_1(U) + a_1(U) \cdot b_0(U)), \\
\frac{N_2(U)}{L_T} &= a_0(U) \cdot b_2(U) + 4 \cdot a_1(U) \cdot b_1(U) + a_2(U) \cdot b_0(U), \\
\frac{N_3(U)}{L_T} &= 2 \cdot (a_1(U) \cdot b_2(U) + a_2(U) \cdot b_1(U)), \\
\frac{N_4(U)}{L_T} &= a_2(U) \cdot b_2(U),
\end{aligned} \tag{2.42}$$

Next we find the kinetic solution of system (2.35) for  $U = U_1$ :

$$\begin{aligned}
\frac{dA_{00}(U, t)}{dt} &= -2k_1^+ \cdot A_{00}(U, t) \cdot U_1 + k_1^- \cdot A_{10}(U, t) + k_1^- \cdot A_{01}(U, t), \\
\frac{dA_{10}(U, t)}{dt} &= k_1^+ \cdot A_{00}(U, t) \cdot U_1 - k_1^- \cdot A_{10}(U, t) - kc_1^+ \cdot A_{10}(U, t) \cdot U_1 + kc_1^- \cdot A_{11}(U, t), \\
\frac{dA_{01}(U, t)}{dt} &= k_1^+ \cdot A_{00}(U, t) \cdot U_1 - k_1^- \cdot A_{01}(U, t) - kc_1^+ \cdot A_{01}(U, t) \cdot U_1 + kc_1^- \cdot A_{11}(U, t), \\
\frac{dA_{11}(U, t)}{dt} &= kc_1^+ \cdot A_{01}(U, t) \cdot U_1 + kc_1^+ \cdot A_{10}(U, t) \cdot U_1 - 2kc_1^- \cdot A_{11}(U, t),
\end{aligned} \tag{2.43}$$

Figure 2.9 shows the model predictions for CaM, where we assume that the molecule has two independent domains, with two identical cooperative sites. In the first domain the affinity of one site changes from  $K_1 = 0.9 \mu\text{M}$  to  $K_1^c = 0.2 \mu\text{M}$  if the other site is occupied and in the second domain the affinity changes from  $K_2 = 0.8 \mu\text{M}$  to  $K_2^c = 0.1 \mu\text{M}$  according to Equation (2.35) and [20]. Figures 2.9A and 2.9B show the influence of cooperativity on the steady-state concentrations of CaM with certain number of bound sites. The presence of cooperativity shifts the dose-response characteristics along the ligand concentration axis and changes the magnitude of intermediate conformations allowing more developed selective regulation of the activity of CaM. The investigation of the dynamic properties of cooperativity in CaM (Figures 2.9C and 2.9D) for intermediate, apo- and saturated species revealed that the cooperativity influences the



magnitudes of time-dependent characteristics. The proposed model predicts that the cooperative binding leads to higher differences between the initial and steady-state levels for the apo- and saturated forms as shown in Figure 2.9.

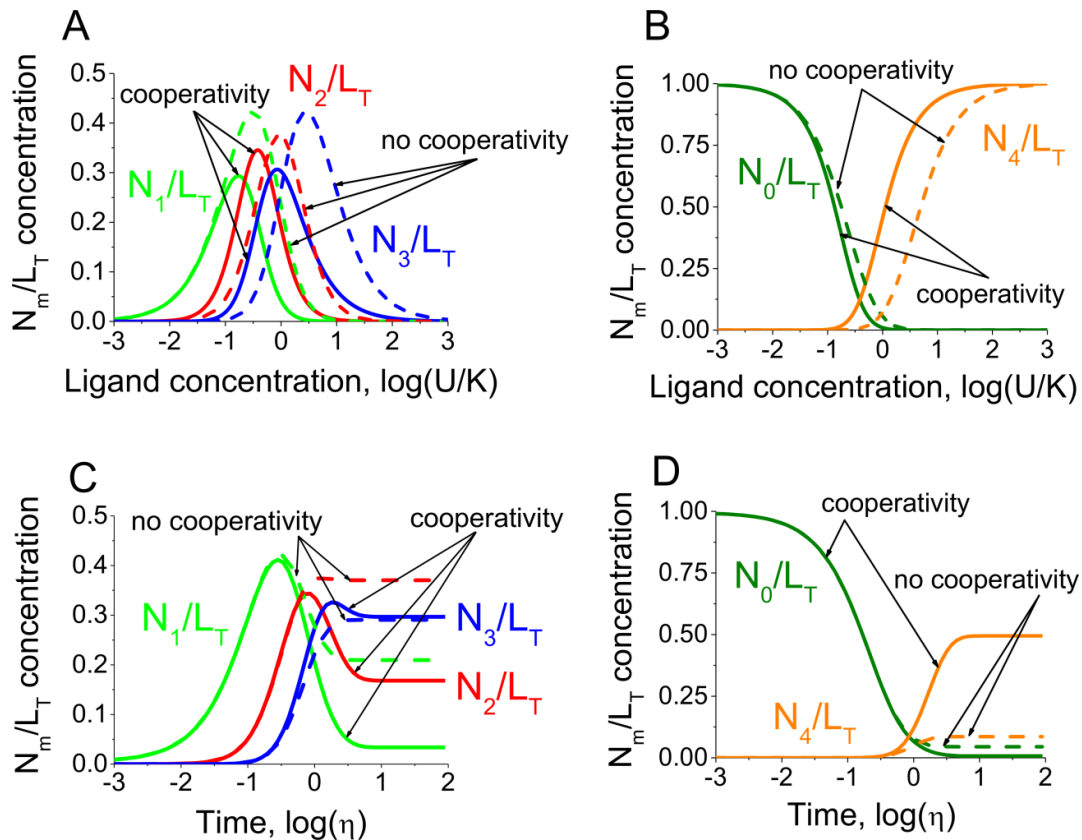


Figure 2.9. Comparative analysis of cooperative versus non-cooperative  $\text{Ca}^{2+}$  binding to CaM.

Two mathematical models for  $\text{Ca}^{2+}$ -CaM interactions are compared under the assumptions for the presence and absence of cooperative binding. The comparison between the two scenarios is performed under steady state conditions (A), (B) and in response to a step change in  $\text{Ca}^{2+}$  concentration from  $U_0/K = 0.001$  to  $U_1/K = 1$  (C), (D). The model predicts that the cooperativity influences the magnitudes the concentrations of the maximums for the intermediate forms. However, the differences observed in the distribution of the conformation species in the presence and absence of the cooperative binding are quantitative while the overall shape of the distributions remain unchanged. Due to this finding the following model analysis will be performed without cooperative binding assumptions. Equations (2.42) are used in (A), (B) and Equations (2.43) are used in (C), (D).

The results of the present analysis suggest that cooperativity plays an important role in the regulation of the activity of multisite proteins by allowing wider

possibilities for selectivity. However, the presence of cooperativity leads to quantitative rather than qualitative changes in the system. Here by qualitative changes we mean the shapes of the distribution of concentrations of corresponding protein conformations. The introduction of cooperative binding is crucial for the experimental data fitting but at the same time brings further complexity to the system, which does not necessarily lead to a better understanding of the underlying mechanisms. As a result of this, further analysis will be carried out without considering this effect.

## 2.4 The model for comparable ligand and protein concentrations

In the previous section we considered the physiological case, where the ligand concentration is above saturation level meaning that the ligand-multisite protein interactions do not affect the availability of the ligand. Here we assume that the amount of ligand is limited. This can occur in cases where the ligand concentration level is comparable to the multisite protein concentration. We also assume that ligand binding to each site of the protein are independent events.

Under these assumptions the system of differential equations for ligand binding to a molecule with single binding site (2.5) needs to be complemented by the equation of ligand conservation:

$$\begin{aligned}\frac{dL^0(U,t)}{dt} &= -k^+ \cdot L^0(U,t) \cdot U(t) + k^- \cdot L^1(U,t), \\ \frac{dL^1(U,t)}{dt} &= k^+ \cdot L^0(U,t) \cdot U(t) - k^- \cdot L^1(U,t), \\ L^0(U,t) + L^1(U,t) &= L_T, \\ U(t) + L^1(U,t) &= U_T,\end{aligned}\tag{2.44}$$

where  $L^0$  is the concentration of the free site,  $L^1$  is the concentration of the occupied site,  $U_T$  and  $L_T$  are the total concentrations of ligand and protein molecules, respectively.

The steady-state solutions (please see Appendix B for the derivation) of the system (2.44) are:

$$\begin{aligned}
L^0(U_T) &= \frac{K}{2} \cdot \left( \frac{L_T}{K} - \frac{U_T}{K} - 1 + F(U_T) \right), \\
L^1(U_T) &= \frac{K}{2} \cdot \left( \frac{L_T}{K} + \frac{U_T}{K} + 1 - F(U_T) \right), \\
U &= U_T - \frac{K}{2} \cdot \left( \frac{L_T}{K} + \frac{U_T}{K} + 1 - F(U_T) \right),
\end{aligned} \tag{2.45}$$

$$\text{where } K = \frac{k^-}{k^+} \text{ and } F(U_T) = \sqrt{\left( \frac{U_T}{K} - \frac{L_T}{K} \right)^2 + 2 \cdot \left( \frac{U_T}{K} + \frac{L_T}{K} \right) + 1}.$$

We use the steady-state solutions (2.45) as initial conditions to find the particular solution. The solution of the system (2.44) in response to the ligand concentration jump from  $U_{T0}$  to  $U_{T1}$  is given by:

$$\begin{aligned}
L^0(U_T, t) &= L_T \cdot \left( \frac{K}{2 \cdot L_T} \cdot \left( \frac{L_T}{K} - \frac{U_{T1}}{K} - 1 + F(U_{T1}) \cdot \frac{C(U_T) \cdot \exp(t \cdot k^- \cdot F(U_{T1})) + 1}{C(U_T) \cdot \exp(t \cdot k^- \cdot F(U_{T1})) - 1} \right) \right), \\
L^1(U_T, t) &= L_T \cdot \left( 1 - \frac{K}{2 \cdot L_T} \cdot \left( \frac{L_T}{K} - \frac{U_{T1}}{K} - 1 + F(U_{T1}) \cdot \frac{C(U_T) \cdot \exp(t \cdot k^- \cdot F(U_{T1})) + 1}{C(U_T) \cdot \exp(t \cdot k^- \cdot F(U_{T1})) - 1} \right) \right), \\
U(t) &= U_{T1} - L_T \cdot \left( 1 - \frac{K}{2 \cdot L_T} \cdot \left( \frac{L_T}{K} - \frac{U_{T1}}{K} - 1 + F(U_{T1}) \cdot \frac{C(U_T) \cdot \exp(t \cdot k^- \cdot F(U_{T1})) + 1}{C(U_T) \cdot \exp(t \cdot k^- \cdot F(U_{T1})) - 1} \right) \right).
\end{aligned} \tag{2.46}$$

(please see Appendix B for the derivation)

The normalisation of the solution (2.46) by the total protein concentration allows the definition of probability of the binding site to be in an occupied  $p^1(U_T, t)$  or unoccupied  $p^0(U_T, t)$  state, respectively, at a given total ligand concentration:

$$\begin{aligned}
p^0(U_T, \eta) &= \frac{K}{2 \cdot L_T} \cdot \left( \frac{L_T}{K} - \frac{U_{T1}}{K} - 1 + F(U_{T1}) \cdot \frac{C_2(U_T) \cdot \exp(\eta \cdot F(U_{T1})) + 1}{C_2(U_T) \cdot \exp(\eta \cdot F(U_{T1})) - 1} \right), \\
p^1(U_T, \eta) &= \frac{K}{2 \cdot L_T} \cdot \left( \frac{L_T}{K} + \frac{U_{T1}}{K} + 1 - F(U_{T1}) \cdot \frac{C_2(U_T) \cdot \exp(\eta \cdot F(U_{T1})) + 1}{C_2(U_T) \cdot \exp(\eta \cdot F(U_{T1})) - 1} \right), \\
\frac{U(\eta)}{K} &= \frac{U_{T1}}{K} - \frac{1}{2} \cdot \left( \frac{L_T}{K} + \frac{U_{T1}}{K} + 1 - F(U_{T1}) \cdot \frac{C_2(U_T) \cdot \exp(\eta \cdot F(U_{T1})) + 1}{C_2(U_T) \cdot \exp(\eta \cdot F(U_{T1})) - 1} \right),
\end{aligned} \tag{2.47}$$

where  $\eta = t \cdot k^-$ .

The concentration of the  $j$ -th molecular form,  $M_j(U_T, t)$ , of a protein with  $n$  independent binding sites in response to a step change in ligand concentration is given by the product of probabilities according to Equation (2.9):

$$M_j(U_T, t) = L_T \cdot \prod_{i=0}^{n-1} p^{c_i(j)}(U_T, t), \quad j = 0, \dots, 2^n - 1 \quad (2.48)$$

where  $c_i(j)$  equals 0 or 1 for free and occupied sites, respectively and

$$j = \sum_{i=0}^{n-1} 2^i c_i(j).$$

The kinetics of the amount of ligand bound to a multisite protein with  $n$  independent binding sites can be written as follows:

$$S(U_T, t) = \sum_{j=0}^{2^n-1} M_j(U_T, t) \sum_{i=0}^{n-1} c_i(j). \quad (2.49)$$

The concentration of free ligand can be written as the difference between the total ligand concentration and the bound ligand concentration (2.49):

$$U(t) = U_{T1} - S(U_T, t). \quad (2.50)$$

The probabilities of the  $i$ -th site to be free or occupied respectively for the molecule with  $n$  independent binding sites in this case:

$$p_i^0(U_T, \eta) = \frac{K_i}{2 \cdot n \cdot L_T} \cdot \left( \frac{n \cdot L_T}{K_i} - \frac{U_{T1}}{K_i} - 1 + F(U_{T1}) \cdot \frac{C(U_T) \cdot \exp(\eta \cdot F(U_{T1})) + 1}{C(U_T) \cdot \exp(\eta \cdot F(U_{T1})) - 1} \right), \quad (2.51)$$

$$p_i^1(U_T, \eta) = \frac{K_i}{2 \cdot n \cdot L_T} \cdot \left( \frac{n \cdot L_T}{K_i} + \frac{U_{T1}}{K_i} + 1 - F(U_{T1}) \cdot \frac{C(U_T) \cdot \exp(\eta \cdot F(U_{T1})) + 1}{C(U_T) \cdot \exp(\eta \cdot F(U_{T1})) - 1} \right),$$

where  $F(U_T) = \sqrt{\left(\frac{U_T - n \cdot L_T}{K_i}\right)^2 + 2 \cdot \left(\frac{U_T + n \cdot L_T}{K_i}\right) + 1}$  and

$$C(U_T) = \frac{F(U_{T0}) + F(U_{T1}) + \frac{U_{T1}}{K_i} - \frac{U_{T0}}{K_i}}{F(U_{T0}) - F(U_{T1}) + \frac{U_{T1}}{K_i} - \frac{U_{T0}}{K_i}}.$$

The dynamic alterations of the molecular forms with  $m$  bound out of  $n$  independent identical binding sites  $N_m(U_T, t)$  in response to the total ligand concentration jump from  $U_{T0}$  to  $U_{T1}$  according to Equations (2.26) and (2.51) are given by:

$$N_m(U_T, t) = L_T \cdot (p^1(U_T, t))^m \cdot (p^0(U_T, t))^{n-m}. \quad (2.52)$$

The concentration of multisite protein conformations,  $N_m$ , bound to  $m$  ligand molecules as a function of ligand concentration in steady-state is given by:

$$N_m(U_T) = L_T \left( \frac{K}{2nL_T} \left( \frac{nL_T}{K} + \frac{U_T}{K} + 1 - F(U_T) \right) \right)^m \cdot \left( \frac{K}{2nL_T} \left( \frac{nL_T}{K} - \frac{U_T}{K} - 1 + F(U_T) \right) \right)^{n-m} \quad (2.53)$$

The ligand concentrations,  $U_m^{max}$ , for the maximal values of intermediate protein conformations,  $N_m(U_m^{max})$ , can be found by differentiating Equation (2.53) with respect to  $U_T$  and solving  $dN_m/dU_T = 0$  for  $U_T$ :

$$U_m^{max} = m \cdot \left( L_T + \frac{K}{n-m} \right) \quad (2.54)$$

The corresponding maximal magnitudes for the intermediate conformations are given by:

$$N_m(U_m^{max}) = L_T \cdot \frac{m^m}{n^n} \cdot (n-m)^{n-m} \quad (2.55)$$

The half maximal effective ligand concentration,  $U_0^{0.5}$  and  $U_n^{0.5}$ , when the protein species equal half of the total concentration  $L_T$ , for the apo- and saturated multisite protein conformations respectively, in this case are given by:

$$U_0^{0.5} = (1 - \sqrt[n]{0.5}) \cdot \left( n \cdot L_T + \frac{K}{\sqrt[n]{0.5}} \right),$$

$$U_n^{0.5} = \sqrt[n]{0.5} \cdot \left( n \cdot L_T + \frac{K}{1 - \sqrt[n]{0.5}} \right).$$
(2.56)

Next, the responses of a multisite protein with four identical binding sites to ligand concentration step change for two different protein concentrations,  $L_T/K = 2$  and  $L_T/K = 50$ , are studied. Instead of considering absolute free ligand concentrations, we consider ratios of the ligand concentration to the affinities of the binding sites. Figure 2.10 shows that the free ligand concentration is barely affected by the interaction for  $L_T/K = 2$ , while the free ligand is nearly exhausted as a result of the binding to the multisite protein for  $L_T/K = 50$ . Figure 2.10 is important due to the fact that it shows the concentration of free ligand as a function of time, which could not be reproduced in Section 2.3, where the ligand concentration was abundant.

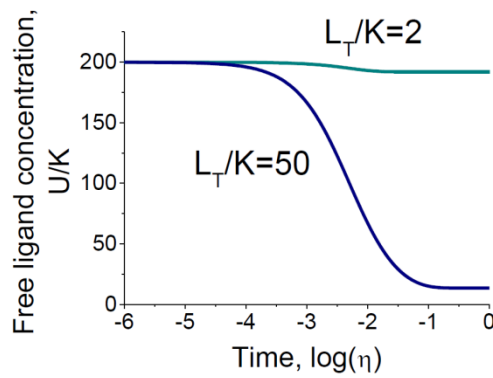


Figure 2.10. The kinetics of free ligand concentration for high and low protein concentrations.

The comparison of free ligand concentration dynamics (Equations (2.47)) after step change in ligand concentration from  $U_{T_0}/K = 0.01$  to  $U_{T_1}/K = 200$ . The amount of available ligand is barely altered for  $L_T/K = 2$ , and exhausted when the ratio of total protein concentration to the binding constant is  $L_T/K = 50$ .

Figures 2.11A and 2.11B illustrate the model predictions for the intermediate and apo- as well as the fully saturated forms, respectively, in the borderline case, where the free ligand concentration is barely affected ( $L_T/K = 2$ ). Figures 2.11C and 2.11D show the model predictions for the multisite protein in the case, where the free ligand is nearly exhausted. Figure 2.11 shows that while the shape of the individual apo-, intermediate and fully saturated forms is the same as in the case of the abundant ligand concentration (Figures 2.7 and 2.8), the strongest effect on the ligand availability, when the free ligand is limited, can be observed for the multisite protein conformations with three and four (fully saturated) bound ligands. A possible explanation for this phenomenon may be that the multisite protein conformations, which form complexes with smaller number of ligand molecules by definition, do not require significant amount of ligand and as a result are not strongly affected under conditions when the free ligand is limited. Whereas the multisite protein interactions with the larger number of ions occur after the significant amount of ligand is “used up” to form the intermediate conformations, however is still required for conformations with larger number of ions. As a result the final levels of the conformations with three and four ions are affected. It can also be seen from Figure 2.11 that the shapes of the intermediate conformations time dependencies are skewed.

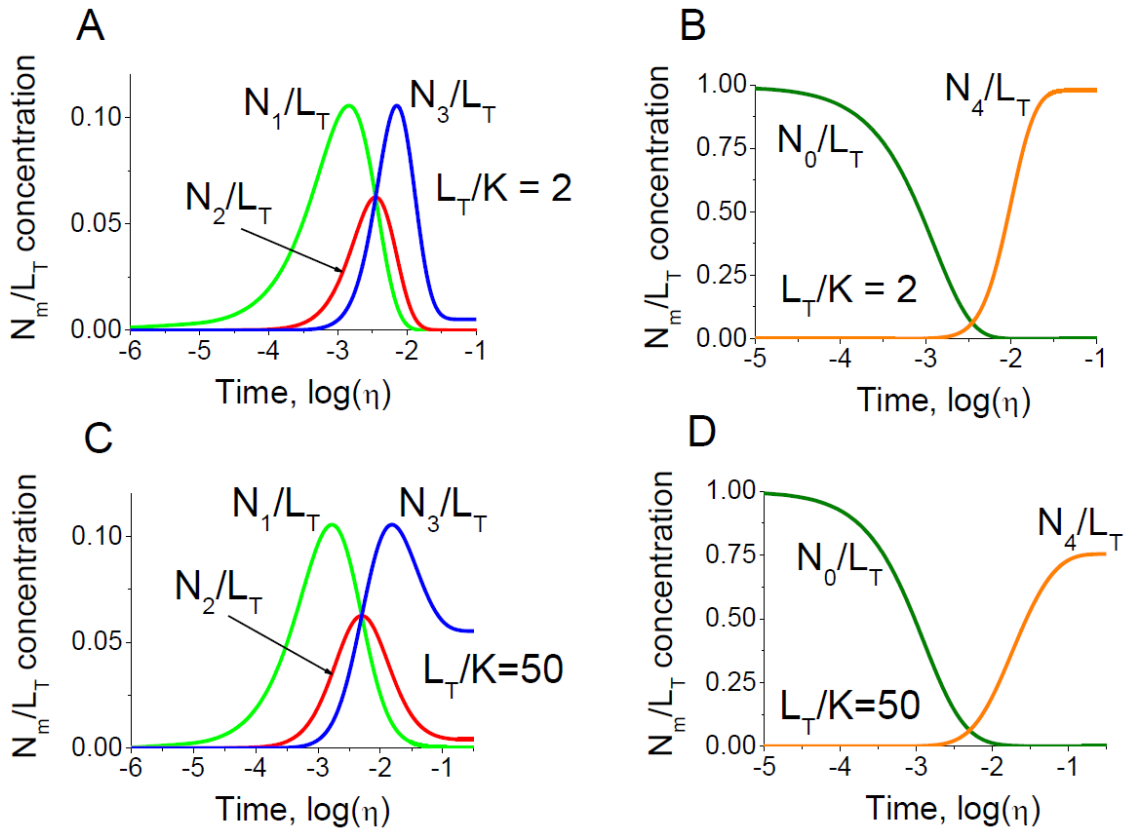


Figure 2.11. The comparison between the cases where the free ligand concentration is barely affected by interactions and exhausted as a result of binding.

The kinetics of multisite protein species alterations in response to step change in ligand concentration from  $U_{T_0}/K = 0.01$  to  $U_{T_1}/K = 200$  for two different ratios of the protein concentration to the affinities of the binding sites  $L_T/K = 2$  (A for the intermediate species, B for the apo- and fully bound species) and  $L_T/K = 50$  (C for the intermediate species, D for the apo- and fully bound species). See Equation (2.52). The model predicts that due to the lack of available ligand and binding to the multisite protein in the case of limited amount of ligand, the multisite protein is unable to become fully saturated after the step change in ligand, and the majority of the ligand becomes distributed among the intermediate species.

Differentiating Equation (2.52) with respect to  $t$  and solving for  $dN_m/dt = 0$  yields (please see Appendix B for the derivation) the time  $\tau_m^{max}$  when the concentration of multisite protein conformations,  $N_m$ , bound to  $m$  ligand molecules is maximal:

$$\tau_m^{max} = H(V(m)), \quad (2.57)$$



where  $H(x) = \frac{1}{F(U_{T1}) \cdot k^-} \cdot \ln \left( \frac{1 + \frac{U_{T1}}{K} + F(U_{T1}) + x}{C(U_T) \cdot \left(1 + \frac{U_{T1}}{K} - F(U_{T1}) + x\right)} \right)$  and

$$V(m) = \frac{L_T}{K} \cdot (n - 2m).$$

Equation (2.57) has an asymptote  $\frac{U_{T1}}{K}$  for  $1 + \frac{U_{T1}}{K} - F(U_{T1}) + x = 0$ :

$$q_m = m \cdot \left( \frac{L_T}{K} + \frac{1}{n - m} \right). \quad (2.58)$$

Figure 2.12 shows the model predictions for the characteristic time required for intermediate protein conformations with one, two and three bound ligands to reach their highest concentrations in response to a step change in ligand concentration from  $U_{T0}/K = 0.1$  to  $U_{T1}/K$  and protein concentration  $L_T/K = 3$ . The shapes of the curves in Figure 2.12 are similar to the ones that were observed for the case of abundant ligand concentration (Figure 2.6). However, the location of vertical asymptotes is different. In Figure 2.12 the curves are steeper, the asymptotes are shifted to the range of higher ligand step magnitudes  $U_{T1}/K$  and located closer to each other compared to the concentrations of corresponding conformations shown in Figure 2.6. This result indicates that when the amount of ligand is limited and the protein concentration is  $L_T/K = 3$ , more time is required to reach the maximum of intermediate protein concentrations. At the same time, when the amount of ligand is limited, there is less difference in time required to reach the maximums between intermediate conformations with one, two and three bound sites.

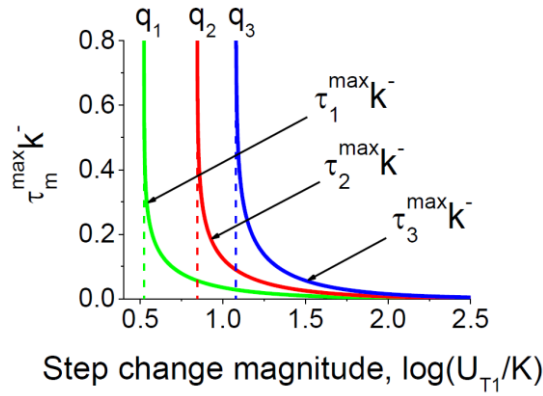


Figure 2.12. Model predictions for the time required for multisite protein conformations to reach their maximal concentrations.

The characteristic times  $\tau_m^{\max} k^-$  (Equation (2.57)) for intermediate multisite protein conformations are shown as a function of the step change ligand concentration from  $U_{T0}/K = 0.1$  to  $U_{T1}/K$  and protein concentration  $L_T/K = 3$ .

Equation (2.52) is further used to define (please see Appendix B for the derivation) the time  $\tau_0^{0.5}$  required for the apo- form  $N_0$  to reach half of the growth concentration and the time period  $\tau_n^{0.5}$  required for the fully saturated protein species to gain half of the growth concentration:

$$\tau_0^{0.5} = H(W), \quad (2.59)$$

$$\tau_n^{0.5} = H(Y), \quad (2.60)$$

where 
$$W = \sqrt[n]{\frac{\left(-\frac{U_{T1}}{K} + \frac{L_T}{K} \cdot n + F(U_{T1}) - 1\right)^n + \left(-\frac{U_{T0}}{K} + \frac{L_T}{K} \cdot n + F(U_{T0}) - 1\right)^n}{2}} - \frac{L_T}{K} \cdot n$$

and 
$$Y = \frac{L_T}{K} \cdot n - \sqrt[n]{\frac{\left(\frac{U_{T1}}{K} + \frac{L_T}{K} \cdot n - F(U_{T1}) + 1\right)^n + \left(\frac{U_{T0}}{K} + \frac{L_T}{K} \cdot n - F(U_{T0}) + 1\right)^n}{2}}.$$

Figure 2.13A shows that the characteristic time  $\tau_0^{0.5}$ , required for the apo- form to reach its half growth level, monotonically decreases with the increase of the total ligand concentration, which corresponds to the case when ligand concentration was abundant (Figure 2.5A). At the same time the model predicts (Figure 2.13A) that the curve is shifted to the range of higher  $U_{T1}/K$  and the magnitude of the time  $\tau_0^{0.5}$  for  $L_T/K = 3$  is lower comparing to Figure 2.5A. Our

model predicts that less time is required for the apo- form to reach its half growth level in the case of limited ligand concentration.

The characteristic time constant  $\tau_4^{0.5}$ , which represents the time required for the saturated conformation to reach its half growth level, reveals a distorted bell shaped dependence on ligand concentration (Figure 2.13B). This bell-like shape, however with higher magnitude, was also observed in the case when ligand concentration was abundant (Figure 2.5B). The disturbance in bell-shape shown in Figure 2.13B is due to the ligand consumption. The model, therefore, predicts possible transient differences in multisite protein signal transduction in response to fast transient kinetics of multisite proteins.

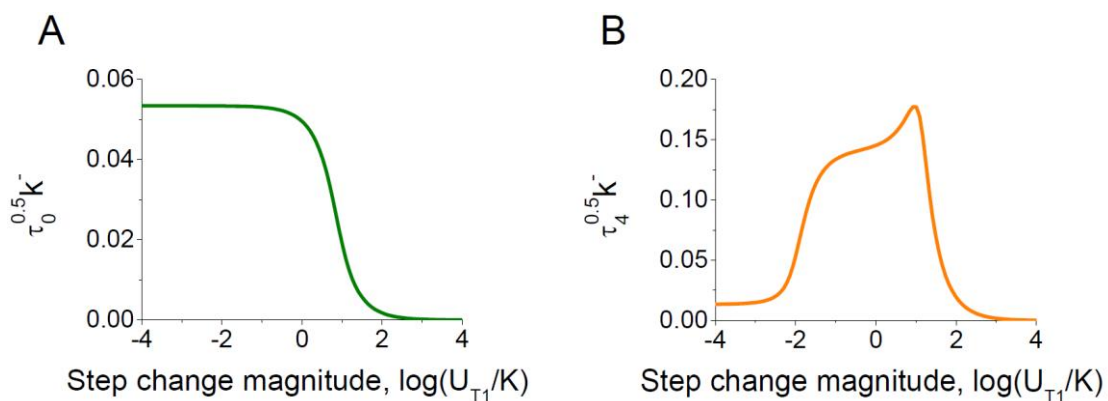


Figure 2.13. Model predictions for the time required for multisite protein conformations to reach their maximal and half growth concentrations.

The characteristic times  $\tau_m^{max} k^-$ ,  $\tau_0^{0.5} k^-$  and  $\tau_4^{0.5} k^-$  for intermediate (A) and apo- and fully bound (B) multisite protein conformations are shown as a function of the step change ligand concentration from  $U_{T0}/K = 0.1$  to  $U_{T1}/K$ . See Equation (2.59) in (A) and Equation (2.60) in (B).

## 2.5 Conclusions

In this chapter we analysed multisite ligand-binding protein kinetics in response to rapid changes in ligand concentrations. Although in this chapter we considered the particular example of CaM, the results can be extended to other multisite proteins with the same number of binding sites, provided that ligand binds to each site independently, for example calcineurin (CaN) and troponin (TnC) [63,64].

The model for multisite protein kinetics for variable number of bound ligands was developed for two physiological cases: i) when the concentration of ligand is much higher [105,106] and ii) when it is comparable with the concentration of the multisite protein [107]. Our model shows, for the first time to our knowledge, that under these two physiological cases the concentration of intermediate conformations as a function of time represents skewed bell shapes (Figures 2.7, 2.8 and 2.11). This result is important as it was suggested in [7], using an example of CaM steady-state analysis, that the intermediate protein conformations can selectively activate a target protein. At the same time, our model predicts that the dependence of the apo- and fully saturated forms represents inhibitory and activatory monotonic shapes, respectively, for the two considered scenarios (Figures 2.4 and 2.11), which was also observed by [19,93].

In the second physiological case (denoted by "ii" above), we found that as the protein concentration rises (Figure 2.10), free ligand concentration becomes exhausted [14], which is opposed to the first case (denoted by "i" above), where the concentration of ligand is abundant. The results obtained by this model increase our understanding of differential activation of protein phosphatase 2B (PP2B) [108,109] and calcium/calmodulin-dependent protein kinase (CaMKII) kinetics [110,111]. PP2B binding increases the affinity of CaM for its targets [108] and, therefore, is likely be activated by low amounts of calcium.

The analysis of the effects of cooperativity performed for the case of abundant ligand concentration (denoted by "i" above) showed that the shapes of the temporal dependences for corresponding protein conformations with 0, 1, 2, 3 and 4 bound ligands of a molecule with four binding sites (for example, CaM) are the same for the two cases, where there is no cooperativity, and where the cooperativity is presented (Figure 2.9). However, the predictions for the case, where there is no cooperativity, and where the cooperativity is presented, differ quantitatively as shown in Figure 2.9.

In this chapter, we also derived and analysed for the two physiological cases ("i" and "ii") the characteristic time  $\tau_m^{max}$ , when the concentration of the intermediate

protein conformations is maximal, and the characteristic times  $\tau_0^{0.5}$  and  $\tau_4^{0.5}$ , required for the apo- and fully saturated forms to reach their half growth level. Our analysis demonstrated that the dependences of  $\tau_m^{max}$  on the final ligand concentration for the two considered cases have the same shape with asymptotes, however the predictions for  $\tau_m^{max}$  differ quantitatively as shown in Figures 2.6 and 2.12 respectively. The dependences of  $\tau_0^{0.5}$  and  $\tau_4^{0.5}$  on the final ligand concentration represent monotonically decreasing inhibitory shape and bell shape respectively (Figures 2.5 and 2.13).

The models developed in this chapter may have applications to analyse the results of kinetic experiments. One possible sort of experiment can include techniques to study chemical kinetics using the pressure jump technique [78,89,112]. According to our model, the effects induced by rapid change in pressure leading to the change in protein-ligand interactions [78,89,112], can be interpreted and explained by the alteration in the affinities of the binding constants of multisite proteins. The time dynamics of the individual multisite protein species may offer new insights into the biophysical mechanism of ligand-protein interactions in response to fast change in ligand concentration in transient kinetics experiments performed by the flash photolysis and stopped-flow techniques [113-115].

In this chapter we developed physiologically more plausible model in comparison to the previously published model [93]. Due to the structure of CaM molecule we assumed that calcium binding to CaM is non-sequential (consistent with [20]), which is opposed to [93]. Therefore, the results obtained by the model proposed in this chapter, may allow for a more accurate interpretation of the experimental data for the concentration of multisite proteins such as CaM, TnC, CaN and other  $\text{Ca}^{2+}$ -dependent secondary messengers regulated by  $\text{Ca}^{2+}$  ions. The model predictions presented in this chapter suggest that the highly versatile intracellular multifunctionality of multisite proteins is achieved not only by the order of ligand-protein interactions and the number of bound ligands, which was demonstrated in [7], but also by temporal regulation.

## **3 A systems model of phosphorylation for inflammatory signalling events**

### **3.1 Literature review**

#### **3.1.1 Biological review**

##### **Phosphorylation of proteins**

Phosphorylation is the enzymatic reaction, by which a phosphate group is added to a protein. It leads to either activation or deactivation of proteins, which form phosphorylation networks [5]. The addition of a phosphate group can occur either on a single site or on several sites of the protein molecule, the latter is known as the multisite phosphorylation [116]. Multisite phosphorylation plays a key role in a number of processes, for example, in Protein Kinase A (PKA) activation of the smooth muscle ATP-sensitive  $K^+$  channel involved in the function of vasodilators [117], in the activation of Hog1 kinase that controls osmo-adaptation properties in yeast [51], in the activation of the epidermal growth factor receptor (EGFR) that is targeted in anti-cancer therapies [118,119]. Multisite phosphorylation is also important in T- and B- cells activation. Aberrations in the phosphorylation mechanism of immunoreceptor tyrosine activation motifs (ITAMs) of the T-cell receptor (TCR), which lead to abnormal T-cell activation, are reported to give rise to autoimmune diseases [120,121].

Phosphorylation plays a critical role in the regulation of the immune system [122]. However, there is a clear gap in the mechanistic understanding of the role of multisite phosphorylation in this process. Phosphorylation governs protein signalling via Signal Transducers and Activators of Transcription (STAT) proteins [123-125].

The phosphorylation of STAT proteins is critical for many fundamental cellular processes such as proliferation, differentiation, cell growth and survival [126]. It operates in the ubiquitous JAK/STAT pathway. A considerable amount of experimental evidence shows that dysfunction in the JAK/STAT signalling mechanisms leads to inflammatory diseases [127-132]. In the next chapter STAT-STAT interactions will be described in more detail.

The multisite phosphorylation regulates the activity of Interferon Regulatory Factor 5 (IRF-5). This is a latent transcription factor involved in autoimmunity [133]. IRF-5 is known to contain six phosphorylation sites: Thr10, Ser158, Ser309, Ser317, Ser451 and Ser462 [134,135].

IRF-5 and STAT3 are involved in the regulation of T cell differentiation [136,137]. The T cells differentiate in the thymus and are involved in cell mediated immunity. They circulate in the lymphoid organs and the blood in the form of naive T cells, which have not been in contact with antigens yet. After an interaction with the antigen, the naive CD4+ T cells are activated and can differentiate into the specific T cell phenotypes, namely T helper 1 (Th1), Th17 and regulatory T cells (Tregs). Each of these phenotypes has its own function in the regulation of the immune response and a specific cytokine signature. Th1 and Th17 cells play a critical role in the regulation of the activity of the immune response and inflammation. Tregs are known for their anti-inflammatory properties and for maintaining the immune tolerance. Th1 cells are defined by expressing cytokine IFN- $\gamma$ , Th17 cells express cytokine IL-17 and Tregs express cytokine IL-10 [138,139]. The specific phenotype is induced by the expression of the specific cytokines. For example Th1 is induced by IL-12, Th17 by IL-6 and Tregs by TGF- $\beta$ . These cytokines activate specific transcription factors, involved in the differentiation of the T cell subsets [140]. Thus, the differentiation of T cells is a complicated process involving a complex scheme of regulation by cytokines and transcription factors.

Protein phosphorylation also controls such properties of erythrocytes as aggregation and deformability. Erythrocytes maintain the concentration of oxygen and carbon dioxide in tissues in a given range of values, in accordance with the needs of metabolism. This is mainly provided by the intensity of ventilation, the regulation of the heart, pre-capillary sphincters, and sphincters of arterio arteriovenous anastomoses. It was shown that the following parameters of erythrocytes can change: the ability to form rouleaux known as aggregation and the ability to change their shape under action of external forces known as deformability [141-145]. The aggregation and deformability of erythrocytes are important for the physiological functioning of the cell and gas transmission function [31].

The process of erythrocyte aggregation is sophisticated and multifactorial. It has a significant impact on the main oxygen transport function of the blood. Aggregation facilitates the axial drift of the red blood cells and the formation of plasma sheet boundary level [146,147]. The increased axial accumulation level of red blood cells reduces the local viscosity in the wall zone of the vessel [148,149] and thereby modulates the activity of the vascular regulatory mechanisms [150] and reduces oxygen release to the vessel walls [151]. For capillaries the efficiency of bloodstream depends on aggregation and deformability [141-145], and it increases for increasing deformability and diminishing aggregation.

### **3.1.2 Modelling review**

#### **Phosphorylation models**

Numerous studies designed to understand phosphorylation-mediated regulatory mechanisms. Early models employed Michaelis-Menten kinetics of the simplest phosphorylation reaction [23]. This model was expanded to include multiple phosphorylation reactions and demonstrated how these could enhance the sensitivity of biochemical systems [152]. It was also reported that this system represents a switch when the total concentration of the substrate protein significantly exceeds the concentration of the enzyme [29].

The classical models [23,152] assume that it is possible to ignore the concentrations of the Michaelis complexes in those cases where the total concentration of protein significantly exceeds the concentrations of the kinase and the phosphatase. This approach was used as a basis in many models of biochemical networks with phosphorylation-dephosphorylation reactions [24-26] and was later extended to multisite phosphorylation [27,28]. However, in real biological systems the concentrations of intermediate phosphorylation complexes cannot always be neglected because the concentrations of kinases, phosphatases and proteins can be comparable [29].

The proportion of maximally phosphorylated protein as a function of the kinase and phosphatase activities was recently determined to show that steeper



switch-like regulation is due to increasing of number of phosphorylation sites [153]. Moreover, the presence of multiple phosphorylation sites enhances the probability of bistable behaviour of the system when the multisite molecule is tethered with scaffold proteins [154]. The multisite phosphorylation can be distributive, when the sites are phosphorylated in a random order, or processive, where the sites are phosphorylated sequentially [155]. The properties of a bistable switch have been investigated to conclude that the mechanism must include independent, i.e. non-sequential phosphorylation, to generate multiple steady states and that bistability is more likely with a large number of phosphorylation sites [156]. It was also reported that increasing number of phosphorylation sites improves the ultrasensitivity of a dose response [157].

Several models for STAT3 and IRF-5 phosphorylation as part of larger models have been published recently. A classical approach for the phosphorylation of STAT3 by JAK was employed in [158]. Another report proposed sigmoid Hill functions (Equation (7.16) in Appendix A) for phosphorylation of STAT3 [159]. An explicit mathematical model for IRF-5 phosphorylation is not currently available, but the phosphorylation of IRF-3 as part of the TLR4 pathway was considered [160].

Erythrocytes have also been a subject of mathematical models in a number of systems biology studies due to their relative simplicity. Early studies captured only the glycolytic pathway [161]. Then the model was expanded to include the pentose phosphate pathway [162]. The first sophisticated model included the sodium–potassium pump and the membrane transport [163]. These mathematical models are good examples of attempts to model human erythrocyte metabolism, but they do not include such properties of erythrocytes, as aggregation and deformability.

### **3.2 Aims and objectives of this chapter**

In the previous chapter we considered the kinetics of multisite ligand binding to proteins. In the current chapter we study steady-state of multisite phosphorylation of proteins. The aims of this chapter are:

- build new models for single- and multisite phosphorylation taking into account the concentrations of enzyme-substrate complexes,
- compare the proposed models with previously reported models [27,28,153,154,157] in the context of intracellular signalling of the inflammatory circuits [164,165],
- specifically, apply the proposed models to investigate the regulation of STAT3 and IRF-5 signalling pathways as well as the aggregation and deformability in erythrocytes,
- employ the developed models to investigate the parametric sensitivity of the inflammatory circuits in response to various inflammatory co-stimuli.

The models proposed in this chapter were published in papers [30] and [31], but in this chapter, only my contribution is described.

### **3.3 A new model for phosphorylation**

In this section a model for phosphorylation in the inflammatory signalling events is presented. The new model is based on and extends the previously published model for phosphorylation [23]. Therefore, the results in this chapter will be compared with the results obtained by employing the model in [23].

It was shown that IRF-5 contributes to the polarization and plasticity of macrophages [164]. Pathogens such as bacteria and viruses cause the activation of the Toll-Like Receptors (TLRs). This signalling leads to the activation of IRF-5 [166] and the production of pro-inflammatory interleukins IL-6, IL-12 and IL-23 [164,167]. These cytokines are able to activate STAT3 and result in the Th17 differentiation [165,168]. Treg cells then can switch to Th17 cells [169] which in turn then can switch to Th1 subpopulation [170]. In this section we introduce an assumption based on the reported experimental data that different types of signals result in different types of immune response.

Figure 3.1 schematically represents the experimental data [164-170] based assumptions for the role of IRF-5 and STAT3 in T cell fate determination. Due to the highly competitive nature of the pathways in the scheme any disturbances in

the mechanism, for example STAT3 overexpression [171] or overexpression of interleukin receptors [172], may lead to the enhancement of the role of other cytokines and possibly to pathological states. Such possible disturbances are schematically represented by red arrows while the normal regulation is highlighted by green arrows (Figure 3.1). The arrows with the names of cytokines represent the cytokines that are produced by the activation of upstream proteins and activate downstream proteins. The unlabelled arrows indicate activation of proteins caused directly by activation of upstream elements. Since the classical approach [23] offers limited power for the regulation of the phosphorylated protein magnitude as it will be shown later in Figures 3.3, 3.5 and 3.9, it might potentially lead to incorrect description of protein phosphorylation level.

Our model assumes that the perturbations can occur at the level of STAT3 or IRF-5 proteins. Later in this chapter we will study the influence of the parameter changes corresponding to these perturbations on the activity of STAT3 and IRF-5 comparing it with the previously published model [23] and discuss their impact on the T cell phenotype formation and plasticity. As it will be shown later, the proposed model may offer physiologically more accurate description of the role of multisite phosphorylation regulation of the T cell differentiation due to the fact that we consider the concentrations of enzyme-substrate complexes, which were neglected in [23].

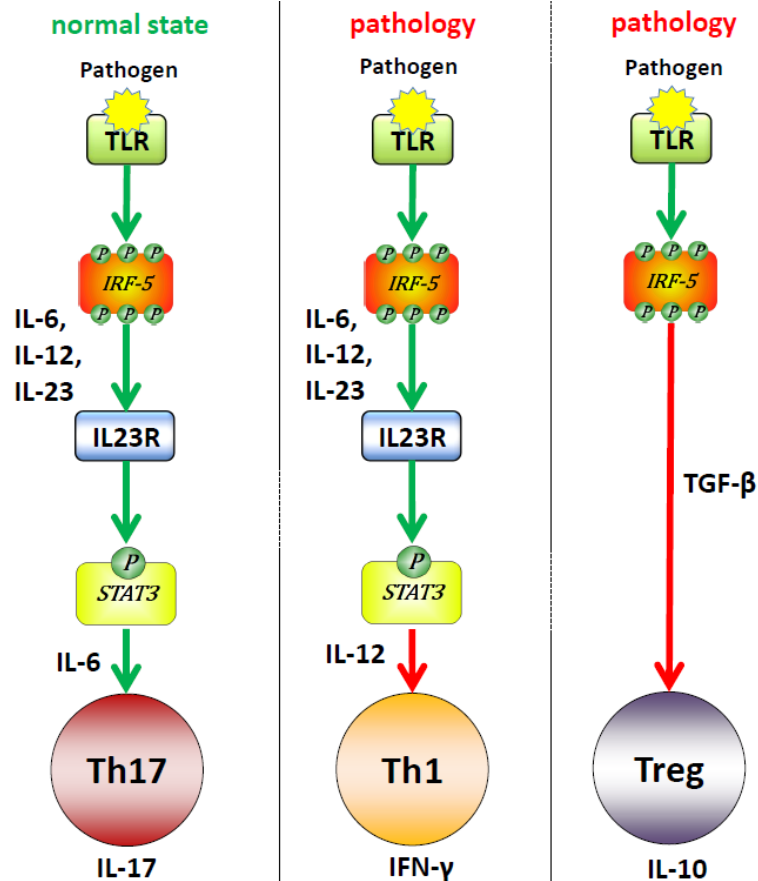


Figure 3.1. A schematic diagram for the dependence of T cell differentiation on intracellular phosphorylation signalling.

A vast amount of experimental evidence suggests that T cell phenotypes depend on the intracellular phosphorylation signalling mechanisms [164-170]. Environmental factors, genetic mutations, cellular and intracellular factors influence the underlying phosphorylation mechanics. The cartoon summarises possible differential responses of TLR downstream phosphorylation signalling events to pathogens leading to the distinct polarization of naive T cells into three distinct phenotypes Th17, Th1 and Treg. According to this model activation or interplay of phosphorylation pathways is responsible for selective differentiation. The model suggests that the cell plasticity observed under pathological conditions can be due to altered intracellular phosphorylation patterns, which are, in turn, dependent on the extracellular cytokine environment. The arrows with cytokine names represent the cytokines that are produced by the activation of upstream proteins and activate downstream proteins. The unlabelled arrows indicate activation of proteins caused directly by activation of upstream elements. Malfunctions are schematically represented by red arrows while the normal regulation is highlighted by green arrows.

In the following subsections we will provide a mathematical description of the developed model for protein phosphorylation. To do this, we will use the law of

mass action [173] and consider the phosphorylation-dephosphorylation cycle. Since a single phosphorylation event is simpler than a multisite phosphorylation event, we will start our description with the single site phosphorylation. When considering the multisite protein phosphorylation, we assume that the multisite protein has identical phosphorylation sites. Therefore, the phosphorylation of each site can be considered as an independent event as it will be shown later in the following subsections.

### 3.3.1 Single site phosphorylation

Here we consider a general mechanism of phosphorylation of protein  $A$  by the kinase  $K$  and dephosphorylation by phosphatase  $P$ .

The reactions can be represented as follows:



We introduce the following notation:  $[A]$ ,  $[A_p]$  – the concentrations of the non-phosphorylated and phosphorylated protein respectively,  $K_T$ ,  $P_T$ ,  $A_T$  – the total concentrations of the proteins in an active form,  $[K]$ ,  $[P]$  – the concentrations of free proteins,  $[KA]$ ,  $[PA_p]$  – the concentrations of kinase-protein and phosphatase-protein complexes, respectively. The kinetic equations of this molecular system are given by:

$$\begin{aligned} \frac{d[A]}{dt} &= -k_1[K][A] + k_1^-[KA] + k_4[PA_p], \\ \frac{d[A_p]}{dt} &= -k_3[P][A_p] + k_3^-[PA_p] + k_2[KA], \\ \frac{d[KA]}{dt} &= k_1[K][A] - (k_1^- + k_2)[KA], \\ \frac{d[PA_p]}{dt} &= k_3[P][A_p] - (k_3^- + k_4)[PA_p], \\ \frac{d[K]}{dt} &= -k_1[K][A] + (k_1^- + k_2)[KA], \\ \frac{d[P]}{dt} &= -k_3[P][A_p] + (k_3^- + k_4)[PA_p]. \end{aligned} \quad (3.2)$$

The conservation equations for the elements involved in the above reactions are as follows:

$$\begin{aligned} A_T &= [A] + [A_p] + [KA] + [PA_p], \\ K_T &= [K] + [KA], \\ P_T &= [P] + [PA_p]. \end{aligned} \quad (3.3)$$

The steady-state solutions of  $[KA]$  and  $[PA_p]$  can be written as follows:

$$\begin{aligned} [KA] &= \frac{K_T [A]}{K_p + [A]}, \\ [PA_p] &= \frac{P_T [A_p]}{K_f + [A_p]}, \end{aligned} \quad (3.4)$$

where  $K_p = \frac{k_2 + k_1^-}{k_1}$  and  $K_f = \frac{k_4 + k_3^-}{k_3}$  are the Michaelis constants for the phosphorylation-dephosphorylation reactions.

The rate of change of  $[A_p]$  can be written as a function of  $[KA]$  and  $[PA_p]$ :

$$\frac{d[A_p]}{dt} = k_2 [KA] - k_4 [PA_p]. \quad (3.5)$$

From Equations (3.3), (3.4) and (3.5) it can be written:

$$\begin{aligned} \frac{d[A_p]}{dt} &= k_2 \frac{K_T (A_T - [A_p] - [KA] - [PA_p])}{K_p + A_T - [A_p] - [KA] - [PA_p]} - k_4 \frac{P_T [A_p]}{K_f + [A_p]}, \\ \frac{d\left(\frac{[A_p]}{A_T}\right)}{d(t \cdot k_4)} &= \frac{P_T}{A_T} \left( \frac{k_2 \frac{K_T \left(1 - \frac{[A_p]}{A_T} - \frac{[KA]}{A_T} - \frac{[PA_p]}{A_T}\right)}{\frac{k_2}{k_4} \frac{K_p}{A_T} + 1 - \frac{[A_p]}{A_T} - \frac{[KA]}{A_T} - \frac{[PA_p]}{A_T}}{\frac{K_f + [A_p]}{A_T}} - \frac{[A_p]}{A_T} \right). \end{aligned} \quad (3.6)$$

The non-dimensional form of the Equations (3.5) and (3.6) can be written as follows:

$$\frac{da_p}{d\tau} = h_3 x - y, \quad (3.7)$$

$$\frac{da_p}{d\tau} = h_5 \left( \frac{h_3 h_4 (1 - a_p - x - y)}{h_1 + 1 - a_p - x - y} - \frac{a_p}{h_2 + a_p} \right), \quad (3.8)$$

where

$$a = \frac{[A]}{A_T}, a_p = \frac{[A_p]}{A_T}, x = \frac{[PA]}{A_T}, y = \frac{[NA_p]}{A_T}, \tau = t \cdot k_4,$$

$$h_1 = \frac{K_P}{A_T}, h_2 = \frac{K_F}{A_T}, h_3 = \frac{k_2}{k_4}, h_4 = \frac{K_T}{P_T}, h_5 = \frac{P_T}{A_T}.$$

According to the above notation, Equations (3.4) in non-dimensional form are given by:

$$x = \frac{h_4 h_5 a}{h_1 + a}, \quad (3.9)$$

$$y = \frac{h_5 a_p}{h_2 + a_p}.$$

We can therefore rewrite the law of mass conservation for  $[A]$  as follows:

$$1 = a + a_p + x + y. \quad (3.10)$$

In [23], the steady state solution of  $a_p$  was found for  $x \ll 1, y \ll 1$ . The sufficient condition to satisfy  $x \ll 1, y \ll 1$  is  $K_T \ll A_T, P_T \ll A_T$ , which means  $h_4, h_5 \ll 1$ . This implies that the concentrations of these complexes are negligible comparing to  $a_p$  and the solution can be written as follows:

$$a_p = \frac{1}{2(1 - h_3 h_4)} \left[ h_1 + h_3 h_4 (h_2 - 1) + 1 - \sqrt{(h_1 + h_3 h_4 (h_2 - 1) + 1)^2 - 4h_2 h_3 h_4 (1 - h_3 h_4)} \right]. \quad (3.11)$$

In general, conditions  $x \ll 1, y \ll 1$  are not satisfied. We find an accurate solution of Equation (3.8). From Equations (3.9) we obtain:

$$a = \frac{h_1 x}{h_4 h_5 - x}, \quad (3.12)$$

$$a_p = \frac{h_2 y}{h_5 - y},$$

where  $y = h_3x$  according to the steady state of Equation (3.7) when  $\frac{da_p}{d\tau} = 0$ .

Substituting Equations (3.12) into Equation (3.8) for steady state, we obtain:

$$\frac{h_1x}{h_4h_5 - x} + \frac{h_2h_3x}{h_5 - h_3x} + x(1 + h_3) = 1. \quad (3.13)$$

The range of  $x$  is limited and determined from the conservation equations:

$$0 < x < \min\left(h_4h_5, \frac{h_5}{h_3}\right).$$

It can be shown that Equation (3.13) has one real root and two complex conjugate roots. Equation (3.13) can be written as follows:

$$\frac{h_1x}{h_4h_5 - x} + \frac{h_2h_3x}{h_5 - h_3x} + x(1 + h_3) - 1 = f(x). \quad (3.14)$$

For any real positive values of the parameter  $h_i (i = 1 \dots 5)$ ,  $f(x)$  is a monotonically increasing function (it is continuous on the domain

$0 < x < \min\left(h_4h_5, \frac{h_5}{h_3}\right)$  and its derivative is positive for any value of  $h_i$ ), it has one

intersection point with the horizontal axis, where  $f(x) = 0$ , which means that there is only one real root of Equation (3.14).

We find the real root of Equation (3.14). Equation (3.13) can be transformed to the following equation:

$$\frac{x^3 - bx^2 + cx - d}{(h_4h_5 - x) \cdot \left(\frac{h_5}{h_3} - x\right)} = 0, \quad (3.15)$$

where



$$\begin{aligned}
b &= \frac{1+h_1+h_2}{1+h_3} + h_4h_5 + \frac{h_5}{h_3}, \\
c &= \frac{(1+h_2)h_4h_5 + (1+h_1)\frac{h_5}{h_3}}{1+h_3} + h_4h_5\frac{h_5}{h_3}, \\
d &= \frac{h_4h_5\frac{h_5}{h_3}}{1+h_3}.
\end{aligned} \tag{3.16}$$

Since the domain is  $0 < x < \min\left(h_4h_5, \frac{h_5}{h_3}\right)$ , the roots of the numerator in Equation (3.15) are equal to the roots of Equation (3.15), thus the latter can be simplified as:

$$x^3 - bx^2 + cx - d. \tag{3.17}$$

To find the roots of Equation (3.17) we use Cardano's method. Based on the fact that this equation has one real root  $x_1$  and two complex conjugate roots  $r - ip$  and  $r + ip$ , it can be written as follows:

$$x^3 - bx^2 + cx - d = (x - x_1)[x - (r - ip)][x - (r + ip)]. \tag{3.18}$$

Thus there is a system of equations for  $x_1$ ,  $r$  and  $p$ :

$$\begin{aligned}
x_1 + 2r &= b, \\
2x_1r + r^2 + p^2 &= c, \\
x_1(r^2 + p^2) &= d.
\end{aligned} \tag{3.19}$$

To simplify the above system of equations, we use the following parameters:

$$\begin{aligned}
D &= \sqrt{3\left[(4c - b^2)c^2 - d(18cb - 27d - 4b^3)\right]}, \\
DD &= \sqrt[3]{4\left[3D - 27d - b(2b^2 - 9c)\right]}.
\end{aligned} \tag{3.20}$$

Solving the system described by Equation (3.19), the real solution of Equation (3.14) can be obtained:

$$x_1 = 2 \frac{c - \frac{1}{3}b^2}{DD} + \frac{1}{3} \left( b - \frac{1}{2}DD \right). \quad (3.21)$$

Figure 3.2 shows the solutions for  $x_1$  as a function of  $h_4$  for the different total protein to kinase concentration ratios (Figure 3.2A) and for the different phosphorylation to dephosphorylation ratios (Figure 3.2B). This figure clearly demonstrates that the solution (3.21) is within the domain  $0 < x < \min\left(h_4 h_5, \frac{h_5}{h_3}\right)$ , thus there is only one real positive root of Equation (3.17).

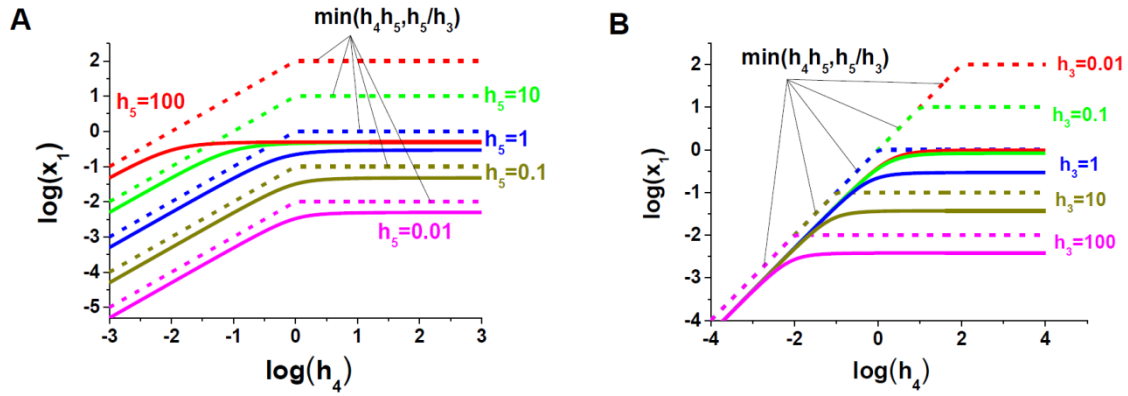


Figure 3.2. Check of the feasibility of the solutions for the kinase-protein complexes concentrations.

Equation (3.17) has one real positive root in the domain  $0 < x_1 < \min(h_4 h_5, h_5/h_3)$ . Here we verify that the value of  $x_1$  provided by (3.21) shown in y-axis is within this domain for different  $h_5$  (A) and different  $h_3$  (B) as a function of  $h_4$  (x-axis). Solid lines represent the solutions (3.21) while dashed lines represent the upper bound of the domain,  $\min(h_4 h_5, h_5/h_3)$ . The parameters are  $h_1 = 1$ ,  $h_2 = 1$ ,  $h_3 = 1$  in (A) and  $h_1 = 1$ ,  $h_2 = 1$ ,  $h_5 = 1$  in (B).

Thus, a steady-state solution for  $a_p$  in a general form is:

$$a_p = \frac{1}{2q_1} \left( q_2 - \sqrt{q_2^2 - 4q_1 q_3} \right), \quad (3.22)$$

where

$$\begin{aligned}
q_1 &= 1 - h_3 h_4, \\
q_2 &= h_1 - x_1 (h_3 + 1) + 1 + h_3 h_4 (h_2 + x_1 (h_3 + 1) - 1), \\
q_3 &= h_2 h_3 h_4 [1 - x_1 (h_3 + 1)].
\end{aligned}$$

From Equations (3.12), parameters  $h_1$  and  $h_2$  can be obtained:

$$\begin{aligned}
h_1 &= a \left( \frac{h_4 h_5}{x} - 1 \right), \\
h_2 &= a_p \left( \frac{h_5}{y} - 1 \right).
\end{aligned} \tag{3.23}$$

Since  $K_T$ ,  $P_T$ ,  $A_T$  are known and  $[A]$ ,  $[A_p]$ ,  $[KA]$ ,  $[PA_p]$  can be measured experimentally, we can find the Michaelis constants  $K_p$ ,  $K_F$ :

$$\begin{aligned}
K_p &= A \left( \frac{K_T}{[KA]} - 1 \right), \\
K_F &= A_p \left( \frac{P_T}{[PA_p]} - 1 \right).
\end{aligned} \tag{3.24}$$

### 3.3.2 Multisite phosphorylation

In this subsection we consider a system with  $m$  independent phosphorylation sites. The ODEs and the equations describing the final formula for the concentration of the protein phosphorylated at one single site are the same as in the previous subsection, but the conservation equation for the total amount of protein differs from Equations (3.3). Instead of  $A_T$ , the total amount of protein is  $mA_T$  as the molecule has  $m$  phosphorylation sites:

$$mA_T = [A] + [A_p] + [KA] + [PA_p]. \tag{3.25}$$

In this case, the normalised parameters are written as follows:

$$\begin{aligned}
a &= \frac{[A]}{mA_T}, a_p = \frac{[A_p]}{mA_T}, x = \frac{[KA]}{mA_T}, y = \frac{[PA_p]}{mA_T}, \tau = t \cdot k_4, \\
h_1 &= \frac{K_p}{mA_T}, h_2 = \frac{K_F}{mA_T}, h_3 = \frac{k_2}{k_4}, h_4 = \frac{K_T}{P_T}, h_5 = \frac{P_T}{mA_T}.
\end{aligned}$$

When  $q$  out of  $m$  sites are phosphorylated it can be assumed that these events are independent and the sites are identical. Thus, the multisite phosphorylation is a combinatorial problem and can be considered in terms of the probabilities of the protein to be phosphorylated at distinct sites. Hence, the concentration of the protein phosphorylated at  $q$  out of  $m$  phosphorylation sites is proportional to the sum of all molecule combinations:

$$s_m^q = \binom{m}{q} a_p^q a^{m-q}, \quad (3.26)$$

where  $a_p$  is the probability of the protein to be phosphorylated at a single site,  $a$  is the probability of the protein to be non-phosphorylated at a single site and  $\binom{m}{q}$  is a binomial coefficient.

Equation (3.26) can be written in detail as follows:

$$s_m^q = \frac{m!}{q!(m-q)!} a_p^q a^{m-q}. \quad (3.27)$$

### 3.4 Applications of the developed models (Equations 3.11, 3.22 and 3.27) to the regulation of the proteins activity

#### 3.4.1 STAT3 phosphorylation

STAT3 can form a dimer and be activated when it is phosphorylated at one site by JAK and dephosphorylated by SHP-1. Thus, Equations (3.11) and (3.22) can be used to denote the STAT3 concentration. The following notation is used in

our model:  $h_3 = \frac{k_p}{k_D}, h_4 = \frac{JAK_T}{SHP1_T}, h_5 = \frac{SHP1_T}{STAT3_T}$ .

Figure 3.3 shows the model predictions for the normalised steady-state activities of the phosphorylated STAT3 proteins denoted by STAT3<sub>p</sub> (Figure 3.3A) and highlights the differences of the predictions for the phosphorylated STATs between the newly developed model (3.22) and previous simple model

(3.11) described in [23]. The model proposed in this chapter is consistent with the experimental observations of the phosphorylation events [164-168,170] summarised in Figure 3.1 and predicts the mechanisms for the role of SHP-1 in modulation of the signal transduction via STATs [44, 45]. At the same time, some of the predictions of the presented and earlier models partially coincide for those cases when the  $JAK_T$  kinase and the  $SHP-1_T$  phosphatase concentrations are significantly smaller than the total concentrations of STAT proteins ( $STAT3_T$ ). However the model predictions differ when the corresponding concentrations are similar.

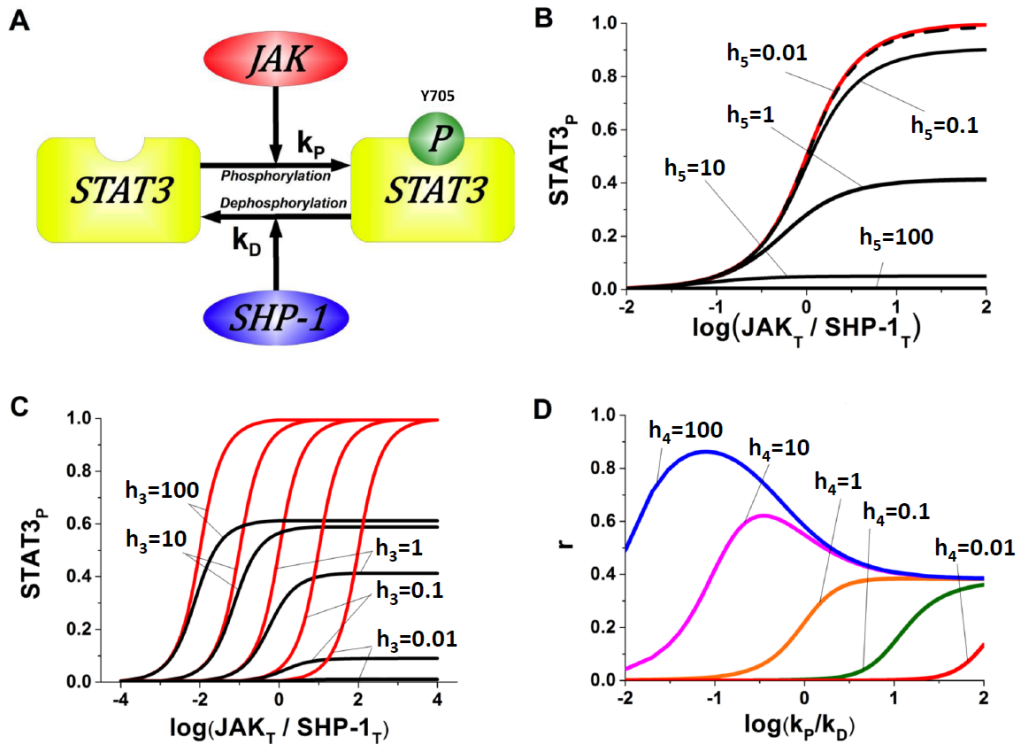


Figure 3.3. Model predictions for the concentration of  $STAT3_p$  phosphorylated by JAK and dephosphorylated by SHP-1.

Investigation of the dependence of STAT3 phosphorylation on the relative activities of JAK and SHP. A. Cartoon diagram of STAT3 phosphorylation and dephosphorylation by JAK and SHP-1, respectively. B. A comparative analysis of the dependencies (Equations (3.11) and (3.22) with  $h_1=1$ ,  $h_2=1$ ,  $h_3=1$ ,  $h_4 = JAK_T/SHP-1_T$ ) produced by the proposed model and the previously published models for STAT3 phosphorylation (y-axis). Ratios of JAK and SHP-1 (x-axis) are found to be critical for STAT3 phosphorylation response and the differences between the model predictions. The red line shows the predictions by [23] whereas the black line offers predictions from the presented model. The STAT3 phosphorylation predictions coincide when STAT3 significantly exceeds SHP-1 concentration. C. The effects of phosphorylation and dephosphorylation rates are studied on the proposed (black line) and previously reported (red line) models [23]. See Equations (3.11) and (3.22) with  $h_1=1$ ,  $h_2=1$ ,  $h_4=1$ ,  $h_4 = JAK_T/SHP-1_T$ . We found that our model predicts the modulation of phosphorylated STAT3 as opposed to the prediction of STAT3 phosphorylation rate offered by [23]. D. The difference  $r = a_p^s - a_p^d$ , where  $a_p^s = a_p$  from Equation (3.11) and  $a_p^d = a_p$  from Equation (3.22), between the simple model [23] and the model developed in this chapter is shown as a function of phosphorylation/dephosphorylation rates for various ratios of JAK and SHP-1. The parameters are  $h_1=1$ ,  $h_2=1$ ,  $h_3 = k_p/k_D$ ,  $h_5=1$ . This analysis clearly demonstrates the differences in STAT3 phosphorylation predictions due to the underlying assumptions employed in the simple model.

The figures show that the system may operate in a switch-like manner with an increasing concentration of JAK<sub>T</sub> kinase, which leads to the ultrasensitivity that is characterised by the concentrations of STAT3<sub>p</sub> being more sensitive to change in stimulus than would be expected from a Michaelis-Menten response [23]. This all-or-none characteristic of the response is observable not only in this particular system but in other cell systems such as *Xenopus* Oocyte extracts [53,174], the glycogen cascade system [175], and ligand-receptor complexes [176].

Figure 3.3B shows the normalised concentration of phosphorylated STAT3 as a function of the kinase to phosphatase ratio (total amounts of JAK and SHP-1, respectively). The model predicts that the degree of STAT3<sub>p</sub> activity depends on the ratio of the total STAT3 and SHP-1 concentrations. This prediction differs from the previous study [23], where the derived formula for phosphorylation could not reproduce this effect under certain physiological conditions, for example when the total concentration of protein (STAT3) is comparable or lower than the total concentration of phosphatase (SHP-1) [29]. This is due to the fact that the concentrations of kinase-protein and phosphatase-protein complexes were neglected in previous work [23]. At the same time, the model predictions virtually coincide with the predictions from [23] if the concentration of SHP-1<sub>T</sub> is significantly (100 times) smaller than STAT3<sub>T</sub>. However, our model offers different predictions for comparable or higher phosphatase concentrations than STATs, consistent with the T cell phenotype dependence on intracellular phosphorylation signalling summarised on Figure 3.1 [164-168,170]. The proposed results are significant, as the relative ratio of STAT3 and SHP-1 was shown to be critical in T cell breast lymphoma and Hepatocellular Carcinoma pathologies [177,178]. The significance of the results can be seen from the following observations. The activation of STAT3 leads to the formation of inflammatory Th17 cells (Figure 3.1). Therefore, in order to reduce inflammation the magnitude of phosphorylated STAT3 should be lowered. Figure 3.3B shows that this can be achieved by increasing the ratio between the total SHP-1 and STAT3 concentrations in the developed model, which was not predicted by the previously published model [23].

Our calculations suggest that if the  $\text{STAT3}_T$  and  $\text{SHP-1}_T$  concentrations are comparable, the phosphorylated  $\text{STAT3}_p$  increase as a function of the ratio of the forward phosphorylation reaction rate,  $k_p$ , to the forward dephosphorylation rate,  $k_d$  (Figure 3.3C). The introduction of the kinase-protein and/or phosphatase-protein complexes enables additional regulatory capacity of the  $\text{STAT}$  signalling events. While the simplified model predicts earlier or later  $\text{STAT}$  activation on the relative kinase/phosphatase activity scale, the new model suggests additional regulatory steps taking place via modulation of the total amplitude. This result is critical from the immunological point of view, as it might potentially explain the molecular basis of the functional plasticity of T cell phenotypes. According to our model, T cell populations may undergo different transcriptional activation events in response to the same stimuli due to different kinase and phosphatase activity levels. Furthermore, since the kinase and phosphatase activities are subject to short and long term modulation, this gives rise to possible phenotype switching. It is critical to highlight that the plasticity effects can be described using the proposed detailed phosphorylation reaction model only. The range of the tested parameters suggests that the difference  $r$  between the previously published model, Equation (3.11), and the proposed model, Equation (3.22), is due to the structure of the models (Figure 3.3D).

Our analysis suggests that the  $\text{STAT3}$  phosphorylation system with switch-like characteristics depends on the parameters of the model. The approach proposed by Goldbeter and Koshland [23] is only applicable for limited physiological conditions when the concentration of  $\text{JAK}_T$  and  $\text{SHP-1}_T$  are significantly smaller than that of  $\text{STAT3}_T$ . While these situations can occur in nature, most living cells exhibit comparable concentrations of enzymes and their substrates. Therefore, the physiological range of applications considered in [23] is rather limited and all other phosphorylation events require the extended analysis described in this chapter.

### 3.4.2 IRF-5 phosphorylation

We next investigate multisite phosphorylation reactions in other inflammatory signalling pathways and studied the activation of IRF-5 as an example. IRF-5 is



phosphorylated by the TBK-1 kinase and dephosphorylated by Alkaline Phosphatase (AP) (Figure 3.4A) [134,135,179]. Our model assumes that the molecule contains 6 independent phosphorylation sites. In this case we use

$$\text{Equation (3.27), assuming } h_3 = \frac{k_p}{k_D}, h_4 = \frac{TBK1_T}{AP_T}, h_5 = \frac{AP_T}{IRF5_T} .$$

Figure 3.4B shows the model predictions for the distribution of the phosphorylated IRF-5 species. It can be seen from Figure 3.4B that the shape of the fully-phosphorylated (blue line) protein species qualitatively coincides with the case of the single site phosphorylation reaction (Figures 3.3B and 3.3C). However, Figure 3.4C shows that the steepness of the phosphorylation response is higher in the multisite phosphorylation reaction (blue line) compared to the single site phosphorylation case (red line). Figure 3.4B shows the bell-shaped dependence for the intermediate species and provides a clear explanation as to how receptor-mediated activatory events can be followed by inhibition in response to the same signal. The model predictions for the bell shapes of the intermediate phosphorylated protein species in the multisite phosphorylation reactions obtained in this chapter are consistent with previously reported results (Figure 1 in [156]) and qualitatively consistent with the experimental data [134,135].

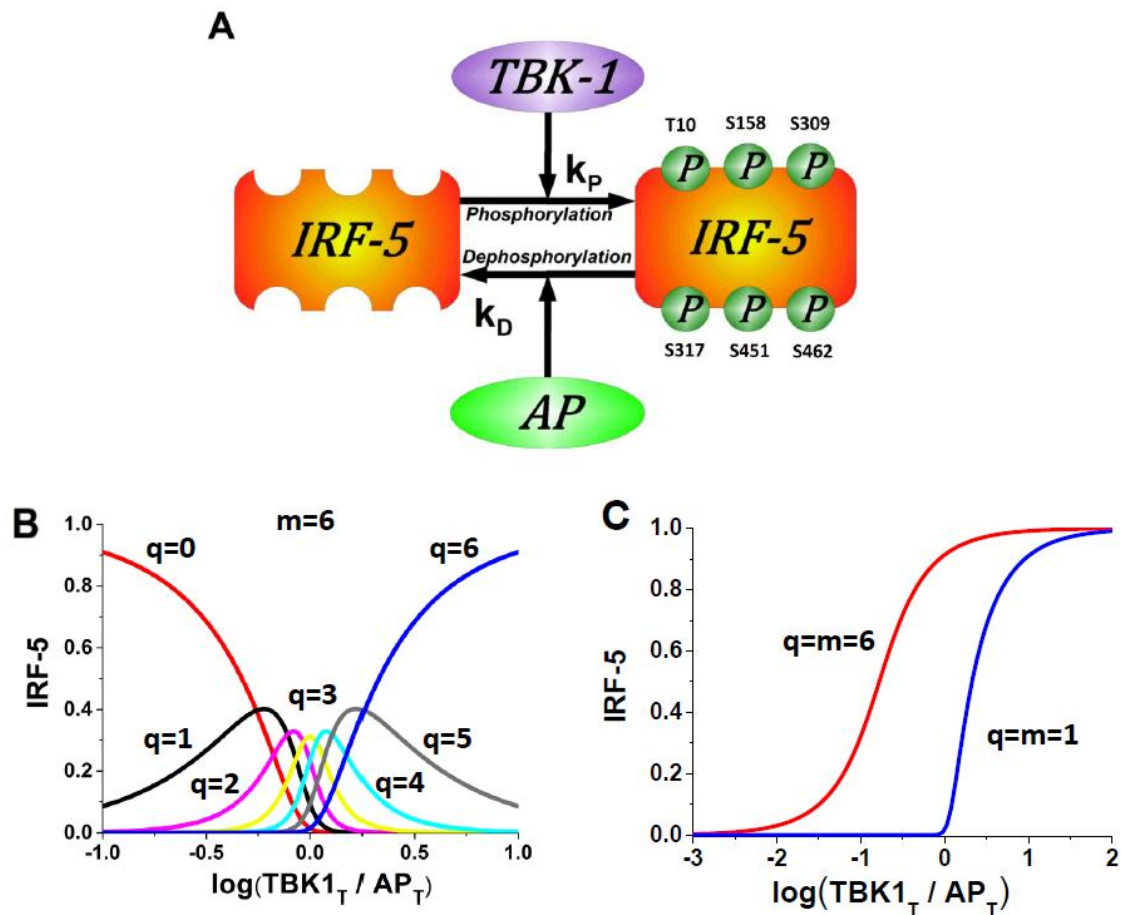


Figure 3.4. Multisite phosphorylation enables switching between multiple T cell phenotypes.

A. Schematic diagram of IRF-5 phosphorylation and dephosphorylation by TBK-1 and AP, respectively, represents one of many intracellular multiphosphorylation examples observed in the immune system. Experimental evidence suggests that proteins phosphorylated at different phosphorylation sites may have selective activity [135,180] and give rise to distinct T cell populations [181]. B. Model predictions for distribution of IRF-5 phosphorylated species (Equation (3.27) with  $h_1 = 1/6$ ,  $h_2 = 1/6$ ,  $h_3 = 1$ ,  $h_4 = TBK_T/AP_T$ ,  $h_5 = 1/6$ ,  $m = 6$ ,  $q = 0, 1, \dots, 6$ ). Extracellular environment, which is modelled as the ratio of total TBK-1 to AP concentration, is hypothesized to cause the distribution of IRF-5 phosphorylated species: one site phosphorylated (black), two (magenta), three (yellow), four (cyan), five (grey) and six (blue). According to the proposed model extracellular environment can actively change the ratio of IRF-5 phosphorylated species and thereby contribute to the mechanism of T cell plasticity by modulating the numbers of T cell phenotypes. By the ratio of IRF-5 phosphorylated species we mean the concentration of phosphorylated IRF-5 species with corresponding number of phosphorylated sites. C. The dose-response curve for fully phosphorylated IRF-5 (blue line), which has 6 phosphorylation sites, is steeper comparing to the single-site protein (red line). Equation (3.27) is used with  $h_1 = 1/6$ ,  $h_2 = 1/6$ ,  $h_3 = 1$ ,  $h_4 = TBK_T/AP_T$ ,  $h_5 = 1/6$ ,  $q = m = 6$  (blue line) and  $q = m = 1$  (red line).

We compare our model predictions for the concentration of phosphorylated IRF-5, Equation (3.27), with the model predictions of previously reported method of Goldbeter and Koshland [23]. There are two key biochemical factors that may significantly vary in living cells and thereby affect the signalling properties: the ratio of total protein to kinase and phosphatase concentrations and the rates of phosphorylation,  $k_p$ , and dephosphorylation,  $k_D$ , reactions. Due to the fact that in experiments, concentration of phosphatases can often be varied while the kinases concentration is not always possible to vary, we do not vary the phosphatase concentration and change the kinase activity only, since it is more interesting.

Our analysis shows that alterations of phosphorylation rates and total IRF-5 to AP ratios do not have any impact on the model in [23]. Figure 3.5 shows the range of the model prediction for the described variation of parameters. It can be seen from the Figure 3.5 that for comparable phosphorylation to dephosphorylation rates, the non-phosphorylated form of IRF-5 appears to be dominant (Figure 3.5A). At the same time, the predictions from this model coincide with the predictions from [23] shown in Figure 3.4B, both when the phosphorylation and dephosphorylation rates are of the same order (Figure 3.5B) or different (Figure 3.5F), but only when the total amount of the IRF-5 concentration exceeds AP. We next decrease the phosphorylation rate (Figure 3.5C and Figure 3.5D) and investigate the case of comparable IRF-5 and AP concentrations (Figure 3.5C) compared with the case where the total concentration of IRF-5 is much larger (Figure 3.5D). The model predicts that most of the potential multisite protein species would remain unphosphorylated in the former case (Figure 3.5C), and would have a distribution very similar to the case of comparable phosphorylation rates and concentration shown in Figure 3.5A (Figure 3.5D). Our model predicts that the overall amount of all the phosphorylated protein species decreases significantly when the total TBK-1 concentration is comparable with the total IRF-5 concentration (Figure 3.5E). Thus, the model predictions shown in Figures 3.5A, 3.5C, 3.5D and 3.5E differ from the model predictions obtained by [23] and shown in Figure 3.4B.

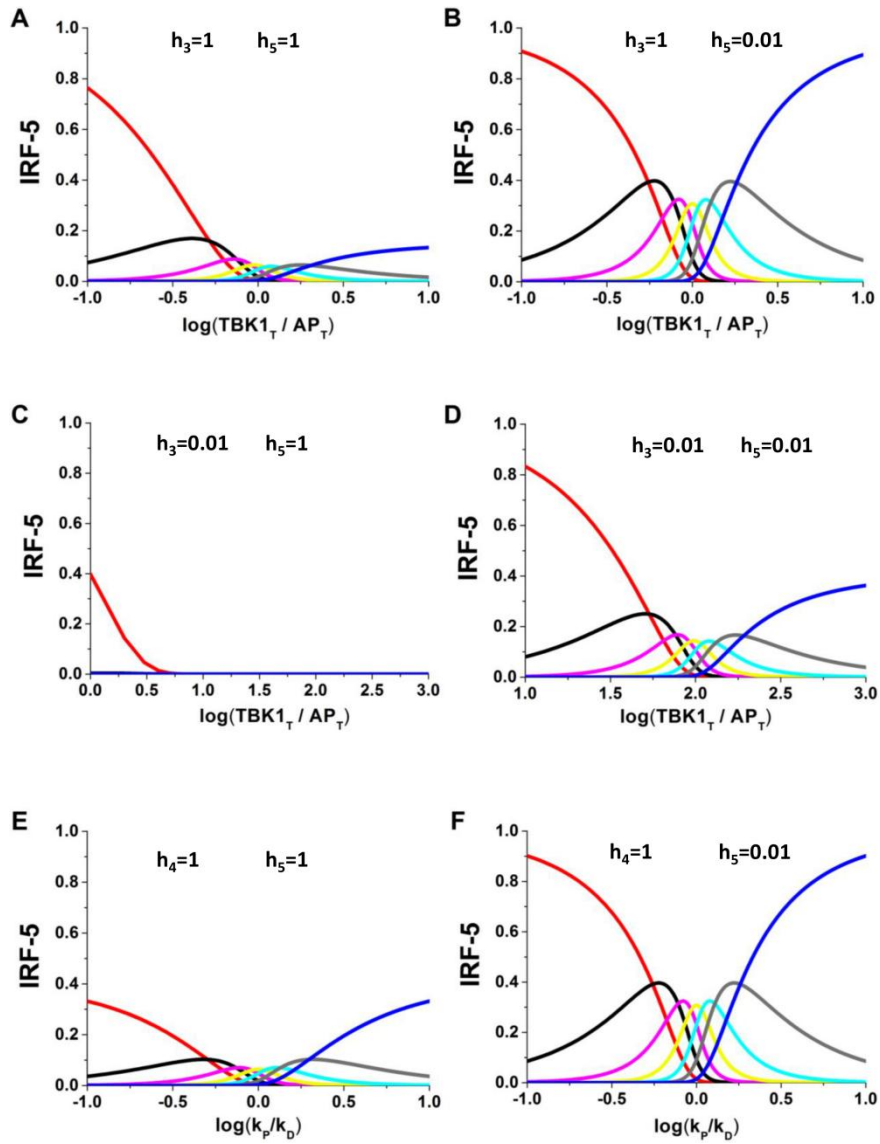


Figure 3.5. Theoretical investigation of the regulation of IRF-5 multisite phosphorylation.

The distribution of IRF-5 species is investigated as a function of kinase to phosphatase (TBK-1 to AP) ratio for comparable IRF-5 and AP concentrations (A), IRF-5 significantly exceeds AP (B). Similar analysis is also performed when the phosphorylation rate was significantly lower than dephosphorylation rate and comparable IRF-5 and AP concentrations (C), IRF-5 significantly exceeds AP (D). The effects of changes in the phosphorylation to dephosphorylation ratio on the IRF-5 species were also investigated with comparable IRF-5 and AP concentrations (E), IRF-5 significantly exceeds AP (F). The presented analyses clearly show that the phosphorylation/dephosphorylation parameters, modulated via extracellular cytokines have prominent impact on the distribution of phosphorylated species. Therefore, physiological or pathological alterations of these parameters represent the multisite phosphorylation-mediated mechanism of T cell plasticity. Here we use Equation (3.27) with  $h_1 = 1/6$ ,  $h_2 = 1/6$ ,  $h_4 = TBK_T/AP_T$ , in (A), (B), (C) and (D),  $h_1 = 1/6$ ,  $h_2 = 1/6$ ,  $h_3 = k_p/k_D$  in (E) and (F).

Our results suggest that the selective activity of the multisite phosphoprotein-mediated response is regulated by the ratio of the total amounts of the protein to phosphatase and by the relative rates of the phosphorylation-dephosphorylation reactions. These effects were not observed in previously reported mathematical models of phosphorylation [23,26,29,116,182]. The comparison of our analysis with experimental data [164-168,170] summarised in Figure 3.1 allows us to conclude that the multisite phosphorylation reactions enable diverse cellular activatory profiles in response to slight variations in the extracellular signal.

### **3.4.3 Phosphorylation in the control of aggregation and deformability of erythrocytes**

Human erythrocytes are highly specialised enucleate cells that are involved in providing efficient gas transport. Erythrocytes have been extensively studied both experimentally and by mathematical modelling in recent years. However, understanding of how aggregation and deformability are regulated is limited. These properties of the erythrocyte are essential for the physiological functioning of the cell.

The model proposed in this subsection for the phosphorylation of EF1 and EF2 proteins that control aggregation and deformability of erythrocytes, was employed by the authors in [31]. The authors proposed a novel mathematical model of the molecular system that controls the aggregation and deformability of the erythrocyte and suggested fundamentally new mechanisms that regulate the aggregation and deformability in a latch-like manner. The results of this work could be used as a possible explanation of how the erythrocytes regulate their aggregation and deformability, which are essential in understanding erythrocyte disorders and aging. In this subsection the module that includes phosphorylation of EF1 and EF2 proteins is described.

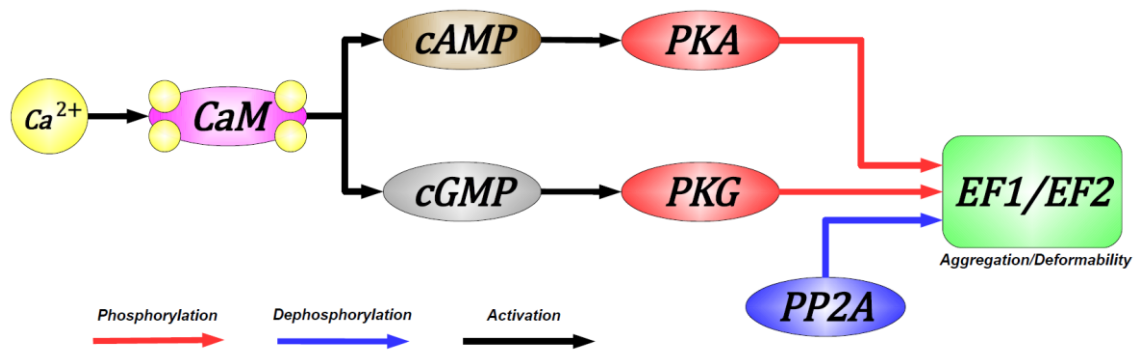


Figure 3.6. Phosphorylation of EF1 and EF2 proteins controls the aggregation and deformability of erythrocytes.

Calcium regulates the activity of cAMP- and cGMP- dependent protein kinases (PKA and PKG respectively), which in turn phosphorylate EF1 and EF2 proteins involved in the regulation of the aggregation and deformability of erythrocytes. Dephosphorylation of EF1/EF2 proteins is performed by PP2A phosphatase.

Figure 3.6 schematically represents the structure of the model developed in this subsection. Calcium ions ( $Ca^{2+}$ ) bind  $Ca^{2+}$  dependent protein calmodulin (CaM) at four binding sites and activate it. CaM controls the shape of erythrocytes [183] and the activation of cyclic adenosine monophosphate (cAMP) and cyclic guanine monophosphate (cGMP). Changes in the concentration of cyclic monophosphates modulate the activity of cAMP-dependent protein kinase (PKA) and cGMP-dependent protein kinase (PKG). These kinases and phosphatase PP2A define the phosphorylation level of the membrane proteins EF1 and cytoskeleton EF2. Phosphorylation of certain proteins affects the rheological properties of blood due to changes in aggregation and deformability [184]. PKA and PKG kinases phosphorylate EF1 and EF2 proteins, which are responsible for the aggregation and deformability of erythrocytes, while PP2A dephosphorylates them (Figure 3.6).

The activity of cAMP dependent kinase PKA is determined by the concentration of cAMP. There are four cAMP binding sites of PKA. When the complex of PKA with cAMP is formed, kinase PKA dissociates into four fragments, two of which have the enzyme activity [185]. According to Equation (2.15) for  $n = 4$ , it can be written for the concentration of PKA as a function of calcium:

$$[PKA(ca)] = 2 \cdot PKA_T \cdot \left( \frac{[cAMP(ca)]}{K_{cAMP}^{PKA} + [cAMP(ca)]} \right)^4, \quad (3.28)$$

where  $PKA_T$  is the total concentration of PKA,  $K_{cAMP}^{PKA}$  is the Michaelis constant for the reaction of complex formation of cAMP with PKA,  $ca$  is non-dimensional concentration of  $Ca^{2+}$ ,  $[cAMP(ca)]$  is the concentration of cAMP.

Equation (3.28) can be written in non-dimensional form as follows:

$$pka(ca) = 2 \cdot \left( \frac{camp(ca)}{\mu_{cAMP}^{PKA} + camp(ca)} \right)^4, \quad (3.29)$$

where  $pka(ca) = \frac{[PKA(ca)]}{PKA_T}$ ,  $\mu_{cAMP}^{PKA} = \frac{K_{cAMP}^{PKA}}{K_{ATP}^{AC}}$ ,  $camp(ca) = \frac{[cAMP(ca)]}{K_{ATP}^{AC}}$ ,  $K_{ATP}^{AC}$  is the

Michaelis constant for the reaction of complex formation of ATP with adenylate cyclase AC.

According to Equation (2.15) for  $n=1$  the concentration of cGMP dependent kinase as a function of cGMP concentration can be written as follows:

$$[PKG(ca)] = PKG_T \cdot \left( \frac{[cGMP(ca)]}{K_{cGMP}^{PKG} + [cGMP(ca)]} \right), \quad (3.30)$$

where  $PKG_T$  is the total concentration of PKG,  $K_{cGMP}^{PKG}$  is the Michaelis constant for the reaction of complex formation of cGMP with PKG,  $[cGMP(ca)]$  is the concentration of cGMP.

Equation (3.30) can be written in non-dimensional form as follows:

$$pkg(ca) = \left( \frac{cgmp(ca)}{\mu_{cGMP}^{PKG} + cgmp(ca)} \right), \quad (3.31)$$

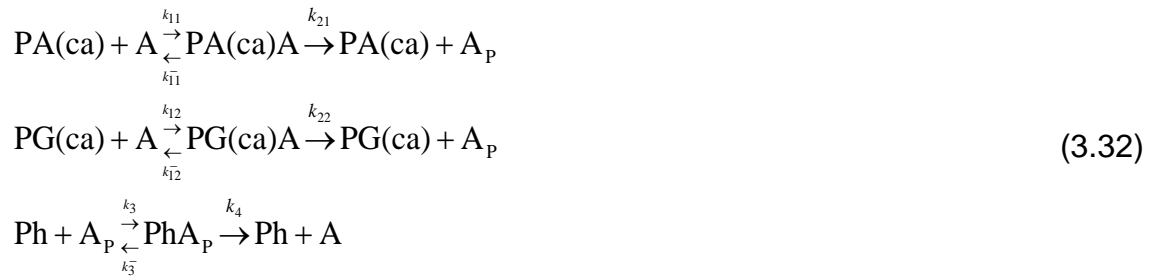
where  $pkg(ca) = \frac{[PKG(ca)]}{PKG_T}$ ,  $\mu_{cGMP}^{PKG} = \frac{K_{cGMP}^{PKG}}{K_{GTP}^{GC}}$ ,  $cgmp(ca) = \frac{[cGMP(ca)]}{K_{GTP}^{GC}}$ ,  $K_{GTP}^{GC}$  is the

Michaelis constant for the reaction of complex formation of GTP with guanylate cyclase GC.

As it was mentioned above, cAMP- and cGMP-dependent kinases

phosphorylate, and PP2A phosphatase dephosphorylates EF1 and EF2 proteins. The latter two define the level of aggregation and deformability. We consider the phosphorylation level of these proteins as a function of the activity of the *PKA* and *PKG* kinases and *Ph* phosphatase. Here we assume for simplicity that phosphorylation of all sites of EF1 and EF2 proteins leads to their activation, which implies that the multisite phosphorylation can be simplified by considering single site phosphorylation (Figure 3.4C).

We use  $A_T$  to denote the total concentration of the protein (either EF1 or EF2);  $Ph_T$  is the total concentration of phosphatase PP2A;  $[PA_A(ca)]$  and  $[PG_A(ca)]$  are the total concentrations of the kinases in their active forms;  $[PA(ca)]$  and  $[PG(ca)]$  are the concentrations of free kinases;  $[PA(ca)A]$ ,  $[PG(ca)A]$  and  $[PhA_p]$  are the concentrations of enzyme–substrate complexes. The phosphorylation-dephosphorylation reactions can be written as follows:



The following ODEs can be written for the above biochemical Equations (3.32):

$$\begin{aligned}
 \frac{d[PA(ca)A]}{dt} &= k_{11} \cdot [PA(ca)] \cdot [A] - (k_{21} + k_{11}^-) \cdot [PA(ca)A], \\
 \frac{d[PG(ca)A]}{dt} &= k_{12} \cdot [PG(ca)] \cdot [A] - (k_{22} + k_{12}^-) \cdot [PG(ca)A], \\
 \frac{d[PhA_p]}{dt} &= k_3 \cdot [Ph] \cdot [A_p] - (k_4 + k_3^-) \cdot [PhA_p], \\
 \frac{d[A_p]}{dt} &= k_{21} \cdot [PA(ca)A] + k_{22} \cdot [PG(ca)A] - k_3 \cdot [Ph] \cdot [A_p] + k_3^- \cdot [PhA_p], \\
 \frac{d[A]}{dt} &= k_4 \cdot [PhA_p] - k_{11} \cdot [PA(ca)] \cdot [A] - k_{12} \cdot [PG(ca)] \cdot [A] + \\
 &\quad + k_{11}^- \cdot [PA(ca)A] + k_{12}^- \cdot [PG(ca)A].
 \end{aligned} \tag{3.33}$$



The conservation equations for the total concentrations are given by:

$$\begin{aligned}
[A] + [A_p] + [PA(ca)A] + [PG(ca)A] + [PhA_p] &= A_T, \\
[PA(ca)] + [PA(ca)A] &= [PA_A(ca)], \\
[PG(ca)] + [PG(ca)A] &= [PG_A(ca)], \\
[Ph] + [PhA_p] &= Ph_T.
\end{aligned} \tag{3.34}$$

Using the QSSA [57,186], according to which  $\frac{d[PA(ca)A]}{dt} = 0$ ,  $\frac{d[PG(ca)A]}{dt} = 0$

and  $\frac{d[PhA_p]}{dt} = 0$ , we find the concentrations of the enzyme-substrate complexes:

$$\begin{aligned}
[PA(ca)A] &= \frac{[PA_A(ca)] \cdot [A]}{K_{1p} + [A]}, \\
[PG(ca)A] &= \frac{[PG_A(ca)] \cdot [A]}{K_{2p} + [A]}, \\
[Ph(ca)A_p] &= \frac{Ph_T \cdot [A_p]}{K_F + [A_p]}.
\end{aligned} \tag{3.35}$$

We can write the rate of the protein phosphorylation as follows:

$$\frac{d[A_p]}{dt} = k_{21} \cdot [PA(ca)A] + k_{22} \cdot [PG(ca)A] - k_4 \cdot [PhA_p] \tag{3.36}$$

It can be written from the first conservation equation in Equations (3.34):

$$[A] = A_T - [A_p] + [PA(ca)A] + [PG(ca)A] + [PhA_p] \tag{3.37}$$

Thus:

$$\begin{aligned}
\frac{d[A_p]}{dt} &= k_{21} \cdot \frac{[PA_A(ca)] \cdot (A_T - [A_p] - [PA(ca)A] - [PG(ca)A] - [PhA_p])}{K_{1p} + A_T - [A_p] - [PA(ca)A] - [PG(ca)A] - [PhA_p]} + \\
&+ k_{22} \cdot \frac{[PG_A(ca)] \cdot (A_T - [A_p] - [PA(ca)A] - [PG(ca)A] - [PhA_p])}{K_{2p} + A_T - [A_p] - [PA(ca)A] - [PG(ca)A] - [PhA_p]} - k_4 \cdot \frac{Ph_T \cdot [A_p]}{K_F + [A_p]},
\end{aligned} \tag{3.38}$$

where  $K_{1p} = \frac{k_{21} + k_{11}^-}{k_{11}}$ ,  $K_{2p} = \frac{k_{22} + k_{12}^-}{k_{12}}$  and  $K_F = \frac{k_4 + k_3^-}{k_3}$ .

We assume that EF1 and EF2 are activated by PKA and PKG by the same mechanism, which implies that  $k_{21} = k_{22} = k_2$ ,  $K_{1P} = K_{2P} = K_P$  and we also assume that the total amounts of PKA and PKG are similar  $PKA_T = PKG_T = PK_T$ .

We can write in this case:

$$\frac{d[A_p]}{dt} = k_2 \cdot \frac{([PA_A(ca)] + [PG_A(ca)]) \cdot (A_T - [A_p]) - [PA(ca)A] - [PG(ca)A] - [PhA_p]}{K_P + A_T - [A_p] - [PA(ca)A] - [PG(ca)A] - [PhA_p]} - k_4 \cdot \frac{Ph_T \cdot [A_p]}{K_F + [A_p]}, \quad (3.39)$$

Assuming that the total concentrations of the kinases in their active forms are  $[PA_A(ca)] = [PKA(ca)]$  and  $[PG_A(ca)] = [PKG(ca)]$  in Equations (3.28) and (3.29) respectively, we can rewrite Equation (3.39) in non-dimensional form as follows:

$$\frac{da_p}{d\tilde{t}} = h_5 \cdot \left( \frac{h_3 \cdot h_4(ca) \cdot (1 - a_p - p1a - p2a - phap)}{h_1 + 1 - a_p - p1a - p2a - phap} - \frac{a_p}{h_2 + a_p} \right), \quad (3.40)$$

where  $a_p = \frac{[A_p]}{A_T}$ ,  $p1a = \frac{[PA(ca)A]}{A_T}$ ,  $p2a = \frac{[PG(ca)A]}{A_T}$ ,  $phap = \frac{[PhA_p]}{A_T}$ ,  $\tilde{t} = t \cdot k_4$ ,

$$h_1 = \frac{K_P}{A_T}, \quad h_2 = \frac{K_F}{A_T}, \quad h_3 = \frac{k_2}{k_4}, \quad h_4(ca) = \frac{PK_T}{Ph_T} \cdot (pka(ca) + pkg(ca)), \quad h_5 = \frac{Ph_T}{A_T}.$$

Equation (3.40) corresponds to Equation (3.8) but here we have  $h_4$  as a function of  $Ca^{2+}$ . To find a steady-state solution of Equation (3.40) we assume that the concentrations of all complexes are negligible since  $h_5 = \frac{Ph_T}{A_T}$  is a small value due the fact that EF1 and EF2 are abundant proteins [187,188]. Thus we can rewrite Equation (3.40) in the following way:

$$\frac{da_p}{d\tilde{t}} = h_5 \left( \frac{\alpha \cdot (pka(ca) + pkg(ca)) \cdot (1 - a_p)}{h_1 + 1 - a_p} - \frac{a_p}{h_2 + a_p} \right), \quad (3.41)$$

where  $\alpha = \frac{k_2}{k_4} \cdot \frac{PK_T}{Ph_T}$ .

According to Equation (3.11) a steady-state solution of Equation (3.41) can be written as follows:

$$a_p(ca) = \frac{h_1 + \beta(ca)(h_2 - 1) + 1 - \sqrt{(h_1 + \beta(ca)(h_2 - 1) + 1)^2 - 4 \cdot h_2 \cdot \beta(ca) \cdot (1 - \beta(ca))}}{2(1 - \beta(ca))}, \quad (3.42)$$

where  $\beta(ca) = h_3 \cdot h_4(ca) = \alpha \cdot (pka(ca) + pkg(ca))$ .

Due to the fact that EF1 and EF2 proteins are more abundant than PKA and PKG kinases [187,188], in Equation (3.37) we can neglect the concentrations of the enzyme-substrate complexes, which is consistent with [23]. Thus according to Equation (3.37) the concentration of the unphosphorylated protein in non-dimensional form can be written as follows:

$$a(ca) = 1 - a_p(ca), \quad (3.43)$$

Next we test how this assumption affects the overall behaviour. In our model we set small  $h_5 = 0.01$  due to the above mentioned assumption. We assume that the concentration of the kinases is similar to the concentration of the phosphatase  $\frac{PK_T}{Ph_T} = 1$ . Since  $pka(ca), pkg(ca) < 1$  then  $h_4(ca) \in (0, 2)$ . We check

the two approaches using the simplified Equations (3.11), (3.42) and the "full" model in Equation (3.22) for the following set of parameters:  $\mu_{cAMP}^{PKA} = 1.8$ ,

$\mu_{cGMP}^{PKG} = 8$ ,  $\alpha = 0.6$ ,  $h_1 = 0.02$ ,  $h_2 = 1.8$ . Since we assume that  $\frac{PK_T}{Ph_T} = 1$ ,  $\alpha = 0.6$  in

fact means that  $h_3 = \frac{k_2}{k_4} = 0.6$ . Figure 3.7 shows the solutions for the two

approaches for the above parameters. It can be clearly seen from the figure that there is almost no difference between the simplified and the "full" approach and thus the assumption introduced above, where we neglected the concentrations of the enzyme-substrate complexes, does not affect the overall behaviour. Due to this fact the analysis is performed using the simplified version of the model.

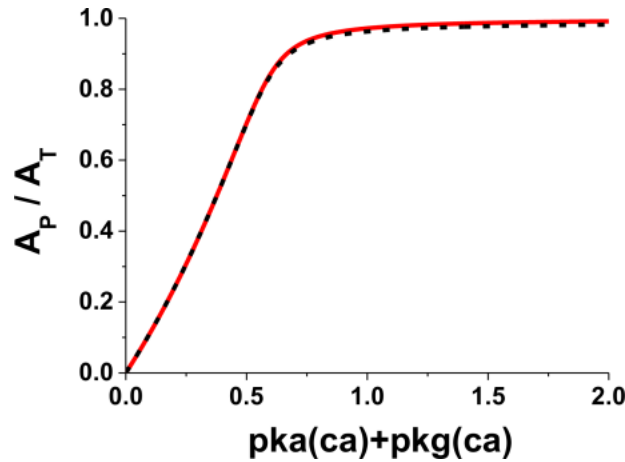


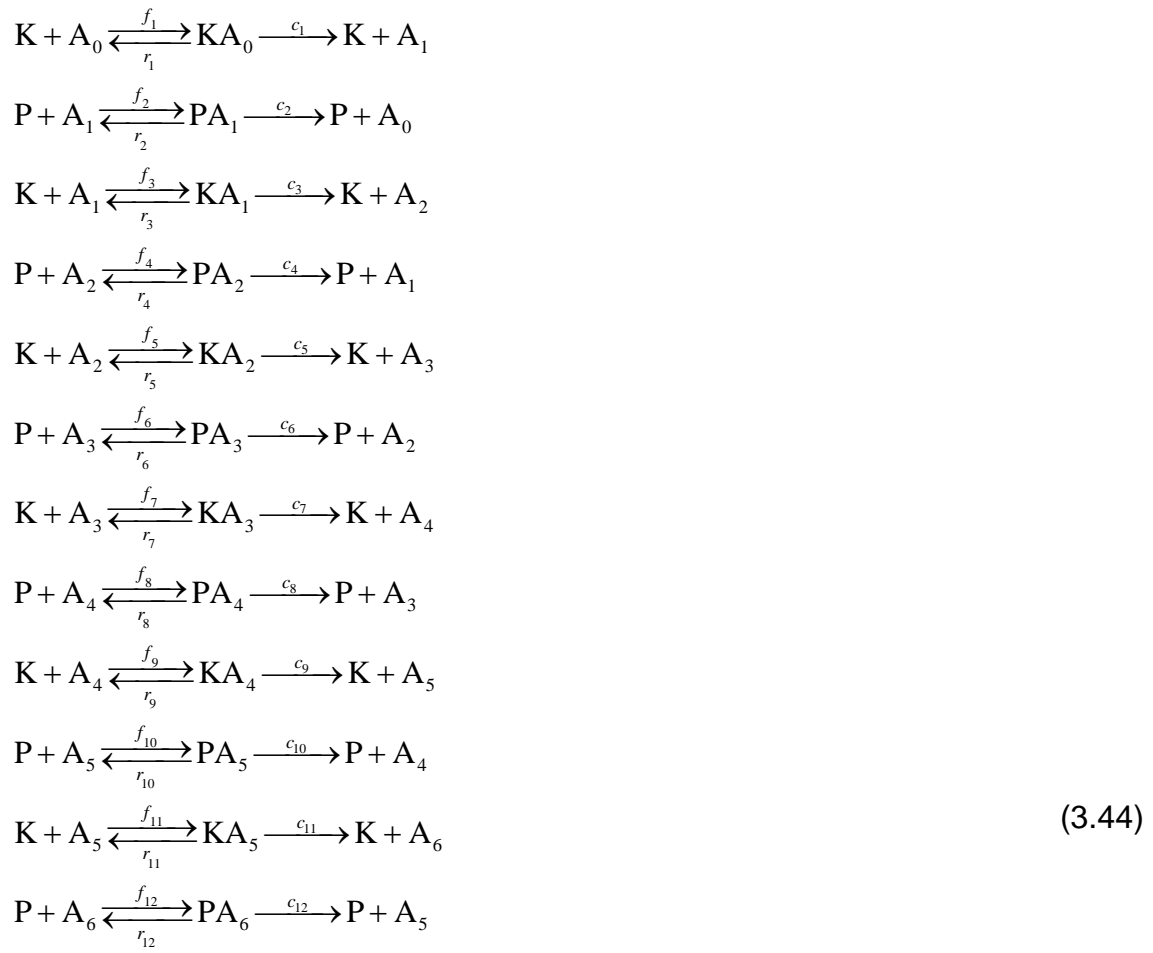
Figure 3.7. Check of the feasibility of the model assumptions, where the concentrations of enzyme-substrate complexes are neglected.

Red line represents the solutions obtained in Equations (3.11) and (3.42). Dotted black line represents the solutions obtained in Equation (3.22). The parameters are  $h_1 = 0.02$ ,  $h_2 = 1.8$ ,  $h_3 = 0.6$ ,  $h_4(ca) = pka(ca) + pkg(ca)$  and  $h_5 = 0.01$ .

In paper [31] Equations (3.42) and (3.43) were used to describe the levels of phosphorylation of the proteins, which determine erythrocyte deformability and aggregation (proportionally to the levels of non-phosphorylated proteins EF1) as a function of calcium concentration.

### 3.5 Sequential multisite phosphorylation

Now we consider sequential phosphorylation of protein  $A$  by kinase  $K$  and dephosphorylation by phosphatase  $P$ . Multisite proteins are sequentially phosphorylated when phosphorylation of the site is possible only when the previous phosphorylation site is phosphorylated. The sequential phosphorylation reactions for a molecule with six sites can be represented as follows:



where  $A_i$  is a protein with  $i$  phosphorylated sites.

The ODEs for this system are:

$$\begin{aligned}
\frac{d[K]}{dt} &= -f_1[K][A_0] + (r_1 + c_1)[KA_0] - f_3[K][A_1] + (r_3 + c_3)[KA_1] - \\
&\quad - f_5[K][A_2] + (r_5 + c_5)[KA_2] - f_7[K][A_3] + (r_7 + c_7)[KA_3] - \\
&\quad - f_9[K][A_4] + (r_9 + c_9)[KA_4] - f_{11}[K][A_5] + (r_{11} + c_{11})[KA_5], \\
\frac{d[P]}{dt} &= -f_2[P][A_1] + (r_2 + c_2)[PA_1] - f_4[P][A_2] + (r_4 + c_4)[PA_2] - \\
&\quad - f_6[P][A_3] + (r_6 + c_6)[PA_3] - f_8[P][A_4] + (r_4 + c_4)[PA_4] - \\
&\quad - f_{10}[P][A_5] + (r_{10} + c_{10})[PA_5] - f_{12}[P][A_6] + (r_{12} + c_{12})[PA_6], \\
\frac{d[A_0]}{dt} &= -f_1[K][A_0] + r_1[KA_0] + c_2[PA_1], \\
\frac{d[KA_0]}{dt} &= f_1[K][A_0] - (r_1 + c_1)[KA_0], \\
\frac{d[A_1]}{dt} &= c_1[KA_0] - f_2[P][A_1] + r_2[PA_1] - f_3[K][A_1] + r_3[KA_1] + c_4[PA_2], \\
\frac{d[PA_1]}{dt} &= f_2[P][A_1] - (r_2 + c_2)[PA_1], \\
\frac{d[KA_1]}{dt} &= f_3[K][A_1] - (r_3 + c_3)[KA_1], \\
\frac{d[A_2]}{dt} &= c_3[KA_1] - f_4[P][A_2] + r_4[PA_2] - f_5[K][A_2] + r_5[KA_2] + c_6[PA_3], \\
\frac{d[PA_2]}{dt} &= f_4[P][A_2] - (r_4 + c_4)[PA_2], \\
\frac{d[KA_2]}{dt} &= f_5[K][A_2] - (r_5 + c_5)[KA_2], \\
\frac{d[A_3]}{dt} &= c_5[KA_2] - f_6[P][A_3] + r_6[PA_3] - f_7[K][A_3] + r_7[KA_3] + c_8[PA_4], \\
\frac{d[PA_3]}{dt} &= f_6[P][A_3] - (r_6 + c_6)[PA_3], \\
\frac{d[KA_3]}{dt} &= f_7[K][A_3] - (r_7 + c_7)[KA_3], \\
\frac{d[A_4]}{dt} &= c_7[KA_3] - f_8[P][A_4] + r_8[PA_4] - f_9[K][A_4] + r_9[KA_4] + c_{10}[PA_5], \\
\frac{d[PA_4]}{dt} &= f_8[P][A_4] - (r_8 + c_8)[PA_4], \\
\frac{d[KA_4]}{dt} &= f_9[K][A_4] - (r_9 + c_9)[KA_4], \\
\frac{d[A_5]}{dt} &= c_9[KA_4] - f_{10}[P][A_5] + r_{10}[PA_5] - f_{11}[K][A_5] + r_{11}[KA_5] + c_{12}[PA_6], \\
\frac{d[PA_5]}{dt} &= f_{10}[P][A_5] - (r_{10} + c_{10})[PA_5], \\
\frac{d[KA_5]}{dt} &= f_{11}[K][A_5] - (r_{11} + c_{11})[KA_5],
\end{aligned}$$

$$\frac{d[A_6]}{dt} = c_{11}[KA_5] - f_{12}[P][A_6] + r_{12}[PA_6],$$

$$\frac{d[PA_6]}{dt} = f_{12}[P][A_6] - (r_{12} + c_{12})[PA_6].$$

The conservation equations for  $[K]$  and  $[P]$  that follow from Equations (3.45) respectively:

$$K_T = [K] + [KA_0] + [KA_1] + [KA_2] + [KA_3] + [KA_4] + [KA_5],$$

$$P_T = [P] + [PA_1] + [PA_2] + [PA_3] + [PA_4] + [PA_5] + [PA_6]. \quad (3.46)$$

We use the QSSA [57,186], according to which  $\frac{d[KA_0]}{dt} = 0$ ,  $\frac{d[PA_1]}{dt} = 0$ ,

$$\frac{d[KA_1]}{dt} = 0, \quad \frac{d[PA_2]}{dt} = 0, \quad \frac{d[KA_2]}{dt} = 0, \quad \frac{d[PA_3]}{dt} = 0, \quad \frac{d[KA_3]}{dt} = 0, \quad \frac{d[PA_4]}{dt} = 0,$$

$$\frac{d[KA_4]}{dt} = 0, \quad \frac{d[PA_5]}{dt} = 0, \quad \frac{d[KA_5]}{dt} = 0, \quad \frac{d[PA_6]}{dt} = 0.$$

We can rewrite Equations (3.45) only for phosphorylated molecules with 1 to 6 sites phosphorylated as follows:

$$\frac{d[A_1]}{dt} = \frac{q_1 K_T (A_T - 2[A_1] - [A_2] - [A_3] - [A_4] - [A_5] - [A_6])}{M_1 + A_T - [A_6]} - \frac{q_2 P_T ([A_1] - [A_2])}{M_2 + [A_1] + [A_2] + [A_3] + [A_4] + [A_5] + [A_6]},$$

$$\frac{d[A_2]}{dt} = \frac{q_1 K_T ([A_1] - [A_2])}{M_1 + A_T - [A_6]} - \frac{q_2 P_T ([A_2] - [A_3])}{M_2 + [A_1] + [A_2] + [A_3] + [A_4] + [A_5] + [A_6]},$$

$$\frac{d[A_3]}{dt} = \frac{q_1 K_T ([A_2] - [A_3])}{M_1 + A_T - [A_6]} - \frac{q_2 P_T ([A_3] - [A_4])}{M_2 + [A_1] + [A_2] + [A_3] + [A_4] + [A_5] + [A_6]},$$

$$\frac{d[A_4]}{dt} = \frac{q_1 K_T ([A_3] - [A_4])}{M_1 + A_T - [A_6]} - \frac{q_2 P_T ([A_4] - [A_5])}{M_2 + [A_1] + [A_2] + [A_3] + [A_4] + [A_5] + [A_6]},$$

$$\frac{d[A_5]}{dt} = \frac{q_1 K_T ([A_4] - [A_5])}{M_1 + A_T - [A_6]} - \frac{q_2 P_T ([A_5] - [A_6])}{M_2 + [A_1] + [A_2] + [A_3] + [A_4] + [A_5] + [A_6]},$$

$$\frac{d[A_6]}{dt} = \frac{q_1 K_T [A_5]}{M_1 + A_T - [A_6]} - \frac{q_2 P_T [A_6]}{M_2 + [A_1] + [A_2] + [A_3] + [A_4] + [A_5] + [A_6]}. \quad (3.47)$$

The system of ODEs (3.47) can be solved numerically since there are six equations and six unknowns.

In a more general case, where a molecule has  $n$  sites and the mechanism of phosphorylation is sequential, we can write equations for the concentrations of kinase-protein and phosphatase-protein complexes respectively:

$$\begin{aligned} [KA_i] &= K_T \frac{[A_i]}{M_1 + \sum_{j=0}^{n-1} [A_j]}, \quad i = 0 \dots n-1, \\ [PA_i] &= P_T \frac{[A_i]}{M_2 + \sum_{j=1}^n [A_j]}, \quad i = 1 \dots n. \end{aligned} \quad (3.48)$$

We can rewrite Equations (3.47) for intermediate forms:

$$\frac{d[A_i]}{dt} = q_1 K_T \frac{[A_{i-1}] - [A_i]}{M_1 + \sum_{j=0}^{n-1} A_j} - q_2 P_T \frac{[A_i] - [A_{i+1}]}{M_2 + \sum_{j=1}^n A_j}, \quad i = 1 \dots n-1. \quad (3.49)$$

We can also rewrite Equations (3.47) for apo- and saturated forms respectively:

$$\begin{aligned} \frac{d[A_0]}{dt} &= -q_1 K_T \frac{[A_0]}{M_1 + \sum_{j=0}^{n-1} A_j} + q_2 P_T \frac{[A_1]}{M_2 + \sum_{j=1}^n A_j}, \\ \frac{d[A_n]}{dt} &= q_1 K_T \frac{[A_{n-1}]}{M_1 + \sum_{j=0}^{n-1} A_j} - q_2 P_T \frac{[A_n]}{M_2 + \sum_{j=1}^n A_j} \end{aligned} \quad (3.50)$$

Equations (3.48), (3.49) and (3.50) are similar to the equations in the previously published papers [8,13,155,156].

We can write Equations (3.47) in non-dimensional form as following:



$$\begin{aligned}
\frac{da_0}{d\tau} &= h_5 \left( -h_3 h_4 \frac{a_0}{h_1 + a_0 + a_1 + a_2 + a_3 + a_4 + a_5} + \frac{a_1}{h_2 + a_1 + a_2 + a_3 + a_4 + a_5 + a_6} \right), \\
\frac{da_1}{d\tau} &= h_5 \left( h_3 h_4 \frac{a_0 - a_1}{h_1 + a_0 + a_1 + a_2 + a_3 + a_4 + a_5} - \frac{a_1 - a_2}{h_2 + a_1 + a_2 + a_3 + a_4 + a_5 + a_6} \right), \\
\frac{da_2}{d\tau} &= h_5 \left( h_3 h_4 \frac{a_1 - a_2}{h_1 + a_0 + a_1 + a_2 + a_3 + a_4 + a_5} - \frac{a_2 - a_3}{h_2 + a_1 + a_2 + a_3 + a_4 + a_5 + a_6} \right), \\
\frac{da_3}{d\tau} &= h_5 \left( h_3 h_4 \frac{a_2 - a_3}{h_1 + a_0 + a_1 + a_2 + a_3 + a_4 + a_5} - \frac{a_3 - a_4}{h_2 + a_1 + a_2 + a_3 + a_4 + a_5 + a_6} \right), \\
\frac{da_4}{d\tau} &= h_5 \left( h_3 h_4 \frac{a_3 - a_4}{h_1 + a_0 + a_1 + a_2 + a_3 + a_4 + a_5} - \frac{a_4 - a_5}{h_2 + a_1 + a_2 + a_3 + a_4 + a_5 + a_6} \right), \\
\frac{da_5}{d\tau} &= h_5 \left( h_3 h_4 \frac{a_4 - a_5}{h_1 + a_0 + a_1 + a_2 + a_3 + a_4 + a_5} - \frac{a_5 - a_6}{h_2 + a_1 + a_2 + a_3 + a_4 + a_5 + a_6} \right), \\
\frac{da_6}{d\tau} &= h_5 \left( h_3 h_4 \frac{a_5}{h_1 + a_0 + a_1 + a_2 + a_3 + a_4 + a_5} - \frac{a_6}{h_2 + a_1 + a_2 + a_3 + a_4 + a_5 + a_6} \right). \tag{3.51}
\end{aligned}$$

where  $h_1 = \frac{M_1}{A_T}, h_2 = \frac{M_2}{A_T}, h_4 = \frac{K_T}{P_T}, h_5 = \frac{P_T}{A_T}, ka_i = \frac{[KA_i]}{A_T}, (i=0...5), \tau = t \cdot k_4, h_3 = \frac{q_1}{q_2}$ .

and  $pa_j = \frac{[PA_j]}{A_T}, (j=1...6), a_k = \frac{[A_k]}{A_T}, (k=1...6)$ .

We found the steady-state solutions of Equations (3.51) numerically. Figure 3.8 shows the dose-response curves for proteins with 0 to 6 phosphorylated sites as a function of total kinase to phosphatase ratio. Our analysis (figures not shown) reveals that alterations of the ratio of the total TBK-1 and AP to IRF-5 do not affect the shapes shown in Figure 3.8 due to the fact that the concentrations of the enzyme-substrate complexes are neglected [23]. Figure 3.8 shows that in the case of sequential phosphorylation the maximums of concentrations for intermediate phosphorylated IRF-5 species are distributed closer to each other compared to the case with independent multisite phosphorylation shown in Figure 3.4B.

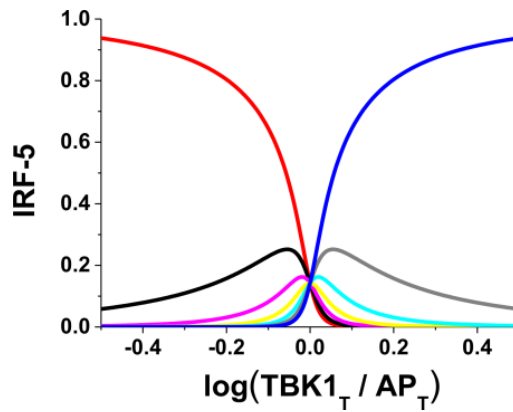
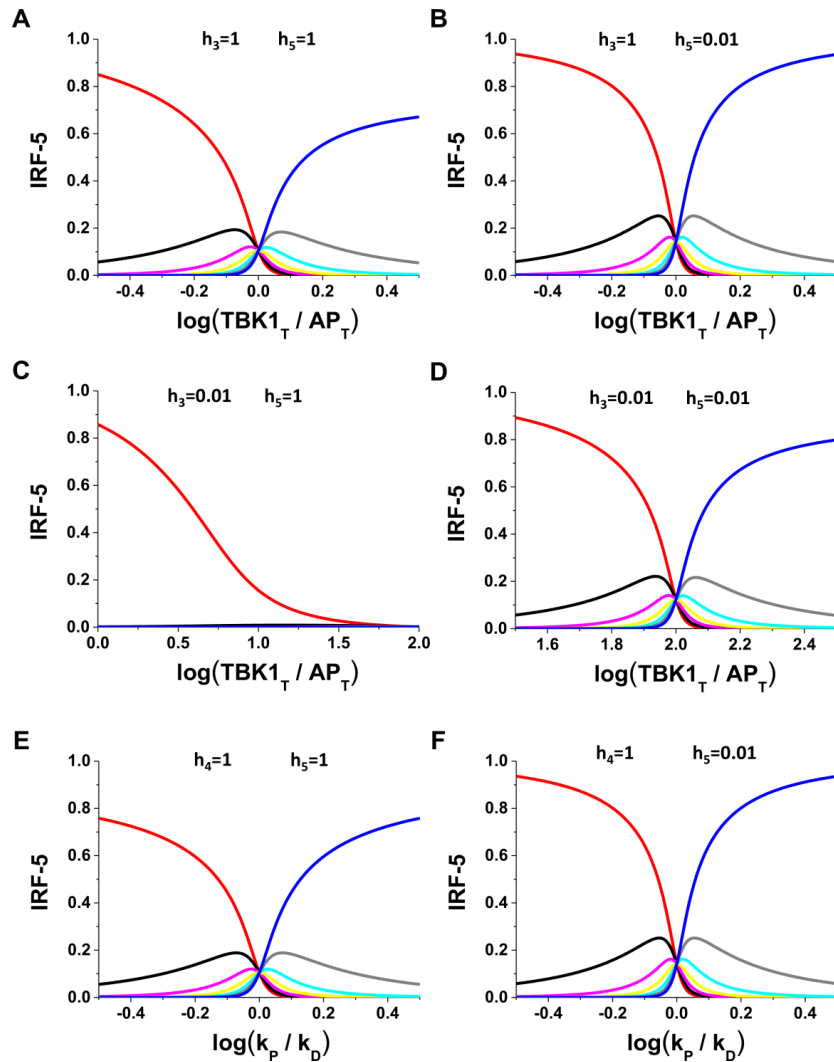


Figure 3.8. Model predictions for the sequential phosphorylation of IRF-5. The concentration of IRF-5 phosphorylated at one (black), two (magenta), three (yellow), four (cyan), five (grey) and six (blue) sites is shown as a function of total TBK-1 to AP ratio (Equations (3.51) with  $h_1=1$ ,  $h_2=1$ ,  $h_3=1$ ,  $h_4 = TBK_T/AP_T$ ,  $h_5=1$ ). Here we consider the first physiological scenario where we assume that the total concentration of protein exceeds the total concentrations of kinase and phosphatase and therefore we neglect the concentrations of enzyme-substrate complexes as it was shown in [23].

We next analyse the alterations of the parameters corresponding to the phosphorylation to dephosphorylation reaction rates as well as IRF-5 to TBK-1 and AP ratios in order to compare the model predictions for the sequential multisite phosphorylation events with the predictions for independent phosphorylation shown in Figure 3.5. Figure 3.9 shows the influence of variation of these parameters on our model. The shapes of the model predictions for the concentrations of individual conformations for sequential phosphorylation events shown in Figure 3.9 are similar to the shapes for the model predictions in the case of independent phosphorylation illustrated in Figure 3.5. However, the difference between the previously published models [23] and the models that are developed in this chapter is less significant for the case of sequential phosphorylation (Figure 3.9). For example, Figure 3.5A shows that the non-dimensional magnitude of IRF-5 phosphorylated at 6 phosphorylation sites is 0.1 whereas it is 0.6 in Figure 3.9A for the case when the total concentration of IRF-5 is equal to the total concentration of AP and for the same phosphorylation and dephosphorylation rate constants. Figure 3.5C illustrates the model predictions, according to which the concentration of apo form for the low total TBK-1 to AP ratio is 0.4 while Figure 3.9C shows that this value is 0.87 when dephosphorylation reaction constant is 100 times higher than the

phosphorylation constant ( $h_3 = 0.01$ ). In the case when the total concentrations of IRF-5, AP and TBK-1 are the same, the magnitudes of concentrations of individual conformations are lower when the protein is phosphorylated independently (Figure 3.5E) compared to the sequential phosphorylation (Figure 3.9E), 0.32 and 0.75, respectively.



*Figure 3.9. Theoretical investigation of the sequential IRF-5 phosphorylation. Dose-response curves for phosphorylated IRF-5 as a function of TBK-1 to AP ratio for comparable total TBK-1, AP and IRF-5 concentrations (A) and when IRF-5 significantly exceeds total TBK-1 and AP. Similar analysis is performed for the case where another important parameter, the ratio between phosphorylation and dephosphorylation reactions, is low (C, D). The amount of phosphorylated IRF-5 species as a function of the ratio of phosphorylation to dephosphorylation reaction rates for comparable IRF-5, TBK-1 and AP concentrations (E) as well as when AP is much lower than IRF-5 (F). See Equations (3.51), with  $h_1 = 1, h_2 = 1, h_4 = \text{TBK}_T / \text{AP}_T$  in (A), (B), (C), (D) and  $h_1 = 1, h_2 = 1, h_3 = k_p / k_D$  in (E), (F).*

### 3.6 Conclusions

In this chapter we proposed a new model for multisite phosphorylation with applications to intracellular signalling in the immune system and erythrocyte regulation of aggregation and deformability. This model is another example of the low-level substrate properties analysis in terms of Figure 1.1 and will be used in the following Chapters 4 and 5 as an element of a higher level analysis.

The proposed model extends previous models for activation of proteins by single- [23-26,29,152] and multisite phosphorylation [27,153,154,156,189]. The model offers more detailed predictions for phosphorylation-mediated regulation. This finding is obtained by the comparison with previously published models and experimental information for intracellular inflammatory circuits. The detailed predictions include the modulation of the magnitude of the phosphorylated proteins as opposed to the previously published model [23]. This modulation by variation of the parameters was shown in Figures 3.3, 3.5, 3.9 and is only possible when considering the concentrations of the corresponding enzyme-substrate complexes. Despite the increased accuracy, there are, however, certain limits of this approach. In this chapter we considered an example of multisite proteins with identical phosphorylation sites, which is not the case in real proteins.

The proposed model was applied to the STAT3 signalling circuit and compared with one of the previously published models [23]. Our analysis suggests that the Goldbeter and Koshland model [23] can be used only in the case when the total concentrations of JAK and SHP-1 are much lower in comparison with the total concentration of STAT3. However, in real systems the concentrations of kinases and their substrates are comparable [29], which means that the concentrations of intermediate phosphorylation complexes cannot be ignored. We will use the latter finding in the next chapter, where we will take into consideration enzyme-substrate complexes in STAT phosphorylation. Therefore, our model may offer more accurate predictions for STAT3 phosphorylation. Since similar stimuli may lead to different transcriptional activation events and T cell phenotype switching, the results obtained in this chapter allow us to demonstrate that the lack of an accurate phosphorylation

magnitude predictions may lead to misleading interpretation of the STAT-mediated T cell fate determination.

We showed here that IRF-5 is activated in a switch-like manner (Figure 3.4 and Figure 3.5), which leads to the production of inflammatory cytokines such as IL-12 and IL-23 [164]. Our model suggests that this switch is highly dependent on the parameters of the system, particularly on the ratio of the total AP to IRF-5 concentrations and phosphorylation/ dephosphorylation reaction rates. Several autoimmune inflammatory diseases including Systemic Lupus Erythematosus (SLE) are due to the aberrations in the mechanism of IRF-5 activation [190]. A more detailed description of the regulatory role of IRF-5, which includes the wider possibility for the regulation of IRF-5 phosphorylation level by the parameter variation (Figures 3.3, 3.5, 3.9), may give a new insight into the inflammatory diseases including Systemic Lupus Erythematosus caused by the malfunctions in the mechanism of IRF-5 phosphorylation.

The model proposed in this chapter for protein phosphorylation was applied to describe EF1 and EF2 proteins phosphorylation in the regulation of erythrocyte aggregation and deformability. The developed model was used by a team of researchers, including the author of this thesis, in [31], where new mechanisms for the regulation of aggregation and deformability of the erythrocyte were proposed. In that work, the authors demonstrated the conditions and parameters values, under which the erythrocyte switches its aggregation and deformability from one steady state to another, in a latch-like manner with approximately the same thresholds ( $A = [0.18, 0.21]$  for  $dT = 4$  as shown in Figure 8 in [31]). The proposed mathematical model might be useful in understanding the mechanisms of erythrocyte diseases and aging.

In summary, this chapter introduces possible mechanisms for single- and multisite phosphorylation and proposes potentially more accurate model for phosphorylation-mediated regulation. The limit of this work includes the consideration of multisite proteins with identical phosphorylation sites. The analysis reveals the physiological conditions, under which the model coincides and differs from the classical models. This approach can have applications in a variety of molecular systems where the information is transmitted through a

phosphorylation mechanism. The predictions of the model applied to the phosphorylation of EF1 and EF2 as well as STAT3 and IRF-5 regulatory circuits may increase our understanding of the regulatory mechanisms of erythrocyte aggregation and deformability as well as inflammatory diseases.

## **4 The competitive nature of STAT complex formation drives phenotype switching of T cells**

### **4.1 Literature review**

#### **4.1.1 Biological review**

Signal Transducers and Activators of Transcription (STATs) regulate cell differentiation, growth, apoptosis and proliferation by transducing signals from the cell membrane to the nucleus. There are seven members of STAT family in mammalian cells: STAT1, STAT2, STAT3, STAT4, STAT5a, STAT5b and STAT6 [34,35].

STAT proteins are activated by binding of a cytokine to its receptor followed by the receptor dimerisation and phosphorylation of their C-terminal transactivation domain (CTD) by Janus Kinases (JAKs). For example, phosphorylation of STAT1 occurs at Tyr701 in response to type II interferons [191] and phosphorylation of STAT3 occurs at Tyr705 in response to Interleukin 6 (IL-6) or Interleukin 10 (IL-10) [192,193]. Phosphorylation at Tyr705 leads to the dimerisation [194] and regulates the activation of STAT3 [195-197].

STATs can form homo- or hetero- dimers only with their dimerisation partners [198]. STAT dimers translocate to the nucleus and activate gene expression. Nuclear phosphatases can dephosphorylate STATs in the nucleus and initiate STATs return to the cytosol [199-202].

In the nucleus, activated STAT dimers induce cytokine production. Aberrations in the mechanism of cytokines production may give rise to various immunity-related pathologies including autoimmune diseases such as rheumatoid arthritis (RA) [203,204], systemic lupus erythematosus (SLE) [205-207], diabetes [208,209] and cancer [210,211]. These aberrations include inappropriate activation of Th1 cells, which are characterised by increased inflammatory IFN- $\gamma$  production. It was reported in [39] that RA patients lack the so called IFN- $\gamma$  to IL-10 switching – the transition of the inflammatory IFN- $\gamma$  only state (Th1 cells) into a state characterised by a significant decrease of IFN- $\gamma$  production and gain of the regulatory IL-10 expression (Tr1 cells).

Several STATs, for example STAT3 and STAT5 [212,213], lead to the production of IFN- $\gamma$  and IL-10. The molecular mechanism of IFN- $\gamma$  and IL-10 production via STAT3 and STAT5 is as follows. Extracellular IL-2, IL-6 and IL-21 bind to their complementary receptors. The receptors remain in complex with JAKs. Binding of the interleukins to their receptors induces the autophosphorylation of the receptors and the bound JAKs [214]. The phosphorylated receptor-JAK complexes can be dephosphorylated by SHP-1 [215]. Phosphorylation of STAT3 and STAT5 is performed by JAK in IL-2R:JAK, IL-6R:JAK and IL-2R:JAK, IL-21R:JAK complexes respectively [216-218] (here and everywhere else in this chapter "R" denotes receptor and ":" stands for the complex with JAK). STAT3 and STAT5 are dephosphorylated by SHP-1 and SHP-2 phosphatases respectively [219,220]. The phosphorylated STAT3 and STAT5 then can form either homo- or hetero- dimers [216,217]. The homodimers translocate into the cell nucleus and promote transcription of genes responsible for IFN- $\gamma$  and IL-10 production. Both IFN- $\gamma$  and IL-10 are degraded by metalloproteases [221], denoted in our model by Mp1 and Mp2, respectively.

There is an additional, STAT-independent, mechanism of the regulation of IL-10 production. It was shown that pathogens activate c3-c3b complement system, which leads to the activation of CD46. For high IL-2 concentrations CD46 activates SPAK/ERK pathway leading to the activation of SP1 kinase [39,222]. SP1 transcription factor induces proliferation of genes responsible for IL-10 production [223].

It should be mentioned that there are also other STAT pathways (other than STAT3 and STAT5) that lead to the induction of IFN- $\gamma$  and IL-10 production. It was experimentally established that the production of IFN- $\gamma$  is induced by the following interleukins: IL-12, IL-21, IL-2 and IL-35 [224-227]. Interleukins IL-12 and IL-35 activate STAT4 through the JAK-STAT pathway [217] while IL-21 and IL-2 activate STAT5 [228,229]. It was also shown that STAT4 [224,225,230] and STAT5 [212,231,232] induce the production of IFN- $\gamma$ . However these facts regarding the role of STAT5 in IFN- $\gamma$  production argue with the results offered in [233]. The production of anti-inflammatory IL-10 is up-regulated by STAT1, STAT3 and STAT6 [213,234,235]. In particular, STAT1 is activated by IL-6 and



IL-35; STAT3 by IL-2 and IL-6; STAT6 by IL-3 and IL-4 [217,218,230,236]. However, the fact that STAT4 activates IFN- $\gamma$  production contradicts with the data in [237] as it was shown that STAT4 induces the production of IL-10. This conflicting evidence about STAT signalling cannot be explained with the currently used approaches.

#### **4.1.2 Modelling review**

Several studies offered insights into STAT signalling on systems level. A mathematical model of JAK-STAT signalling pathway leading to the activation of STAT1 in liver cells was proposed in [40]. In that work the dynamical properties of this system were investigated. The model showed that nuclear phosphatase is one of the most important regulators in this JAK-STAT pathway. Another attempt to model STAT1 activation was made in [41] studying JAK-STAT signalling in pancreatic stellate cells (PSC). By using ODEs to describe the rates of the biochemical reactions in the JAK-STAT pathway, the model developed in that study could explain the temporal profiles of STAT1 activation.

In [42], a mathematical model for JAK2-STAT5 pathway was proposed. The quantitative behaviour of STAT5 phosphorylation was determined. The parameters for nuclear import and export were identified as most sensitive in that work. In [43] the authors investigated IL-6 mediated JAK1-STAT3 pathway activation and the dynamics of JAK1 and STAT3 phosphorylation. They proposed a new approach to analyse JAK-STAT pathways by using Petri nets that describe the biomolecular mechanism of reactions and functional interactions with other components.

Thus there are several examples [40-43], where STAT signalling was investigated using mathematical modelling. However, in these works only one JAK-STAT pathway was studied at a time. In phenotype development and plasticity in response to environmental changes in T-cells, more than one JAK-STAT pathways are involved [39,44], Due to this fact, these models of STAT signalling [40-43] cannot be used to explain the underlying molecular mechanisms (Figure 1.1) of these processes. The molecular mechanisms of T cell phenotype development and plasticity are crucial for an efficient T-cell

response, which could prevent the disease states such as autoimmune states and allergic reactions [32,39].

## **4.2 Aims and objectives of this chapter**

In the previous chapter we studied phosphorylation of one STAT protein at a time. In this chapter we consider an example of high-level analysis (Figure 1.1) investigating the role of STAT proteins in T cell plasticity. To improve our understanding of the molecular mechanisms underlying STAT signalling in T cell phenotype plasticity and in the IFN- $\gamma$  to IL-10 switching [39], in this chapter we aim to do the following:

- develop a new, integrative approach to study STAT signalling,
- divide the integrated scheme into simpler parts,
- build a mathematical model for the simpler parts and analyse them,
- validate the developed model using experimental data,
- use the model to investigate how the JAK-STAT pathways interact with each other,
- suggest the role of the STAT heterodimers,
- elucidate potential mechanism of the IFN- $\gamma$  to IL-10 switching,
- using the parameter sensitivity analysis identify the parameter conditions for the conclusions to hold,
- find the most sensitive parameters and test their influence on the model,
- combine the smaller parts and analyse the combined scheme.

The developed model is based on previously published experimental results [216-218,224-226,228-230,236,238-244] and also in line with our informal discussions with Dr Claudia Kemper from Kings College London.

## **4.3 Model assumptions**

In order to fulfil the objectives of this chapter, in this section we introduce a novel approach to integrate multiple pieces of experimental data related to STAT signalling in T cells. In most works [40-43], described in Modelling review section in this chapter, only one signalling pathway is studied at a time, but this

cannot fully predict cellular behaviour in response to the interplay of STAT signalling pathways, which include cell fate determination, polarisation and associate plasticity. Here we will attempt to build a systems biology model that integrates STAT signalling pathways to analyse the possible interplay.

Figure 4.1A summarises previously published experimental results [216-218,224-226,228-230,236,238-243] and schematically represents the interdependent events in STAT signalling. In order to design the diagram in Figure 4.1A the information regarding the cytokines that activate the JAK-STAT pathways has been gathered from a number of studies [216-218,224-226,228-230,236,238-243]. The diagram shows which cytokines activate the known STAT proteins and illustrates the fact that the STAT proteins form homodimers as well as heterodimers only with their dimerisation partners [198]. In our model we assume that STAT1 interacts with STAT2, STAT3 and STAT4 only [216,239,240]. Heterodimerisation partners for STAT3 are STAT4 and STAT5. STAT4 forms a heterodimer with STAT3 and STAT5 whereas the only partner for STAT6 is STAT2 [241-243]. Despite the fact that STAT interactions have been studied extensively in recent years, the necessity of heterodimer complex formation and functional implications of the complexes still remain unclear [217].

In the scheme shown in Figure 4.1A, it is essential to study the mechanism of cross-talk as it influences the signalling of the participants and the outcome of the overall cellular response, which contributes to the T cell plasticity. Our model will predict that interdependent effects take place in the cytokine signalling system.

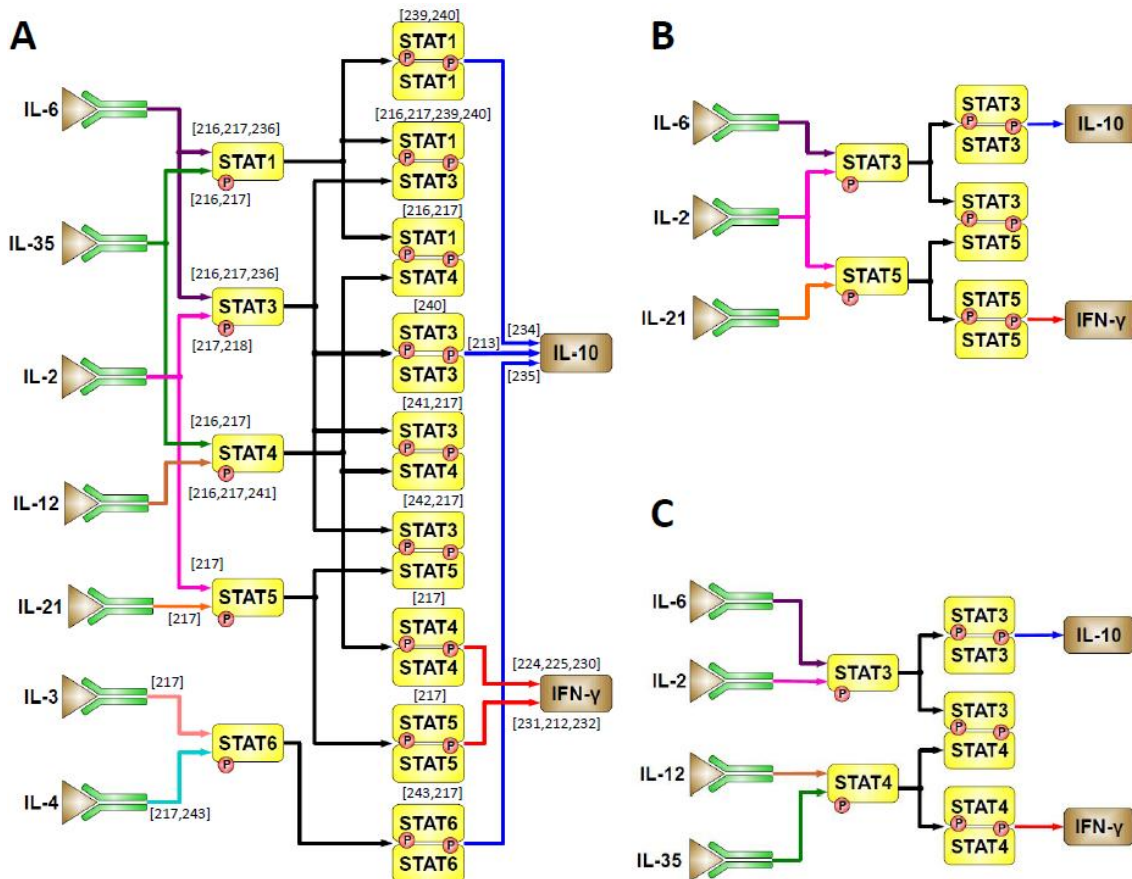


Figure 4.1. The map of interleukins involved in induction of IFN- $\gamma$  and IL-10 production via the STAT-activating mechanisms.

A. The map of interactions between the cytokines and the STATs based on experimental studies [216-218,224-226,228-230,236,238-243]. According to the map, STAT proteins are activated in response to extracellular cytokines. STATs can form dimer complexes only with certain dimerisation partners. STAT dimers induce IFN- $\gamma$  and IL-10 gene expression. B. STAT3-STAT5 subsystem extracted from the full map shown in (A). This subsystem activates IFN- $\gamma$  and IL-10 production in response to IL-2, IL-6 and IL-21. In this model IL-2 activates both STAT3 and STAT5 while the concentration of other cytokines is maintained constant. C. STAT3-STAT4 subsystem extracted from the full map (A). This subsystem induces the expression of IFN- $\gamma$  and IL-10 in response to IL-2, IL-6, IL-12 and IL-35. In this case the varied IL-2 activates STAT3 only.

The fact that the STATs can form heterodimer complexes only with their dimerisation partners [198,241-243] allows us to propose the map of cross-talk interactions illustrated in Figure 4.1A. We assume here that the STAT homodimers are more effective in mediating gene induction and therefore have a greater contribution to cytokine production compared to the heterodimers, which is consistent with [245]. This leads to the next assumption that the ratio

between the STAT homodimers defines the type of produced cytokine and, thereby, the T cell phenotype. Our model assumes that there is a natural balance of the STAT hetero- and homo- dimers. When there is no signal to switch, the ratio between the homodimers is balanced. After the T cell received the signal to switch, the balance is disrupted and then restored again, however for some new ratio between the competing STATs. This newly balanced ratio between the STAT homo- and hetero- dimers leads to the new type of produced cytokine and to T cell phenotype switching.

Here for the first time to our knowledge we suggest the underlying competition mechanism between the STAT dimers. We assume that this competition is modulated by the extracellular cytokines and reveals the role of STAT heterodimers in the produced cytokines switching, that has been remained unclear [217]. We further assume that the role of STAT heterodimers is to provide a "buffer", which can be defined as an intermediate state of species between two STAT homodimers that allows the STAT species to transfer from one state to another (for example, from STAT3 to STAT5). The scheme in Figure 4.1A illustrates cytokine-mediated influence of the STAT dimers on each other. The understanding of the resulting cytokine switching is crucial as it includes cytokine-mediated STAT-STAT interactions and potentially captures not only T cell phenotypes (IFN- $\gamma$ -secreting Th1 and IL-10-secreting T regulatory type 1 - Tr1) but also the plasticity of other cells as well as the overall activity of the immune system.

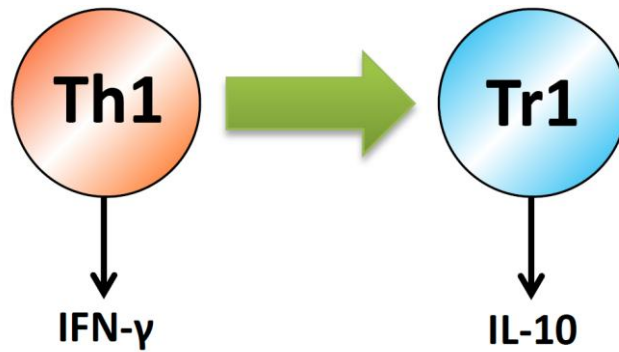


Figure 4.2. Schematic diagram for IFN- $\gamma$  and IL-10 production in Th1/Tr1 switching.

The switching of the type of the produced cytokine from IFN- $\gamma$  to IL-10 leads to the switching of the T cell phenotype from Th1 to Tr1 respectively [39].

The model proposed in this chapter will be applied to investigate previously reported plasticity effects between Th1 and Tr1 cell populations. One of the expressed cytokines, IFN- $\gamma$ , is widely associated with the inflammatory Th1 phase while the other, IL-10, is dominant during the regulatory Tr1 phase [39]. Figure 4.2 schematically represents the fact that IFN- $\gamma$  to IL-10 switching leads to the switching of T cell phenotype from Th1 to Tr1. The structure of the proposed model shown in Figure 4.1A allows for assumptions that the competition between the STAT proteins defines the expression levels of IFN- $\gamma$  and IL-10. The direct result of the described experimental data integration followed by systems biology analysis is the proposition that cytokine-dependent STAT interactions lead to the switching of the tightly regulated system from the inflammatory IFN- $\gamma$  only Th1 state into the regulatory Tr1 state characterised by increased IL-10 and decreased IFN- $\gamma$  production levels [39].

#### 4.3.1 The model for coupled STAT3-STAT5 signal transduction

Next we build a mathematical description of the model. Due to the relative complexity of Figure 4.1A we divide the full diagram into separate functional circuits (Figures 4.1B and 4.1C) based on the cytokine-cytokine interactions. In our model, IFN- $\gamma$  inducing STATs include STAT4 [224,225,230] and STAT5 [212,231,232] while IL-10 production is supported by STAT1, STAT3 and STAT6 [213,234,235]. To investigate the role of each of the STAT pairs, the

scheme is divided into subsystems in such a way that one STAT in the pairing induces the expression of IFN- $\gamma$  while the other induces the expression of IL-10. Here we only focus on the STAT pairs that produce the opposite (inflammatory and regulatory) immune responses, therefore STAT1-STAT3 combination is not considered since both STAT1 and STAT3 lead to the expression of the regulatory IL-10.

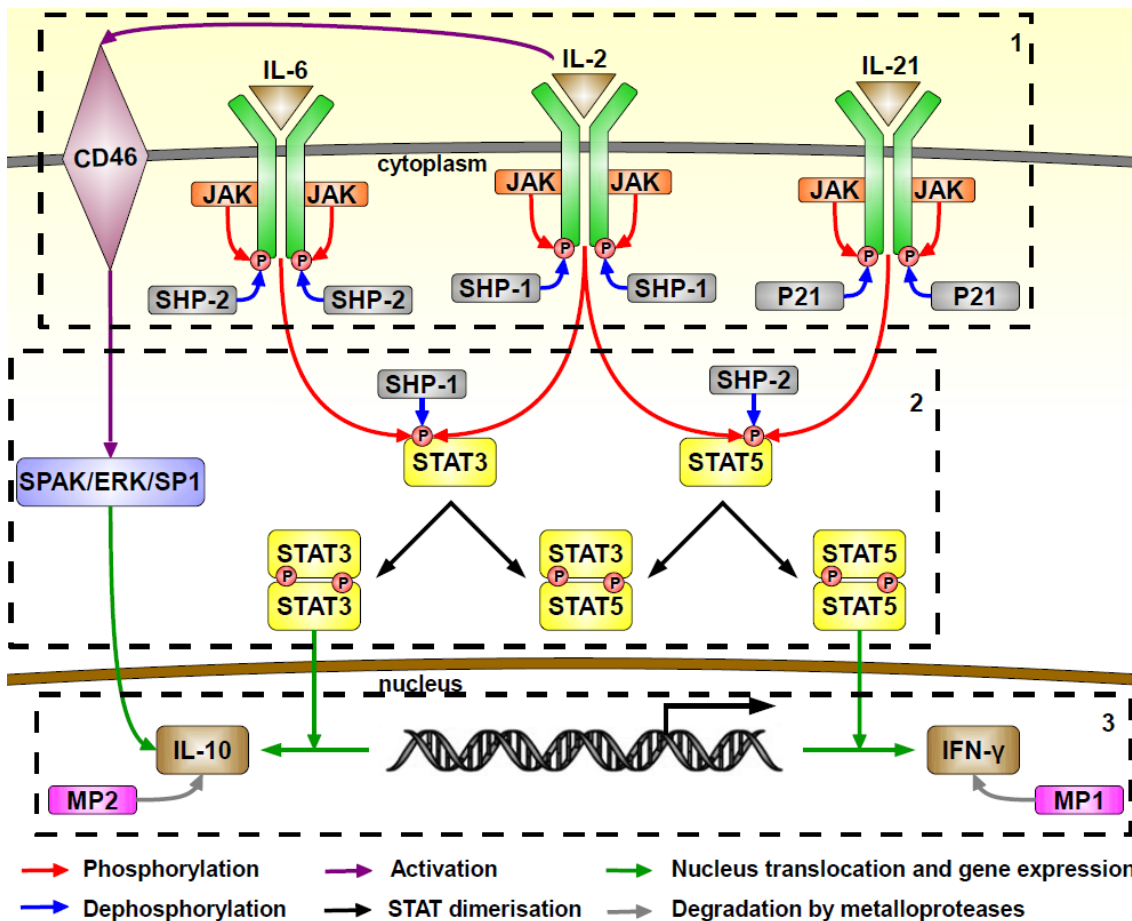
Figure 4.1B shows that IL-2 is the only "input" cytokine in our model that can activate both STAT3 and STAT5, IL-10 and IFN- $\gamma$  inducing STATs, respectively. At the same time, each IL-6 and IL-21 can activate only one STAT at a time, STAT3 or STAT5, respectively. The other IL-2-activated STAT combination, which induces the production of both IFN- $\gamma$  and IL-10, is STAT3-STAT4 (Figure 4.1C). However, in contrast to the STAT3 and STAT5 pair, in the STAT3-STAT4 pairing IL-2 activates only STAT3 and not STAT4. Due to this role of IL-2 in STAT3, STAT4 and STAT5 activation, we study the effects of varied IL-2 concentration assuming the continuous presence of other input cytokines (IL-6 and IL-21) by fixing their concentrations at constant levels. Therefore, we will not consider STAT1-STAT4 model since IL-2 does not activate any of the STATs involved in this pairing.

The STAT3-STAT5 subsystem shown in Figure 4.1B can be considered separately if we assume that the amount of STAT3 is mainly consumed on STAT3:STAT3 and STAT3:STAT5 and not on other dimers. Similarly, the STAT3-STAT4 subsystem shown in Figure 4.1C can be considered separately if we assume that the amount of STAT3 is mainly consumed on STAT3:STAT3 and STAT3:STAT4 dimers. These assumptions are made in the absence of experimental data but can be tested when the experimental data for the amount of STAT3 in the corresponding dimers become available. Despite these limitations the consideration of two STATs shown in Figures 4.1B and 4.1C is a step forward compared to previous modelling works [40-43], where only one STAT signalling pathway is studied at a time. As a result the complicated scheme depicted in Figure 4.1A is divided into the two functionally similar but architecturally different submodules shown in Figures 4.1B and 4.1C that can now be described mathematically. We start our analysis with the STAT3-STAT5 system illustrated in Figure 4.1B. Later in Subsection 4.5.3 we will also analyse

the STAT3-STAT4 system (Figure 4.1C) and the combined STAT3-STAT4-STAT5 system.

In order to model the STAT3-STAT5 molecular system (Figure 4.1B), we include more biological details into the molecular mechanism. Figure 4.3 shows the detailed version of the circuit represented in Figure 4.1B. The elements of morphological scheme in Figure 4.3 are combined into functional blocks, the functions of which can be "informally" described as follows. Block 1 (cytokine-receptor interactions) receives and performs preliminary processing of the signal, which is the concentration of IL-6, IL-2 and IL-21. The function of Block 2 (STAT phosphorylation/dimerisation and SP1 activation) is signal processing, including comparison (competition) of different signals. The function of Block 3 is implementation (cytokine production), which results in T cell differentiation and expression of IL-10 and IFN- $\gamma$ . The consideration of functional component of this scheme is consistent with the definition of mechanism presented in [1] and schematically illustrated in Figure 1.1. The detailed description of the governed reactions and equations can be found in Appendix C.





1. Reception and preliminary processing 2. Processing and competition 3. Implementation (expression)

Figure 4.3. Schematic diagram for IFN- $\gamma$  and IL-10 production in response to IL-6, IL-2 and IL-21 as input signals, via signal processing by STAT3 and STAT5.

The detailed scheme of experimentally established interactions [39,221-223] involved in IFN- $\gamma$  and IL-10 production by T cells. Phosphorylation of the members of these signalling pathways leads to the signal transduction and activation of the cytokines production. The dashed boxes identify three functional blocks (1, 2, 3), corresponding to three different stages in signal processing. More explanations in the text.

We assume here that the rates of the biochemical reactions differ significantly. Specifically, the complex formation is assumed to be much faster than phosphorylation/dephosphorylation reactions and thus the concentration of complexes reaches its steady-state while the concentration of phosphorylated proteins still changing, according to the quasi-steady-state assumption (QSSA) and [24,57,186]. In this chapter, we will study the steady state solutions of the phosphorylated proteins (STATs) and produced cytokines. The QSSA discussed above is therefore unnecessary for the results presented in this

chapter, but may become essential if and when this theory is extended to dynamic processes.

### Cytokine-receptor interactions

Concentrations of phosphorylated Receptor-JAK complexes activated by IL-2, IL-6 and IL-21, respectively, as functions of the corresponding cytokine concentration can be written as follows:

$$\begin{aligned}
 [w2] &= -\frac{M_2 - r2_t + p2_t \left( \frac{M_1}{n_1 [i2]} + \frac{1}{n_1} + 1 \right)}{2} + \\
 &+ \frac{\sqrt{\left( M_2 - r2_t + p2_t \left( \frac{M_1}{n_1 [i2]} + \frac{1}{n_1} + 1 \right) \right)^2 + 4r2_t M_2}}{2}, \\
 [w6] &= -\frac{M_4 - r6_t + p6_t \left( \frac{M_3}{n_2 [i6]} + \frac{1}{n_2} + 1 \right)}{2} + \\
 &+ \frac{\sqrt{\left( M_4 - r6_t + p6_t \left( \frac{M_3}{n_2 [i6]} + \frac{1}{n_2} + 1 \right) \right)^2 + 4r6_t M_4}}{2}, \\
 [w21] &= -\frac{M_6 - r21_t + p21_t \left( \frac{M_5}{n_3 [i21]} + \frac{1}{n_3} + 1 \right)}{2} + \\
 &+ \frac{\sqrt{\left( M_6 - r21_t + p21_t \left( \frac{M_5}{n_3 [i21]} + \frac{1}{n_3} + 1 \right) \right)^2 + 4r21_t M_6}}{2},
 \end{aligned} \tag{4.1}$$

$$\text{where } [i2] = \frac{[IL-2]}{STAT3_T}, \quad [w2] = \frac{[IL2Rp:JAK]}{STAT3_T}, \quad r2_t = \frac{IL2R_T}{STAT3_T}, \quad p2_t = \frac{SHP-1_T}{STAT3_T},$$

$$[i6] = \frac{[IL-6]}{STAT3_T}, \quad [w6] = \frac{[IL6Rp:JAK]}{STAT3_T}, \quad r6_t = \frac{IL6R_T}{STAT3_T}, \quad p6_t = \frac{SHP-2_T}{STAT3_T},$$

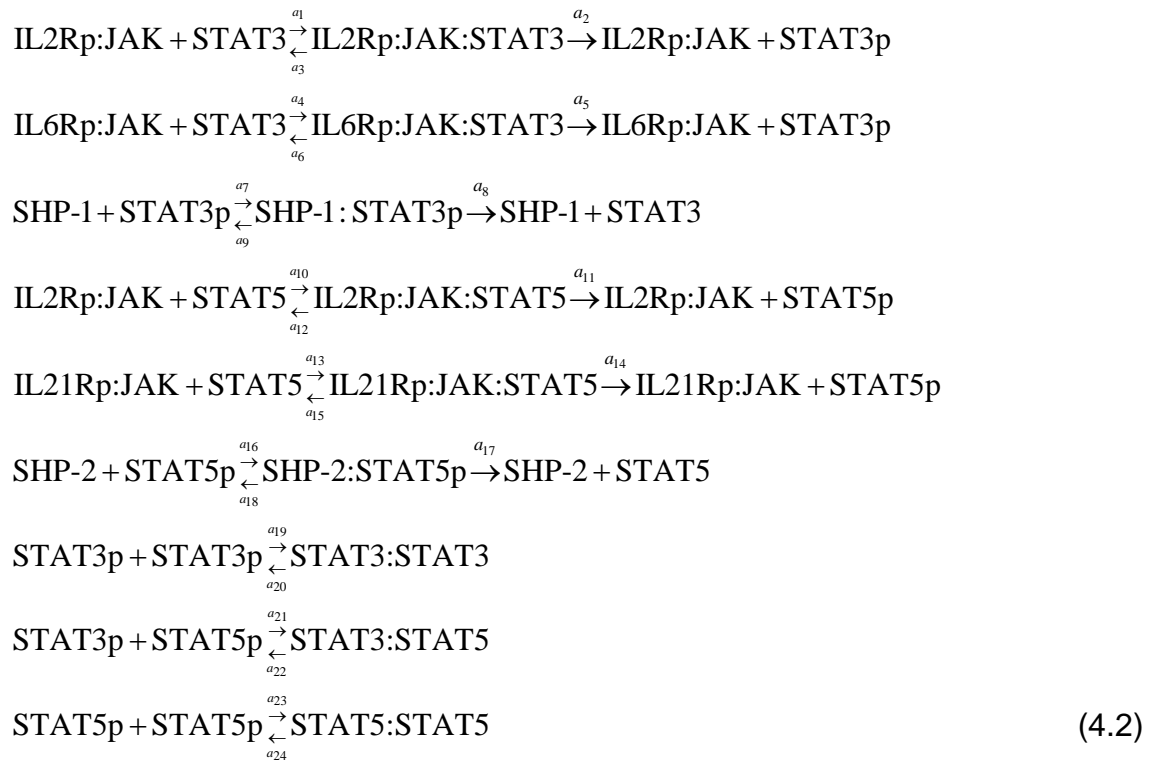
$$[i21] = \frac{[IL-21]}{STAT3_T}, \quad [w21] = \frac{[IL21Rp:JAK]}{STAT3_T}, \quad r21_t = \frac{IL21R_T}{STAT3_T}, \quad p21_t = \frac{P21_T}{STAT3_T} \quad (\text{here}$$

subscripts  $t$  and  $T$  denote the total amount of protein in non-dimensional and dimensional forms, respectively, small  $p$  represents phosphorylated state),  $M_1$ ,

$M_2, M_3, M_4, M_5$  and  $M_6$  are non-dimensional Michaelis constants,  $n_1, n_2$  and  $n_3$  denote the ratio of receptor phosphorylation/dephosphorylation rates. Equations (4.1) follow from the stationary conditions of the phosphorylation and dephosphorylation of the receptors mentioned previously. The detailed derivation of Equations (4.1) can be found in Appendix C, Equations (7.58)-(7.69).

### STAT phosphorylation and dimerisation

STAT proteins are phosphorylated by the activated interleukin-receptor-JAK complexes IL2Rp:JAK, IL6Rp:JAK and IL21Rp:JAK (Figure 4.1B). The reactions involved in STAT activation are given by:



The corresponding Ordinary Differential Equations (ODEs) for Reactions (4.2) can be written as follows:

$$\begin{aligned}
\frac{d}{dt}[IL2Rp:JAK:STAT3] &= a_1[IL2Rp:JAK][STAT3] - (a_2 + a_3)[IL2Rp:JAK:STAT3], \\
\frac{d}{dt}[IL6Rp:JAK:STAT3] &= a_4[IL6Rp:JAK][STAT3] - (a_5 + a_6)[IL6Rp:JAK:STAT3], \\
\frac{d}{dt}[STAT3p] &= a_2[IL2Rp:JAK:STAT3] + a_5[IL6Rp:JAK:STAT3] - \\
&\quad -a_7[SHP-1][STAT3p] + a_9[SHP-1:STAT3p] - 2a_{19}[STAT3p]^2 + \\
&\quad + 2a_{20}[STAT3:STAT3] - a_{21}[STAT3p][STAT5p] + a_{22}[STAT3:STAT5], \\
\frac{d}{dt}[SHP-1:STAT3p] &= a_7[SHP-1][STAT3p] - (a_8 + a_9)[SHP-1:STAT3p], \\
\frac{d}{dt}[IL2Rp:JAK:STAT5] &= a_{10}[IL2Rp:JAK][STAT5] - (a_{11} + a_{12})[IL2Rp:JAK:STAT5], \\
\frac{d}{dt}[IL21Rp:JAK:STAT5] &= a_{13}[IL21Rp:JAK][STAT5] - (a_{14} + a_{15})[IL21Rp:JAK:STAT5], \\
\frac{d}{dt}[STAT5p] &= a_{11}[IL2Rp:JAK:STAT5] + a_{14}[IL21Rp:JAK:STAT5] - \\
&\quad -a_{16}[SHP-2][STAT5p] + a_{18}[SHP-2:STAT5p] - a_{21}[STAT3p][STAT5p] + \\
&\quad + a_{22}[STAT3:STAT5] - 2a_{23}[STAT5p]^2 + 2a_{24}[STAT5:STAT5], \\
\frac{d}{dt}[SHP-2:STAT5p] &= a_{16}[SHP-2][STAT5p] - (a_{17} + a_{18})[SHP-2:STAT5p], \\
\frac{d}{dt}[STAT3:STAT3] &= a_{19}[STAT3p]^2 - a_{20}[STAT3:STAT3], \\
\frac{d}{dt}[STAT3:STAT5] &= a_{21}[STAT3p][STAT5p] - a_{22}[STAT3:STAT5], \\
\frac{d}{dt}[STAT5:STAT5] &= a_{23}[STAT5p]^2 - a_{24}[STAT5:STAT5],
\end{aligned} \tag{4.3}$$

Conservation equations of the total proteins concentrations are given by:

$$\begin{aligned}
STAT3_T &= [STAT3] + [STAT3p] + 2[STAT3:STAT3] + [STAT3:STAT5] + \\
&\quad + [IL2Rp:JAK:STAT3] + [IL6Rp:JAK:STAT3] + [SHP-1:STAT3p], \\
STAT5_T &= [STAT5] + [STAT5p] + 2[STAT5:STAT5] + [STAT3:STAT5] + \\
&\quad + [IL2Rp:JAK:STAT5] + [IL21Rp:JAK:STAT5] + [SHP-2:STAT5p], \\
SHP-1_T &= [SHP-1] + [SHP-1:STAT3p], \\
SHP-2_T &= [SHP-2] + [SHP-2:STAT5p].
\end{aligned} \tag{4.4}$$

Conservation Equations (4.4) can be written in non-dimensional form:

$$\begin{aligned}
1 &= [s3] + [s3p] + 2[s33] + [s35] + [w2s3] + [w6s3] + [p3s3p] + [pps3p], \\
s5_t &= [s5] + [s5p] + 2[s55] + [s35] + [w2s5] + [w21s5] + [p5s5p], \\
p3_t &= [p3] + [p3s3p], \\
p5_t &= [p5] + [p5s5p], \\
pp_t &= [pp] + [pps3p],
\end{aligned} \tag{4.5}$$

where we introduced the non-dimensional concentrations of the proteins

$$\begin{aligned}
\text{normalised by } STAT3_T : [s3] &= \frac{[STAT3]}{STAT3_T}, [s3p] = \frac{[STAT3p]}{STAT3_T}, \\
[w2s3] &= \frac{[IL2Rp:JAK:STAT3]}{STAT3_T}, [w6s3] = \frac{[IL6Rp:JAK:STAT3]}{STAT3_T}, \\
[p3s3p] &= \frac{[SHP-1:STAT3p]}{STAT3_T}, s5_t = \frac{STAT5_T}{STAT3_T}, [s5] = \frac{[STAT5]}{STAT3_T}, [s5p] = \frac{[STAT5p]}{STAT3_T}, \\
[w2s5] &= \frac{[IL2Rp:JAK:STAT5]}{STAT3_T}, [w21s5] = \frac{[IL21Rp:JAK:STAT5]}{STAT3_T}, \\
[p5s5p] &= \frac{[SHP-2:STAT5p]}{STAT3_T}, [s33] = \frac{[STAT3:STAT3]}{STAT3_T}, [s35] = \frac{[STAT3:STAT5]}{STAT3_T}, \\
[s55] &= \frac{[STAT5:STAT5]}{STAT3_T}, [p3] = \frac{[SHP-1]}{STAT3_T}, [p5] = \frac{[SHP-2]}{STAT3_T}, p3_t = \frac{SHP-1_T}{STAT3_T}, \\
p5_t &= \frac{SHP-2_T}{STAT3_T}.
\end{aligned}$$

Here we use one of the findings of Chapter 3, according to which we take into consideration the concentrations of all enzyme-substrate complexes. In order to find the steady-state solutions of Equations (4.3) we need to solve the following system of algebraic equations:

$$\begin{cases}
0 = [s3p] + 2 \frac{[s3p]^2}{M_{13}} + \frac{[s3p][s5p]}{M_{14}} + \frac{p3_t [s3p]}{M_9 + [s3p]} \left( 1 + \frac{M_7 + [w2] + M_7 Q_6}{n_4 [w2] + n_5 M_7 Q_6} \right) - 1, \\
0 = [s5p] + 2 \frac{[s5p]^2}{M_{15}} + \frac{[s3p][s5p]}{M_{14}} + \frac{p5_t [s5p]}{M_{12} + [s5p]} \left( 1 + \frac{M_{10} + [w2] + M_{10} Q_{21}}{n_6 [w2] + n_7 M_{10} Q_{21}} \right) - s5_t,
\end{cases} \quad (4.6)$$

$$\text{where } M_7 = \frac{a_2 + a_3}{a_1 STAT3_T}, \quad M_8 = \frac{a_5 + a_6}{a_4 STAT3_T}, \quad M_9 = \frac{a_8 + a_9}{a_7 STAT3_T}, \quad M_{10} = \frac{a_{11} + a_{12}}{a_{10} STAT3_T},$$

$$M_{11} = \frac{a_{14} + a_{15}}{a_{13} STAT3_T}, \quad M_{12} = \frac{a_{17} + a_{18}}{a_{16} STAT3_T}, \quad M_{13} = \frac{a_{20}}{a_{19} STAT3_T}, \quad M_{14} = \frac{a_{22}}{a_{21} STAT3_T},$$

$$M_{15} = \frac{a_{24}}{a_{23} STAT3_T} \text{ are non-dimensional Michaelis constants, } Q_6 = \frac{[w6]}{M_8} \text{ and}$$

$$Q_{21} = \frac{[w21]}{M_{11}}. \text{ Equation (4.6) is in line with one of the conclusions of Chapter 3,}$$

according to which we do not neglect the concentrations of enzyme-substrate

complexes. System (4.6) is solved numerically to obtain steady-state concentrations of STAT proteins as a function of IL-2.

### SP1 activation

Experimental data on the molecular mechanism of how CD46 enhances IL-10 production are not available at present. However it was established that CD46 can facilitate the secretion of IL-10 through the SPAK-ERK pathway and SP1 transcription factor only in the presence of high environmental IL-2 [39]. This dependence is described by hypothetical enzymatic reactions shown in Equations (7.89). Thus, it can be written for the concentration of the active SP1 in non-dimensional form:

$$[sp1a] = sp1_t \frac{[i2]}{M_{16} + [i2]} \frac{[cd46]}{M_{17} + [cd46]}, \quad (4.7)$$

where  $[sp1a] = \frac{[SP1a]}{STAT3_T}$ ,  $sp1_t = \frac{SP1_T}{STAT3_T}$ ,  $[cd46] = \frac{[CD46]}{STAT3_T}$ ,  $M_{16}$  and  $M_{17}$  are

Michaelis constants.

### Cytokine production

We assume that the production of IFN- $\gamma$  and IL-10 is induced by the STAT dimer interactions with the genes responsible for production of IFN- $\gamma$  and IL-10 [217]. The produced cytokine can be degraded by metalloprotease Mp [221]. The concentration of the produced IFN- $\gamma$  in non-dimensional form can be written as follows:

$$[ig] = \frac{M_{18}}{\frac{mp1_t}{n_8 gg_t \frac{[s55]}{M_{19} + [s55]} - 1}}, \quad (4.8)$$

where  $[ig] = \frac{[IFN-\gamma]}{STAT3_T}$ ,  $mp1_t = \frac{Mp1_T}{STAT3_T}$ ,  $gg_t = \frac{Gene_T^{IFN-\gamma}}{STAT3_T}$ ,  $M_{18}$  and  $M_{19}$  are

Michaelis constants,  $n_8$  is the ratio of IFN- $\gamma$  production to degradation rates. In order to achieve the steady-state, IFN- $\gamma$  production rate should be less than its maximal degradation rate, which implies  $n_8 < 1$ .

Both STAT3:STAT3 homodimer and CD46 (through SPAK-ERK pathway) can activate the same IL-10 gene but they bind different binding regions, as shown in [246]. IL-10 is produced after binding of either of the transcription factors to the gene, which corresponds to [247]. Thus it can be written for IL-10 concentration:

$$[i10] = \frac{M_{20}}{mp2_t} \frac{1}{n_9 g10_t \left( \frac{[s33]}{M_{21} + [s33]} + \frac{[sp1a]}{M_{22} + [sp1a]} - \frac{[s33]}{M_{21} + [s33]} \frac{[sp1a]}{M_{22} + [sp1a]} \right)^{-1}}, \quad (4.9)$$

where  $[i10] = \frac{[IL-10]}{STAT3_T}$ ,  $mp2_t = \frac{Mp2_T}{STAT3_T}$ ,  $g10_t = \frac{Gene_T^{IL-10}}{STAT3_T}$ ,  $n_9 = \frac{l_6}{k_{11}}$ ,  $n_9 < 1$ ,  $M_{20}$ ,

$M_{21}$  and  $M_{22}$  are Michaelis constants,  $n_9$  is the ratio of IL-10 production to degradation rates,  $n_9 < 1$ . Equations (4.8) and (4.9) are then applied to describe the concentration of produced IFN- $\gamma$  and IL-10 as a function of IL-2.

Equations (4.7) (4.8) and (4.9) are derived in Appendix C (Equations (7.98), (7.110) and (7.111), respectively).

## 4.4 Model parameters

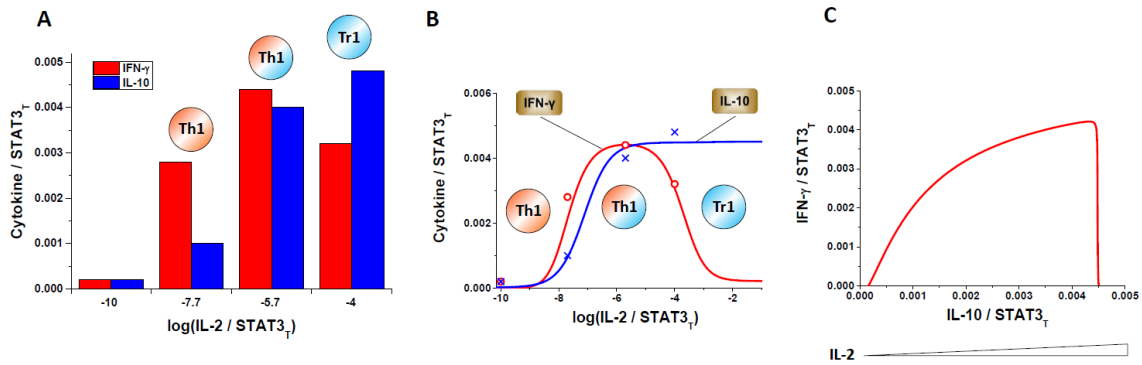


Figure 4.4. The regulation of IL-2-dependent IFN- $\gamma$  and IL-10 production in Th1/Tr1 switching.

A. Normalised experimental data from [244] show that the concentration of produced IFN- $\gamma$  and IL-10 depends on IL-2 concentration. With an increase of IL-2, the production of IFN- $\gamma$  initially increases compared to the production of IL-10 under the same IL-2 concentration. Further increase of IL-2 leads to the decrease of IFN- $\gamma$  and increase of IL-10 concentration. B. Model predictions (solid lines) compared to the experimental data for IFN- $\gamma$  and IL-10 production as a function of IL-2 concentration (red circles and blue crosses respectively). We assume that low IL-10 and high IFN- $\gamma$  correspond to Th1 cell, the medium IFN- $\gamma$  and IL-10 concentrations correspond to the IL-10-producing Th1 cells and high IL-10 and low IFN- $\gamma$  correspond to Tr1 cells, which is in line with the experimentally observed fact that the switching occurs for high amounts of IL-2 and that the activation of IFN- $\gamma$  always precedes IL-10 [39]. For the medium IL-2 concentrations Th1 cell produces both IFN- $\gamma$  and IL-10, which corresponds to IL-10 producing Th1 cell. C. Cross-correlation between produced IFN- $\gamma$  and IL-10 demonstrates inhibition of IFN- $\gamma$  production by IL-10 for higher IL-2 concentrations. See Equations (4.1), (4.6), (4.7), (4.8) and (4.9) with parameters taken from set "O3" in Table 7.2.

Next we obtain a set of parameters that would make the developed model to demonstrate the expected behaviour. We fit our model predictions to the experimental data for IL-2 dependent IFN- $\gamma$  and IL-10 production in Th1/Tr1 switching [244] shown in Figure 4.4A. It was reported that Th1 cells are characterised by high levels of pro-inflammatory IFN- $\gamma$  expression, whereas Tr1 cells induce high amounts of regulatory IL-10 [39]. Figure 4.4A illustrates the normalised IFN- $\gamma$  and IL-10 concentrations as a function of IL-2. For the parameter fitting, we use the Genetic Algorithm (GA) tool integrated to MATLAB. As the criterion for fitting we choose the squared error, which can be



described as  $SM = \sum_{i=1}^N (E_i - M_i)^2$ , where  $E_i$  is experimental data for cytokine concentration (IFN- $\gamma$  or IL-10) corresponding to the  $i$ -th value of IL-2 concentration,  $M$  is the model predictions for cytokine concentration corresponding to the same IL-2 concentration,  $i$  is the number of experimental data point,  $N = 4$  is the total number of experimental data points. The GA tool allows to minimize the squared error using the integrated algorithms for the optima search.

We select a "nominal" set of parameters "by hand", which qualitatively demonstrates the switching between IFN- $\gamma$  and IL-10. This set of parameters is represented as "Nom" in Table 7.2 in Appendix C. The sets of the optimised parameters and corresponding squared errors are shown in Table 7.2. We perform 15 optimisation tests setting the allowable ranges for the parameters ten-fold either side of the nominal values of parameters and choose the best fitting (set "O3" in Table 7.2) with the smallest squared error  $SM = 7.34 \cdot 10^{-7}$ . Figure 7.2 in Appendix C shows the distribution of five parameter sets with the closest minimum squared errors  $SM$ , namely sets "O2", "O3", "O9", "O10" and "O12".

Figure 4.4B illustrates the model predictions for the optimised set of parameters, compared to the experimental data from [244] and also shown in Figure 4.4A. Figure 4.4B visually demonstrates a good fitness supported by the small squared error  $SM = 7.34 \cdot 10^{-7}$  and shows that with the increase of IL-2, the concentration of IFN- $\gamma$  initially increases reaching a peak and then decreases while the concentration of IL-10 keeps increasing. In our model, the phenotype switching is due to the change in the type of produced cytokine that depends on IL-2 concentration.

The developed model predictions (Figure 4.4B) clearly show the switching between the two populations of Th1 and Tr1 cells. At the same time there is evidence that there is a population that produces both IFN- $\gamma$  and IL-10, the origin of which has not yet been established [39]. Figure 4.4C shows the correlation between the production of IFN- $\gamma$  and IL-10. This figure clearly

demonstrates initial co-expression of IFN- $\gamma$  and IL-10 as well as the inhibitory effects of IFN- $\gamma$  and IL-10 on each other with the increasing IL-2 concentration.

## 4.5 Model predictions

### 4.5.1 STAT switching

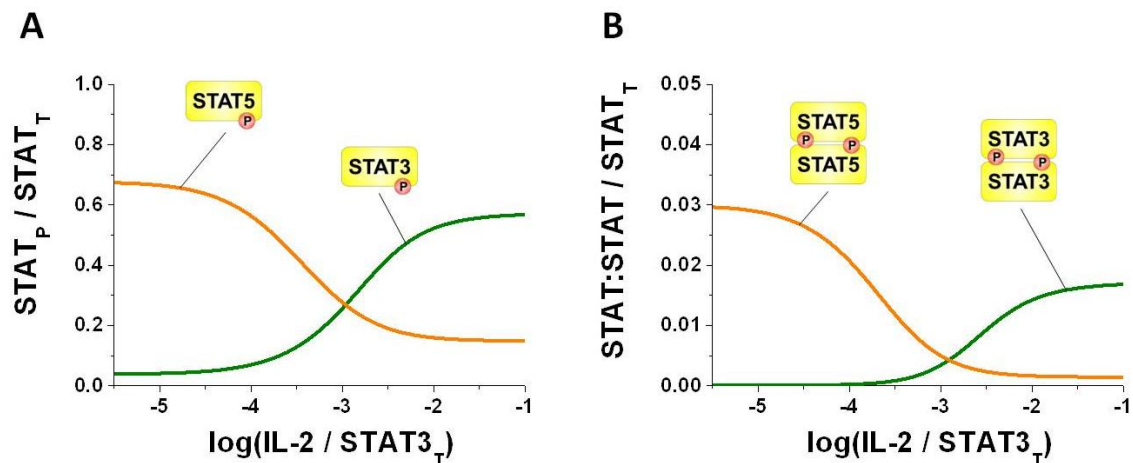


Figure 4.5. Model predictions for STAT3 and STAT5 activation in response to IL-2.

A. Dose-response dependencies of STAT3p and STAT5p monomers on IL-2 concentration. The model suggests that STAT3 is activated whereas STAT5 is inhibited for high IL-2 concentrations. B. The activation profiles of STAT heterodimers demonstrate the switching from STAT5:STAT5 to STAT3:STAT3 species for high IL-2 concentrations. The model predictions illustrate the competition between STAT3 and STAT5. See Equations (4.1) and (4.6) with parameters taken from set "O3" in Table 7.2.

The mathematical model proposed in this chapter captures several circuits involved in IFN- $\gamma$  and IL-10 production. We start the systems analysis with the circuit shown in Figure 4.1B. The diagram in Figure 4.1 schematically illustrates the experimentally observed facts, according to which STAT3 induces IL-10 production by forming STAT3:STAT3 homodimer [245,248] and STAT5 induces IFN- $\gamma$  production by forming STAT5:STAT5 complex [212,232]. We hypothesize here that the experimentally established IFN- $\gamma$  to IL-10 switching (Figure 4.4) is due to the STAT competition and caused by the STAT switching. In order to test our hypothesis, in this section we study the model predictions for both STAT monomers and homodimers.

First, we consider the range of medium IL-2 concentrations (from -5.5 to -1 in logarithmic scale normalised to the total STAT3 concentration as shown in Figure 4.4). This range corresponds to the state where T cells already developed into Th1 and are switching to Tr1 cells. Figure 4.5 illustrates quantitative model predictions for STAT proteins phosphorylation as a function of IL-2 concentration. It can be seen from Figure 4.5 that STAT3 phosphorylation represents a dose-response activation curve whereas STAT5 phosphorylation demonstrates the reverse, inhibitory shape (Figure 4.5A). For low IL-2 concentrations the level of STAT3 phosphorylation is also low while the phosphorylation level of STAT5 is high. However the results of the simulation show that for high IL-2 concentrations phosphorylated STAT3 dominates over phosphorylated STAT5. The switching occurs for modest IL-2 concentrations. In this chapter, we refer to the decrease of the phosphorylated STAT5 and increase of the phosphorylated STAT3 as well as their homodimers, with the increasing IL-2 concentration, as STAT redistribution.

Figure 4.5B illustrates the dependences of the STAT3:STAT3 and STAT5:STAT5 dimers, normalised by the total STAT3, on IL-2 concentration. The shapes of the curves for the dimers are similar to the shapes of their monomers due to the high dependence of the dimer concentrations on their monomers. However the curves for the dimers are steeper, which can be explained by the fact that two molecules of monomers are required to form a dimer. Figure 4.5 shows that for low IL-2 concentrations STAT5 is more phosphorylated than STAT3, whereas for higher IL-2 concentrations phosphorylated STAT3 prevails over STAT5.

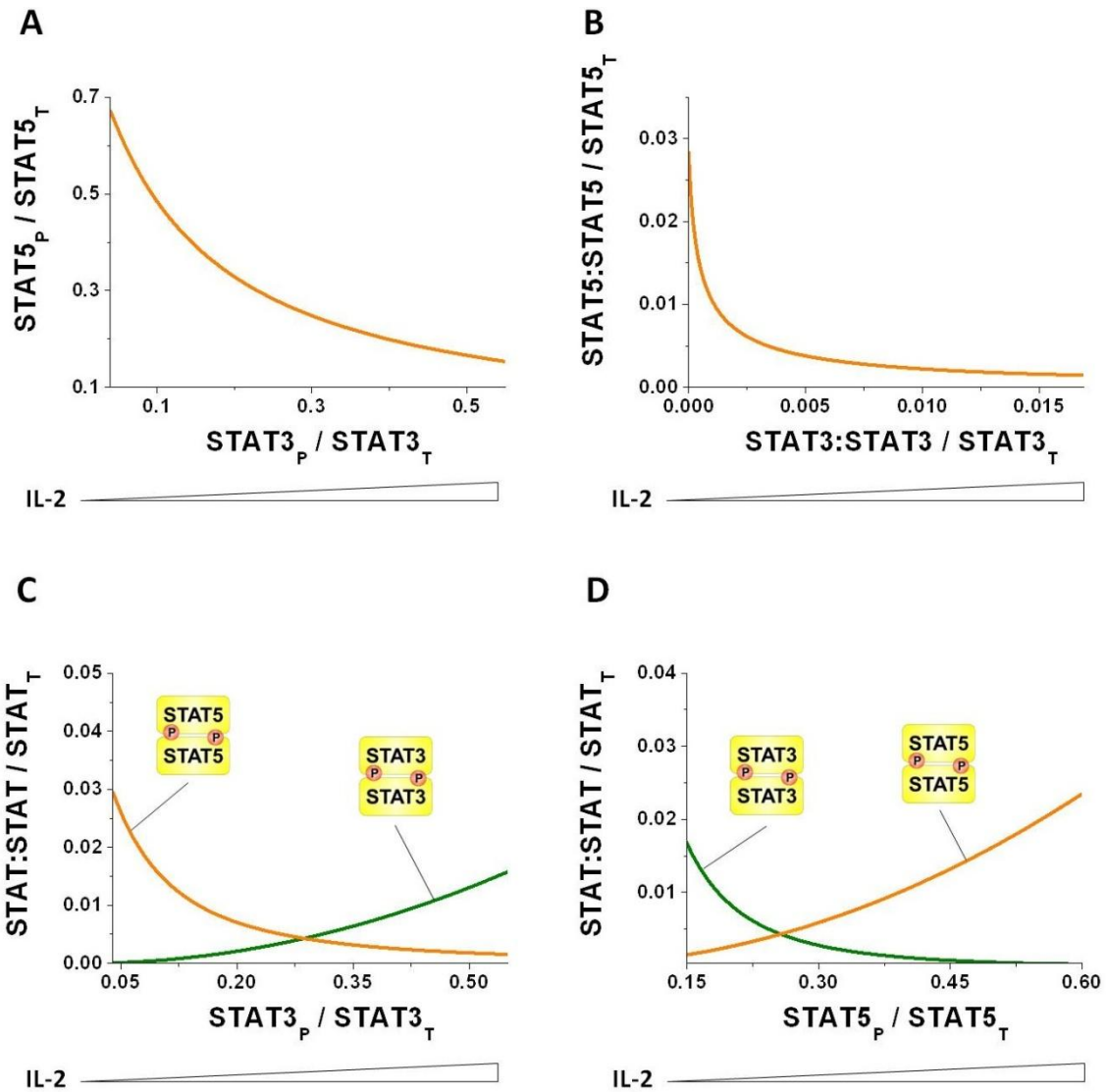


Figure 4.6. Model predictions demonstrate cross-interaction effects between STAT3 and STAT5 signalling pathways.

Correlation between phosphorylated STAT5 and STAT3 monomers reveals STAT5 inhibition and STAT3 activation for increasing IL-2 (A). STAT3 and STAT5 can form either homo- or hetero- dimers. Our model predictions demonstrate that STAT3:STAT3 inhibits the formation of STAT5:STAT5 homodimer (B). Due to the fact that dimers require two molecules for binding, the dependence of STAT5:STAT5 on STAT3:STAT3 concentration is steeper than the dependence for their monomers. Phosphorylated STAT3 and STAT5 can activate their homodimers and inhibit STAT5:STAT5 and STAT3:STAT3 homodimers, respectively (C and D). See Equations (4.1) and (4.6) with parameters taken from set "O3" in Table 7.2.

### **Mutual inhibition of the competing STAT proteins**

In order to illustrate the competition between the STAT species, in this subsection we study the STAT monomers and dimers interdependence effects on each other (Figure 4.6). It can be seen from Figure 4.6A that the competing STAT proteins inhibit each other for high IL-2 concentrations via the correlation between them (indirect inhibition). With the increasing of IL-2, STAT3 becomes more phosphorylated than STAT5. The effect of STAT redistribution is also predicted by our model for the STAT5:STAT5 dependence on STAT3:STAT3 with higher degree of steepness (Figure 4.6B). Figures 4.6C and 4.6D show that phosphorylated STAT monomers not only activate their corresponding dimers but at the same time inhibit the competing dimers for higher IL-2 concentrations.

The experimental procedures offer various techniques to study both STAT monomer and dimer subunits. One of the widely used techniques of measuring the rate constants for homodimer subunit exchange is double electron-electron resonance (DEER) or nuclear magnetic resonance spectroscopy based paramagnetic relaxation enhancement (PRE) [249]. Here and anywhere else in this chapter by the homodimer subunit exchange we mean the increase of one STAT homodimer concentration that used to be initially low and decrease of the other due to the STAT redistribution. These experiments could be performed to obtain more experimental information about STAT protein dimerisation. In particular, the experimental information that needs to be obtained includes the concentrations of STAT3 and STAT5 dimers for different concentrations of IL-2 in order to verify our model predictions shown in Figure 4.6.

The results obtained in this subsection demonstrate STAT proteins redistribution. The proposed model predicts that STAT3 and STAT5 compete with each other and for high IL-2 concentrations STAT3 inhibits STAT5. This effect is amplified for the STAT dimers.

## IL-2-dependent selective regulation of the STAT competition

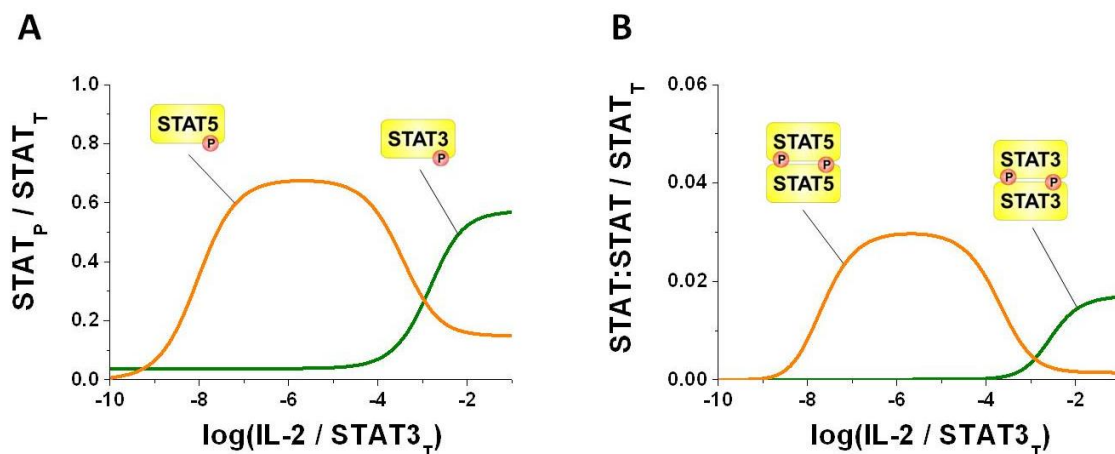


Figure 4.7. Model predictions for low IL-2 reveal selectivity of the immune response.

A. Selective concentration-dependent STAT5 activation profile emerging from consideration of low IL-2. B. STAT5:STAT5 homodimers also demonstrate selectivity for IL-2 due to the high dependence on STAT5p. See Equations (4.1) and (4.6) with parameters taken from set "O3" in Table 7.2.

Experiments published in [244] established the bell shaped IFN- $\gamma$  dependence on low IL-2 concentrations (Figure 4.4B). In order to test whether the bell-shape is also present in STAT activation dependence on IL-2, in this subsection our model is tested in the range of very low IL-2 concentrations compared to IL-2 concentrations tested in the previous subsections (less than  $10^{-8}$  according to Figure 4.4B, which corresponds to less than 0.5 U/ml in [244]). Figure 4.7A reveals the bell-shaped dependence for phosphorylated STAT5 on IL-2 as well as for STAT5:STAT5 homodimer on IL-2 that is illustrated in Figure 4.7B.

The predicted bell-shaped relationship may offer new insights into the dual role of STAT-mediated cytokine production. Experimental evidence suggests that significant amount of STAT5p is present in Th1 cells characterised by IFN- $\gamma$  production (Figure 4.4A, [39]). Applying the systems approach (Figure 4.1A) we suggest that STAT5 induces IFN- $\gamma$  production. These results are consistent with the experiments in [212,231,232]. However it was also shown in [233] that STAT5 can induce IL-10 production.

Our model predicts that the same amount of phosphorylated STAT5 may lead to both low and high IL-10 production levels, depending on the extracellular concentration of IL-2. The established possibility for the STAT-mediated bell-shaped dependence between IFN- $\gamma$  and IL-10 cytokines production offers a potential explanation for their co-expression in childhood celiac disease [250].

The model predictions presented in this section support our hypothesis that the switching between IFN- $\gamma$  producing Th1 cells and IL-10 producing Tr1 cells is due to the switching between the competing STAT proteins. Therefore we suggest that the cells, that produce IFN- $\gamma$  and IL-10 simultaneously (IFN- $\gamma^+$ IL-10 $^+$  cells), develop from IFN- $\gamma$  producing Th1 cells that have received IL-2-dependent signal to switch, rather than represent a specific T cell population. The model predictions support the idea that the same T cell can express both regulatory and effector cytokines in response to the same antigen. This result is essential for understanding the mechanism of cytokine switching [39,244]. Additionally, the model predicts the initial increase of both STATs phosphorylation that leads to the initial IFN- $\gamma$  and IL-10 co-expression.

#### **4.5.2 Parameter sensitivity analysis**

In the previous subsections we showed that our model predicts that IFN- $\gamma$  to IL-10 switching (Figure 4.4) is due to the competition between STAT3 and STAT5 proteins (Figures 4.5 and 4.7). These model predictions are not obvious from the model assumptions due to the following. The structure of our model presented in Figure 4.1 is symmetrical in relation to the varied IL-2, i.e. IL-2 activates both STAT3 and STAT5. The model predictions for the phosphorylated states of STAT3, STAT5 and their homodimers could be swapped in Figures 4.5 and 4.7 if the parameters for STAT3 and STAT5 are swapped (Figures 7.1A and 7.1B in Appendix C). However in this case there would be no cytokine switching (Figure 7.1C). Thus the model predictions depend on the assumed structure of our model as well as on the chosen set of parameters. In this subsection we perform the parameter sensitivity analysis (SA) [251,252] to identify the parameter conditions for the conclusions to hold.

First, we test if the IFN- $\gamma$  to IL-10 and STAT5 to STAT3 switching are still present if we vary the parameters compared to their optimal values (set "O3" in Table 7.2). Quantitatively, we define the switching of either IFN- $\gamma$  to IL-10 or STAT5 to STAT3 as follows. We assume that the switching occurs when the 2-fold changes take place, which is typically considered as significant change in Biology (gene expression) [253,254]. Thus the changes should include at least 2-fold increase in IL-10 and STAT3 as well as decrease of the peak of IFN- $\gamma$  and STAT5 concentrations within the range of the tested IL-2 concentration.

We vary the parameters up to 10-fold either side of their values in the optimised set. We use the Latin Hypercube Sampling (LHS), which is considered as one of the most effective strategies for sampling the parameters [252,255]. We perform the LHS sampling and check the assumed condition for switching for 1000 samples of the optimised parameters. Figure 4.8 illustrates the probability of the cases, in percent, where the switching of both cytokine and STAT (C+S+), cytokine and not STAT (C+S-), not cytokine and STAT (C-S+), neither cytokine not STAT (C-S-) occurs for 1-10 fold change of the optimised parameters. The obvious result that follows from Figure 4.8 that when the parameters are not perturbed, which corresponds to the 1-fold change, the probability of the presence of both cytokine and STAT switching is 100%. However, with an increase of the fold change up to ten, the probability for switching of both cytokine and STAT decreases down to 2.1% (data shown in Table 7.3 in Appendix C). The probability of either of the cases (cytokine or STAT switching) is almost equal with the increase of the fold change as it can be seen from Figure 4.8. Thus, we can conclude that the model with the optimised parameters demonstrates both IFN- $\gamma$  to IL-10 and STAT5 to STAT3 switching with higher probability (more than 50%) when the parameters are perturbed within 2-fold, with modest probability (between 10% and 50%) when the parameters are perturbed within 3-6-fold and with low probability (less than 10%) when the parameters are perturbed within 7-fold and higher.



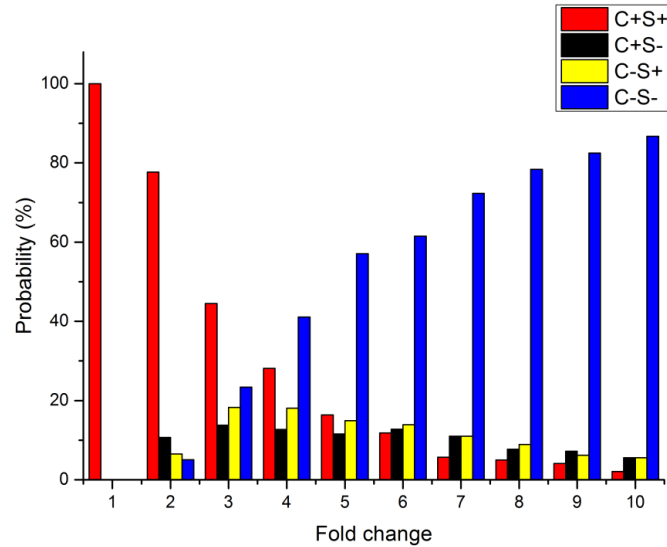


*Figure 4.8. The probability of cases when the switching occurs. The percentage of cases when the switching of both cytokine and STAT (C+S+), cytokine and not STAT (C+S-), not cytokine and STAT (C-S+), neither cytokine not STAT (C-S-) occurs for 1-10 fold change of the optimised parameters.*

Next we identify the most sensitive parameters that have the greatest effect on the steady-state concentrations of IFN- $\gamma$ , IL-10, STAT5 and STAT3 for the three concentrations of IL-2:  $10^{-10}$ ,  $10^{-6}$  and  $10^{-1}$ , which correspond to the three assumed T cell phenotypes shown in Figure 4.4B: Th1, Th1/Tr1 and Tr1 respectively. We perform the SA using the eFast method [256], because it was reported as one of the most reliable methods of parameter sensitivity analysis [255]. As a tool for the eFast sensitivity analysis, we use the SBToolbox software [257], which is similar to a related study [258]. We perform the SA over one order of magnitude of perturbation for 10000 simulations.

Figures 4.9-4.11 illustrate the results of the sensitivity analysis for IFN- $\gamma$ , IL-10, STAT5 and STAT3 by the SBToolbox under the non-dimensional IL-2 concentrations  $[i2]=10^{-10}$  (Figure 4.9),  $[i2]=10^{-6}$  (Figure 4.10) and  $[i2]=10^{-1}$  (Figure 4.11). The bars indicate the sensitivity indices for each of the parameters of our model. Here we classify the parameters as sensitive if the corresponding sensitivity index is more than 0.5.

It can be seen from Figures 4.9A, 4.10A and 4.11A that IFN- $\gamma$  is the most sensitive to the following parameters:  $M_{18}$ ,  $gg_t$ ,  $n_8$ ,  $M_{19}$ ,  $mp1_t$  and  $s5_t$ , which demonstrate high sensitivity indices (more than 0.5) under the all three IL-2 concentrations. The parameters  $n_1$ ,  $r2_t$ ,  $n_6$  and  $M_2$  are sensitive under  $[i2]=10^{-10}$  (Figure 4.9A) and  $[i2]=10^{-6}$  (Figure 4.10A). The parameter  $M_{14}$  is sensitive only under  $[i2]=10^{-6}$  (Figure 4.10A) and  $[i2]=10^{-1}$  (Figure 4.11A). The result that the concentration of IFN- $\gamma$  is sensitive to  $M_{18}$ ,  $gg_t$ ,  $n_8$ ,  $M_{19}$  and  $mp1_t$  is not surprising because these parameters are included into Equation (4.8) of IFN- $\gamma$  production. The other group of IFN- $\gamma$ -sensitive parameters that includes  $s5_t$  and  $n_6$  is involved in the STAT5 pathway activation, which leads to the production of IFN- $\gamma$  as shown in Figure 4.3 and Equations (4.6). Therefore, this is also an obvious result. There is also the third group of IFN- $\gamma$ -sensitive parameters consisting of  $n_1$ ,  $r2_t$ ,  $M_2$  that are involved in the upstream activation of IL-2 receptor described by Equation (4.1). Finally, IFN- $\gamma$  is sensitive to the Michaelis constant of heterodimerisation  $M_{14}$ .

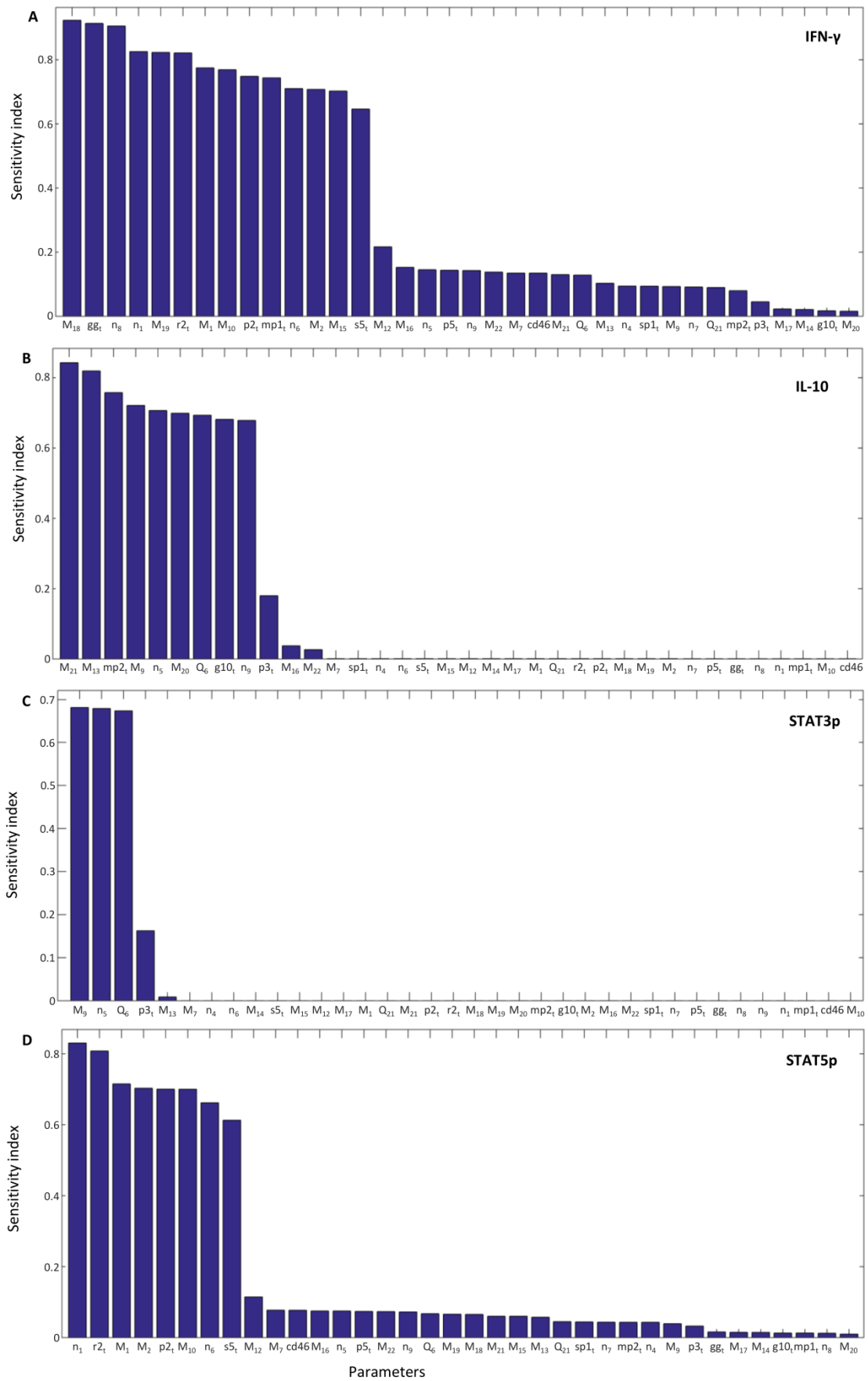


Figure 4.9. Parameter sensitivity analysis performed by eFAST. Sensitivity indicators for the developed model for IFN- $\gamma$  (A), IL-10 (B), STAT3 (C) and STAT5 (D) under IL-2 concentration  $[i_2] = 10^{-10}$ .

The parameter sensitivity analysis reveals that the concentration of IL-10 is the most sensitive to  $g_{10_t}$  and  $n_9$  under  $[i2]=10^{-10}$  (Figure 4.9B),  $[i2]=10^{-6}$  (Figure 4.10B) and  $[i2]=10^{-1}$  (Figure 4.11B). This result is obvious as both  $g_{10_t}$  and  $n_9$  are involved in the production of IL-10 as shown in Equation (4.9).

The parameter  $M_9$  is the most sensitive for the phosphorylated STAT3 under all three IL-2 concentrations as it is shown in Figure 4.9C, Figure 4.10C and Figure 4.11C. Two parameters, namely,  $n_5$  and  $Q_6$ , show high sensitivity only under  $[i2]=10^{-10}$  (Figure 4.9C) and  $[i2]=10^{-6}$  (Figure 4.10C). These results are predictable since  $M_9$ ,  $n_5$  and  $Q_6$  are involved in the STAT3 pathway activation as indicated in Figure 4.3 and Equation (4.6).

The concentration of phosphorylated STAT5 is the most sensitive to the total amount of STAT5,  $s_{5_t}$ , under all three tested IL-2 concentrations as it is shown in Figure 4.9D, Figure 4.10D and Figure 4.11D respectively. This is an expected result. The parameter  $n_6$  demonstrates high sensitivity indices for STAT5p under  $[i2]=10^{-10}$  (Figure 4.9D) and  $[i2]=10^{-6}$  (Figure 4.10D). This parameter is involved in the activation of STAT5 pathway as shown in Figure 4.3 and Equation (4.6). The concentration of STAT5p is sensitive to the Michaelis constant of heterodimerisation  $M_{14}$  under  $[i2]=10^{-6}$  (Figure 4.10D) and  $[i2]=10^{-1}$  (Figure 4.11D). Three parameters,  $n_1$ ,  $r_{2_t}$  and  $M_2$ , are sensitive under  $[i2]=10^{-10}$  (Figure 4.9D) and  $[i2]=10^{-6}$  (Figure 4.10D), involved in the activation of the IL-2 receptor described by Equation (4.1).

Thus, in this subsection we identified the parameters that mostly affect the model predictions. In the next subsection we will test our model for the perturbations of some of the identified parameters looking for the potential causes of the inflammatory diseases theoretically.

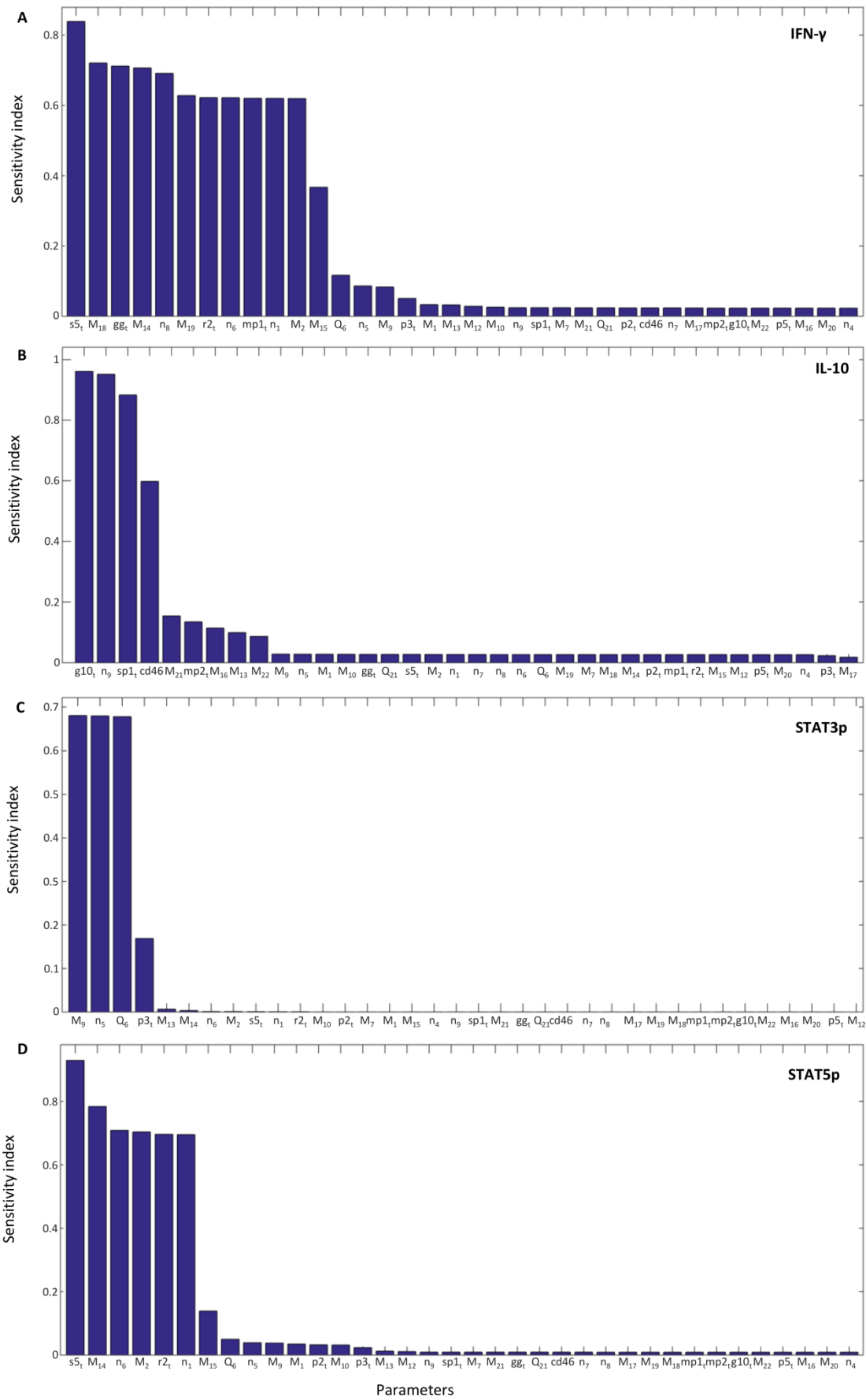


Figure 4.10. Parameter sensitivity analysis performed by eFAST. Sensitivity indicators for the developed model for IFN- $\gamma$  (A), IL-10 (B), STAT3 (C) and STAT5 (D) under IL-2 concentration  $[i2] = 10^{-6}$ .

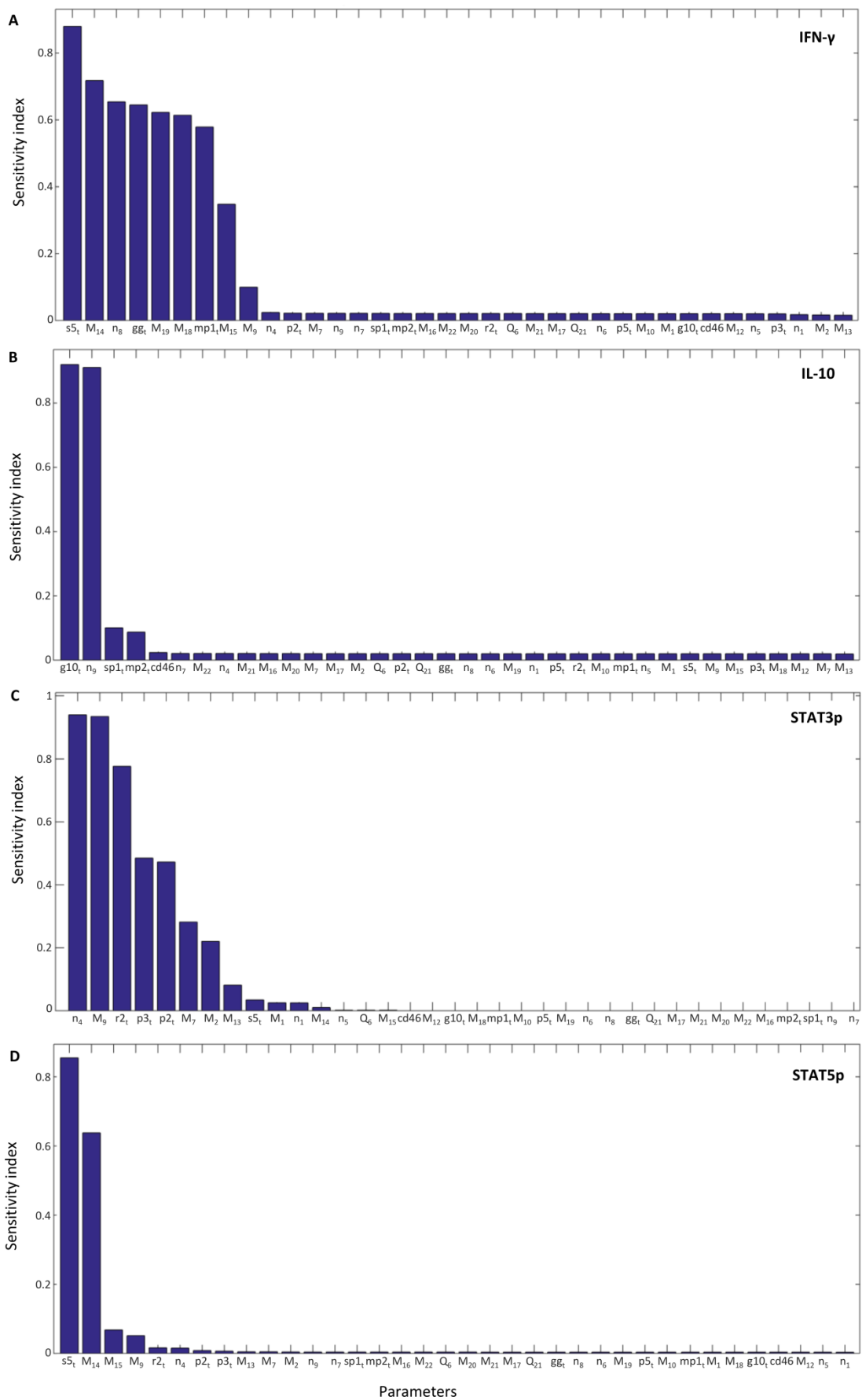


Figure 4.11. Parameter sensitivity analysis performed by eFAST. Sensitivity indicators for the developed model for IFN- $\gamma$  (A), IL-10 (B), STAT3 (C) and STAT5 (D) under IL-2 concentration  $[i_2] = 10^{-1}$ .

## Investigation of possible mechanisms of JAK-STAT mediated inflammatory pathologies

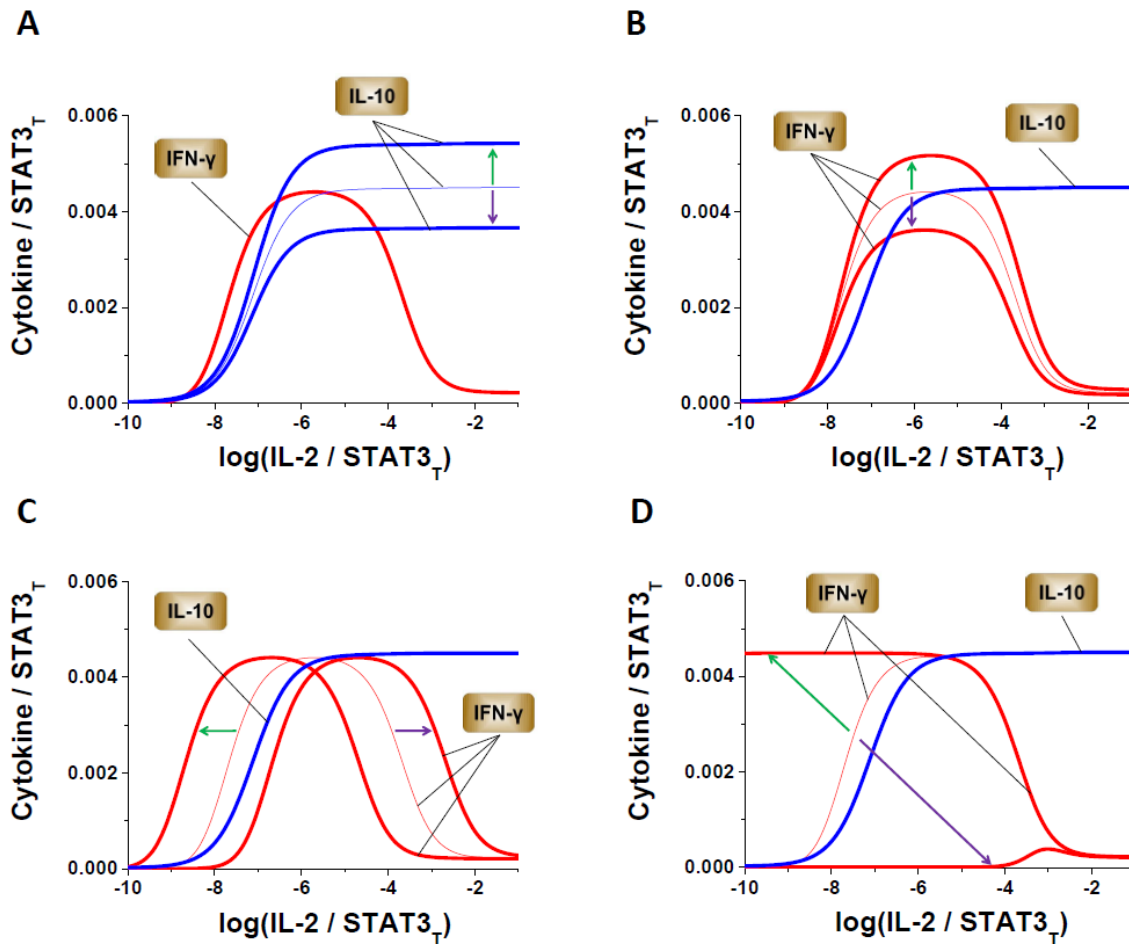


Figure 4.12. Systems model predictions for the produced IFN- $\gamma$  and IL-10 dependence on the change in intracellular regulation.

The aberrations in both activating or competing JAK-STAT pathways regulate the amounts of produced IL-10 (A) and IFN- $\gamma$  (B). The profile of IFN- $\gamma$  production can be shifted along IL-2 axis by changes in IL-2R signalling (C). The mutations in STAT5 phosphorylation may lead to IFN- $\gamma$  profile shift along IL-2 axis with the reduction of its magnitude at the same time (D). Thin lines represent the model predictions for the optimised set of parameters shown in Appendix C, while bold lines show the model predictions for the perturbed parameters shown in Table 4.1. Equations (4.1), (4.6), (4.7), (4.8) and (4.9). Parameters taken from set "O3" in Table 7.2, with changes according to Table 4.1.

Now we apply our newly developed model to investigate potential deviations in the immune system caused by the changes in the parameters starting with the highest sensitivity indices. It was reported that IFN- $\gamma$  and IL-10 play crucial role

in autoimmune pathologies [259,260]. Figure 4.12 illustrates the influence of the changes in STAT pathways on IFN- $\gamma$  and IL-10 production. The model shows that the production of IL-10 can be increased by attenuating the degradation of IL-10 by metalloproteases (increase of  $n_9$  and  $M_{20}$ ) or, alternatively, by an increase of  $g_{10_i}$ , as shown in Figure 4.12A and consistent with [261]. The changes in Figure 4.12A are illustrated for 15% parameter perturbation of  $n_9$ . Our model also suggests that the level of produced IFN- $\gamma$  can be controlled by various intracellular mechanisms (Figure 4.12B). For example, our model predicts that the magnitude of pro-inflammatory IFN- $\gamma$  can be reduced by the attenuation of the STAT5 pathway signalling (decrease of  $s_{5_t}$ ) [231] or by enhancement of metalloprotease-induced degradation of the produced IFN- $\gamma$  (decrease of  $M_{18}$  and  $n_8$ ). This prediction may sound obvious as it follows from the structure of the model shown in Figure 4.3. However another prediction of the model is that changes in the STAT3 pathway can also reduce the level of the produced IFN- $\gamma$ , which is not obvious from Figure 4.3. This effect could be achieved by enhancing the formation of STAT3:STAT5 heterodimer complex (decrease of  $M_{14}$ ) or alternatively by attenuation of STAT3 dephosphorylation (increase of  $M_9$ ). Figure 4.12B shows the effects of perturbations of these model parameters for the 1.5-fold change of  $M_9$ .



As a result of the parametric alterations the shape of IFN- $\gamma$  dependence shifts along IL-2 axis (Figure 4.12C). According to our model, the alterations of the parameters, that cause the IFN- $\gamma$  dependence shown in Figure 4.12C to shift to higher IL-2 concentrations, represent the changes in IL-2 receptor activation. These changes include the decrease of the total amount of IL-2R (decrease of  $r_{2_t}$ ) or enhancement of the dephosphorylation of phosphorylated IL-2R by SHP-1 (decrease of  $n_1$ ). It is notable that the peak shifts along IL-2 axis, however the magnitude does not change during this transformation. These results might be important since it was shown that IL-2R signalling controls tolerance and immunity and that IL-2R deficiencies give rise to various pathologies including Inflammatory Bowel Disease (IBD) [39,262]. Figure 4.12C shows the effects of  $n_1$  perturbation of one order of its magnitude.



The proposed model suggests new potential strategies for the control of IFN- $\gamma$  selectivity. According to the model predictions, the IFN- $\gamma$  peak shift along IL-2 axis can be also achieved by the alterations in competing STAT3 signalling pathway [263], namely by IL-2 mediated STAT3 phosphorylation (parameter  $M_7$ ) as shown in Figure 7.3A. This effect is a result of indirect interactions due to the redistribution of the STAT complexes as STAT3 does not directly regulate IFN- $\gamma$  production. Our model predicts that due to the competition effects between STATs, STAT3 indirectly inhibits STAT5, which induces the production of IFN- $\gamma$ .

The developed model also suggests that attenuation of IL-2-induced phosphorylation of STAT5 (increase of  $M_{10}$ ) reduces IFN- $\gamma$  magnitude and shifts the peak to the range of higher IL-2 concentrations [212,264,265] (Figure 4.12D). Our model predicts that the peak disappears when we apply the opposite changes (decrease of  $M_{10}$ ).

*Table 4.1. The effects of the parametric changes on the concentration of produced IFN- $\gamma$  and IL-10 shown in Figure 4.12.*

Figure 4.12	Parameters	Perturbation		
			thin line (optimised)	
<b>A</b>	$n_9$	$163 \cdot 10^{-4}$	$191 \cdot 10^{-4}$	$220 \cdot 10^{-4}$
	$M_{20}$	$119 \cdot 10^{-4}$	$149 \cdot 10^{-4}$	$179 \cdot 10^{-4}$
	$g10_t$	6.136	7.218	8.301
<b>B</b>	$s5_t$	$198 \cdot 10^{-4}$	$247 \cdot 10^{-4}$	$297 \cdot 10^{-4}$
	$M_{18}$	7.93	9.913	11.896
	$n_8$	$81 \cdot 10^{-4}$	$101 \cdot 10^{-4}$	$121 \cdot 10^{-4}$
	$M_{14}$	0.068	0.1	0.145
	$M_9$	69.185	47.714	32.445
<b>C</b>	$r2_t$	$2.7 \cdot 10^{-4}$	$27 \cdot 10^{-4}$	$268 \cdot 10^{-4}$
	$n_1$	11.842	118.42	1184.2
<b>D</b>	$M_{10}$	470	$47 \cdot 10^{-4}$	$47 \cdot 10^{-9}$

Our model predictions demonstrate possible scenarios of alterations in JAK-STAT pathways that influence IFN- $\gamma$  and IL-10 production. The scenarios include the change of IL-10 (Figure 4.12A) and IFN- $\gamma$  (Figures 4.12B and 4.12C) as well as the selective regulation of IFN- $\gamma$  by IL-2 (Figure 4.12D). The effects of the parametric changes on the concentrations of produced IFN- $\gamma$  and IL-10 are summarised in Table 4.1. The colour of the arrows in Table 4.1 corresponds to the colour of the arrows that represent changes shown in Figure 4.12. The results illustrated in Figure 4.12 show how the production of IFN- $\gamma$  and IL-10 is regulated by their activating STAT pathways. Moreover, our model suggests alternative approaches for the regulation of IFN- $\gamma$  and IL-10 production by employing their competing STAT pathways, STAT3 and STAT5 respectively.

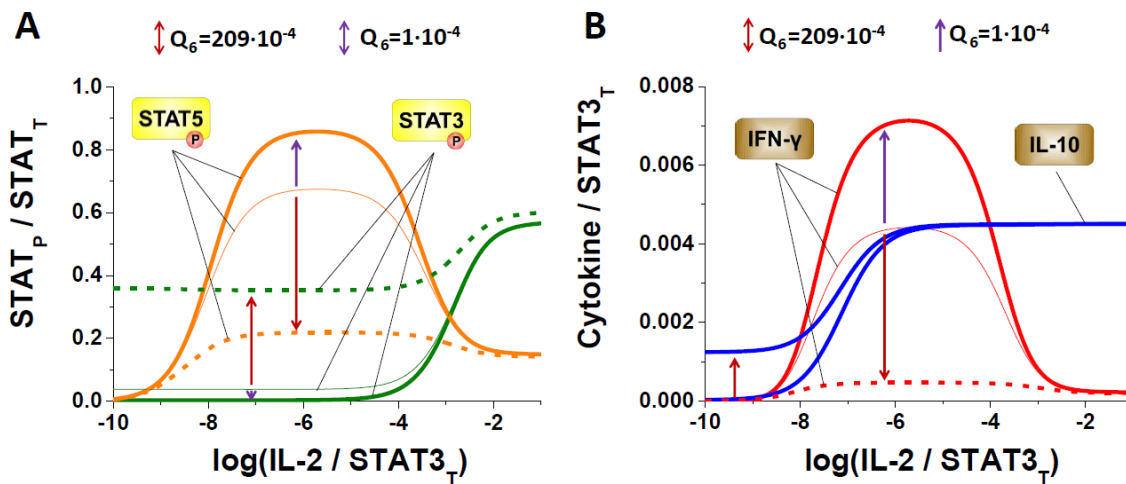


Figure 4.13. The effects of change in extracellular IL-6 concentration.

A. The model predictions show that increased IL-6 (modelled by parameter  $Q_6$ ) leads to the lack of STAT redistribution (dotted lines) while reduced amount of IL-6 may lead to the more pronounced STAT redistribution. B. The lack of STAT redistribution observed for increased IL-6 leads to significantly lower level of IFN- $\gamma$  production. Thus, our model predicts that the level of IFN- $\gamma$  production can be reduced by the IL-6-dependent changes in the competing STAT3 pathway. Thin lines represent the model predictions for the optimised set of parameters shown in Appendix C, while bold lines show the model predictions for the perturbed parameters. See Equations (4.1), (4.6), (4.7), (4.8) and (4.9) with parameters taken from set "O3" in Table 7.2. The parametric changes are:  $Q_6 = 1 \cdot 10^{-4}$  (purple arrow),  $Q_6 = 14 \cdot 10^{-4}$  (thin line),  $Q_6 = 209 \cdot 10^{-4}$  (red arrow).

In our model, in addition to the control function of IL-2, which includes the control of Th1/Tr1 switching [39], other functional cytokines also play an important role in T cell polarization. In the chosen example (Figure 4.1B) the production of anti-inflammatory IL-10 is up-regulated by IL-6 via the STAT3 signalling pathway [266]. Next, we employ our model to study the interplay between IL-2 and IL-6 through the STAT signalling pathways and their role in T cell polarization.

The developed model predicts how IL-6 variations impact the STAT switching ability (Figure 4.13A). In our model, the concentration of IL-6 is described by  $Q_6$  parameter as shown in Equations (4.6). Figure 4.13A illustrates that IL-6 decrease ( $Q_6$ ) leads to more pronounced STAT5 to STAT3 switching, whereas an increase in IL-6 concentration ( $Q_6$ ) causes less significant changes in both STAT3 and STAT5 phosphorylation levels as a function of IL-2 and thereby the lack of switching. It can be seen from Figure 4.13A that IL-6 activates STAT3 but at the same time inhibits STAT5 due to the STAT redistribution, consistent with observations in [267]. As a result of IL-6 impact on the STAT redistribution, the structure of our model suggests that IL-6 also affects the STAT-mediated production of IFN- $\gamma$  and IL-10 (Figure 4.13B). In particular, our model predicts that due to the redistribution between STAT3 and STAT5, increased IL-6 leads to the reduced level of pro-inflammatory IFN- $\gamma$  production. This result might be clinically important since it may offer novel strategies for reducing IFN- $\gamma$ , which is essential in abnormal production of this pro-inflammatory cytokine during inflammation [39].

In this subsection we analysed the effect of parametric alterations in JAK-STAT pathways on the concentration of produced IFN- $\gamma$  and IL-10. However, there is another pathway that regulates the production of IL-10, which is STAT independent, but IL-2 dependent. This is so called CD46-SP1 pathway, it is illustrated in Figure 4.3. The effect of the CD46-SP1 pathway is characterised by parameter  $sp1_t$  (Equation (4.7)), the total amount of the transcription factor SP1, which enacts this pathway. Figure 7.3B shows the effects of perturbations of  $sp1_t$  within 10-fold of either side of its optimised value. An increase of  $sp1_t$  leads to IL-10 shift to lower IL-2 concentrations, while a decrease of  $sp1_t$  results

in IL-10 shift to higher IL-2 concentrations accompanied by a slight decrease of IL-10 magnitude (Figure 7.3B). If  $sp1_t = 0$ , which can be interpreted as the absence of CD46-SP1 signalling, the magnitude of IL-10 decreases significantly (two times) compared to the optimised value. Thus blocking CD46-SP1 signalling leads to the lack of regulatory phase that is observed in patients with RA, which is consistent with [39,244]. Figure 7.3B shows that for the perturbed  $sp1_t$ , switching from IFN- $\gamma$  to IL-10 nevertheless takes place. This finding allows us to suggest that in our model, with the chosen set of parameters, switching is due to the STAT competition whereas CD46-SP1 signalling only plays a role in additional regulation of switching.

#### **4.5.3 Comparative analysis of STAT3-STAT4 versus STAT3-STAT5 machinery**

In this subsection we combine the STAT3-STAT4 and STAT3-STAT5 modules, one of which (Figure 4.1B) was thoroughly investigated in the previous subsections, to understand integral properties emerging from the STAT-STAT circuit couplings. To this end, we first highlight the structural differences between the STAT3-STAT4 (Figure 4.1C) and STAT3-STAT5 (Figure 4.1B) circuits. The most crucial difference between the two circuits is in the role of IL-2. In STAT3-STAT5 subsystem IL-2 activates both STAT3 and STAT5 while in STAT3-STAT4 subsystem IL-2 activates only STAT3 and not STAT4. The other cytokines, that activate STAT4, include IL-12 and IL-35 (Figure 4.1C). We assume here that during the experiment the concentrations of IL-12, IL-35 and STAT3-activating IL-6 are maintained constant while IL-2 is varied. This implies that only the amount of phosphorylated STAT3 in the pairing can be directly changed by varied IL-2 concentration. To study the nature of the STAT redistribution and cytokines interdependence we next investigate the STAT3-STAT4 circuit for various IL-2 concentrations. The detailed description of the model for STAT3-STAT4 subsystem can be found in Appendix C.

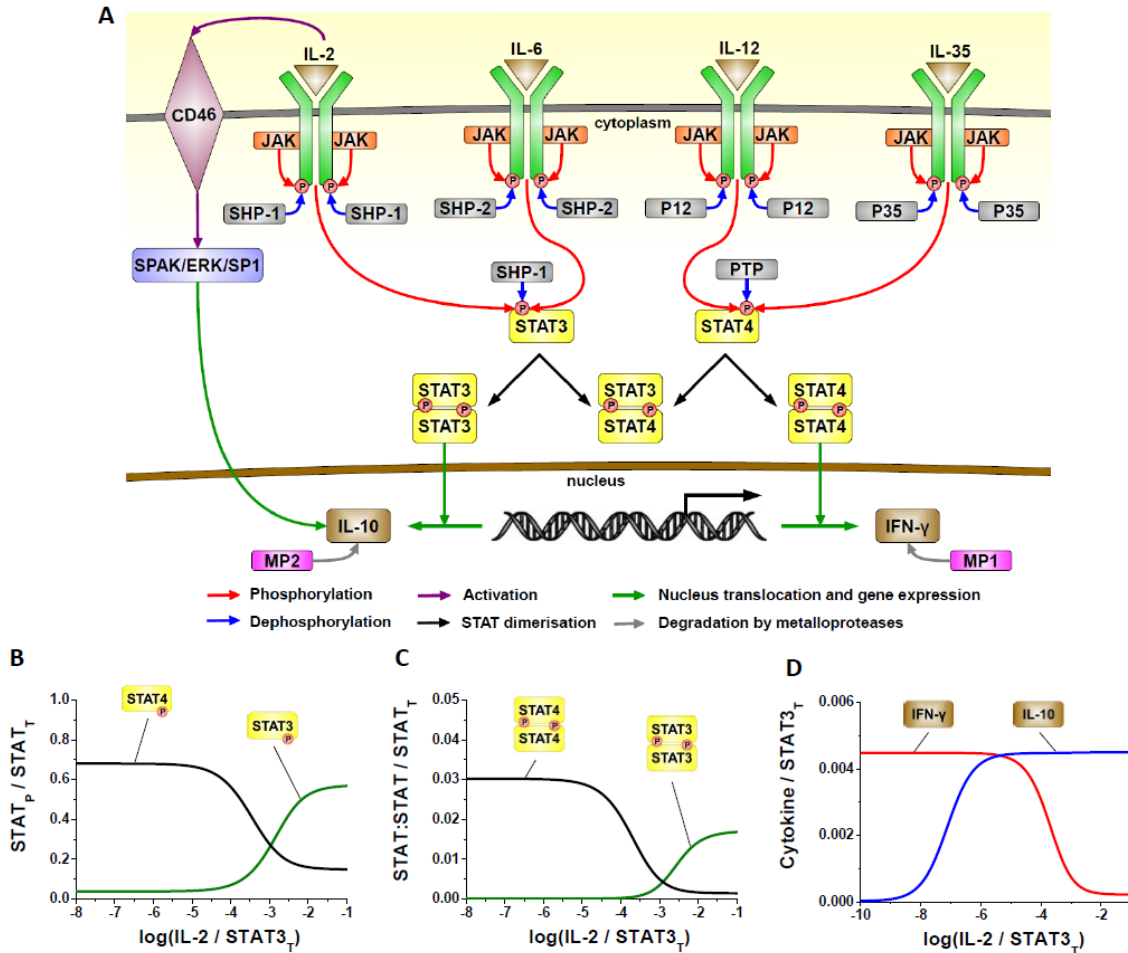


Figure 4.14. The model predictions for STAT3-STAT4 circuit.

Schematic diagram for the intracellular signalling that leads to IFN- $\gamma$  and IL-10 production through the STAT3-STAT4 mechanism (A). Redistribution between STAT3 and STAT4 monomers (B) as well as STAT3:STAT3 and STAT4:STAT4 homodimers (C) leads to the IFN- $\gamma$  to IL-10 switching for higher IL-2 concentrations shown in (D). Our model predicts that there is a significant basal level of STAT4p and thereby STAT4:STAT4 homodimer for low IL-2. This is due to the fact that in our model IL-12 and IL-35 are maintained constant while varied IL-2 activates only STAT3 and not STAT4 in this pairing. The basal STAT4:STAT4 homodimer leads to the background level of IFN- $\gamma$  production and the lack of initial co-expression between produced IFN- $\gamma$  and IL-10 (D). See Equations (7.113), (7.124), (7.125), (7.126) and (7.127) with parameters taken from Table 7.4.

In absence of experimental data for STAT4 signalling, we assume that the parameters in the STAT3-STAT4 subsystem are similar to the parameters in the STAT3-STAT5 subsystem (Table 7.4). Figures 4.14B-4.14D represent the model predictions for the STAT3-STAT4 subsystem (Figure 4.14A). The figures

include STAT3, STAT4 monomers (Figure 4.14B), STAT3:STAT3, STAT4:STAT4 homodimers (Figure 4.14C) as well as IFN- $\gamma$  and IL-10 dependences on IL-2 concentration (Figure 4.14D). It can be seen from Figure 4.14 that the STAT3-STAT4 subsystem demonstrates dependence on IL-2 similar to that of STAT3-STAT5 shown in Figure 4.5. Despite the fact that IL-2 does not affect phosphorylation of STAT4 in STAT3-STAT4 circuit, the switching is nonetheless present in this submodule.

The model suggests that the STAT and subsequent phenotype switching is due to the competition between STAT3 and STAT4 species rather than competition for the source of IL-2. This suggestion is supported by the structure of our model (Figure 4.1C) where IL-2 activates STAT3 and not STAT4 in the pairing and therefore there is no competition for the source. Mechanistically, the competition between STAT3 and STAT4 includes redistribution between these species that is implemented by the formation of STAT3:STAT4 heterodimer.

Despite the fact that the switching is present in both STAT3-STAT5 and STAT3-STAT4 circuits, the model predictions significantly differ between these two circuits for the low IL-2 concentrations. STAT3-STAT5 circuit demonstrates the bell shaped characteristics with the low IFN- $\gamma$  production for the low amounts of IL-2 (Figure 4.4B) whereas STAT3-STAT4 circuit reveals the significant background level of IFN- $\gamma$  (Figure 4.14D). Figure 4.14B shows that for low IL-2 concentrations there is also a basal phosphorylation level of STAT4. Our model suggests that these background levels of STAT4p (Figure 4.14B) and subsequent IFN- $\gamma$  production (Figure 4.14D) are due to the STAT4 activation by the maintained concentrations of IL-12 and IL-35 [217].

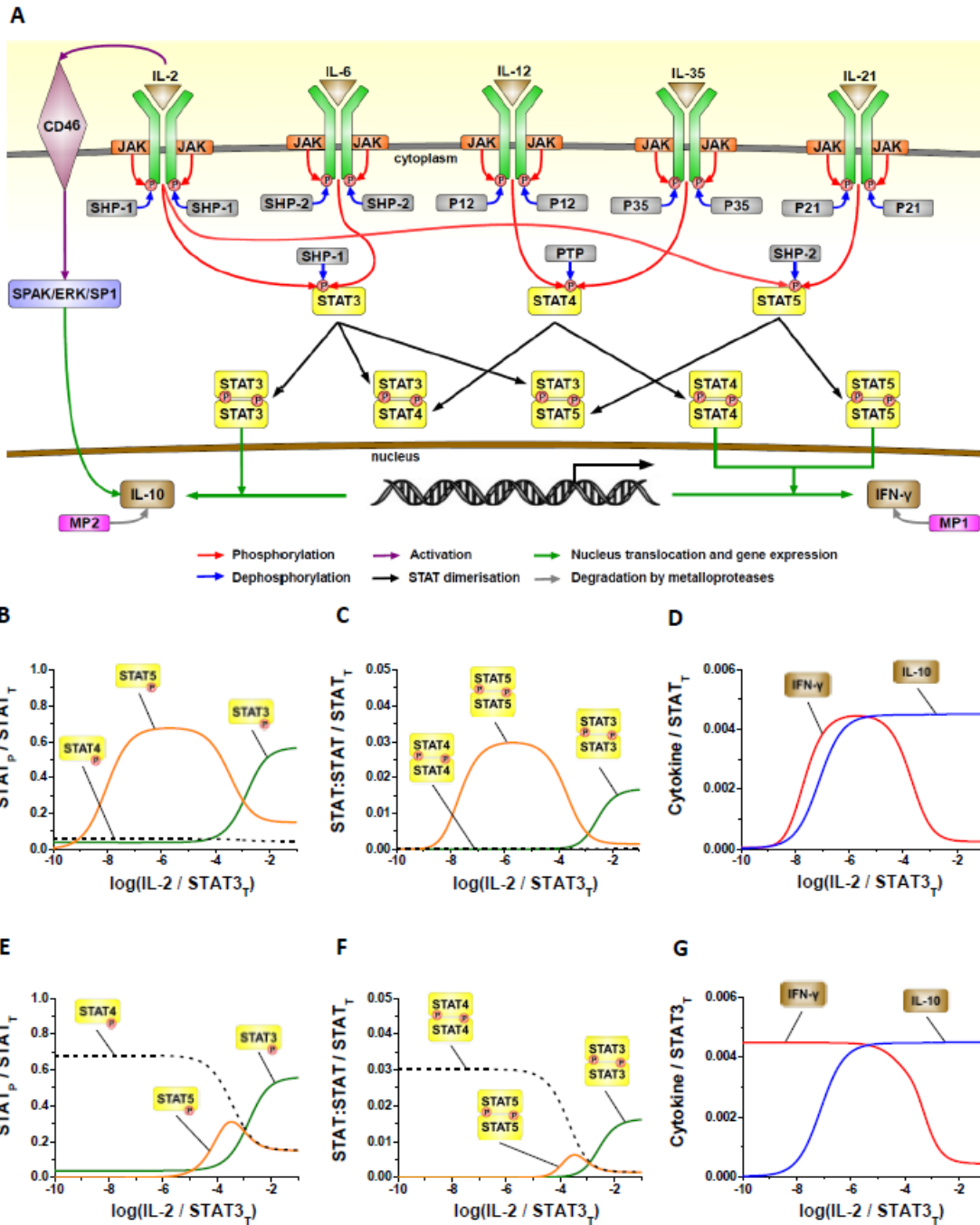


Figure 4.15. The model predictions for the combined STAT3-STAT4-STAT5 circuit.

A. Schematic diagram for the combined STAT3-STAT4-STAT5 model. B-D. The dose-response profiles show that for significantly dephosphorylated STAT4, the STAT3-STAT5 like responses prevail and the selective production of IFN- $\gamma$  arises. E-G. The model predictions for dephosphorylated STAT5 reveal STAT3-STAT4 like responses with no selectivity for IFN- $\gamma$  production observed. See Equations (7.129), (7.140), (7.141), (7.142) and (7.143). Parameters are taken from set "O3" in Table 7.2 and Table 7.4 except  $p_{4_i} = 236.96$  in (A-C) and  $p_{5_i} = 23.7$  in (D-F).

After the establishment of the individual properties of STAT pathways, we next combine these two circuits (Figure 4.15A). Previously we studied individual contribution of each of them to the overall response of the system. The detailed description of the model for STAT3-STAT4-STAT5 subsystem is shown in Appendix C. The parameters are taken from Tables 7.2 and 7.4.

Figures 4.15B-4.15G illustrate the model predictions for the combined STAT3-STAT4-STAT5 circuit. Our model shows that the IFN- $\gamma$  to IL-10 switching is still present in the combined model (Figures 4.15D and 4.15G). One of the major differences between the full circuit and the smaller submodules is that in the full circuit STAT3 competes with STAT4 and STAT5 at the same time (Figures 4.15B and 4.15E) while in the smaller submodules it competes only with either at a time.

Previously we showed that the two subsystems have similar dose-response characteristics for medium and high IL-2, whereas the dose-response curves for low IL-2 are different (Figures 4.7 and 4.14). In the range of low IL-2 concentrations our model demonstrates two possible scenarios for IFN- $\gamma$  and IL-10 production depending on which of the two submodules, STAT3-STAT4 or STAT3-STAT5, prevails. Figures 4.15B-4.15D show that the combined model predictions qualitatively coincide with the predictions for STAT3-STAT5 subsystem (Figures 4.4B and 4.7) when the amount of phosphorylated STAT4 is significantly reduced in comparison to phosphorylated STAT5. In our model the reduction of STAT4p is performed by an increase of the total PTP phosphatase concentration ( $p4_t = 236.96$ ). The case shown in Figures 4.15E-4.15G, where STAT5p is strongly dephosphorylated by increased SHP-2 ( $p5_t = 23.7$ ), suggests that the response of the combined model is similar to that of STAT3-STAT4 circuit considered previously (Figure 4.14). For this system we observe a significant (compared to phosphorylated STAT5) basal level of STAT4 phosphorylation (Figure 4.15E) as well as the background IFN- $\gamma$  production (Figure 4.15G). Our model predicts that for the low IL-2 the phosphorylation level of STAT4 and STAT5 controls the balance between the competing STAT3-STAT4 and STAT3-STAT5 modules.



#### 4.5.4 The role of individual cytokines in STAT dimer redistribution

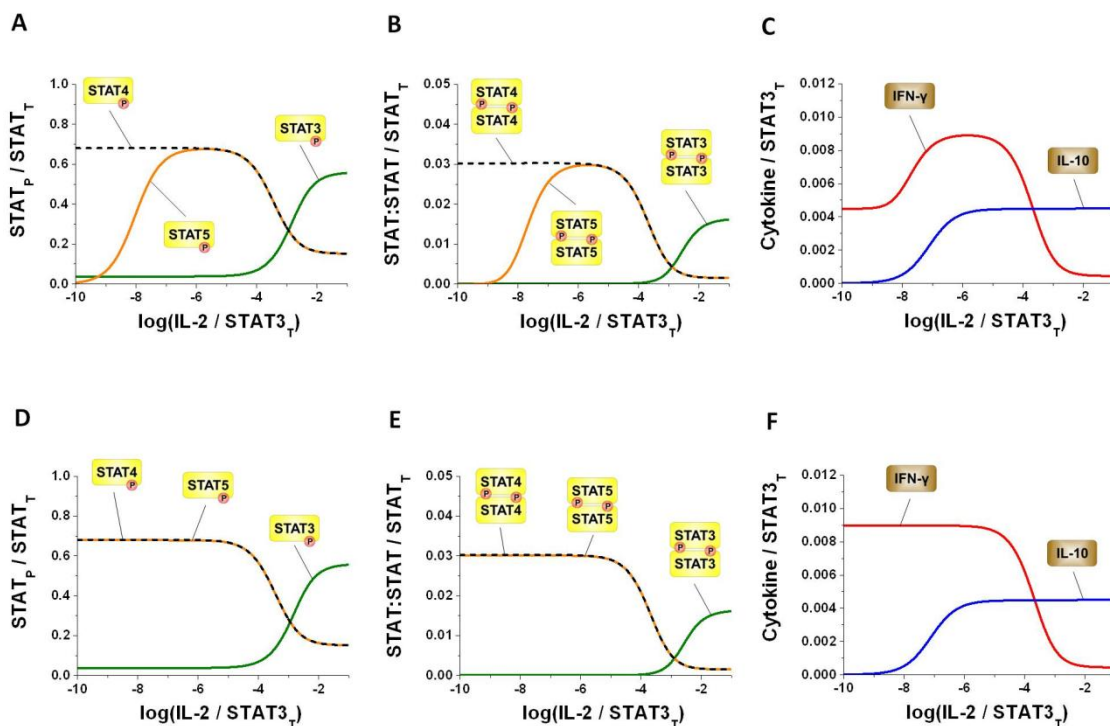


Figure 4.16. The competition between STAT3-STAT4 and STAT3-STAT5 modules in the combined model depends on IL-21 concentration.

The systems model predicts that low IL-21 can alter the balance between the competing circuits to the STAT3-STAT5 like responses (A-C). In this case the amount of STAT5:STAT5 homodimers is selectively regulated by IL-2 (B). The background level of IFN- $\gamma$  production (C) is due to the basal phosphorylation level of STAT4 (A) and STAT4:STAT4 homodimer (B). At the same time, when IL-21 is significantly increased, STAT3-STAT4 like responses prevail as shown in (D-F) with no observed selectivity for STAT5 (D and E) and IFN- $\gamma$  production (F). See Equations (7.129), (7.140), (7.141), (7.142) and (7.143). Parameters are taken from set "O3" in Table 7.2 and Table 7.4. The parametric changes are  $Q_{21} = 3.42 \cdot 10^{-11}$  in (A-C) and  $Q_{21} = 3.42 \cdot 10^{-3}$  in (D-F).

Our model suggests that the STAT dimer redistribution is also driven by the cytokines other than IL-2. We demonstrated earlier in this chapter the influence of STAT3-activating cytokine, IL-6, on the switching. Next, we investigate the role of STAT5-activating IL-21 in the competition between the STAT3-STAT4 and STAT3-STAT5 circuits and its influence to the overall response (Figure 4.16). The concentration of IL-21 is modelled by parameter  $Q_{21}$  defined in Equations (4.6).

The developed model predicts that IL-21 controls the STAT dimer redistribution in the following way. In our model IL-21 phosphorylates STAT5 (Figure 4.1B). Figure 4.16 shows that the influence of IL-21 is especially significant for low IL-2 concentrations. Our combined model suggests that low IL-21 ( $Q_{21} = 3.42 \cdot 10^{-11}$ ) leads to the low initial STAT5p, which demonstrates the bell-shape for increasing IL-2 (Figure 4.16A), whereas increased IL-21 ( $Q_{21} = 3.42 \cdot 10^{-3}$ ) leads to higher STAT5p with no bell-shape (Figure 4.16D). When phosphorylated, STAT5p forms STAT5:STAT5 homodimer structure. Thus, IL-21-driven STAT5 phosphorylation defines the amount of STAT5:STAT5 homodimer for low IL-2 (Figures 4.16B and 4.16E). The STAT5:STAT5 homodimer, in turn, up-regulates IFN- $\gamma$  production. Our model predicts that IL-21 also controls the balance between the competing STAT3-STAT4 and STAT3-STAT5 circuits in IFN- $\gamma$  production. Figure 4.16 shows that for low IL-2 the bell-shaped STAT3-STAT5 (Figure 4.16C) and monotonic STAT3-STAT4 (Figure 4.16F) production of IFN- $\gamma$  is due to the low and increased IL-21, respectively. However in contrast to the STAT3-STAT5 like responses when STAT4p was dephosphorylated (Figures 4.15B-4.15D), here we observe the background IFN- $\gamma$  production for low IL-2 (Figure 4.16C), which is due to the basal level of STAT4:STAT4 homodimer (Figure 4.16B).

In this subsection we analysed the influence of cytokines other than IL-2 on the STAT redistribution and produced cytokine switching using the example of IL-21. The combined model shows that the increased IL-21 concentration up-regulates STAT5 under the low IL-2 concentration and therefore leads to the STAT3-STAT4 like production of IFN- $\gamma$  without the bell-shaped dependence (Figures 4.16D-F). At the same time the model predicts that the lower IL-21 concentration leads to the STAT3-STAT5 like responses in relation to IFN- $\gamma$  production for low IL-2 (Figures 4.16A-C). These results can be explained by the fact that IL-21 increases the amount of STAT5:STAT5 homodimers and thereby leads to basal IFN- $\gamma$  production observed for STAT3-STAT4 circuit separately [225,232].

## 4.6 Conclusions

In this chapter we extended the model for single STAT phosphorylation proposed in previous chapter to the system of interacting STATs and developed a new integrative modelling approach to study STAT signalling. The approach encompasses the network representation of the interactions between cytokines and JAK-STAT pathways. Based on the proposed approach, we built a mathematical model for STAT signalling in T cells. The proposed model was employed to explain the T cell phenotype plasticity effects using the example of Th1 to Tr1 switching [39]. While it is widely accepted that JAK-STAT pathways regulate the phenotype switching, the underlying mechanism and possible interdependence effects between the JAK-STAT pathways need further clarification. In order to propose potential mechanisms we considered the immune response from the systems perspective. The model developed in this chapter for the first time takes into account the interdependence effects between the JAK-STAT pathways and predicts the conditions, under which the phenotype switching occurs. The proposed model explains how the same cytokines can activate different STATs and induce the production of other cytokines with opposite immune function. The model predictions are consistent with the experimental data for IFN- $\gamma$  and IL-10 production [244].

The molecular mechanisms underlying T cell plasticity have been a subject of extensive systems biology research in recent years. Our model extends previously published mathematical models that analyse JAK-STAT signalling [40-43]. While the previous models studied cytokine production considering single JAK-STAT activation pathways only, our model introduces cross-regulation effects and STAT-related modulation of signals. The developed model establishes relationship between cytokines, STAT proteins and the overall immune response. Our model predicts that the Th1 to Tr1 phenotype switching is due to the competition and switching between the STAT proteins. The parameter sensitivity analysis presented in this chapter (Figure 4.8) demonstrates that this conclusion is valid with the probabilities of 78% within the 2-fold, 45% within the 3-fold and 28% within the 4-fold parametric changes.

The analysis of our model showed that depending on extracellular cytokine concentrations the competing STAT species can inhibit each other. Another

finding of this chapter offers an insight into the role of STAT heterodimer complexes that has been remained unclear [217]. We suggested here that STAT homodimers rather than heterodimers induce the cytokines production, which is consistent with [245], and that the heterodimers can serve as a "buffer" between the various STAT homodimer complexes. The presence of heterodimers allows the redistribution of STAT homodimers and therefore causes the switching of produced cytokines and T cell phenotype. The suggested regulatory role of STAT heterodimers could be studied experimentally by proteomic identification of nuclear STAT heterodimers. This would allow one to check our model predictions regarding the STAT homodimers correlation shown in Figure 4.6.

The proposed model was applied to study interdependent interactions in the pathways that lead to the production of IFN- $\gamma$  and IL-10 (Figure 4.6). The model predictions show the cross-inhibition effects between the production of IFN- $\gamma$  and IL-10 as well as the produced cytokines dependence on STAT monomers and dimers. These results demonstrate how the same STAT proteins induce the production of certain cytokines and inhibit the production of the others. Our model shows how such extracellular stimuli as IL-2 control the threshold of the switching between IL-10 and IFN- $\gamma$  inducing STAT dimers, STAT3:STAT3 and STAT5:STAT5 respectively. The proposed model suggests that mutual inhibition of competing STATs is the basis of the inhibition effects in IFN- $\gamma$  and IL-10 production.

Our model suggests new explanations for JAK-STAT signalling regulation involved in the T cell phenotype switching. A number of external and internal factors can alter the model parameters and biomolecular interactions in JAK-STAT signalling pathways and as a result influence the levels of produced cytokines as well as the T cell phenotype. We investigated how these alterations (possibly caused by genetic mutations) can lead to various pathological states without changing the structure of the model. Our model predicts that inappropriate regulation of IL-2 receptor system leads to the dysfunctions or lack of the IFN- $\gamma$  to IL-10 switching, which in turn may mediate the autoimmune and IBD states [262].

Immunity-related pathologies caused by *Leishmania major* or Epstein-virus are associated with an inappropriate balance between the pro-inflammatory and anti-inflammatory cytokines [268,269]. The proposed model suggests strategies for regulation of IFN- $\gamma$  and IL-10 production during the diseases. We showed that the IFN- $\gamma$  to IL-10 switching can be controlled biochemically by enhancing or reducing signalling through certain JAK-STAT pathways. Our model predicts that the reduction of the uncontrolled inflammation could be achieved by reducing the role of STAT5 pathway or by enhancing the IL-6-induced STAT3 phosphorylation, which up-regulates anti-inflammatory IL-10 production. Alternatively, the enhancement of STAT3 phosphorylation can be performed via lowering the SHP-1-mediated dephosphorylation of phosphorylated STAT3. The predictions of our model might have clinical applications in drug discovery and could be tested experimentally.

The model proposed in this chapter shows that the alterations in intracellular signalling may lead not only to the change in the levels of the produced cytokines but also to the lack of T cell phenotype switching, which is associated with the immunity-related pathologies. Figure 4.13 shows that the increased IL-6 leads to the lack of switching in phosphorylated STAT proteins, whereas the switching is stronger for the reduced IL-6. Due to the high dependence of cytokine production on the STAT balance, the lack of switching in STATs leads to the lack of switching in IFN- $\gamma$  and IL-10 production.

A number of pharmacological and clinical studies observed aberrant STATs activation in human tumour diseases. The inhibition of certain STATs and induced cytokine production might have clinical applications in immunity-related pathologies including cancer [210,211,270] and uncontrolled inflammation [271]. It was reported that STAT3 is a promising target for anti-cancer treatment [210,211,270]. Experimental studies investigating STAT3 inhibition have been grown in recent years [272-275]. However there is still a limited understanding of the underlying mechanisms of the inhibition. Our model proposes new interdependent strategies for STAT3 inhibition, which include the activation of competing STAT pathways. The results of the proposed model suggest that the inhibitor selectivity to specific STAT proteins might enhance the anti-cancer effect.

Systems modelling can offer new insights into the interpretation of experimental data. The fact that our model considers multiple JAK-STAT pathways at a time might potentially explain the conflicting experimental results [212,231-233,250] supported by the wrong data interpretation. For example it was shown in [212,231,232] that the activated STAT5 leads to the production of IFN- $\gamma$  while in [233] it was demonstrated that IL-10 production is also enhanced through STAT5 activation. The proposed model can explain the duality in experimental data by introducing the selective effects in JAK-STAT pathways depending on IL-2 concentration (Figures 4.4 and 4.7). Thus the experimental data cannot be interpreted in the way that certain input cytokine can activate other cytokine production but the concentration of other input extracellular cytokines should also be considered.

The model predictions may contribute to better understanding of the molecular basis of autoimmune states [39]. Using the example of IL-6 can explain how some cytokines have a dual role in inducing both pro- and anti-inflammatory cytokine production [266]. We suggested here the mechanism how the STAT signalling and subsequent cytokine production depend on the combination of extracellular cytokines using the examples of STAT3, STAT4, STAT5, IL-2, IL-6, IL-21, IL-12, IL-35 in IFN- $\gamma$  and IL-10 production. Our model is in line with the observations that the cytokine milieu rather than a single cytokine defines the overall immune response [276]. Thus, systems approach offers broader understanding of the mechanisms involved in JAK-STAT signalling.

Here we used the systems biology approach, according to which all sophisticated systems of biomolecular interactions can be divided into subsystems if it is physiologically meaningful. Using this method we extracted from the scheme shown in Figure 4.1A the STAT3-STAT5 and STAT3-STAT4 subsystems and then combined them together. The analysis revealed that all three subsystems can reproduce the phenotype switching for certain amounts of IL-2 however the model predictions differ for low IL-2 concentrations. The model predictions for low IL-2 concentrations showed selective activation of IFN- $\gamma$  production for STAT3-STAT5 subsystem (Figure 4.4B) whereas STAT3-STAT4 subsystem demonstrated no selective activation caused by

basal, relatively significant level of IFN- $\gamma$  production (Figure 4.14D). The combined model suggests that extracellular cytokines can switch the overall response of the system to selective or non-selective responses for low concentrations of IL-2. Thus our model reveals that there is a competition not only between the STATs but also between the subsystems. Using the example of IL-21 we showed how the change in this extracellular cytokine concentration can shift the balance between the competing subsystems (Figure 4.16).

T cells can be divided into the phenotypes that produce pro-inflammatory and anti-inflammatory cytokines. One of such examples was investigated in this chapter in the context of Th1/Tr1 phenotype switching. We focused on pro-inflammatory IFN- $\gamma$  and regulatory IL-10 production in the Th1/Tr1 phenotype switching via STAT proteins. However it should be noted that the considered STATs, shown in Figure 4.1A, can also induce the production of cytokines other than IFN- $\gamma$  and IL-10. We suggested here that the proposed model can be applied to describe the plasticity effects and the switching not only between Th1 and Tr1, but also the other T cell phenotypes. Our model might potentially have clinical applications in the Th1/Th2 [277], Treg/Th17 or Th17/Th2 [278] phenotype switching. For example, the proposed model for pro-inflammatory IFN- $\gamma$  producing Th1 and anti-inflammatory IL-10 producing Tr1 cells can be extended to pro-inflammatory IL-17 producing Th17 and anti-inflammatory IL-4 producing Th2 as well as anti-inflammatory IL-10 producing Treg cells, which is one of directions for future research.

## 5 The interplay between MAPK signalling and biophysical regulation in *Candida glabrata* adaptation to osmotic stress

### 5.1 Literature review

#### 5.1.1 Biological review

*Candida glabrata* is a pathogenic yeast, which is especially prevalent in patients with immunodeficiency [279]. It is one of the most common cause of candidiasis [280]. *C. glabrata* lives on human mucosal surfaces as a biofilm and rarely penetrates tissue [45]. Due to the fact that for many years *C. glabrata* was thought to be a non-pathogenic organism, it is now one of the less studied *Candida* species [281]. However, further studies revealed that this fungi are opportunistic pathogens in the group of people who have the lack in immune response, which includes HIV positive people, the elderly and people who received immunosuppressive therapies or antibiotic treatment [45,282,283]. Moreover, the mortality rate associated with *C. glabrata* is one of the highest (40-70%) compared to other non-*C. albicans Candida* species (20-40%) [284,285].

Evolutionary, among all the non-*C. albicans Candida* species, *C. glabrata* is the most closely related to *Saccharomyces cerevisiae* baker yeast [45]. *S. cerevisiae* is one of the best studied model organisms due to their easy culturing, short generation time and gene transformation. They naturally inhabit on surface of decomposing fruits and widely used in bakery, brewing and winemaking [286,287].

To maintain their normal functioning, both *C. glabrata* and *S. cerevisiae* have to adapt to a range of external stimuli and stresses such as pheromone, starvation and osmolarity. These stimuli are detected by receptors and transmitted to the effector molecules leading to signal transduction pathways. The information is transmitted through the conformational changes of molecules, such as phosphorylation [30,288]. Due to the fact that *C. glabrata* has to survive in more extreme changes in external conditions, evolutionary it has developed better adaptation mechanisms. It was reported that comparing to *S. cerevisiae*, *C. glabrata* is more tolerant to osmotic stress [45].



The cell senses changes in osmotic pressure by its transmembrane mechanoreceptors. In yeast the receptors are presented by Sho1 and Sln1 sensors [289]. They are located on the cell membrane. The receptors activate intracellular signalling pathways by phosphorylation of MAP kinases (MAPK). The MAPK form important modules, each of them consists of three kinases: a MAPK kinase kinase (MAPKKK), a MAPK kinase (MAPKK), and a MAPK. The mechanism of their activation is based on sequential phosphorylation of each level in the MAPK cascade [290]. This multilevel structure of the MAPK cascade leads to amplification of signal and attenuation of noise [58,59]. In *S. cerevisiae* and *C. glabrata* Ste11 serves as MAPKKK, Ste7 and Pbs2 as MAPKK and Fus3, Kss1, Hog1 as MAPK [291].

The osmo-adaptation pathway contains two branches: Sho1 and Sln1. Both branches split at the shared MAPKK, Pbs2. In the Sln1 branch a transmembrane (TM) Sln1 kinase serves as an osmosensor. The signal is transmitted through Sln1, Ypd1, Ssk1 by a multistep phosphorelay mechanism, which implies the direct transfer of a phosphate group and inhibition of Ssk2/Ssk22 [292]. It was shown that Ssk2 is presented in both *S. cerevisiae* and *C. glabrata* species whereas Ssk22 only in *S. cerevisiae* [293]. Under the hyper-osmotic stress Sln1 is inhibited and this leads to the activation of Ssk2 and Hog1 activation [289]. In Sho1 branch another TM protein named Sho1 initiates the signalling through the MAPK module, which includes Ste11, Pbs2 and Hog1 [289]. Hog1 is phosphorylated on two sites, Thr-174 and Tyr-176, and regulates osmo-adaptation genes in the nucleus [51,294]. It was shown that the mechanism of multisite phosphorylation of Pbs2 and Hog1 is sequential [53,295]. Dephosphorylation of these sites is necessary for Hog1 inactivation. There are several phosphatases known as negative regulators of the Hog1 pathway: Ptc2, Ptp2 and Ptp3 [296,297].

In the nucleus the activated MAPKs start the transcriptional programme required for the completion of the stress response by associating via specific transcription factors and stimulating gene expression [298]. To adapt to high osmotic stress, the downstream component Hot1 targets Hog1 to specific

osmostress-responsive promoters and regulates Hog1 responsive genes. Anchoring of active Hog1 to promoters by Hot1 is crucial for RNA Polymerase (Pol) II activation [299]. The completed Hog1 pathway response to osmotic stress includes the production of osmotically active glycerol, which compensates the difference in osmotic pressures [33].

Glycerol is one of the main osmolytes in the cell [300]. The cell regulates the concentration of glycerol not only by its production under the hyper-osmotic stress but also by its efflux under the hypo-osmotic stress in order to rapidly decrease the concentration of osmotically active compounds inside the cell and prevent the cell from bursting [301]. The transport of glycerol is performed by glycerol Fps1 channels. These membrane channels are open when Fps1 and Hog1 are non-phosphorylated [302].

Glycerol is produced from the glucose [303,304]. Intracellular glucose can be increased due to the glucose uptake from extracellular media across the cell membrane [305,306] and also by a conversion from osmotically inactive glycogen [307]. Glucose and glycerol serve as an intracellular resource to adapt to hyper-osmotic stress. The transformation from glycogen is performed by the phosphorylated glycogen phosphorylase (Gph) while the reverse transformation from glucose to glycogen is supported by non-phosphorylated glycogen synthase (Gsy) [308,309]. The phosphorylation of Gsy and Gph is performed by protein kinase A (PKA) [310,311].

Now consider the above explained biological details using functional representation (Figure 1.1). Figure 5.1 illustrates the functional diagram of the yeast adaptation to osmotic stress, which can be "informally" described as follows. The yeast cell receives the stress signal and processes it. Depending on the type of the signal, namely hyper- or hypo- osmotic stress, the cell performs a certain functional programme to adapt to it. In case of hyper-osmotic stress the cell increases the concentration of intracellular osmotically active compounds using its resource (intracellular glycerol, glucose), which was accumulated when the cell was in the resting, free-from-stress state. In contrast, when the cell is exposed to hypo-osmotic stress, it tends to decrease the

concentration of intracellular osmotically active compounds. The regulation of the concentration of osmotically active compounds inside the cell allows compensation the difference in osmotic pressures and, as a result, adaptation to osmotic stress. Once the adaptation is completed the cell sends the signal to the Reception functional block that cancels the adaptation program.

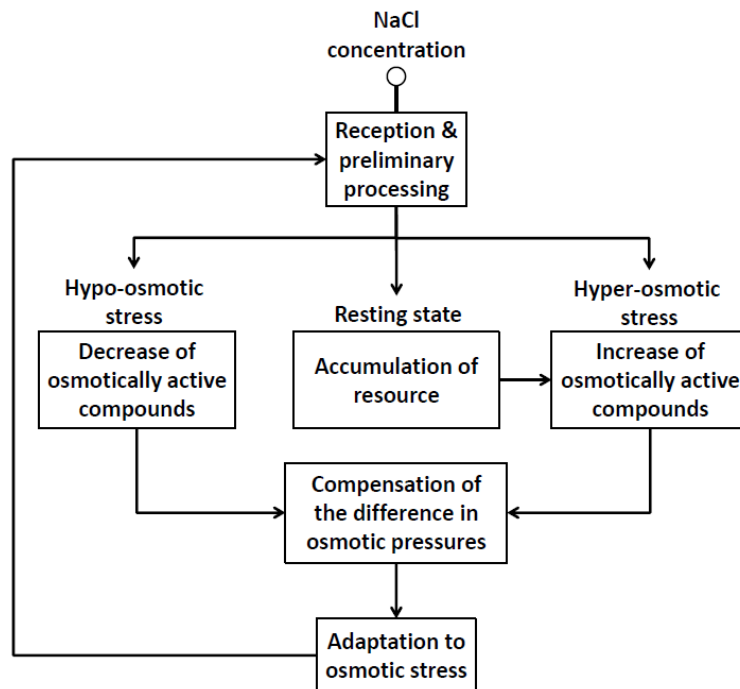


Figure 5.1. Functional diagram for the yeast adaptation to osmotic stress. This diagram shows the functions that the yeast cell tends to complete in order to adapt to osmotic stress.

Current *C. glabrata* treatment includes the use of boric acid, nystatin (NYST), Amphotericin B (AMB) and azoles including fluconazole (FLU) and itraconazole (ITRA) [281]. However it was established that *C. glabrata* is resistant to azole drugs and AMB [312,313]. Another problem associated with the currently used therapies is their adverse side effects. It was reported that boric acid is potentially toxic [281] and AMB may lead to renal dysfunction [314]. Therefore, there is a real need for an alternative, more effective therapies against *C. glabrata*. Mathematical modelling of the yeast adaptation to osmotic stress may reveal conditions, under which the pathogen yeast become more vulnerable and thus help the treatment.

### 5.1.2 Modelling review

The adaptation properties of *S. cerevisiae* to osmotic stress have been extensively studied using both computational modelling and experimental data in recent years [47-57]. Some early works were focused only on MAPK cascade and its properties because it was not clear how the osmotic stress activates the MAPK cascade. The studied properties included ultrasensitivity, multistability and oscillations [53-57]. Other studies extended this approach by adding possible feedback mechanisms and included the receptor systems that lead to the activation of Hog1 through the MAPK cascade [51,52]. However consideration of the ubiquitous MAPK cascade alone and with the receptor systems cannot fully explain the mechanism of adaptation due to the fact that it does not include such important physical parameters as the cell volume, turgor pressure and osmolytes concentration. These parameters are vital for the yeast cell survival under the osmotic stress conditions [33,315].

To extend the knowledge of osmo-adaptation mechanisms in *S. cerevisiae*, mathematical models were developed for investigation of the Hog1 response to fluctuating osmotic stress [49,50]. However, these models used simplified description of Hog1 pathway activation, i.e. not all of the proteins were presented, for example Sho1 pathway was absent. This makes it impossible to test the models under various mutations in the pathways (for instance, Ssk2 knock-down).

In order to understand deeper the underlying molecular mechanisms of Hog1 signalling pathway activation and downregulation in adaptation of the yeast to osmotic stress, next studies included both biochemical and biophysical regulation. One of the most detailed mathematical models of osmo-regulation in *S. cerevisiae* was presented in [48]. This model contains 70 parameters and 35 ordinary differential equations (ODEs) plus 2 algebraic equations to provide a plausible description of the mechanisms underlying the adaptation of yeast to hyper-osmotic stress. Despite the detailed description and good fitting to the experimental data this detailed model is rather difficult to analyse due to a high number of parameters. Moreover, the results from [48] seem to be not

reproducible, see <http://www.lancs.ac.uk/~winterh/biologyCS.pdf>, which is also consistent with our own attempts. To overcome the issues related to the complexity of the model published in [48], Gennemark in [47] offered a simplified version of the model [48] that demonstrates the essential biochemical and biophysical properties. This model consists of only 10 parameters, 4 ODEs and 3 algebraic equations. Thus, in this chapter we chose the Gennemark model [47] as the basis for our new model. The Gennemark model will be described in more detail in the next section. We stress here that our development of [47] concerns completely different aspects than the simplification of [47] compared to [48].

Mathematical modelling of *S. cerevisiae* adaptation to osmotic stress has contributed to a better understanding of the underlying molecular mechanisms and architecture of the yeast. The models developed in [47-57] demonstrated a good fit to the experimental observations. However, despite the close relation between *S. cerevisiae* and *C. glabrata*, these models have limitations in application to *C. glabrata* adaptation to osmotic stress. The current models can only describe the adaptation of the yeast to hyper-osmotic stress, however it is also important to understand how *S. cerevisiae* and *C. glabrata* adapt to hypo-osmotic stress conditions. Previously published models [47-57] lack the detailed biochemical description of the MAPK pathway activation and glycerol metabolism, which limits the investigation of the yeast viability under the osmotic stress conditions. The simplified description of MAPK pathways activation also does not allow to test them in the case of mutations in the pathways.

## 5.2 Gennemark model

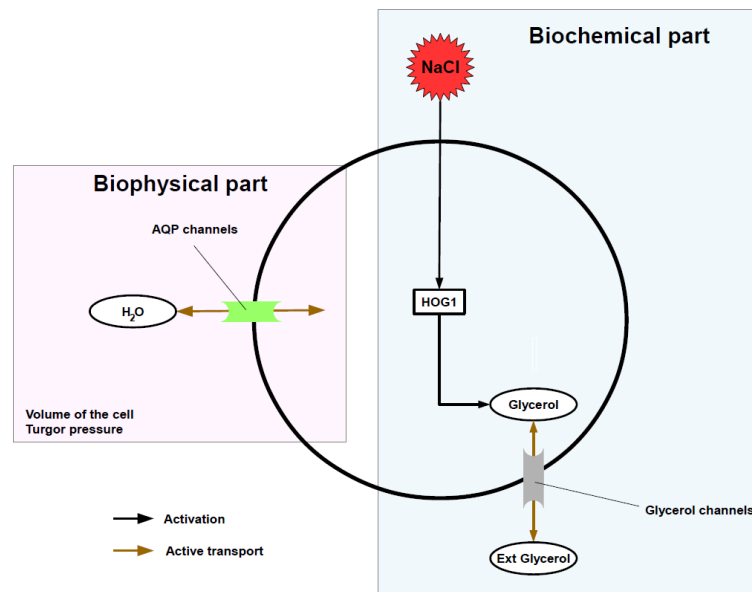


Figure 5.2. Schematic diagram for the model developed by Gennemark. This model includes simplified biochemical and biophysical regulation.

Figure 5.2 schematically shows the structure of the model developed by Gennemark in [47]. It consists of biophysical and biochemical parts. The biophysical part describes the volume of the cell and turgor pressure. The biochemical parts describes Hog1 activation and glycerol metabolism modules. The model proposed by Gennemark is relatively simple and easy to understand but it lacks the following structural details. First, the interactions between the components of the model were described by proportional control functions rather than by molecular reactions. This makes the model simpler but at the same time less physiologically meaningful. Second, the lack of the detailed MAPK cascade in [47] makes it impossible to test the model for various mutations in the pathways. Third, the lack of glucose and other components (glycogen, glycogen synthase, glycogen phosphorylase) in the glycerol metabolism module limits the testing of the model for different external glucose concentrations. Later in this chapter, we will show why these details are important for the yeast adaptation to osmotic stress.

The cell membrane is permeable to water and glycerol. In the normal conditions, in equilibrium, the concentration of osmotically active elements inside the cell is higher than the concentration of NaCl outside the cell. This difference is compensated by the turgor pressure, which represents a mechanical pressure based on membrane's mechanical properties. Under osmotic stress, the cell tends to maintain both the volume and the turgor pressure that are characteristic of the equilibrium [47,48].

In [47], the change of the volume  $V$  of the cell due to the water efflux and influx was described as follows:

$$Q = \frac{dV}{dt} = k_{p1} \cdot (\Pi^i - \Pi^e - \Pi^t), \quad (5.1)$$

where  $k_{p1}$  is the hydraulic water permeability constant,  $\Pi^i$  is the intracellular,  $\Pi^e$  is the extracellular and  $\Pi^t$  is the turgor osmotic pressures.

The following equation can be obtained from Equation (5.1) in equilibrium:

$$\Pi_0^i = \Pi_0^e + \Pi_0^t, \quad (5.2)$$

where  $\Pi_0^i$  is the intracellular,  $\Pi_0^e$  is the extracellular and  $\Pi_0^t$  is the turgor osmotic pressures in equilibrium.

The intracellular osmotic pressure was calculated as:

$$\Pi^i = \frac{n + gly}{v - v_b}, \quad (5.3)$$

where  $gly$  is the concentration of glycerol,  $n$  is the concentration of other osmotically active elements in the cell, which was assumed constant, and  $v_b$  is the non-osmotic volume of the cell.

The turgor pressure was described as follows:

$$\Pi^t = \begin{cases} \Pi_0^t \cdot \frac{v - v_p}{v_0 - v_p}, & v > v_p \\ 0, & \text{otherwise,} \end{cases} \quad (5.4)$$

where  $\Pi_0^t$  is the turgor pressure in equilibrium and  $v_p$  is the volume of the cell when  $\Pi^t = 0$ .

The difference between the equilibrium turgor pressure and the current turgor pressure was written as:

$$u = \Pi_0^t - \Pi^t. \quad (5.5)$$

The activation of Hog1 was described in [47] by the following ODE:

$$\frac{dU_{p_{hog}}}{dt} = \frac{1}{t_d} \cdot (U_{hog} - U_{p_{hog}}), \quad (5.6)$$

where  $t_d$  is the time delay,  $U_{hog} = k_{hog} \cdot u$ ,  $k_{hog}$  is the proportional control constant.

The concentration of the intracellular glycerol was described as follows:

$$\frac{dgly}{dt} = U_{p_{hog}} - U_{diff}, \quad (5.7)$$

where  $U_{diff} = U_{fps1} \cdot \left( \frac{gly}{v - v_b} - \frac{gly_e}{v - v_e} \right)$ ,  $gly_e$  is the concentration of extracellular

glycerol,  $v_e$  is the extracellular volume,  $U_{fps1} = k_{p2} \cdot \frac{\Pi_0^t - u}{\Pi_0^t}$  when  $u > 0$  or

$U_{fps1} = k_{p2}$  when  $u \leq 0$  and  $k_{p2}$  is the glycerol permeability coefficient.



The concentration of the external glycerol can be described as follows:

$$\frac{dgly_e}{dt} = U_{diff}. \quad (5.8)$$

Next we analyse the Gennemark model predictions in response to hyper-osmotic stress signal shown in Figure 5.3. We test the model predictions under NaCl concentration of 1M, which corresponds to  $\Pi^e = 2 \text{ Osm}$ , applied at time 0 and maintained during the experiment. Before the time point  $t = 0 \text{ min}$  the cell was assumed to be in equilibrium. The parameter values are taken from the paper published by Gennemark et al [47]:  $k_{p1} = 1 \text{ Osm}^{-1}$ ,  $\Pi_0^i = 0.636 \text{ Osm}$ ,  $\Pi_0^e = 0.24 \text{ Osm}$ ,  $v_b = 0.368$ ,  $gly_0 = 0.0002$ ,  $v_p = 0.99$ ,  $k_{p2} = 0.316$ ,  $v_e = 4790$ ,  $k_{nog} = 0.416 \text{ Osm}^{-1}$ ,  $t_d = 8.61 \text{ min}$ . Here and anywhere further, the parameters without a dimension are values of the parameters after a certain non-dimensionalisation, the details of which can be found in [47].

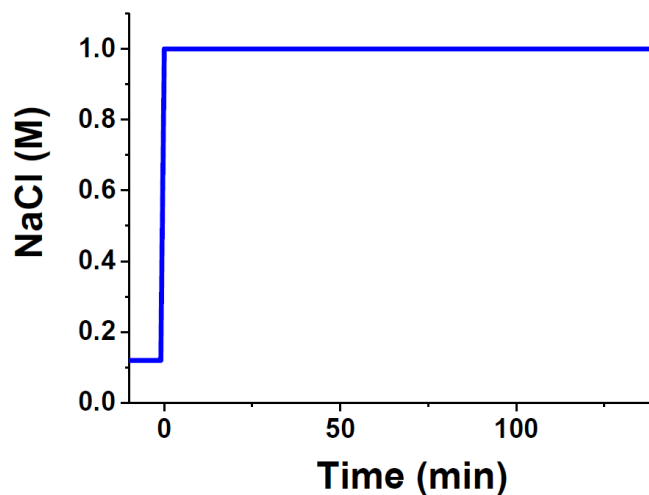


Figure 5.3. Hyper-osmotic NaCl signal as a function of time. The Gennemark model is tested under 1M of NaCl. The concentration of 1.5M is applied after  $t = 0 \text{ min}$  and maintained during the experiment.

Figure 5.4 schematically shows the Gennemark model [47] predictions for yeast cell under hyper- and hypo-osmotic stress. The quantitative predictions are

shown in Appendix D (Figures 7.4-7.6). The analysis of the Gennemark model allowed us to suggest that there are two possible types of the hyper-osmotic stress: strong and mild.

When  $\Pi^e > \Pi_0^i$ , which corresponds to the strong hyper-osmotic stress (Figure 5.4), the first reaction of the system is a decrease in turgor pressure down to zero (Figure 7.4D in Appendix D). Water starts to come out of the cell through the aquaporin channels since there is a gradient in concentrations, which leads to the cell shrinking (Figure 7.4A). At the same time, since  $u > 0$ , Hog1 becomes phosphorylated and thereby activated (Figure 7.4B). As Fps1 channels are closed in this case, glycerol is being accumulated in the cell and increases the total concentration of osmotic active elements inside the cell. These processes continue until  $\Pi^i$  exceeds  $\Pi^e$ . It leads to the effect that the water flow changes its direction from efflux to influx and this continues until the cell restores its initial volume. Then the water channels close and glycerol channels remain to be closed but the glycerol keeps accumulating (Figure 7.4C) since  $u$  is still positive. The glycerol accumulation should stop when the cell restores its initial volume and turgor pressure. The restore of the initial volume and turgor pressure is vital for the cell adaptation to osmotic stress [47,48]. However in the Gennemark model the turgor pressure does not return to its equilibrium level (Figure 7.4D). Moreover in this model Hog1 phosphorylation increases in response to the osmotic stress but does not come down to its equilibrium level (Figure 7.4B), which contradicts experimental observations [316].

When  $\Pi_0^e < \Pi^e < \Pi_0^i$ , which corresponds to the mild hyper-osmotic stress (Figure 5.4), the system works to decrease the turgor pressure to its equilibrium level  $\Pi_0^t$ . The volume of the cell remains at the same level (Figure 7.5A). Then, since  $u > 0$  in this case, phosphorylated Hog1 activates glycerol production (Figure 7.5C). This is supported by the closing of Fps1 glycerol channels, and glycerol starts to accumulate inside the cell. Again, in this case the turgor pressure (Figure 7.5D) and phosphorylated Hog1 (Figure 7.5B) do not return to

their equilibrium level.

When the cell is exposed to hypo-osmotic stress (for instance, the rain in nature), which implies that the concentration of NaCl outside the cell and thereby  $\Pi^e$  become less than it was initially (Figure 5.4), the system reacts by an increase in the turgor pressure since the concentration of osmotically active elements inside the cell cannot be changed instantaneously (Figure 7.6D). In this case the difference in the turgor pressure, compared to the equilibrium, is negative:  $u < 0$ . This should serve as a signal for opening Fps1 glycerol channels and glycerol efflux out of the cell. However in Gennemark model the glycerol efflux is not observed (Figure 7.6C) and therefore the turgor pressure does not return to its equilibrium level. The lack of the glycerol efflux contradicts the experiments from [317].

Thus the model developed by Gennemark in [47] lacks the structural details mentioned above and gives the model predictions that contradict the experiments for Hog1 phosphorylation and turgor pressure [48,316] as well as the glycerol efflux under the hypo-osmotic stress [317]. Considering these facts, next we will modify the model by Gennemark [47] to overcome the above mentioned issues.

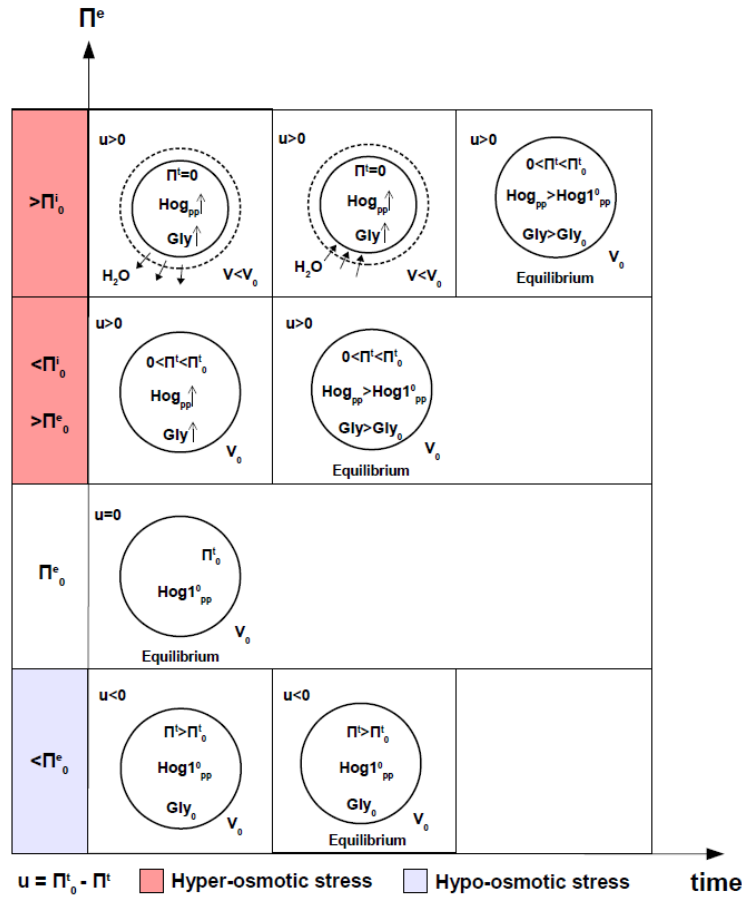


Figure 5.4. Schematic representation of the yeast cell adaptation to osmotic stress by the Gennemark model.

According to the model developed by Gennemark in [47], the cell demonstrates different types of behaviour in response to different types of osmotic shock: strong hyper- ( $\Pi^e > \Pi_0^i$ ), mild hyper- ( $\Pi_0^e < \Pi^e < \Pi_0^i$ ) and hypo- osmotic ( $\Pi^e < \Pi_0^e$ ) shock. See Equations (5.1)-(5.8) with parameters  $k_{p1} = 1 \text{ Osm}^{-1}$ ,  $\Pi_0^i = 0.636 \text{ Osm}$ ,  $\Pi_0^e = 0.24 \text{ Osm}$ ,  $v_b = 0.368$ ,  $gly_0 = 0.0002$ ,  $v_p = 0.99$ ,  $k_{p2} = 0.316$ ,  $v_e = 4790$ ,  $k_{hog} = 0.416 \text{ Osm}^{-1}$ ,  $t_d = 8.61 \text{ min}$  taken from [47].

### 5.3 Aims and objectives of this chapter

In this chapter we consider the second (after Chapter 4) example of high-level analysis (in terms of Figure 1.1) investigating the yeast adaptation to osmotic stress. The main aim of this chapter is to build a new model for *C. glabrata* adaptation to both hyper- and hypo- osmotic stress starting from the model developed by Gennemark [47]. The new model should:

- describe the biochemical reactions involved in the osmotic regulation,

- include the detailed Hog1 activation and glycerol metabolism modules,
- demonstrate the consistency with the previously published experiments,
- describe the adaptation under mutations in the pathways (Ssk2 knock-down),
- fit the experimental observations provided by Professor Ken Haynes' group,
- make predictions with a potentially clinical use.

It should be mentioned that in this chapter, where referred to experiments, all experimental data were collected by Emily Cook from Professor Ken Haynes' group in Biosciences, University of Exeter. The permission to use the experimental data in this thesis is attached in Appendix E. The experimental data will be used to validate our model.

## **5.4 A new systems model for *C. glabrata* adaptation to osmotic stress**

In this section we describe the details of our proposed model for the molecular interactions that regulate adaptation of *C. glabrata* to osmotic stress. We will improve the model proposed by Gennemark in [47] and introduce the newly added assumptions one by one, identifying the effects of each of the newly added assumptions. We will refer these newly added assumptions as modification to the Gennemark model. It should be noted that in this section we focus on qualitative rather than quantitative results. The quantitative analysis of the developed model will be performed in the next Section 5.5.

### **5.4.1 Modification 1 of the biophysical part**

In this subsection we will introduce modification of the biophysical part of the Gennemark model [47] and see the effects of this modification to the results produced by the model.

The volume  $V$  of the cell changes due to the water efflux and influx through aquaporin channels (AQPs). The rate of the volume change is a flow of water  $Q$  through the membrane, which can be represented as follows:

$$Q = \frac{dV}{dt} = A \cdot L \cdot (\Pi^i - \Pi^e - \Pi^t), \quad (5.9)$$

where  $A$  is a surface of the cell in  $\text{m}^2$ ,  $L$  is hydraulic water permeability of the cell in  $\text{m} \cdot \text{s}^{-1} \cdot \text{Pa}^{-1}$ ,  $\Pi^i$  is the internal osmotic pressure,  $\Pi^e$  is the external osmotic pressure and  $\Pi^t$  is the turgor pressure, in Pa [48].

According to the Boyle-Van't Hoff relation [318] the osmotic pressure can be written as follows:

$$\Pi = RT \frac{W}{V}, \quad (5.10)$$

where  $R$  is the universal gas constant,  $T$  is temperature,  $W$  is the number of moles of osmotically active compounds inside the cell and  $V$  is the cell volume. We can rewrite Equation (5.9) using Equation (5.10) in the following way:

$$\frac{dV}{dt} = A \cdot L \cdot (RT ([Osm] - [NaCl]) - \Pi^t), \quad (5.11)$$

where  $[Osm]$  and  $[NaCl]$  are the molar concentrations of the osmotic active elements inside and salt outside the cell, respectively, in M.

The concentration of the osmotic active elements inside the cell is given by:

$$[Osm] = \frac{N}{V - V_b} + [Gly], \quad (5.12)$$

where  $N$  is the number of moles of osmotically active elements except glycerol,  $[Gly]$  is the concentration of intracellular glycerol,  $V_b$  is the volume of osmotically inactive elements. We assume that  $N$  and  $V_b$  are constant, which is consistent with [47,48].

There is no water flow through the membrane in equilibrium, therefore it can be written for the equilibrium turgor pressure:

$$\Pi_0^t = \Pi_0^i - \Pi_0^e = RT ([Osm_0] - [NaCl_0]), \quad (5.13)$$

where  $\Pi_0^i$ ,  $\Pi_0^e$  and  $\Pi_0^t$  are internal, external osmotic and turgor pressures in equilibrium, respectively.  $[Osm_0]$  and  $[NaCl_0]$  are molar concentrations of the osmotic active elements inside and salt outside the cell in equilibrium, respectively.

The cell wall is elastic and the volumetric elastic modulus [319] is given by:

$$\varepsilon = V \frac{d\Pi^t}{dV}. \quad (5.14)$$

It is assumed that  $\varepsilon$  is a constant. Thus the turgor pressure is given by:

$$\Pi^t = \Pi_0^t + \varepsilon \cdot \ln\left(\frac{V}{V_0}\right). \quad (5.15)$$

We assume here that the turgor pressure cannot be negative and is equal to zero under plasmolysis, which is also consistent with [47]:

$$\Pi^t = \max\left(0, \Pi_0^t + \varepsilon \cdot \ln\left(\frac{V}{V_0}\right)\right). \quad (5.16)$$

Instead of Equation (5.5) we use the following equation for the difference between the initial and current turgor pressures:

$$u = \Pi_0^t - \Pi^t = \min\left(\Pi_0^t, \varepsilon \cdot \ln\left(\frac{V_0}{V}\right)\right). \quad (5.17)$$

We also denote by  $H(u) = H\left(\min\left(\Pi_0^t, \varepsilon \cdot \ln\left(\frac{V_0}{V}\right)\right)\right) = H(V_0 - V)$  the Heaviside

function  $H(u) = \begin{cases} 1, & \text{if } u > 0 \\ 0, & \text{if } u \leq 0 \end{cases}$ . Due to the fact that under the hyper-osmotic stress

the volume decreases, we will further use  $U(V, u) = u(V) \cdot H(u)$ .

Therefore, the rate of the volume change can be written as follows:

$$\frac{dV}{dt} = A \cdot L \cdot \left( RT \left( \frac{N}{V - V_b} + [Gly] - [NaCl] \right) - \max \left( 0, \Pi_0^t + \varepsilon \cdot \ln \left( \frac{V}{V_0} \right) \right) \right). \quad (5.18)$$

Equation (5.18) can be written in non-dimensional form as follows:

$$\frac{dv}{dt} = K \cdot \left( RT \left( \left( \frac{n}{v - v_b} + gly \right) \cdot Km_{16} - [NaCl] \right) - \max \left( 0, \Pi_0^t + \varepsilon \cdot \ln(v) \right) \right) \quad (5.19)$$

where  $Km_{16}$  will be introduced later in Equation (5.25),  $v = \frac{V}{V_0}$ ,  $v_b = \frac{V_b}{V_0}$ ,  $K = \frac{A \cdot L}{V_0}$

and  $n = \frac{N}{V_0 \cdot Km_{16}}$ .

It should be noted that the other equations and parameters for the biochemical part, including Hog1 phosphorylation and glycerol, for now remain the same as in the Gennemark model (Equations (5.6), (5.7) and (5.8) respectively). However, in order to keep the same dimension in Equation (5.6) for Hog1 phosphorylation, we need to write  $U_{hog} = 2k_{hog} \cdot \frac{u}{RT}$  instead of  $U_{hog} = k_{hog} \cdot u$  since  $u$  now, as shown in Equations (5.17) and (5.9), has a dimension of Pa and not Osm.



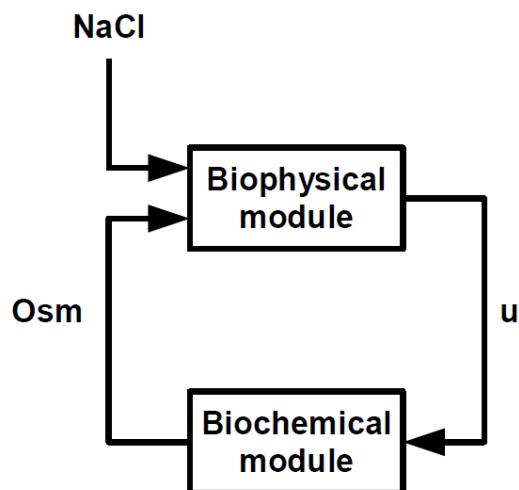


Figure 5.5. Functional link between the biophysical and biochemical parts of the proposed model.

External NaCl concentration and the intracellular concentration of osmotically active compounds (denoted by  $O_{sm}$ ) serve as input signals for the biophysical module that produces its output signal  $u$ , which is the difference between the initial and current turgor pressures. The  $u$ , in turn, serves as an input for the biochemical module. In equilibrium there are no changes in both biophysical and biochemical modules. When the concentration of salt changes, the system starts the adaptation mechanism and returns to a new equilibrium.

The structure of our new biophysical part suggests the functional link between the biophysical and biochemical parts and how they interact. This link is schematically represented in Figure 5.5. The NaCl concentration serves as an input signal to the biophysical module along with the concentration of osmotically active elements inside the cell that serves as an output of the biochemical part. The output of the biophysical module is  $u$  that serves as an input for the biochemical module. The concentration of NaCl in equilibrium makes no change to the biophysical module. In equilibrium there is no change in turgor pressure and therefore the difference between the initial and current turgor pressures is  $u=0$ , which serves as a zero-signal to the biochemical module. This allows calculating the equilibrium state of the biochemical module and obtaining the equilibrium concentration of phosphorylated Hog1 and osmotically active elements inside the cell. Under osmotic stress the biophysical

module returns  $u \neq 0$ . This  $u$  causes the activation of the biochemical module, which in turns leads to either production of osmotically active elements under hyper-osmotic stress or glycerol efflux through the glycerol channels under the hypo-osmotic stress. The changes in biochemical part lead to the changes in biophysical part and thereby in  $u$ . After some time the system returns to a new equilibrium characterised by  $u = 0$ . Thus the system should now adapt to the change in NaCl concentration and return to the equilibrium state.

We test the effect of the newly added assumptions using the following parameter values:  $R = 8.31 \text{ kPa} \cdot \text{M}^{-1} \cdot \text{K}^{-1}$ ,  $T = 300 \text{ K}$ ,  $A \cdot L = 86 \cdot 10^{-3} \text{ min}^{-1} \cdot \text{kPa}^{-1}$ ,  $V_0 = 6.5 \cdot 10^{-14} \text{ L}$  are taken from [48],  $\varepsilon = 1 \cdot 10^5$  from [320],  $Km_{16} = 0.6 \text{ M}$ ,  $[NaCl_0] = 0.175 \text{ M}$  are the parameters values selected "by hand" in order to obtain the expected qualitative behaviour.

Figure 5.6 schematically illustrates the model predictions for the newly added assumptions. The quantitative results can be found in Appendix D (Figures 7.7-7.9). With the chosen parameters, there is no qualitative difference between the model predictions compared to the Gennemark model illustrated in Figure 5.4. The difference between this version of the model and the Gennemark model is that the modified model now describes separately the concentrations of NaCl and osmotically active elements inside the cell, rather than simply the internal and external osmotic pressures. The turgor pressure is now described by  $P_a$  and reflects the fact that it is a mechanical pressure. However, as it was in the Gennemark model, the cell does not restore its equilibrium Hog1 phosphorylation level (Figures 7.7B and 7.8B) and turgor pressure (Figures 7.7D and 7.8D) under hyper-osmotic stress. Moreover, under the hypo-osmotic conditions, there is still no glycerol efflux (Figure 7.9C) and the turgor pressure does not restore (Figure 7.9D). Due to these drawbacks and to the lack of details in the glycerol metabolism module, we will next make changes to the glycerol metabolism module.

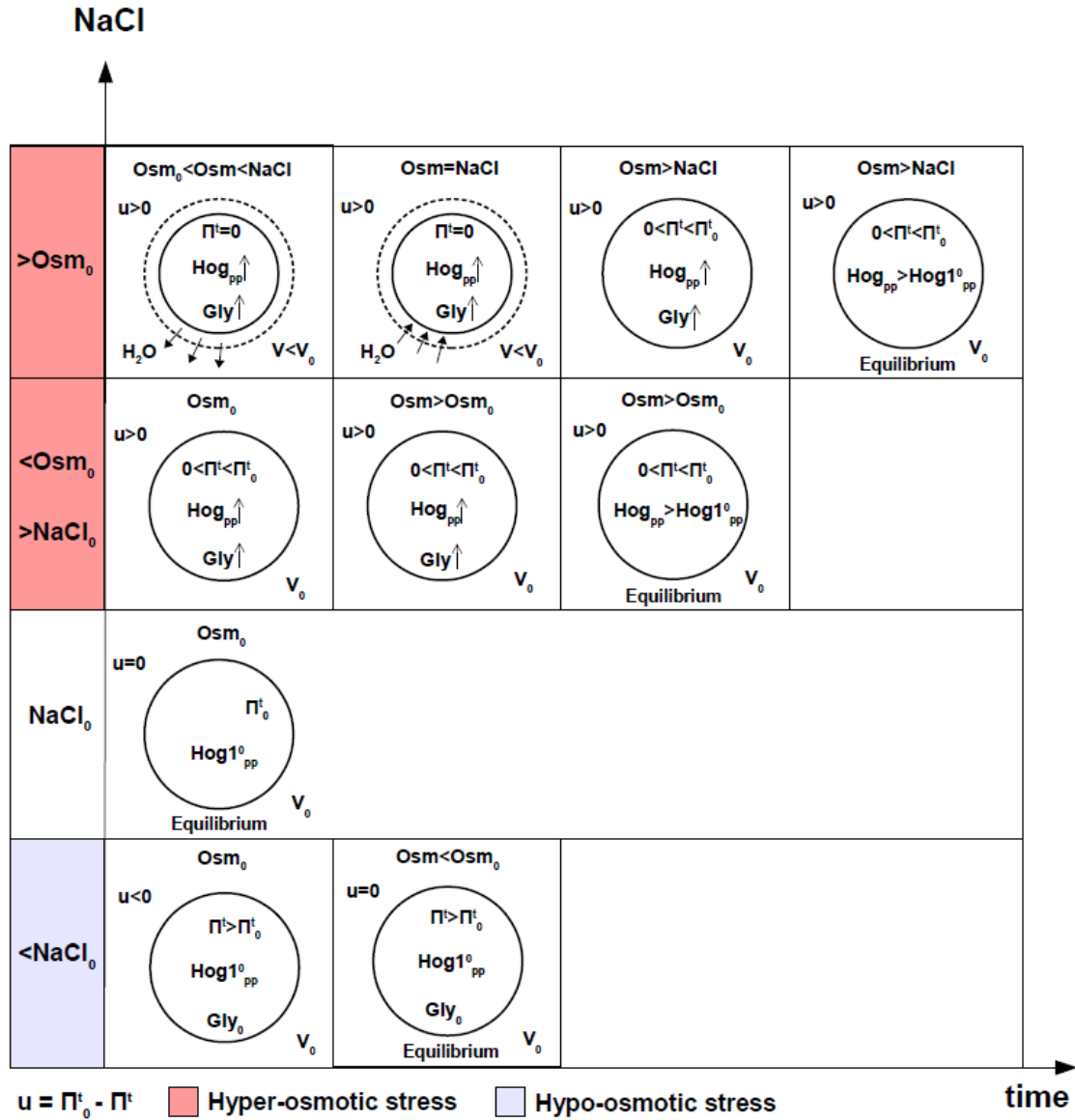


Figure 5.6. Schematic representation of the yeast cell adaptation to osmotic stress after the introduction of modified biophysical part of the Gennemark model.

While the model still demonstrates the volume recovery and glycerol accumulation, it now shows the restore of the turgor pressure and Hog1 phosphorylation level under the hyper-osmotic stress. However, there is still a lack of glycerol efflux and the restore of the turgor pressure under the hypo-osmotic stress. See Equations (5.6)-(5.19) with parameters  $R = 8.31 \text{ kPa} \cdot \text{M}^{-1} \cdot \text{K}^{-1}$ ,  $T = 300 \text{ K}$ ,  $A \cdot L = 86 \cdot 10^{-3} \text{ min}^{-1} \cdot \text{kPa}^{-1}$ ,  $V_0 = 6.5 \cdot 10^{-14} \text{ L}$ ,  $\varepsilon = 1 \cdot 10^5$ ,  $Km_{16} = 0.6 \text{ M}$ ,  $[NaCl_0] = 0.175 \text{ M}$ ,  $v_b = 0.368$ ,  $gly_0 = 0.0002$ ,  $k_{p2} = 0.316$ ,  $v_e = 4790$ ,  $k_{hog} = 0.416 \text{ Osm}^{-1}$ ,  $t_d = 8.61 \text{ min}$ .

### 5.4.2 Modification 2 of the glycerol metabolism module

In this subsection we will introduce modified glycerol metabolism module in order to overcome the issues raised in the previous subsection. Figure 5.7 schematically shows the modified glycerol metabolism module in the structure of the model. We assume here that osmotic stress causes the activation of PKA through a mechanoreceptor MchR2. Dephosphorylation of phosphorylated Gsy and Gph is performed by PP-1 phosphatase [321,322].

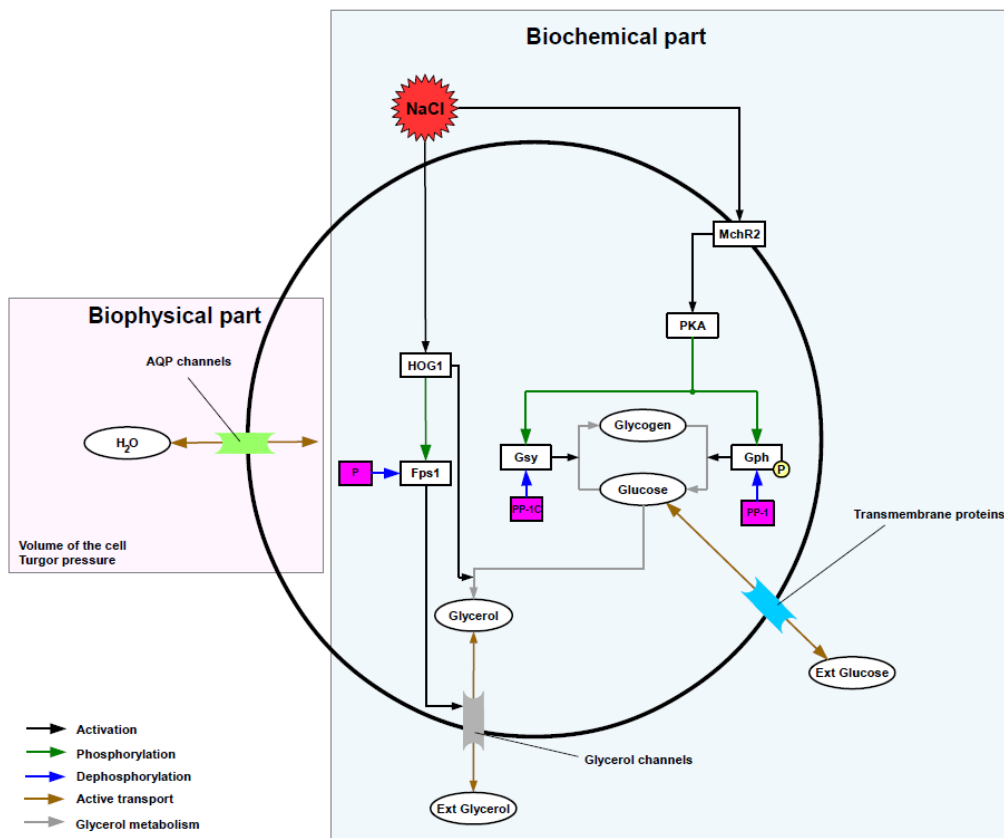


Figure 5.7. The structure of the new model after the introduction of the modified glycerol metabolism module.

In yeast adaptation properties are regulated by the intracellular production of osmotically active glycerol. Glycerol is activated through the signalling pathways that are activated in response to the change in salt concentration and thereby, turgor pressure. The glycerol efflux from the cell is regulated by the glycerol Fps1 channels.

Due to the fact that concentration depends on the volume and that the cell volume changes under the plasmolysis [48], we now introduce the following term:

$$D(V) = \frac{1}{V - V_b} \cdot \frac{dV}{dt}. \quad (5.20)$$

We assume that the phosphorylation and dephosphorylation of glycogen synthase (Gsy) as well as glycogen phosphorylase (Gph) are performed by hypothetical kinases  $K_s$ ,  $K_p$  and phosphatases  $P_s$ ,  $P_p$  respectively. For simplicity, we also assume that the formation of enzyme-substrate complexes is much faster than the phosphorylation reactions and therefore we can use the QSSA, which is in line with [57,186]. Using Equations (3.48) from Chapter 3, the rates of phosphorylation of Gsy and Gph can be written as follows:

$$\begin{aligned} \frac{d[Gsy_p]}{dt} &= k_{s1} \cdot k_r \cdot (U(V, u) + L_1) \cdot \frac{K_{sT}}{V - V_b} \cdot \frac{[Gsy]}{K_{m11} + [Gsy]} - k_{s2} \cdot \frac{P_{sT}}{V - V_b} \cdot \frac{[Gsy_p]}{K_{m12} + [Gsy_p]} - \\ &\quad - [Gsy_p] \cdot D(V), \quad (5.21) \\ \frac{d[Gph_p]}{dt} &= k_{p3} \cdot k_r \cdot (U(V, u) + L_2) \cdot \frac{K_{pT}}{V - V_b} \cdot \frac{[Gph]}{K_{m13} + [Gph]} - k_{p4} \cdot \frac{P_{pT}}{V - V_b} \cdot \frac{[Gph_p]}{K_{m14} + [Gph_p]} - \\ &\quad - [Gph_p] \cdot D(V), \end{aligned}$$

where  $K_{m11}$ ,  $K_{m12}$ ,  $K_{m13}$ ,  $K_{m14}$  are Michaelis constants,  $K_{sT}$ ,  $K_{pT}$ , are the total amounts of kinases that phosphorylate and  $P_{sT}$ ,  $P_{pT}$  are total amounts of phosphatases that dephosphorylate Gsy and Gph, respectively.  $L_2$  and  $L_3$  represent the basal phosphorylation levels of Gsy and Gph.  $[Gsy]$  and  $[Gph]$  can be found from the conservation equations for the total concentrations below:

$$\begin{aligned} \frac{G_{syT}}{V - V_b} &= [Gsy] + [Gsy_p], \\ \frac{G_{phT}}{V - V_b} &= [Gph] + [Gph_p]. \end{aligned} \quad (5.22)$$

Equations (5.22) can be written in non-dimensional form as follows:

$$\frac{1}{v - v_b} = gsy + gsy_p, \quad (5.23)$$

$$\frac{1}{v - v_b} = gph + gph_p,$$

where  $gsy = \frac{[Gsy]}{Gsy_T} \cdot V_0$ ,  $gsy_p = \frac{[Gsy_p]}{Gsy_T} \cdot V_0$ ,  $gph = \frac{[Gph]}{Gph_T} \cdot V_0$  and  $gph_p = \frac{[Gph_p]}{Gph_T} \cdot V_0$ .

Equations (5.21) can be represented in non-dimensional form:

$$\frac{dgsy_p}{dt} = k_r \cdot (U(v, u) + L_1) \cdot \frac{k_1}{v - v_b} \cdot \frac{gsy}{m_{11} + gsy} - \frac{k_2}{v - v_b} \cdot \frac{gsy_p}{m_{12} + gsy_p} - gsy_p \cdot D(v), \quad (5.24)$$

$$\frac{dgph_p}{dt} = k_r \cdot (U(v, u) + L_2) \cdot \frac{k_3}{v - v_b} \cdot \frac{gph}{m_{13} + gph} - \frac{k_4}{v - v_b} \cdot \frac{gph_p}{m_{14} + gph_p} - gph_p \cdot D(v),$$

where  $k_1 = k_{s1} \cdot \frac{Ks_T}{Gsy_T}$ ,  $k_2 = k_{s2} \cdot \frac{Ps_T}{Gsy_T}$ ,  $k_3 = k_{p3} \cdot \frac{Kp_T}{Gph_T}$ ,  $k_4 = k_{p4} \cdot \frac{Pp_T}{Gph_T}$ ,  $m_{11} = \frac{Km_{11}}{Gsy_T} V_0$ ,

$$m_{12} = \frac{Km_{12}}{Gsy_T} \cdot V_0, \quad m_{13} = \frac{Km_{13}}{Gph_T} \cdot V_0, \quad m_{14} = \frac{Km_{14}}{Gph_T} \cdot V_0.$$

The change in intracellular glucose can be described as follows:

$$\frac{d[Glu]}{dt} = k_{g5} \cdot H([Glu_{ext}] - [Glu]) \cdot \frac{[Glu_{ext}] - [Glu]}{Km_{15} + [Glu_{ext}] - [Glu]} - k_{g6} \cdot [Gsy] \cdot \frac{[Glu]}{Km_{16} + [Glu]} + \quad (5.25)$$

$$+ k_{g7} \cdot [Gph_p] \cdot \frac{[Gln]}{Km_{17} + [Gln]} - k_{g8} \cdot [Z2pp] \cdot \frac{[Glu]}{Km_{18} + [Glu]} - [Glu] \cdot D(V),$$

where  $Glu_{ext}$  is the extracellular glucose [305,306],  $Km_{15}$ ,  $Km_{16}$ ,  $Km_{17}$ ,  $Km_{18}$  are Michaelis constants.

Equation (5.25) can be represented in non-dimensional form:

$$\frac{d}{dt} glu = k_5 \cdot H(glu_{ext} - glu) \cdot \frac{glu_{ext} - glu}{m_{15} + glu_{ext} - glu} - k_6 \cdot gsy \cdot \frac{glu}{1 + glu} + \quad (5.26)$$

$$+ k_7 \cdot gph_p \cdot \frac{gln}{m_{17} + gln} - k_8 \cdot z2_{pp} \cdot \frac{glu}{m_{18} + glu} - glu \cdot D(v),$$

where  $glu = \frac{[Glu]}{Km_{16}}$ ,  $glu_{ext} = \frac{[Glu_{ext}]}{Km_{16}}$ ,  $k_5 = \frac{k_{g5}}{Km_{16}}$ ,  $k_6 = k_{g6} \cdot \frac{Gsy_T}{Km_{16} \cdot V_0}$ ,  
 $k_7 = k_{g7} \cdot \frac{Gph_T}{Km_{16} \cdot V_0}$ ,  $k_8 = k_{g8} \cdot \frac{Z2_T}{Km_{16} \cdot V_0}$ ,  $m_{15} = \frac{Km_{15}}{Km_{16}}$ ,  $m_{17} = \frac{Km_{17}}{Km_{16}}$ ,  $m_{18} = \frac{Km_{18}}{Km_{16}}$ .

The rate of glycogen change is given by:

$$\frac{d[Gln]}{dt} = k_{g6} \cdot [Gsy] \cdot \frac{[Glu]}{Km_{16} + [Glu]} - k_{g7} \cdot [Gph_p] \cdot \frac{[Gln]}{Km_{17} + [Gln]} - [Gln] \cdot D(V). \quad (5.27)$$

Equation (5.27) can be written in non-dimensional form as follows:

$$\frac{d}{dt} gln = k_6 \cdot gsy \cdot \frac{glu}{1 + glu} - k_7 \cdot gph_p \cdot \frac{gln}{m_{17} + gln} - gln \cdot D(v), \quad (5.28)$$

Glycerol is exported from the cell under the hypo-osmotic stress in order to decrease turgor pressure and prevent the cell from bursting. The glycerol export is controlled by the Fps1 channels regulated by phosphorylation of Fps1 and Hog1 proteins [302,323]. We assume that Fps1p is phosphorylated by Hog1 and dephosphorylated by a hypothetical phosphatase  $Pf$ . The Fps1 protein phosphorylation can be described by the following ODE:

$$\frac{d[Fps1p]}{dt} = k_{f9} \cdot [Z2pp] \cdot \frac{[Fps1]}{Km_{19} + [Fps1]} - k_{f10} \cdot \frac{Pf_T}{V - V_b} \cdot \frac{[Fps1p]}{Km_{20} + [Fps1p]} - [Fps1p] \cdot D(V), \quad (5.29)$$

where  $Km_{19}$ ,  $Km_{20}$  are Michaelis constants and  $Pf_T$  is a hypothetical phosphatase that dephosphorylates Fps1,  $[Z2pp]$  is the concentration of the phosphorylated Hog1. The concentration  $[Fps1]$  can be found from the conservation equation for the total concentration of Fps1:

$$\frac{Fps1_T}{V - V_b} = [Fps1] + [Fps1p]. \quad (5.30)$$

We can rewrite Equation (5.30) in non-dimensional form as follows:

$$\frac{1}{v - v_b} = fps1 + fps1_p, \quad (5.31)$$

where  $f_{ps1} = \frac{[Fps1]}{Fps1_T} \cdot V_0$  and  $f_{ps1_p} = \frac{[Fps1_p]}{Fps1_T} \cdot V_0$ .

Equation (5.29) in non-dimensional form is given by:

$$\frac{df_{ps1_p}}{dt} = k_9 \cdot z_{2pp} \cdot \frac{f_{ps1}}{m_{19} + f_{ps1}} - \frac{k_{10}}{v - v_b} \cdot \frac{f_{ps1_p}}{m_{20} + f_{ps1_p}} - f_{ps1_p} \cdot D(v), \quad (5.32)$$

where  $k_9 = k_{f9} \cdot \frac{Z_{2T}}{Fps1_T}$ ,  $k_{10} = k_{f10} \cdot \frac{Pf_T}{Fps1_T}$ ,  $m_{19} = \frac{Km_{19}}{Fps1_T} \cdot V_0$ ,  $m_{20} = \frac{Km_{20}}{Fps1_T} \cdot V_0$ .

The phosphorylated Hog1 translocates to the nucleus and initiates the gene transcription, which in turn leads to the activation of the gene responsible for glycerol production from glucose [303,304]. In our model we assume that the produced glycerol is proportional to the phosphorylated Hog1, which is consistent with [47]. It can be written for the rate of intracellular glycerol change:

$$\frac{d[Gly]}{dt} = k_{g8} \cdot [Z2pp] \cdot \frac{[Glu]}{Km_{18} + [Glu]} - k_{g11} \cdot \bar{U}(V, u) \cdot [Fps1] \cdot [Gly] - [Gly] \cdot D(V), \quad (5.33)$$

where  $k_{g11}$  is the permeability of glycerol channels and  $\bar{U}(V, u) = -u(V) \cdot H(-u)$  represents the fact that the Fps1 channels are open under hypo-osmotic stress and closed under hyper-osmotic stress [302,323].

Equation (5.33) can be represented in non-dimensional form as follows:

$$\frac{dgly}{dt} = k_8 \cdot z_{2pp} \cdot \frac{glu}{m_{18} + glu} - k_{11} \cdot \bar{U}(v, u) \cdot f_{ps1} \cdot gly - gly \cdot D(v), \quad (5.34)$$

where  $k_{11} = \frac{k_{g11} \cdot Fps1_T}{V_0}$ .

The change in extracellular glucose concentration can be described as follows:

$$\frac{d[Glu_{ext}]}{dt} = k_{12} \cdot [Glu_{ext}] - k_{g5} \cdot H([Glu_{ext}] - [Glu]) \cdot \frac{[Glu_{ext}] - [Glu]}{Km_{15} + [Glu_{ext}] - [Glu]} - [Glu_{ext}] \cdot D(V), \quad (5.35)$$

where  $k_{12}$  is the constant for the increase of  $Glu_{ext}$ .



Equation (5.25) can be represented in non-dimensional form:

$$\frac{d}{dt} glu_{ext} = k_{12} \cdot glu_{ext} - k_5 \cdot H(glu_{ext} - glu) \cdot \frac{glu_{ext} - glu}{m_{15} + glu_{ext} - glu} - glu_{ext} \cdot D(v). \quad (5.36)$$

Next we test the newly introduced assumptions using the following parameter values:

$k_1 = 0.005 \text{ kPa}^{-1} \cdot \text{min}^{-1}$ ,  $k_2 = 0.1 \text{ min}^{-1}$ ,  $k_3 = 0.2 \text{ kPa}^{-1} \cdot \text{min}^{-1}$ ,  $k_4 = 0.02 \text{ min}^{-1}$ ,  
 $k_5 = 0.03 \text{ min}^{-1}$ ,  $k_6 = 0.003 \text{ min}^{-1}$ ,  $k_7 = 15 \text{ min}^{-1}$ ,  $k_8 = 1 \text{ min}^{-1}$ ,  $k_9 = 0.74 \text{ min}^{-1}$ ,  
 $k_{10} = 0.005 \text{ min}^{-1}$ ,  $k_{11} = 0.006 \text{ kPa}^{-1} \cdot \text{min}^{-1}$ ,  $gsy_p^0 = 0.05$ ,  $gph_p^0 = 0.7$ ,  $glu_{ext}^0 = 3.3$  are  
the concentrations of Gsy, Gph and external glucose in equilibrium respectively,  
 $m_{11} = 0.6$ ,  $m_{12} = 3.4$ ,  $m_{13} = 1$ ,  $m_{14} = 1$ ,  $m_{15} = 0.1$ ,  $m_{17} = 0.1$ ,  $m_{18} = 0.2$ ,  $m_{19} = 0.2$ ,  
 $m_{20} = 60$ .

These parameter values are selected "by hand" in order to obtain the expected qualitative behaviour. In Section 5.5 we will perform the quantitative analysis of the parameter set. The following parameters are found analytically from equilibrium conditions of the corresponding ODEs:  $L_1$  and  $L_2$  from Equations (5.24), equilibrium concentration of intracellular glucose  $glu_0$  from Equation (5.26), equilibrium concentration of glycogen  $gln_0$  from Equation (5.28), equilibrium Fps1p concentration  $fps1_p^0$  from Equation (5.32), equilibrium concentration of glycerol  $gly_0$  from Equation (5.34),  $k_{12}$  from Equation (5.36).

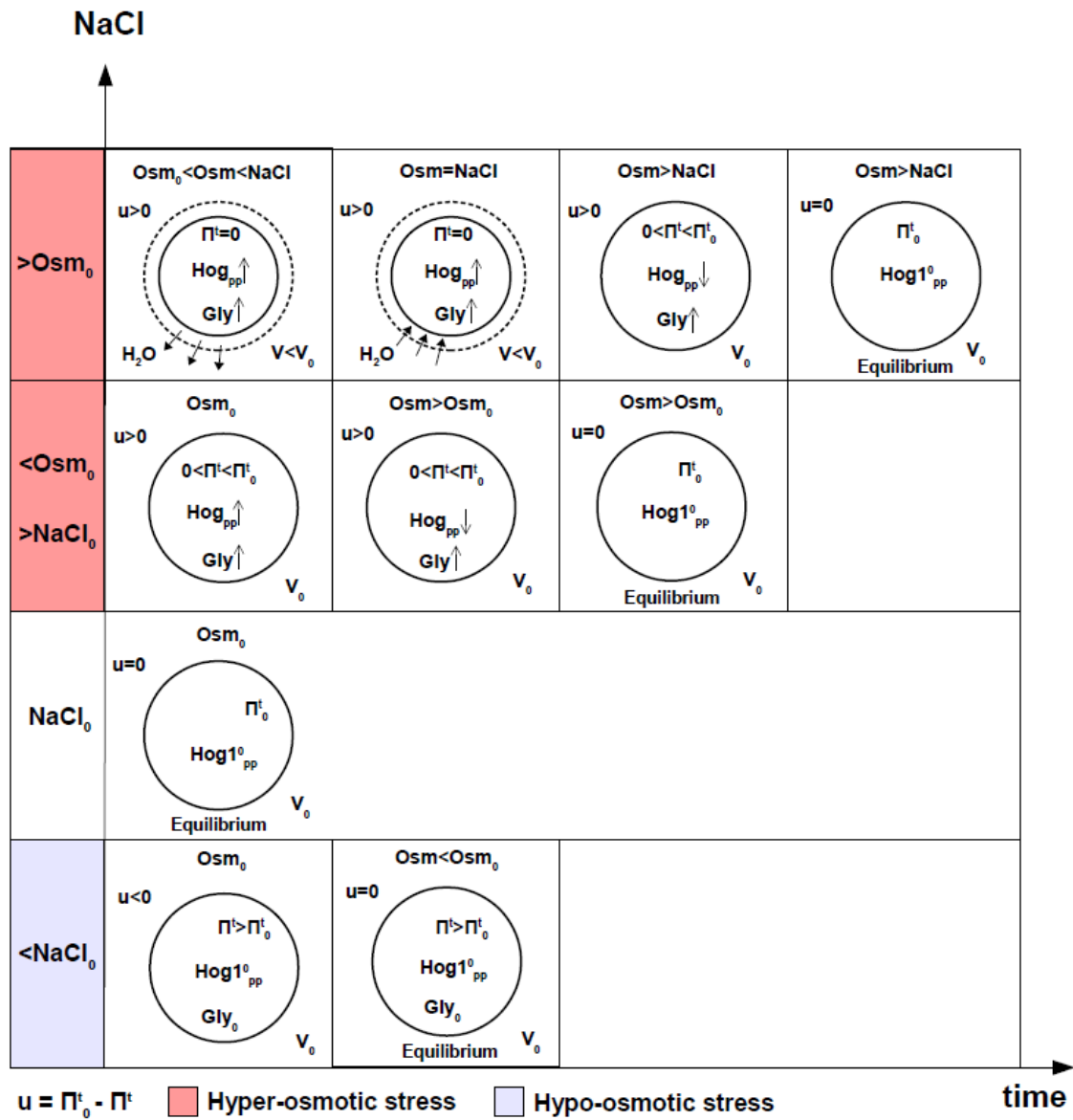


Figure 5.8. Schematic representation of the yeast cell adaptation to osmotic stress after the introduction of the modified glycerol metabolism module.

While the model still demonstrates the volume restore and glycerol accumulation, it now shows the restore of the turgor pressure and *Hog1* phosphorylation level under the hyper-osmotic stress. However, there is still a lack of glycerol efflux and the restore of the turgor pressure under the hypo-osmotic stress. See Equations (5.6), (5.9)-(5.36) with  $R = 8.31 \text{ kPa} \cdot \text{M}^{-1} \cdot \text{K}^{-1}$ ,  $T = 300 \text{ K}$ ,  $A \cdot L = 86 \cdot 10^{-3} \text{ min}^{-1} \cdot \text{kPa}^{-1}$ ,  $V_0 = 6.5 \cdot 10^{-14} \text{ L}$ ,  $\varepsilon = 1 \cdot 10^5$ ,  $Km_{16} = 0.6 \text{ M}$ ,  $[NaCl_0] = 0.175 \text{ M}$ ,  $v_b = 0.368$ ,  $k_{hog} = 0.416 \text{ Osm}^{-1}$ ,  $t_d = 8.61 \text{ min}$ ,  $k_1 = 0.005 \text{ kPa}^{-1} \cdot \text{min}^{-1}$ ,  $k_2 = 0.1 \text{ min}^{-1}$ ,  $k_3 = 0.2 \text{ kPa}^{-1} \cdot \text{min}^{-1}$ ,  $k_4 = 0.02 \text{ min}^{-1}$ ,  $k_5 = 0.03 \text{ min}^{-1}$ ,  $k_6 = 0.003 \text{ min}^{-1}$ ,  $k_7 = 15 \text{ min}^{-1}$ ,  $k_8 = 1 \text{ min}^{-1}$ ,  $k_9 = 0.74 \text{ min}^{-1}$ ,  $k_{10} = 0.005 \text{ min}^{-1}$ ,  $k_{11} = 0.006 \text{ kPa}^{-1} \cdot \text{min}^{-1}$ ,  $gsy_p^0 = 0.05$ ,  $gph_p^0 = 0.7$ ,  $glu_{ext}^0 = 3.3$ ,  $m_{11} = 0.6$ ,  $m_{12} = 3.4$ ,  $m_{13} = 1$ ,  $m_{14} = 1$ ,  $m_{15} = 0.1$ ,  $m_{17} = 0.1$ ,  $m_{18} = 0.2$ ,  $m_{19} = 0.2$ ,  $m_{20} = 60$ .

Figure 5.8 schematically illustrates the model predictions for the newly added assumptions. Quantitative results produced by the model are shown in Appendix D (Figures 7.10-7.12). Now, after the introduction of the modification of the glycerol metabolism module, one can compare the new results with the previous case of the modification in the biophysical module only (Figure 5.6). While still demonstrating the volume recovery under the strong hyper-osmotic stress (Figure 7.10A), which corresponds to  $[NaCl] > [Osm_0]$ , the cell now restores its equilibrium Hog1 phosphorylation level (Figures 7.10B and 7.11B) and turgor pressure (Figures 7.10D and 7.11D).

Another quantitative advantage of the new version of the model is that it is now possible to test the effects of various mutations in the glycerol metabolism module and for different external glucose concentration. However, the model still lacks the glycerol efflux (Figure 7.12C) and the restore of the turgor pressure (Figure 7.12D) under the hypo-osmotic stress. It also lacks the detailed Hog1 activation module and therefore this version of the model cannot be used to describe effects of various mutations in the MAPK pathways. In the next subsection we seek to address these drawbacks by introducing the detailed Hog1 activation module.

### **5.4.3 Modification 3 of the Hog1 activation module**

In this subsection we will introduce modified module of Hog1 activation described in the Gennemark model by Equation (5.6). Figure 5.9 illustrates the new structure of our model including these modifications based on the established [51,289,291-293,296,297,324] signal transduction pathways involved in the regulation of yeast adaptation to osmotic stress. The structure of the model still includes the biophysical part, which incorporates the volume of the cell and turgor pressure as well as the biochemical part, which includes the glycerol metabolism module and now also detailed MAPK signalling.

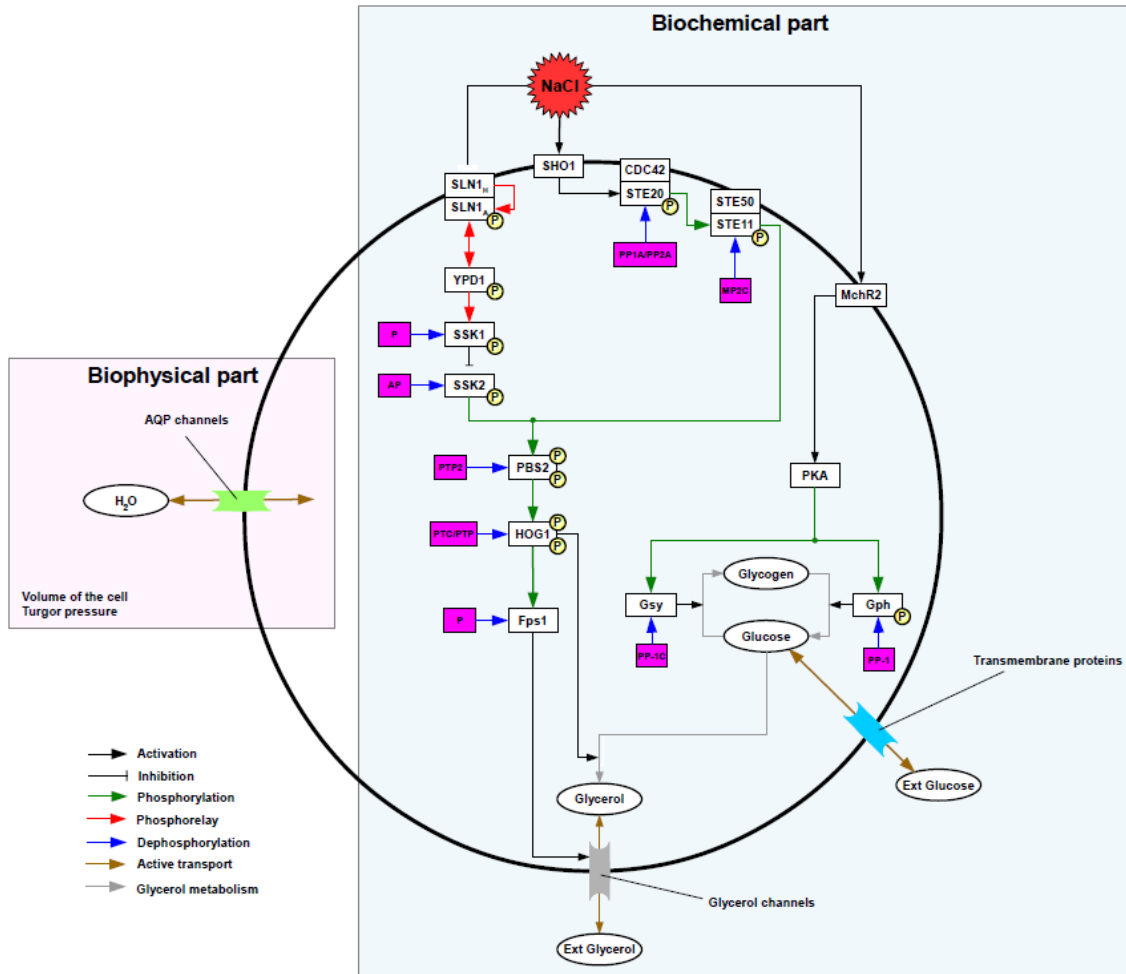
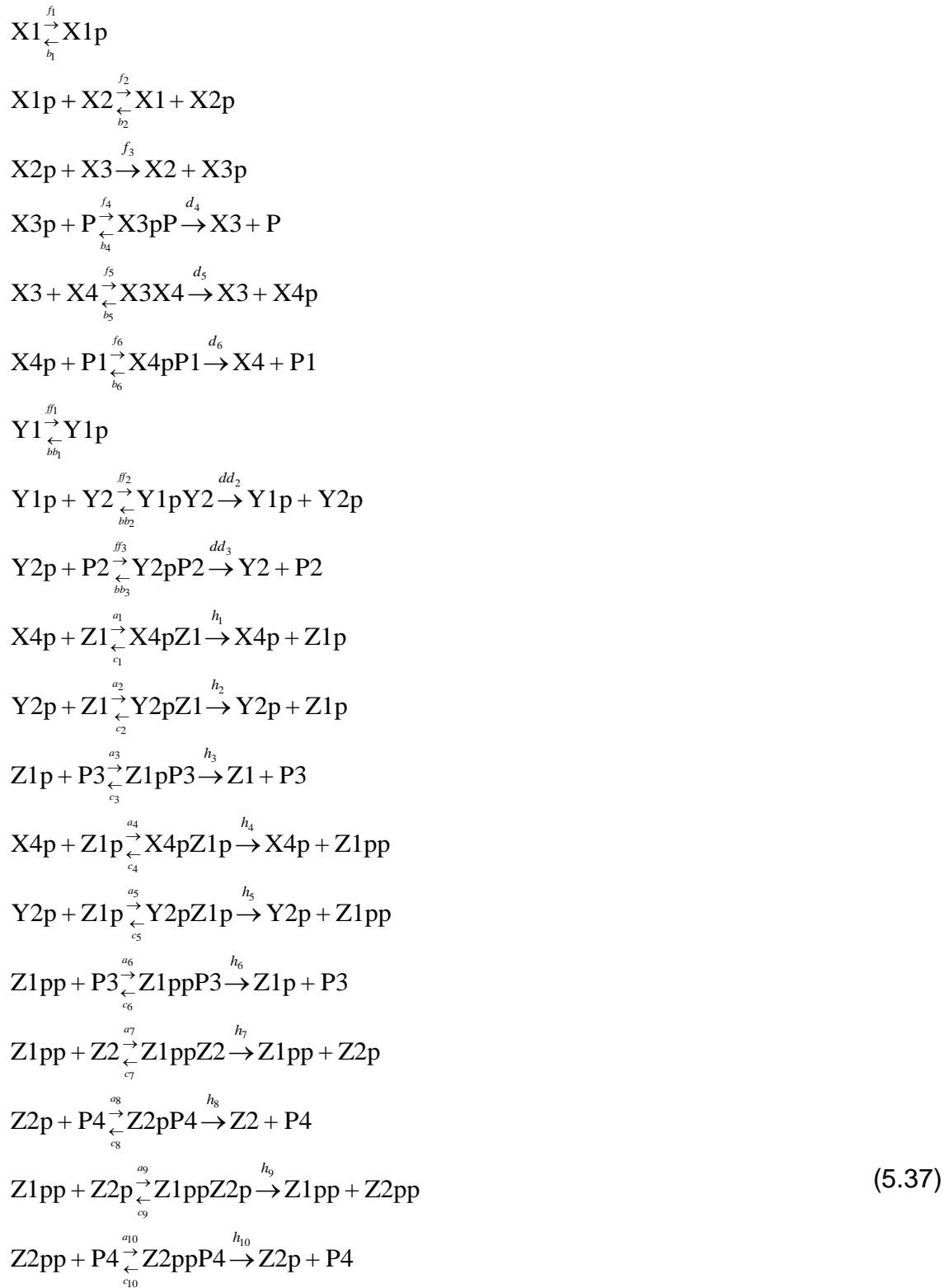


Figure 5.9. The structure of the new model after the introduction of the modified Hog1 activation module.

This model includes MAPK cascade pathways, leading to the activation of Hog1, with more detail compared to the Gennemark model [47]. The activation of Hog1 is performed by the two branches, Sho1 and Sln1.

We introduce the following notation for the elements in MAPK pathways:  
 $X1 = SLN1$ ,  $X2 = YPD1$ ,  $X3 = SSK1$ ,  $X4 = SSK2$ ,  $Y1 = SHO1/CDC42/STE20$ ,  
 $Y2 = STE50/STE11$ ,  $Z1 = PBS2$ ,  $Z2 = HOG1$ ,  $AP = P1$ ,  $MP2C = P2$ ,  $PTP2 = P3$ ,  
 $PTC/PTP = P4$ ,  $L_T = SLN1_T$ ,  $H_T = SHO1_T$ .

The biochemical reactions of the MAPK cascade, that were previously described in [53] and [48], are given by:



Based on the fact that under hyper-osmotic stress, when  $u$  is increased, Sln1 is inhibited [289], we assume in Equations (5.37) that the reaction rate  $b_1$  depends

on  $u$  as follows:  $b_1 = b_1^p \cdot u \cdot H(u)$ , where  $b_1^p$  is a constant and  $H(u) = \begin{cases} 1, & \text{if } u > 0 \\ 0, & \text{if } u \leq 0 \end{cases}$ .

Based on the fact that under hyper-osmotic stress, when  $u$  is increased, Sho1 is activated [292], we also assume that the reaction rate  $ff_1$  depends on  $u$  in the following way:  $ff_1 = ff_1^p \cdot u \cdot H(u)$ , where  $ff_1^p$  is a constant.

Ordinary Differential Equations that describe the rates of the chemical reactions (5.37) are given by:

$$\begin{aligned}
\frac{d}{dt}[X1p] &= f_1 \cdot [X1] - b_1 \cdot [X1p] - f_2 \cdot [X1p] \cdot [X2] + b_2 \cdot [X1] \cdot [X2p] - [X1p] \cdot D(V), \\
\frac{d}{dt}[X2p] &= f_2 \cdot [X1p] \cdot [X2] - b_2 \cdot [X1] \cdot [X2p] - f_3 \cdot [X2p] \cdot [X3] - [X2p] \cdot D(V), \\
\frac{d}{dt}[X3p] &= f_3 \cdot [X2p] \cdot [X3] - f_4 \cdot [X3p] \cdot [P] + b_4 \cdot [X3pP] - [X3p] \cdot D(V), \\
\frac{d}{dt}[X3pP] &= f_4 \cdot [X3p] \cdot [P] - (b_4 + d_4) \cdot [X3pP] - [X3pP] \cdot D(V), \\
\frac{d}{dt}[X3X4] &= f_5 \cdot [X3] \cdot [X4] - (b_5 + d_5) \cdot [X3X4] - [X3X4] \cdot D(V), \\
\frac{d}{dt}[X4p] &= d_5 \cdot [X3X4] - f_6 \cdot [X4p] \cdot [P1] + b_6 \cdot [X4pP1] - a_1 \cdot [X4p] \cdot [Z1] + \\
&\quad + (c_1 + h_1) \cdot [X4pZ1] - a_4 \cdot [X4p] \cdot [Z1p] + (c_4 + h_4) \cdot [X4pZ1p] - [X4p] \cdot D(V), \\
\frac{d}{dt}[X4pP1] &= f_6 \cdot [X4p] \cdot [P1] - (b_6 + d_6) \cdot [X4pP1] - [X4pP1] \cdot D(V), \\
\frac{d}{dt}[Y1p] &= ff_1 \cdot [Y1] - bb_1 \cdot [Y1p] - ff_2 \cdot [Y1p] \cdot [Y2] + (bb_2 + dd_2) \cdot [Y1pY2] - [Y1p] \cdot D(V), \\
\frac{d}{dt}[Y1pY2] &= ff_2 \cdot [Y1p] \cdot [Y2] - (bb_2 + dd_2) \cdot [Y1pY2] - [Y1pY2] \cdot D(V), \\
\frac{d}{dt}[Y2p] &= dd_2 \cdot [Y1pY2] - ff_3 \cdot [Y2p] \cdot [P2] + bb_3 \cdot [Y2pP2] - a_2 \cdot [Y2p] \cdot [Z1] + \\
&\quad + (c_2 + h_2) \cdot [Y2pZ1] - a_5 \cdot [Y2p] \cdot [Z1p] + (c_5 + h_5) \cdot [Y2pZ1p] - [Y2p] \cdot D(V), \\
\frac{d}{dt}[Y2pP2] &= ff_3 \cdot [Y2p] \cdot [P2] - (bb_3 + dd_3) \cdot [Y2pP2] - [Y2pP2] \cdot D(V),
\end{aligned} \tag{5.38}$$

$$\begin{aligned}
\frac{d}{dt}[X4pZ1] &= a_1 \cdot [X4p] \cdot [Z1] - (c_1 + h_1) \cdot [X4pZ1] - [X4pZ1] \cdot D(V), \\
\frac{d}{dt}[Y2pZ1] &= a_2 \cdot [Y2p] \cdot [Z1] - (c_2 + h_2) \cdot [Y2pZ1] - [Y2pZ1] \cdot D(V), \\
\frac{d}{dt}[Z1p] &= h_1 \cdot [X4pZ1] + h_2 \cdot [Y2pZ1] - a_3 \cdot [Z1p] \cdot [P3] + c_3 \cdot [Z1pP3] - a_4 \cdot [X4p] \cdot [Z1p] + \\
&\quad + c_4 \cdot [X4pZ1p] - a_5 \cdot [Y2p] \cdot [Z1p] + c_5 \cdot [Y2pZ1p] + h_6 \cdot [Z1ppP3] - [Z1p] \cdot D(V), \\
\frac{d}{dt}[Z1pP3] &= a_3 \cdot [Z1p] \cdot [P3] - (c_3 + h_3) \cdot [Z1pP3] - [Z1pP3] \cdot D(V), \\
\frac{d}{dt}[X4pZ1p] &= a_4 \cdot [X4p] \cdot [Z1p] - (c_4 + h_4) \cdot [X4pZ1p] - [X4pZ1p] \cdot D(V), \\
\frac{d}{dt}[Z1pp] &= h_4 \cdot [X4pZ1p] + h_5 \cdot [Y2pZ1p] - a_6 \cdot [Z1pp] \cdot [P3] + c_6 \cdot [Z1ppP3] - a_7 \cdot [Z1pp] \cdot [Z2] + \\
&\quad + (c_7 + h_7) \cdot [Z1ppZ2] - a_9 \cdot [Z1pp] \cdot [Z2p] + (c_9 + h_9) \cdot [Z1ppZ2p] - [Z1pp] \cdot D(V), \\
\frac{d}{dt}[Y2pZ1p] &= a_5 \cdot [Y2p] \cdot [Z1p] - (c_5 + h_5) \cdot [Y2pZ1p] - [Y2pZ1p] \cdot D(V), \\
\frac{d}{dt}[Z1ppP3] &= a_6 \cdot [Z1pp] \cdot [P3] - (c_6 + h_6) \cdot [Z1ppP3] - [Z1ppP3] \cdot D(V), \\
\frac{d}{dt}[Z1ppZ2] &= a_7 \cdot [Z1pp] \cdot [Z2] - (c_7 + h_7) \cdot [Z1ppZ2] - [Z1ppZ2] \cdot D(V), \\
\frac{d}{dt}[Z2p] &= h_7 \cdot [Z1ppZ2] - a_8 \cdot [Z2p] \cdot [P4] + c_8 \cdot [Z2pP4] - a_9 \cdot [Z1pp] \cdot [Z2p] + \\
&\quad + c_9 \cdot [Z1ppZ2p] + h_{10} \cdot [Z2ppP4] - [Z2p] \cdot D(V), \\
\frac{d}{dt}[Z2pP4] &= a_8 \cdot [Z2p] \cdot [P4] - (c_8 + h_8) \cdot [Z2pP4] - [Z2pP4] \cdot D(V), \\
\frac{d}{dt}[Z1ppZ2p] &= a_9 \cdot [Z1pp] \cdot [Z2p] - (c_9 + h_9) \cdot [Z1ppZ2p] - [Z1ppZ2p] \cdot D(V), \\
\frac{d}{dt}[Z2pp] &= h_9 \cdot [Z1ppZ2p] - a_{10} \cdot [Z2pp] \cdot [P4] + c_{10} \cdot [Z2ppP4] - [Z2pp] \cdot D(V), \\
\frac{d}{dt}[Z2ppP4] &= a_{10} \cdot [Z2pp] \cdot [P4] - (c_{10} + h_{10}) \cdot [Z2ppP4] - [Z2ppP4] \cdot D(V).
\end{aligned}$$

The total concentration of the proteins involved in the reactions remains constant:

$$\begin{aligned}
k_r \cdot \frac{L_T}{V - V_b} &= [X1] + [X1p], \\
\frac{X2_T}{V - V_b} &= [X2] + [X2p], \\
\frac{X3_T}{V - V_b} &= [X3] + [X3p] + [X3X4] + [X3pP], \\
\frac{X4_T}{V - V_b} &= [X4] + [X4p] + [X3X4] + [X4pP1] + [X4pZ1] + [X4pZ1p], \\
k_r \cdot \frac{H_T}{V - V_b} &= [Y1] + [Y1p] + [Y1pY2], \\
\frac{Y2_T}{V - V_b} &= [Y2] + [Y2p] + [Y1pY2] + [Y2pP2] + [Y2pZ1] + [Y2pZ1p], \\
\frac{Z1_T}{V - V_b} &= [Z1] + [Z1p] + [Z1pp] + [X4pZ1] + [Y2pZ1] + [Z1pP3] + [X4pZ1p] + \\
&\quad + [Y2pZ1p] + [Z1ppP3] + [Z1ppZ2] + [Z1ppZ2p], \\
\frac{Z2_T}{V - V_b} &= [Z2] + [Z2p] + [Z2pp] + [Z1ppZ2] + [Z2pP4] + [Z1ppZ2p] + [Z2ppP4], \\
\frac{P_T}{V - V_b} &= [P] + [X3pP], \\
\frac{P1_T}{V - V_b} &= [P1] + [X4pP1], \\
\frac{P2_T}{V - V_b} &= [P2] + [Y2pP2], \\
\frac{P3_T}{V - V_b} &= [P3] + [Z1pP3] + [Z1ppP3], \\
\frac{P4_T}{V - V_b} &= [P4] + [Z2pP4] + [Z2ppP4].
\end{aligned} \tag{5.39}$$

For simplicity, we assume that the formation of complexes is much faster than the phosphorylation reactions and therefore we can use the QSSA, which is in line with [57,186]. We also assume that the formation of complexes is much faster than the volume change and therefore the term  $D(V)$  is small and can be neglected. In the QSSA the concentrations of complexes are given by:

$$\begin{aligned}
\frac{d}{dt}[X3pP] &= 0, \quad \frac{d}{dt}[X3X4] = 0, \quad \frac{d}{dt}[X4pP1] = 0, \quad \frac{d}{dt}[Y1pY2] = 0, \quad \frac{d}{dt}[Y2pP2] = 0, \\
\frac{d}{dt}[X4pZ1] &= 0, \quad \frac{d}{dt}[Y2pZ1] = 0, \quad \frac{d}{dt}[Z1pP3] = 0, \quad \frac{d}{dt}[X4pZ1p] = 0,
\end{aligned}$$



$$\frac{d}{dt}[Y2pZ1p]=0, \frac{d}{dt}[Z1ppP3]=0, \frac{d}{dt}[Z1ppZ2]=0, \frac{d}{dt}[Z2pP4]=0,$$

$$\frac{d}{dt}[Z1ppZ2p]=0, \frac{d}{dt}[Z2ppP4]=0.$$

We can rewrite Equations (5.39) in the following way:

$$k_r \cdot \frac{L_T}{V - V_b} = [X1] + [X1p],$$

$$\frac{X2_T}{V - V_b} = [X2] + [X2p],$$

$$\frac{X3_T}{V - V_b} = [X3] + [X3p],$$

$$\frac{X4_T}{V - V_b} = [X4] + [X4p],$$

$$k_r \cdot \frac{H_T}{V - V_b} = [Y1] + [Y1p],$$

$$\frac{Y2_T}{V - V_b} = [Y2] + [Y2p],$$

$$\frac{Z1_T}{V - V_b} = [Z1] + [Z1p] + [Z1pp],$$

$$\frac{Z2_T}{V - V_b} = [Z2] + [Z2p] + [Z2pp],$$

$$\frac{P_T}{V - V_b} = [P] + [X3pP],$$

$$\frac{P1_T}{V - V_b} = [P1] + [X4pP1], \tag{5.40}$$

$$\frac{P2_T}{V - V_b} = [P2] + [Y2pP2],$$

$$\frac{P3_T}{V - V_b} = [P3] + [Z1pP3] + [Z1ppP3],$$

$$\frac{P4_T}{V - V_b} = [P4] + [Z2pP4] + [Z2ppP4].$$

Next, using Equations (3.48) from Chapter 3, the concentrations of the complexes can be found:

$$\begin{aligned}
[X3pP] &= \frac{P_T}{V - V_b} \cdot \frac{[X3p]}{KM_1 + [X3p]}, \\
[X3X4] &= [X3] \cdot \frac{[X4]}{KM_2 + [X4]}, \\
[X4pP1] &= \frac{P1_T}{V - V_b} \cdot \frac{[X4p]}{KM_3 + [X4p]}, \\
[Y1pY2] &= [Y1p] \cdot \frac{[Y2]}{KM_4 + [Y2]}, \\
[Y2pP2] &= \frac{P2_T}{V - V_b} \cdot \frac{[Y2p]}{KM_5 + [Y2p]}, \\
[X4pZ1] &= [X4p] \cdot \frac{[Z1]}{KM_6 + [Z1] + [Z1p]}, \\
[Y2pZ1] &= [Y2p] \cdot \frac{[Z1]}{KM_7 + [Z1] + [Z1p]}, \\
[Z1pP3] &= \frac{P3_T}{V - V_b} \cdot \frac{[Z1p]}{KM_8 + [Z1p] + [Z1pp]}, \\
[X4pZ1p] &= [X4p] \cdot \frac{[Z1p]}{KM_6 + [Z1] + [Z1p]}, \\
[Y2pZ1p] &= [Y2p] \cdot \frac{[Z1p]}{KM_7 + [Z1] + [Z1p]}, \\
[Z1ppP3] &= \frac{P3_T}{V - V_b} \cdot \frac{[Z1pp]}{KM_8 + [Z1p] + [Z1pp]}, \\
[Z1ppZ2] &= [Z1pp] \cdot \frac{[Z2]}{KM_9 + [Z2] + [Z2p]}, \\
[Z2pP4] &= \frac{P4_T}{V - V_b} \cdot \frac{[Z2p]}{KM_{10} + [Z2p] + [Z2pp]}, \\
[Z1ppZ2p] &= [Z1pp] \cdot \frac{[Z2p]}{KM_9 + [Z2] + [Z2p]}, \\
[Z2ppP4] &= \frac{P4_T}{V - V_b} \cdot \frac{[Z2pp]}{KM_{10} + [Z2p] + [Z2pp]}.
\end{aligned} \tag{5.41}$$

Using Equations (5.41) we can rewrite Equations (5.38) as follows:

$$\begin{aligned}
\frac{d}{dt}[X1p] &= f_1 \cdot [X1] - b_1 \cdot [X1p] - f_2 \cdot [X1p] \cdot [X2] + b_2 \cdot [X1] \cdot [X2p] - [X1p] \cdot D(V), \\
\frac{d}{dt}[X2p] &= f_2 \cdot [X1p] \cdot [X2] - b_2 \cdot [X1] \cdot [X2p] - f_3 \cdot [X2p] \cdot [X3] - [X2p] \cdot D(V), \\
\frac{d}{dt}[X3p] &= f_3 \cdot [X2p] \cdot [X3] - d_4 \cdot [X3pP] - [X3p] \cdot D(V), \\
\frac{d}{dt}[X4p] &= d_5 \cdot [X3X4] - d_6 \cdot [X4pP1] - [X4p] \cdot D(V), \\
\frac{d}{dt}[Y1p] &= ff_1 \cdot [Y1] - bb_1 \cdot [Y1p] - [Y1p] \cdot D(V), \\
\frac{d}{dt}[Y2p] &= dd_2 \cdot [Y1pY2] - dd_3 \cdot [Y2pP2] - [Y2p] \cdot D(V), \\
\frac{d}{dt}[Z1p] &= h_1 \cdot [X4pZ1] + h_2 \cdot [Y2pZ1] - h_3 \cdot [Z1pP3] - \\
&\quad - h_4 \cdot [X4pZ1p] - h_5 \cdot [Y2pZ1p] + h_6 \cdot [Z1ppP3] - [Z1p] \cdot D(V), \\
\frac{d}{dt}[Z1pp] &= h_4 \cdot [X4pZ1p] + h_5 \cdot [Y2pZ1p] - h_6 \cdot [Z1ppP3] - [Z1pp] \cdot D(V), \\
\frac{d}{dt}[Z2p] &= h_7 \cdot [Z1ppZ2] - h_8 \cdot [Z2pP4] - h_9 \cdot [Z1ppZ2p] + h_{10} \cdot [Z2ppP4] - [Z2p] \cdot D(V), \quad (5.42) \\
\frac{d}{dt}[Z2pp] &= h_9 \cdot [Z1ppZ2p] - h_{10} \cdot [Z2ppP4] - [Z2pp] \cdot D(V).
\end{aligned}$$

We can write Equations (5.40) in non-dimensional form by normalizing the concentrations to the total amount of Hog1 denoted by  $Z2_T$  and the cell volume in equilibrium  $V_0$ :

$$\begin{aligned}
k_r \cdot \frac{l_t}{v - v_b} &= x1 + x1_p, \\
\frac{x2_t}{v - v_b} &= x2 + x2_p, \\
\frac{x3_t}{v - v_b} &= x3 + x3_p, \\
\frac{x4_t}{v - v_b} &= x4 + x4_p, \\
k_r \cdot \frac{h_t}{v - v_b} &= y1 + y1_p, \\
\frac{y2_t}{v - v_b} &= y2 + y2_p, \\
\frac{z1_t}{v - v_b} &= z1 + z1_p + z1_{pp}, \\
\frac{1}{v - v_b} &= z2 + z2_p + z2_{pp}, \\
\frac{p_t}{v - v_b} &= p + x3_p p, \\
\frac{p1_t}{v - v_b} &= p1 + x4_p p1, \\
\frac{p2_t}{v - v_b} &= p2 + y2_p p2, \\
\frac{p3_t}{v - v_b} &= p3 + z1_p p3 + z1_{pp} p3, \\
\frac{p4_t}{v - v_b} &= p4 + z2_p p4 + z2_{pp} p4.
\end{aligned} \tag{5.43}$$

We can write Equations (5.41) in non-dimensional form as follows:

$$\begin{aligned}
x3_p p &= \frac{p_t}{v - v_b} \cdot \frac{x3_p}{m_1 + x3_p}, \\
x3x4 &= x3 \cdot \frac{x4}{m_2 + x4}, \\
x4_p p1 &= \frac{p1_t}{v - v_b} \cdot \frac{x4_p}{m_3 + x4_p}, \\
y1_p y2 &= y1_p \cdot \frac{y2}{m_4 + y2}, \\
y2_p p2 &= \frac{p2_t}{v - v_b} \cdot \frac{y2_p}{m_5 + y2_p}, \\
x4_p z1 &= x4_p \cdot \frac{z1}{m_6 + z1 + z1_p}, \\
y2_p z1 &= y2_p \cdot \frac{z1}{m_7 + z1 + z1_p}, \\
z1_p p3 &= \frac{p3_t}{v - v_b} \cdot \frac{z1_p}{m_8 + z1_p + z1_{pp}}, \\
x4_p z1_p &= x4_p \cdot \frac{z1_p}{m_6 + z1 + z1_p}, \\
y2_p z1_p &= y2_p \cdot \frac{z1_p}{m_7 + z1 + z1_p}, \\
z1_{pp} p3 &= \frac{p3_t}{v - v_b} \cdot \frac{z1_{pp}}{m_8 + z1_p + z1_{pp}}, \\
z1_{pp} z2 &= z1_{pp} \cdot \frac{z2}{m_9 + z2 + z2_p}, \\
z2_p p4 &= \frac{p4_t}{v - v_b} \cdot \frac{z2_p}{m_{10} + z2_p + z2_{pp}}, \\
z1_{pp} z2_p &= z1_{pp} \cdot \frac{z2_p}{m_9 + z2 + z2_p}, \\
z2_{pp} p4 &= \frac{p4_t}{v - v_b} \cdot \frac{z2_{pp}}{m_{10} + z2_p + z2_{pp}}.
\end{aligned} \tag{5.44}$$

Equations (5.42) can be represented in non-dimensional form as follows:

$$\begin{aligned}
\frac{d}{dt} x1_p &= f_1 \cdot x1 - b_1 \cdot x1_p - f_2^p \cdot x1_p \cdot x2 + b_2^p \cdot x1 \cdot x2_p - x1_p \cdot D(v), \\
\frac{d}{dt} x2_p &= f_2^p \cdot x1_p \cdot x2 - b_2^p \cdot x1 \cdot x2_p - f_3^p \cdot x2_p \cdot x3 - x2_p \cdot D(v), \\
\frac{d}{dt} x3_p &= f_3^p \cdot x2_p \cdot x3 - d_4 \cdot x3_p p - x3_p \cdot D(v), \\
\frac{d}{dt} x4_p &= d_5 \cdot x3x4 - d_6 \cdot x4_p p1 - x4_p \cdot D(v), \\
\frac{d}{dt} y1_p &= ff_1 \cdot y1 - bb_1 \cdot y1_p - y1_p \cdot D(v), \\
\frac{d}{dt} y2_p &= dd_2 \cdot y1_p y2 - dd_3 \cdot y2_p p2 - y2_p \cdot D(v), \\
\frac{d}{dt} z1_p &= h_1 \cdot x4_p z1 + h_2 \cdot y2_p z1 - h_3 \cdot z1_p p3 - h_4 \cdot x4_p z1_p - \\
&\quad - h_5 \cdot y2_p z1_p + h_6 \cdot z1_{pp} p3 - z1_p \cdot D(v), \\
\frac{d}{dt} z1_{pp} &= h_4 \cdot x4_p z1_p + h_5 \cdot y2_p z1_p - h_6 \cdot z1_{pp} p3 - z1_{pp} \cdot D(v), \\
\frac{d}{dt} z2_p &= h_7 \cdot z1_{pp} z2 - h_8 \cdot z2_p p4 - h_9 \cdot z1_{pp} z2_p + h_{10} \cdot z2_{pp} p4 - z2_p \cdot D(v), \\
\frac{d}{dt} z2_{pp} &= h_9 \cdot z1_{pp} z2_p - h_{10} \cdot z2_{pp} p4 - z2_{pp} \cdot D(v),
\end{aligned} \tag{5.45}$$

where  $b_2^p = b_2 \cdot \frac{Z2_T}{V_0}$ ,  $f_2^p = f_2 \cdot \frac{Z2_T}{V_0}$ ,  $f_3^p = f_3 \cdot \frac{Z2_T}{V_0}$  and  $D(v) = \frac{dv}{(v - v_b)dt}$ .

For simplicity, we assume that the two phosphorylation sites in each Hog1 and Pbs2 are identical. Therefore, Equations (5.45) can be rewritten as follows:

$$\begin{aligned}
\frac{d}{dt} x1_p &= f_1 \cdot x1 - b_1 \cdot x1_p - f_2^p \cdot x1_p \cdot x2 + b_2^p \cdot x1 \cdot x2_p - x1_p \cdot D(v), \\
\frac{d}{dt} x2_p &= f_2^p \cdot x1_p \cdot x2 - b_2^p \cdot x1 \cdot x2_p - f_3^p \cdot x2_p \cdot x3 - x2_p \cdot D(v), \\
\frac{d}{dt} x3_p &= f_3^p \cdot x2_p \cdot x3 - d_4 \cdot x3_p p - x3_p \cdot D(v), \\
\frac{d}{dt} x4_p &= d_5 \cdot x3x4 - d_6 \cdot x4_p p1 - x4_p \cdot D(v), \\
\frac{d}{dt} y1_p &= ff_1 \cdot y1 - bb_1 \cdot y1_p - y1_p \cdot D(v), \\
\frac{d}{dt} y2_p &= dd_2 \cdot y1_p y2 - dd_3 \cdot y2_p p2 - y2_p \cdot D(v), \\
\frac{d}{dt} z1_p &= hh_1 \cdot x4_p z1 + hh_2 \cdot y2_p z1 - hh_3 \cdot z1_p p3 - hh_1 \cdot x4_p z1_p - \\
&\quad - hh_2 \cdot y2_p z1_p + hh_3 \cdot z1_{pp} p3 - z1_p \cdot D(v), \\
\frac{d}{dt} z1_{pp} &= hh_1 \cdot x4_p z1_p + hh_2 \cdot y2_p z1_p - hh_3 \cdot z1_{pp} p3 - z1_{pp} \cdot D(v), \\
\frac{d}{dt} z2_p &= hh_4 \cdot z1_{pp} z2 - hh_5 \cdot z2_p p4 - hh_4 \cdot z1_{pp} z2_p + hh_5 \cdot z2_{pp} p4 - z2_p \cdot D(v), \\
\frac{d}{dt} z2_{pp} &= hh_4 \cdot z1_{pp} z2_p - hh_5 \cdot z2_{pp} p4 - z2_{pp} \cdot D(v),
\end{aligned} \tag{5.46}$$

where  $hh_1 = h_1 = h_4$ ,  $hh_2 = h_2 = h_5$ ,  $hh_3 = h_3 = h_6$ ,  $hh_4 = h_7 = h_9$  and  $hh_5 = h_8 = h_{10}$ .

Due to the close genetic proximity of *C. glabrata* to *S. cerevisiae* [45] and to the fact that *C. glabrata* is a less studied organism, we assume here that the total number of moles of the kinases in the MAPK cascades is the same in these two species. Table 5.1 shows the values for the total amount of moles in Equation (5.39) taken from the online Yeast GFP Fusion Localization Database (<http://yeastgfp.yeastgenome.org/>), which is also consistent with [48].

*Table 5.1. The total number of moles of the kinases in MAPK pathways.*

Kinase	$L_T$	$X2_T$	$X3_T$	$X4_T$	$H_T$	$Y2_T$	$Z1_T$	$Z2_T$
$\text{mol} \times 10^{-23}$	108.934	1051.146	199.269	36.034	43.009	122.218	358.685	1125.872

The model by Gennemark [47] is the model for *S. cerevisiae*. After the introduction of the modified biophysical and biochemical parts we now seek to

model *C. glabrata*. We are going to do this by assuming that *C. glabrata* is more tolerant to osmotic shock compared to *S. cerevisiae*, which is also consistent with [45]. In particular, we assume that 1.5M of NaCl that used to be a strong hyper-osmotic stress in the Gennemark model and in the previous changes, now becomes a mild hyper-osmotic stress. Therefore, in this subsection we test our model under 2.5M hyper-osmotic concentration of salt.

We test the effects of the assumptions introduced in this subsection for the following set of parameters:  $l_t = 0.097$ ,  $x_{2_t} = 0.934$ ,  $x_{3_t} = 0.177$ ,  $x_{4_t} = 0.032$ ,  $h_t = 0.038$ ,  $y_{2_t} = 0.108$ ,  $z_{1_t} = 0.319$ ,  $z_{2_t} = 1$  from Table 5.1,  $p_t = 0.02$ ,  $p_{1_t} = 0.005$ ,  $p_{2_t} = 0.01$ ,  $p_{3_t} = 0.021$ ,  $p_{4_t} = 0.1$ ,  $m_1 = 2$ ,  $m_2 = 2$ ,  $m_3 = 2$ ,  $m_4 = 1$ ,  $m_5 = 1$ ,  $m_6 = 1$ ,  $m_7 = 2$ ,  $m_8 = 2$ ,  $m_9 = 2$ ,  $m_{10} = 1$ ,  $f_1 = 5 \text{ min}^{-1}$ ,  $f_2^p = 12 \text{ min}^{-1}$ ,  $f_3^p = 17 \text{ min}^{-1}$ ,  $ff_1 = 0.005 \text{ min}^{-1}$ ,  $b_1 = 0.003 \text{ min}^{-1}$ ,  $b_2^p = 2.3 \text{ min}^{-1}$ ,  $bb_1 = 3.2 \text{ min}^{-1}$ ,  $d_4 = 5 \text{ min}^{-1}$ ,  $d_5 = 4.6 \text{ min}^{-1}$ ,  $d_6 = 5.4 \text{ min}^{-1}$ ,  $dd_2 = 4.3 \text{ min}^{-1}$ ,  $dd_3 = 1.7 \text{ min}^{-1}$ ,  $hh_1 = 5.4 \text{ min}^{-1}$ ,  $hh_2 = 1.5 \text{ min}^{-1}$ ,  $hh_3 = 5 \text{ min}^{-1}$ ,  $hh_4 = 5 \text{ min}^{-1}$ ,  $hh_5 = 5 \text{ min}^{-1}$  are the parameters chosen "by hand".



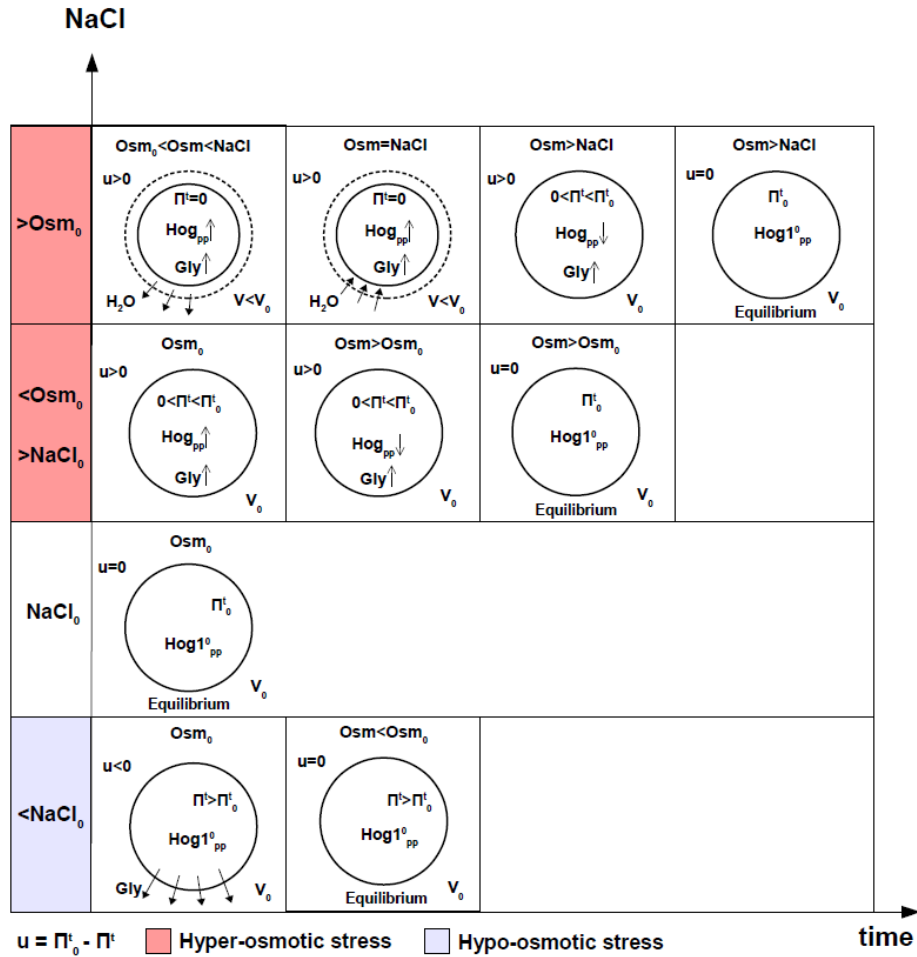


Figure 5.10. Schematic representation of the yeast cell adaptation to osmotic stress after the introduction of the modified Hog1 activation module.

The newly added assumptions to the module of Hog1 activation now allow to answer the research questions we set to investigate. The new model now shows the glycerol efflux and the restore of turgor pressure as well as makes it possible to model effects of various mutations in the MAPK pathways. See Equations (5.9)-(5.36), (5.38)-(5.46) with  $R = 8.31 \text{ kPa} \cdot \text{M}^{-1} \cdot \text{K}^{-1}$ ,  $T = 300 \text{ K}$ ,  $A \cdot L = 86 \cdot 10^{-3} \text{ min}^{-1} \cdot \text{kPa}^{-1}$ ,  $V_0 = 6.5 \cdot 10^{-14} \text{ L}$ ,  $\varepsilon = 1 \cdot 10^5$ ,  $Km_{16} = 0.6 \text{ M}$ ,  $[NaCl_0] = 0.175 \text{ M}$ ,  $v_b = 0.368$ ,  $k_1 = 0.005 \text{ kPa}^{-1} \cdot \text{min}^{-1}$ ,  $k_2 = 0.1 \text{ min}^{-1}$ ,  $k_3 = 0.2 \text{ kPa}^{-1} \cdot \text{min}^{-1}$ ,  $k_4 = 0.02 \text{ min}^{-1}$ ,  $k_5 = 0.03 \text{ min}^{-1}$ ,  $k_6 = 0.003 \text{ min}^{-1}$ ,  $k_7 = 15 \text{ min}^{-1}$ ,  $k_8 = 1 \text{ min}^{-1}$ ,  $k_9 = 0.74 \text{ min}^{-1}$ ,  $k_{10} = 0.005 \text{ min}^{-1}$ ,  $k_{11} = 0.006 \text{ kPa}^{-1} \cdot \text{min}^{-1}$ ,  $gsy_p^0 = 0.05$ ,  $gph_p^0 = 0.7$ ,  $glu_{ext}^0 = 3.3$ ,  $m_{11} = 0.6$ ,  $m_{12} = 3.4$ ,  $m_{13} = 1$ ,  $m_{14} = 1$ ,  $m_{15} = 0.1$ ,  $m_{17} = 0.1$ ,  $m_{18} = 0.2$ ,  $m_{19} = 0.2$ ,  $m_{20} = 60$ ,  $l_t = 0.097$ ,  $x_{2_t} = 0.934$ ,  $x_{3_t} = 0.177$ ,  $x_{4_t} = 0.032$ ,  $h_t = 0.038$ ,  $y_{2_t} = 0.108$ ,  $z_{1_t} = 0.319$ ,  $z_{2_t} = 1$ ,  $p_t = 0.02$ ,  $p_{1_t} = 0.005$ ,  $p_{2_t} = 0.01$ ,  $p_{3_t} = 0.021$ ,  $p_{4_t} = 0.1$ ,  $m_1 = 2$ ,  $m_2 = 2$ ,  $m_3 = 2$ ,  $m_4 = 1$ ,  $m_5 = 1$ ,  $m_6 = 1$ ,  $m_7 = 2$ ,  $m_8 = 2$ ,  $m_9 = 2$ ,  $m_{10} = 1$ ,  $f_1 = 5 \text{ min}^{-1}$ ,  $f_2^p = 12 \text{ min}^{-1}$ ,  $f_3^p = 17 \text{ min}^{-1}$ ,  $ff_1 = 0.005 \text{ min}^{-1}$ ,  $b_1 = 0.003 \text{ min}^{-1}$ ,  $b_2^p = 2.3 \text{ min}^{-1}$ ,  $bb_1 = 3.2 \text{ min}^{-1}$ ,  $d_4 = 5 \text{ min}^{-1}$ ,  $d_5 = 4.6 \text{ min}^{-1}$ ,  $d_6 = 5.4 \text{ min}^{-1}$ ,  $dd_2 = 4.3 \text{ min}^{-1}$ ,  $dd_3 = 1.7 \text{ min}^{-1}$ ,  $hh_1 = 5.4 \text{ min}^{-1}$ ,  $hh_2 = 1.5 \text{ min}^{-1}$ ,  $hh_3 = 5 \text{ min}^{-1}$ ,  $hh_4 = 5 \text{ min}^{-1}$ ,  $hh_5 = 5 \text{ min}^{-1}$ .

Figure 5.10 schematically illustrates the model results for the yeast adaptation to the osmotic stress after the introduction of the detailed Hog1 activation module. The quantitative results can be found in Appendix D (Figures 7.13-7.15). Now, after the introduction of the detailed Hog1 activation module, the cell demonstrates the glycerol efflux under the hypo-osmotic stress (Figure 7.15C) as well as to restore its equilibrium turgor pressure (Figure 7.15D) while demonstrating the same results for the adaptation of other components to the previously added assumption such as restore of the volume and the turgor pressure under the hyper-osmotic conditions (Figures 7.13-7.14). Here we assume that the volume fluctuation within 10% from the equilibrium level is not significant and therefore we will further refer to this fluctuation as if it was no change in the volume. Moreover, after the introduction of the detailed glycerol metabolism and Hog1 activation modules, we can now perform the analysis of the effects of mutations in Hog1 pathway as well as test the model under the conditions where the external glucose is consumed.

Figure 5.11 shows the comparison between the two biological strains of *C. glabrata*, BG2 (Figure 5.11A) and 2001 (Figure 5.11C). *C. glabrata* 2001 strain differs from BG2 strain by the truncated Ssk2 gene [293]. Therefore, in 2001 strain the signal is transmitted through the Sho1 branch only. Figure 5.11B shows the new model predictions for Hog1 phosphorylation time course in BG2 strain under the three levels of the hyper-osmotic stress: 0.4M, 0.8M and 1.5M. The assumptions, introduced in this subsection for the signalling in the yeast Hog1 pathway, allow to model the 2001 strain by deletion of Ssk2 protein in the Sln1 signalling pathway. Figure 5.11D illustrates the model predictions for Hog1 phosphorylation in 2001 strain under the three NaCl concentrations tested in BG2 strain. It can be seen from the comparison of Figures 5.11B and 5.11D that there is no qualitative difference between these two strains. The variation of the model parameters also makes no difference to this qualitative result (data not shown). This is not what has been expected because it contradicts unpublished information we received from Professor Ken Haynes' experimental group (University of Exeter), that in 2001 strain under high NaCl concentration (1.5M)

there is a decrease in magnitude, which is not observed in BG2 strain. In the next subsection we will propose a hypothetical mechanism of this effect.

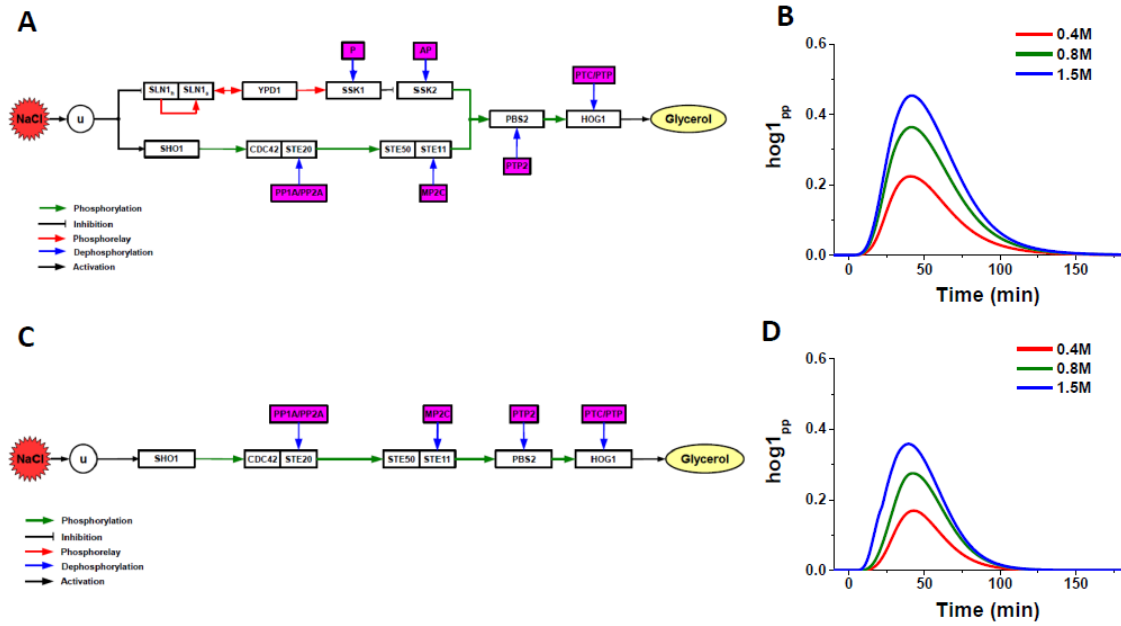


Figure 5.11. The comparison of the model predictions for Hog1 phosphorylation in *C. glabrata* BG2 and 2001 strains response to the different hyper-osmotic NaCl concentrations.

A. The schematic representation of the pathways that lead to the activation of Hog1 in *C. glabrata* BG2 strain. B. The phosphorylation of Hog1 in response to 0.4M, 0.8M and 1.5M of NaCl in *C. glabrata* BG2 strain. C. The schematic representation of the pathways that lead to the activation of Hog1 in *C. glabrata* 2001 strain. D. The phosphorylation of Hog1 in response to 0.4M, 0.8M and 1.5M of NaCl in *C. glabrata* 2001 strain. See Equations (5.9)-(5.36), (5.38)-(5.46) with  $R = 8.31 \text{ kPa} \cdot \text{M}^{-1} \cdot \text{K}^{-1}$ ,  $T = 300 \text{ K}$ ,  $A \cdot L = 86 \cdot 10^{-3} \text{ min}^{-1} \cdot \text{kPa}^{-1}$ ,  $V_0 = 6.5 \cdot 10^{-14} \text{ L}$ ,  $\varepsilon = 1 \cdot 10^5$ ,  $Km_{16} = 0.6 \text{ M}$ ,  $[NaCl_0] = 0.175 \text{ M}$ ,  $v_b = 0.368$ ,  $k_1 = 0.005 \text{ kPa}^{-1} \cdot \text{min}^{-1}$ ,  $k_2 = 0.1 \text{ min}^{-1}$ ,  $k_3 = 0.2 \text{ kPa}^{-1} \cdot \text{min}^{-1}$ ,  $k_4 = 0.02 \text{ min}^{-1}$ ,  $k_5 = 0.03 \text{ min}^{-1}$ ,  $k_6 = 0.003 \text{ min}^{-1}$ ,  $k_7 = 15 \text{ min}^{-1}$ ,  $k_8 = 1 \text{ min}^{-1}$ ,  $k_9 = 0.74 \text{ min}^{-1}$ ,  $k_{10} = 0.005 \text{ min}^{-1}$ ,  $k_{11} = 0.006 \text{ kPa}^{-1} \cdot \text{min}^{-1}$ ,  $gsy_p^0 = 0.05$ ,  $gph_p^0 = 0.7$ ,  $glu_{ext}^0 = 3.3$ ,  $m_{11} = 0.6$ ,  $m_{12} = 3.4$ ,  $m_{13} = 1$ ,  $m_{14} = 1$ ,  $m_{15} = 0.1$ ,  $m_{17} = 0.1$ ,  $m_{18} = 0.2$ ,  $m_{19} = 0.2$ ,  $m_{20} = 60$ ,  $l_t = 0.097$ ,  $x_{2_t} = 0.934$ ,  $x_{3_t} = 0.177$ ,  $x_{4_t} = 0.032$  in (B) and  $x_{4_t} = 0$  in (D),  $h_t = 0.038$ ,  $y_{2_t} = 0.108$ ,  $z_{1_t} = 0.319$ ,  $z_{2_t} = 1$ ,  $p_t = 0.02$ ,  $p_{1_t} = 0.005$ ,  $p_{2_t} = 0.01$ ,  $p_{3_t} = 0.021$ ,  $p_{4_t} = 0.1$ ,  $m_1 = 2$ ,  $m_2 = 2$ ,  $m_3 = 2$ ,  $m_4 = 1$ ,  $m_5 = 1$ ,  $m_6 = 1$ ,  $m_7 = 2$ ,  $m_8 = 2$ ,  $m_9 = 2$ ,  $m_{10} = 1$ ,  $f_1 = 5 \text{ min}^{-1}$ ,  $f_2^p = 12 \text{ min}^{-1}$ ,  $f_3^p = 17 \text{ min}^{-1}$ ,  $ff_1 = 0.005 \text{ min}^{-1}$ ,  $b_1 = 0.003 \text{ min}^{-1}$ ,  $b_2^p = 2.3 \text{ min}^{-1}$ ,  $bb_1 = 3.2 \text{ min}^{-1}$ ,  $d_4 = 5 \text{ min}^{-1}$ ,  $d_5 = 4.6 \text{ min}^{-1}$ ,  $d_6 = 5.4 \text{ min}^{-1}$ ,  $dd_2 = 4.3 \text{ min}^{-1}$ ,  $dd_3 = 1.7 \text{ min}^{-1}$ ,  $hh_1 = 5.4 \text{ min}^{-1}$ ,  $hh_2 = 1.5 \text{ min}^{-1}$ ,  $hh_3 = 5 \text{ min}^{-1}$ ,  $hh_4 = 5 \text{ min}^{-1}$ ,  $hh_5 = 5 \text{ min}^{-1}$ .

#### 5.4.4 Modification 4 of receptor activation

Under the plasmolysis, when the cell shrinks due to the water efflux through the AQP channels, the membrane is deformed [301]. Due to the fact that both Sho1 and Sln1 are located on the cell membrane, in this subsection we introduce a new experimentally testable hypothesis that activity of the mechanoreceptors depends on the mechanical properties of the cell membrane and therefore that under the plasmolysis part of the membrane receptors lose their functionality. We propose that the part of the active membrane receptors  $k_r$  can be described as follows:

$$\frac{dk_r}{dt} = \frac{1}{t_r} (k_r^* - k_r(t)), \quad (5.47)$$

$$\text{where } k_r^* = \begin{cases} 1, V \geq V_0 \\ \left(\frac{V}{V_0}\right)^m, V_1 \leq V \leq V_0 \\ \left(\frac{V_1}{V_0}\right)^m = k_{r\min}^*, V \leq V_1 \end{cases},$$

$k_{r\min}^*$  is the minimum part of active receptors for the volume  $V_1$ ,  $t_r = \begin{cases} t_r^1, k_r > k_r^* \\ t_r^2, k_r \leq k_r^* \end{cases}$ .

We assume that the time required for the increase in number of receptors is much greater than the time required for their decrease:  $t_r^2 \gg t_r^1$ . We also assume  $m=8$  since it seems to be sufficient to describe the rapid decrease in number of receptors when the volume is decreasing.

We now test the effect of the new assumption on our model for the following assumed parameters:  $k_{r\min}^* = 0.1$ ,  $t_r^2 = 1 \cdot 10^6$  min,  $t_r^1 = 1 \cdot 10^{-3}$  min. It can be seen from Figures 7.16-7.18 in Appendix D that there is no qualitative difference to the model predictions for BG2 strain after the introduction of the new assumption, compared to Figures 7.13-7.15. The cell behaviour remains the same to the previous case shown in Figure 5.10.

Next we check if the new model produces any qualitative difference to the

behaviour shown in Figure 5.11. Figure 5.12 shows the model predictions for BG2 (Figure 5.11A) and 2001 (Figure 5.11B) strains under 0.4M, 0.8M and 1.5M of NaCl after the introduction of the changes to the receptors activation. In contrast to Figure 5.11, the developed model now demonstrates a decrease in magnitude of Hog1 phosphorylation observed only for 2001 strains under high salt concentrations (Figure 5.12E) while BG2 lacks the decrease in magnitude of Hog1 phosphorylation for 1.5M of NaCl (Figure 5.12B). This is in line with the observations reported by Professor Ken Haynes' experimental group. Moreover, the developed model predicts that there is a time delay in *C. glabrata* Hog1 phosphorylation under higher concentrations of NaCl (Figures 5.12B and 5.12E). This delay, but not the decrease of phosphorylated Hog1 for higher NaCl concentrations, was also experimentally established for *S. cerevisiae* in [316].

It can be seen from the figure that our model predicts the volume loss due the water efflux only for 2001 but not for BG2 strains under 1.5M of NaCl (Figure 5.12D). According to the assumptions of our model, the amount of the active mechanoreceptors depends on the cell volume. Figure 5.12F shows that the number of the active receptors significantly decreases (down to 10%) under the plasmolysis, which occurs only for 2001 strains under 1.5M of NaCl. In contrast, the model predictions for BG2 strains demonstrate no volume loss (Figure 5.12A) and as a consequence of this, most (about 80%) mechanoreceptors on the cell membrane remained in their active state (Figure 5.12C).

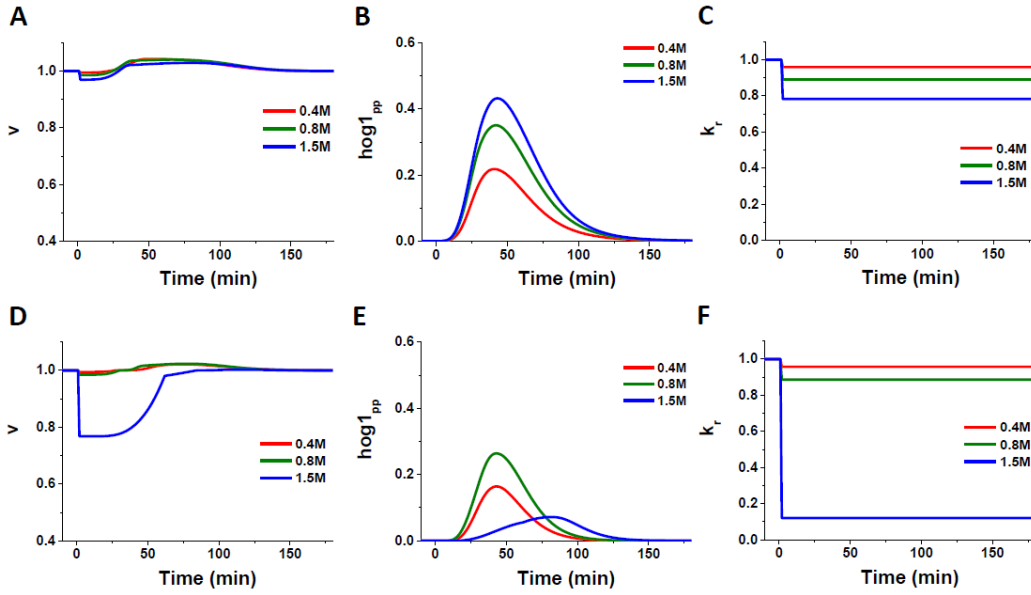


Figure 5.12. The comparison of the model predictions for *C. glabrata* 2001 and BG2 strains response to the hyper-osmotic stress.

The model results for *C. glabrata* BG2 (A-C) and 2001 (D-F) species. While the cell volume remains constant in BG2 strain (A), it changes only in 2001 strain under 1.5M of NaCl (D). The model suggests experimentally testable prediction for the delay of Hog1 phosphorylation in both BG2 (B) and 2001 (E) species accompanied with a decrease in phosphorylation level of Hog1 in 2001 strain under 1.5M of NaCl (E), which is not observed in BG2 strains (B). The structure of our model suggests that this Hog1 phosphorylation magnitude decrease for 2001 strains under 1.5M of NaCl is due to a significant (by 90%) decrease in the number of active receptors (F) caused by the volume loss shown in (D). In contrast, the number of active membrane receptors shows less decrease in BG2 strain (C). See Equations (5.9)-(5.36), (5.38)-(5.47) with  $R = 8.31 \text{ kPa} \cdot \text{M}^{-1} \cdot \text{K}^{-1}$ ,  $T = 300 \text{ K}$ ,  $A \cdot L = 86 \cdot 10^{-3} \text{ min}^{-1} \cdot \text{kPa}^{-1}$ ,  $V_0 = 6.5 \cdot 10^{-14} \text{ L}$ ,  $\varepsilon = 1 \cdot 10^5$ ,  $Km_{16} = 0.6 \text{ M}$ ,  $[NaCl_0] = 0.175 \text{ M}$ ,  $v_b = 0.368$ ,  $k_1 = 0.005 \text{ kPa}^{-1} \cdot \text{min}^{-1}$ ,  $k_2 = 0.1 \text{ min}^{-1}$ ,  $k_3 = 0.2 \text{ kPa}^{-1} \cdot \text{min}^{-1}$ ,  $k_4 = 0.02 \text{ min}^{-1}$ ,  $k_5 = 0.03 \text{ min}^{-1}$ ,  $k_6 = 0.003 \text{ min}^{-1}$ ,  $k_7 = 15 \text{ min}^{-1}$ ,  $k_8 = 1 \text{ min}^{-1}$ ,  $k_9 = 0.74 \text{ min}^{-1}$ ,  $k_{10} = 0.005 \text{ min}^{-1}$ ,  $k_{11} = 0.006 \text{ kPa}^{-1} \cdot \text{min}^{-1}$ ,  $gsy_p^0 = 0.05$ ,  $gph_p^0 = 0.7$ ,  $glu_{ext}^0 = 3.3$ ,  $m_{11} = 0.6$ ,  $m_{12} = 3.4$ ,  $m_{13} = 1$ ,  $m_{14} = 1$ ,  $m_{15} = 0.1$ ,  $m_{17} = 0.1$ ,  $m_{18} = 0.2$ ,  $m_{19} = 0.2$ ,  $m_{20} = 60$ ,  $l_t = 0.097$ ,  $x_{2_t} = 0.934$ ,  $x_{3_t} = 0.177$ ,  $x_{4_t} = 0.032$  in (A), (B), (C) and  $x_{4_t} = 0$  in (D), (E), (F),  $h_t = 0.038$ ,  $y_{2_t} = 0.108$ ,  $z_{1_t} = 0.319$ ,  $z_{2_t} = 1$ ,  $p_t = 0.02$ ,  $p_{1_t} = 0.005$ ,  $p_{2_t} = 0.01$ ,  $p_{3_t} = 0.021$ ,  $p_{4_t} = 0.1$ ,  $m_1 = 2$ ,  $m_2 = 2$ ,  $m_3 = 2$ ,  $m_4 = 1$ ,  $m_5 = 1$ ,  $m_6 = 1$ ,  $m_7 = 2$ ,  $m_8 = 2$ ,  $m_9 = 2$ ,  $m_{10} = 1$ ,  $f_1 = 5 \text{ min}^{-1}$ ,  $f_2^p = 12 \text{ min}^{-1}$ ,  $f_3^p = 17 \text{ min}^{-1}$ ,  $ff_1 = 0.005 \text{ min}^{-1}$ ,  $b_1 = 0.003 \text{ min}^{-1}$ ,  $b_2^p = 2.3 \text{ min}^{-1}$ ,  $bb_1 = 3.2 \text{ min}^{-1}$ ,  $d_4 = 5 \text{ min}^{-1}$ ,  $d_5 = 4.6 \text{ min}^{-1}$ ,  $d_6 = 5.4 \text{ min}^{-1}$ ,  $dd_2 = 4.3 \text{ min}^{-1}$ ,  $dd_3 = 1.7 \text{ min}^{-1}$ ,  $hh_1 = 5.4 \text{ min}^{-1}$ ,  $hh_2 = 1.5 \text{ min}^{-1}$ ,  $hh_3 = 5 \text{ min}^{-1}$ ,  $hh_4 = 5 \text{ min}^{-1}$ ,  $hh_5 = 5 \text{ min}^{-1}$ ,  $k_{r_{min}}^* = 0.1$ ,  $t_r^2 = 1 \cdot 10^6 \text{ min}$ ,  $t_r^1 = 1 \cdot 10^{-3} \text{ min}$ .

The structure of our model suggests an explanation for the effect of phosphorylated Hog1 magnitude decrease under 1.5M of NaCl. Due to the fact that in 2001 strains only the Sho1 branch is present, the biochemical part returns lower (comparing to BG2 strains) phosphorylation level of Hog1 in equilibrium (Figure 5.5). This in turn leads to the lower level of glycerol production and lower threshold concentration of osmotically active elements inside the cell in equilibrium  $[Osm_0]$ . In this case 1.5M of NaCl becomes larger than the  $[Osm_0]$ , which makes the yeast cell more sensitive to osmotic shock. Our model suggests that when  $[NaCl] > [Osm_0]$ , the cell is subject to a strong hyper-osmotic stress (Figure 5.10) and decreases its volume (Figure 5.12D). According to the assumptions of our model, the loss of the cell volume leads to the significant decrease in the number of the active mechanoreceptors (Figure 5.12F) and therefore to the decrease in Hog1 phosphorylation level (Figure 5.12E). Thus, according to our model, *C. glabrata* 2001 strain is more sensitive to hyper-osmotic stress compared to BG2 strain.

Now, after the introduction of all modifications made to the Gennemark model [47] and identifying the effects of each of the newly added assumptions in this section, we will perform the quantitative analysis of the developed model in the next section.

## 5.5 Quantitative analysis of the developed model

In the previous section we proposed a new model for the yeast adaptation to the osmotic stress using the previously published model by Gennemark [47] and performed its qualitative analysis. In this section we will perform quantitative analysis of the newly developed model.

First, we summarise the final system of equations that will be used in this section. Using Equations (5.19), (5.24), (5.26), (5.28), (5.32), (5.34), (5.36), (5.46) and (5.47) we can write the system of ODEs:

$$\begin{aligned}
\frac{dv}{dt} &= K \cdot \left( RT \left( \left( \frac{n}{v-v_b} + gly \right) \cdot Km_{16} - [NaCl] \right) - \max(0, \Pi'_0 + \varepsilon \cdot \ln(v)) \right) \\
\frac{dgsy_p}{dt} &= k_r \cdot (U(v, u) + L_1) \cdot \frac{k_1}{v-v_b} \cdot \frac{gsy}{m_{11} + gsy} - \frac{k_2}{v-v_b} \cdot \frac{gsy_p}{m_{12} + gsy_p} - gsy_p \cdot D(v), \\
\frac{dgph_p}{dt} &= k_r \cdot (U(v, u) + L_2) \cdot \frac{k_3}{v-v_b} \cdot \frac{gph}{m_{13} + gph} - \frac{k_4}{v-v_b} \cdot \frac{gph_p}{m_{14} + gph_p} - gph_p \cdot D(v), \\
\frac{d}{dt} glu &= k_5 \cdot H(glu_{ext} - glu) \cdot \frac{glu_{ext} - glu}{m_{15} + glu_{ext} - glu} - k_6 \cdot gsy \cdot \frac{glu}{1 + glu} + \\
&\quad + k_7 \cdot gph_p \cdot \frac{gln}{m_{17} + gln} - k_8 \cdot z2_{pp} \cdot \frac{glu}{m_{18} + glu} - glu \cdot D(v), \\
\frac{d}{dt} gln &= k_6 \cdot gsy \cdot \frac{glu}{1 + glu} - k_7 \cdot gph_p \cdot \frac{gln}{m_{17} + gln} - gln \cdot D(v), \\
\frac{dfps1_p}{dt} &= k_9 \cdot z2_{pp} \cdot \frac{fps1}{m_{19} + fps1} - \frac{k_{10}}{v-v_b} \cdot \frac{fps1_p}{m_{20} + fps1_p} - fps1_p \cdot D(v), \\
\frac{d}{dt} gly &= k_8 \cdot z2_{pp} \cdot \frac{glu}{m_{18} + glu} - k_{11} \cdot \bar{U}(v, u) \cdot fps1 \cdot gly - gly \cdot D(v), \\
\frac{d}{dt} glu_{ext} &= k_{12} \cdot glu_{ext} - k_5 \cdot H(glu_{ext} - glu) \cdot \frac{glu_{ext} - glu}{m_{15} + glu_{ext} - glu} - glu_{ext} \cdot D(v), \\
\frac{d}{dt} x1_p &= f_1 \cdot x1 - b_1 \cdot x1_p - f_2^p \cdot x1_p \cdot x2 + b_2^p \cdot x1 \cdot x2_p - x1_p \cdot D(v), \\
\frac{d}{dt} x2_p &= f_2^p \cdot x1_p \cdot x2 - b_2^p \cdot x1 \cdot x2_p - f_3^p \cdot x2_p \cdot x3 - x2_p \cdot D(v), \\
\frac{d}{dt} x3_p &= f_3^p \cdot x2_p \cdot x3 - d_4 \cdot x3_p p - x3_p \cdot D(v), \\
\frac{d}{dt} x4_p &= d_5 \cdot x3x4 - d_6 \cdot x4_p p1 - x4_p \cdot D(v), \\
\frac{d}{dt} y1_p &= ff_1 \cdot y1 - bb_1 \cdot y1_p - y1_p \cdot D(v), \\
\frac{d}{dt} y2_p &= dd_2 \cdot y1_p y2 - dd_3 \cdot y2_p p2 - y2_p \cdot D(v), \\
\frac{d}{dt} z1_p &= hh_1 \cdot x4_p z1 + hh_2 \cdot y2_p z1 - hh_3 \cdot z1_p p3 - hh_1 \cdot x4_p z1_p - \\
&\quad - hh_2 \cdot y2_p z1_p + hh_3 \cdot z1_{pp} p3 - z1_p \cdot D(v), \\
\frac{d}{dt} z1_{pp} &= hh_1 \cdot x4_p z1_p + hh_2 \cdot y2_p z1_p - hh_3 \cdot z1_{pp} p3 - z1_{pp} \cdot D(v), \\
\frac{d}{dt} z2_p &= hh_4 \cdot z1_{pp} z2 - hh_5 \cdot z2_p p4 - hh_4 \cdot z1_{pp} z2_p + hh_5 \cdot z2_{pp} p4 - z2_p \cdot D(v), \\
\frac{d}{dt} z2_{pp} &= hh_4 \cdot z1_{pp} z2_p - hh_5 \cdot z2_{pp} p4 - z2_{pp} \cdot D(v),
\end{aligned} \tag{5.48}$$



$$\frac{dk_r}{dt} = \frac{1}{t_r} (k_r^* - k_r(t)),$$

where the algebraic Equations (5.23), (5.31), (5.43) and (5.44) are also used.

The parameter values are taken from the previous section where they have been chosen "by hand". We will further refer to this chosen parameter set as "nominal". Now we need to find the set of parameters that demonstrates a reasonable fitting to the experimental data provided by Professor Ken Haynes' group.

### 5.5.1 Obtaining the set of parameters

In simulations described in Section 5.4, we have been using parameter sets selected "by hand", for the sake of illustration of qualitative features afforded by the newly introduced parts of the model. In this subsection, in order to set our new model on a more quantitative footing, we select the parameters based on some experimental data. The experimental data available to us are seven time-dependent experimental measurements of Hog1 phosphorylation level in *C. glabrata* BG2 strain for 1.5M of NaCl obtained by the western blot experiments and kindly provided to us by Emily Cook (University of Exeter). The data can be seen in Figure 5.14 (red crosses). In order to perform the parameter fitting to the experimental data, we employ the Genetic Algorithm (GA) for optimisation integrated to MATLAB (<http://uk.mathworks.com/discovery/genetic-algorithm.html>). We use this algorithm to minimise the sum of the absolute squared errors between the experimental data and the model predictions for each point:  $SM = \sum_{i=1}^N (E_i - M_i)^2$ , where  $E$  is the experimental data,  $M$  is the model predictions and  $N = 7$  is the number of experimental measurements.

### 5.5.2 Identifiability of the parameters

We performed 15 optimisation procedures using the GA within 2-fold range of the nominal parameter set. The results of these experiments along with the nominal parameters are shown in Table 7.5 in Appendix D. Figure 5.13 illustrates the box plots for the distribution of the tested parameters after 15 optimisations. The deviation is presented in normalised form, i.e. each of the

parameters after 15 optimisations is divided by the corresponding value of the nominal parameter. Therefore, the deviation can be compared to 1 for each of the parameters. It can be seen from this figure that the deviated parameters are located within the tested range, which is expected and used to check the accuracy. Figure 5.13 shows that the deviation of the optimised parameters is relatively insignificant except the two parameters, namely  $hh_2$  and  $hh_4$ , have quite high divergence compared to the others.

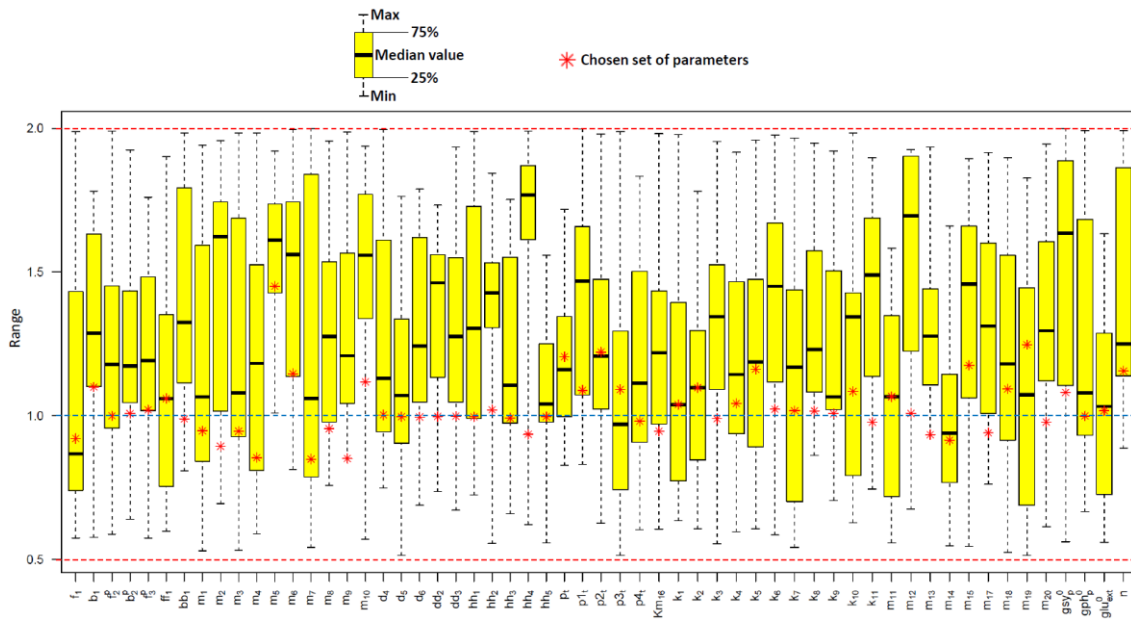


Figure 5.13. Distribution of the optimised parameters. The optimised model parameters are compared to the nominal set of parameters.

Unfortunately, even with the help of GA, a fully automatic choice of parameters appears to be impractical, as some of the essential constraints are hard to formalize in the form acceptable by the Matlab implementation of GA. So, despite the good fitting of the parameter sets presented in Table 7.5, some of these sets of parameters demonstrate unrealistic value for the concentration of osmotically active elements or "wrong" qualitative behaviour. For example, only 2 sets out of 15, namely sets "O13" and "O15", demonstrate the Hog1 phosphorylation decrease for 1.5M of NaCl shown in Figure 7.19 in Appendix D. However, despite this fact and the small squared error  $SM = 0.015$ , set "O13" gives unrealistically high  $[Osm_0] = 116.6$  M.

Therefore we choose the parameter set "O15" that also shows a reasonable fitting  $SM = 0.02$  with  $[Osm_0] = 1.96$  M while still demonstrating the Hog1 phosphorylation decrease for 1.5M of NaCl (Figure 7.19 in Appendix D). This set of parameters will be further used for the quantitative analysis and demonstration of the developed model predictions for BG2 and 2001 *C. glabrata* strains. Figure 5.14 shows the comparison of the experimental data for Hog1 phosphorylation time-course with the model predictions obtained by using the chosen set of the optimised parameters.

Limited however the presented evidence is, it suggests that within the selected ranges, there appears to be just one parameter set, up to relatively small variations, which satisfies all the qualitative constraints and reasonably conforms with the available experimental data.

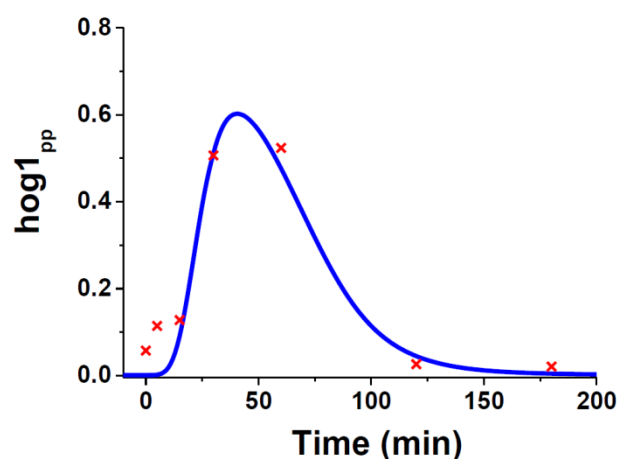


Figure 5.14. The comparison of the model predictions with the experimental data.

In order to validate the model we compare the experimental data (red crosses) with the model predictions (solid line, Equations (5.48), parameter set "O15" in Table 7.5.). The chosen set of the optimised parameters demonstrates a reasonable fitting with the squared error  $SM = 0.02$ .

### 5.5.3 Parameter sensitivity analysis

Now after we found the set of the optimised parameters that fits the experimental data we can perform the parameter sensitivity analysis in order to identify the most sensitive parameters for Hog1 phosphorylation time-course. We use the extended Fourier Amplitude Sensitivity Testing (eFAST) method

described in [256] and implemented in the SBToolbox [257]. Figure 5.15 shows the parameter sensitivity indices found for the phosphorylated Hog1.

Figure 5.15 shows that the most sensitive parameters for Hog1 phosphorylation are the total concentration of phosphatase  $p3_t$  that dephosphorylates Pbs2 and the forward reaction constant of Pbs2 dephosphorylation  $hh_3$ . The phosphorylated Hog1 also demonstrates sensitivity to  $p4_t$ , total concentration of phosphatase that dephosphorylates Hog1, and the forward reaction constant of Hog1 dephosphorylation  $hh_5$ .

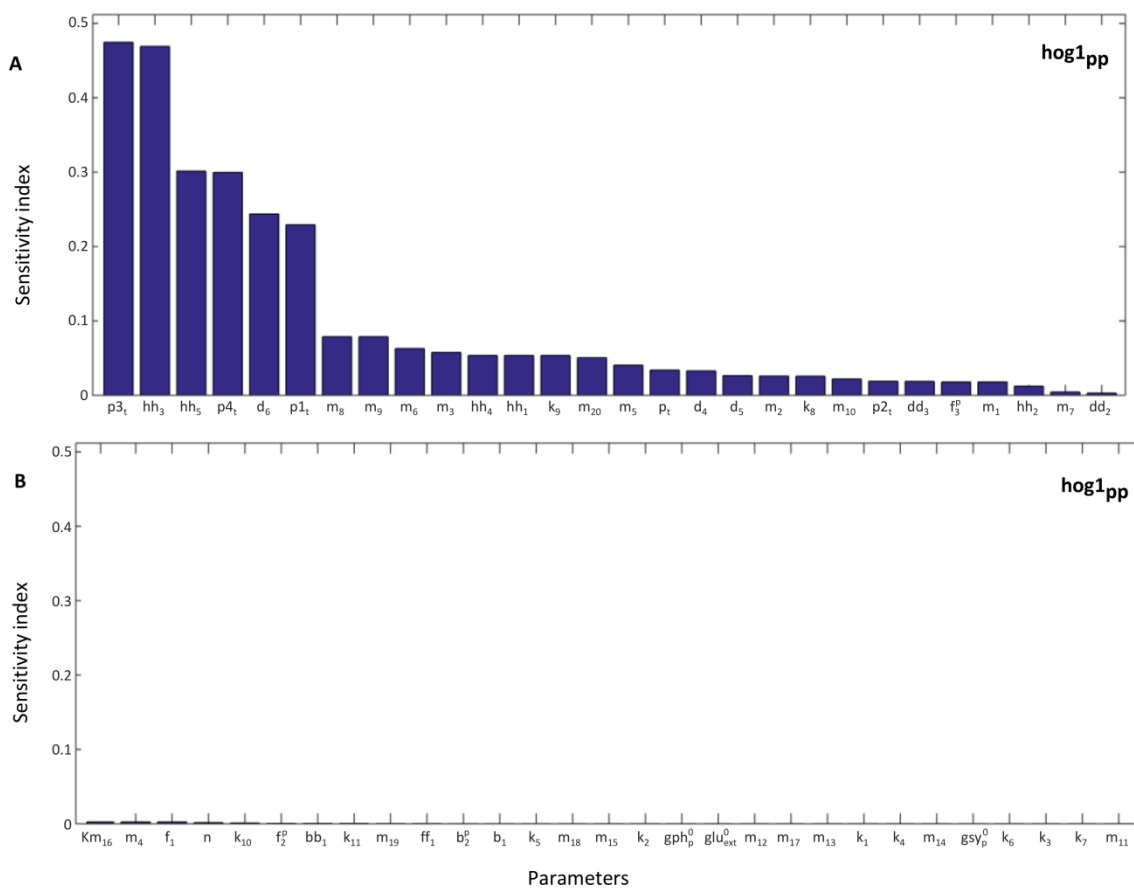


Figure 5.15. Sensitivity indices for Hog1 phosphorylation obtained by eFAST. Global sensitivity analysis of the developed model for the overall model predictions reveal the most sensitive (A) and the least sensitive (B) model parameters. The parameters are perturbed by 2-fold for 10000 simulations in eFAST.

Figure 5.16 illustrates the effects of perturbations of the most sensitive parameters on the model predictions for Hog1 phosphorylation (Figure 5.14). The most sensitive parameters  $p3_t$ ,  $hh_3$ ,  $hh_5$  and  $p4_t$  are perturbed within

2-fold range of their optimised values shown in parameter set "O15" in Table 7.5. It can be seen from Figure 5.16 that within this range of perturbation the overall shape of Hog1 phosphorylation time-course remains the same however the magnitude of Hog1p is different for the shown parametric changes. The perturbations of both  $p3_t$  and  $hh_3$  lead to the same effect on Hog1p as shown in Figure 5.16A. The perturbations of both  $hh_5$  and  $p4_t$  also lead to the same effect on Hog1p (Figure 5.16B). Increase of  $p3_t$ ,  $hh_3$ ,  $hh_5$  and  $p4_t$  leads to decrease of Hog1p magnitude. This is expected result as with an increase of phosphatase or enhancement of dephosphorylation, the concentration of phosphorylated Pbs2 and Hog1 should decrease.

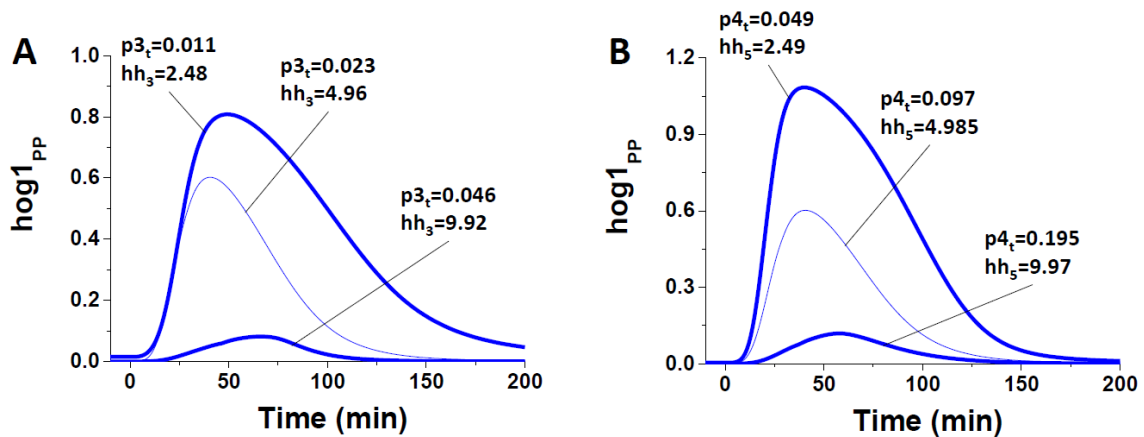


Figure 5.16. The effects of the perturbations of the most sensitive parameters on Hog1 phosphorylation.

The parameters  $p3_t$ ,  $hh_3$ ,  $hh_5$  and  $p4_t$  are perturbed within 2-fold range (bold lines) compared to their optimised values (thin line). Increase of  $p3_t$ ,  $hh_3$ ,  $hh_5$  and  $p4_t$  results in decrease of the phosphorylated Hog1. See Equations (5.48) with parameter set "O15" in Table 7.5.

## 5.6 Model predictions

After obtaining the parameters with a reasonable fitting and their analysis, in this section we show the model predictions using this set of parameters. Figure 5.17 shows the developed model time-course predictions under the strong hyper-osmotic stress 2.5M for the cell volume change (Figure 5.17A), phosphorylation level of Hog1 (Figure 5.17B), turgor pressure (Figure 5.17C)

and number of the active receptors (Figure 5.17D). We assume that under the plasmolysis (Figure 5.17A) some part of the membrane mechanoreceptors, that sense the changes in turgor pressure (Figure 5.17C), becomes less sensitive due to the cell volume loss and thereby change in the mechanical properties of the membrane. Therefore, the average number of the receptors decreases rapidly (Figure 5.17D).

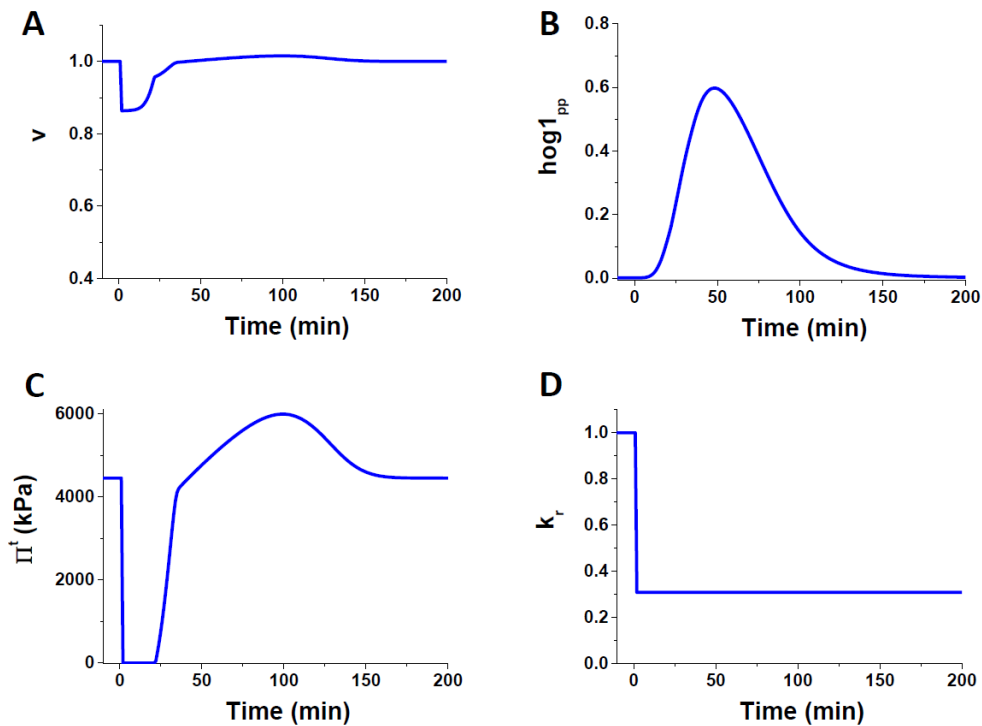


*Figure 5.17. The model predictions for biophysical changes and Hog1 phosphorylation in BG2 strains adaptation to hyper-osmotic stress.*

*A. The volume of the cell decreases immediately after the appliance of the hyper-osmotic stress and further restored. B. The model predictions for Hog1 phosphorylation level as a function of time. C. Turgor pressure falls down to zero due to the volume loss and restores after 150 minutes. D. Our model hypothesizes that under the plasmolysis some part of the membrane receptors lose their sensitivity. See Equations (5.48) with Parameter set "O15" in Table 7.5.*

Figure 5.18 illustrates our model predictions for the change in the concentrations of the glycerol metabolism module elements under the strong hyper-osmotic shock of 2.5M. It can be seen from the figure that the cell tends to adapt to extreme changes in osmolarity by increasing the production of

intracellular glycerol (Figure 5.18A). During the adaptation, intracellular glucose decreases due to its consumption for the glycerol production as shown in Figure 5.18B. Figure 5.18C illustrates the model predictions, according to which the amount of glycogen is decreased under the hyper-osmotic shock. This is due to the fact that glycogen is used as intracellular glucose storage and can be converted to glucose [307]. Glycerol contributes to the overall concentration of the osmotically active compounds inside the cell (Figure 5.18D). Our model suggests that the initial rapid increase in concentration of the osmotically active compounds in the cell is due to the initial volume loss under the plasmolysis, however then it maintains at the same level for the time corresponding to the volume increase (Figure 5.17A) and finally reaches the new equilibrium in order to compensate the change in NaCl.

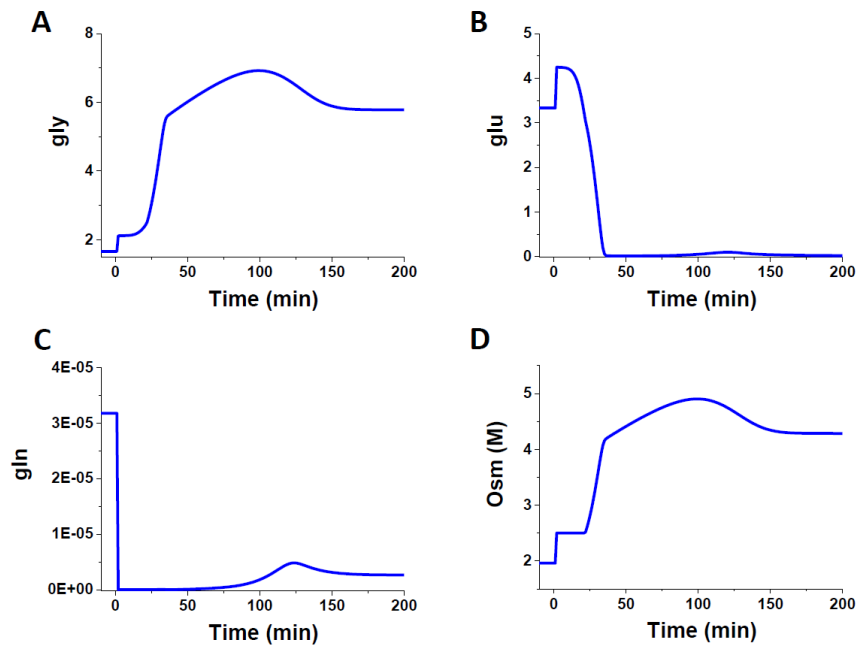


*Figure 5.18. The model predictions for the change in concentrations of the osmotically active compounds inside the cell in BG2 strains under hyper-osmotic stress.*

*The effects of change in extracellular NaCl concentration on the concentrations of intracellular glycerol (A), glucose (B), glycogen (C) and the concentration of all osmotic compounds inside the cell (D). Our model predicts that an increase in the intracellular osmotic concentration is supported by the consumption of the intracellular glycogen, which serves as the intracellular storage of glucose. See Equations (5.48) with parameter set "O15" in Table 7.5.*

As a next step, we test our model under the mild hyper-osmotic stress (1M of NaCl) and the hypo-osmotic stress (0.05M of NaCl) conditions, which was schematically shown in Figure 5.10. According to the model predictions, Hog1 is phosphorylated and thereby activated in the case of the mild hyper-osmotic stress (Figure 5.19A). Hog1 phosphorylation leads to an increase in the production of glycerol (Figure 5.19B). Our model predicts that under the hypo-osmotic stress Hog1 is not phosphorylated (Figure 5.19C). Figure 5.19D illustrates the model predictions for the glycerol change under the hypo-osmotic stress. This figure shows that the intracellular glycerol is rapidly exported from the cell through the glycerol channels in order to prevent the cell from bursting [325].

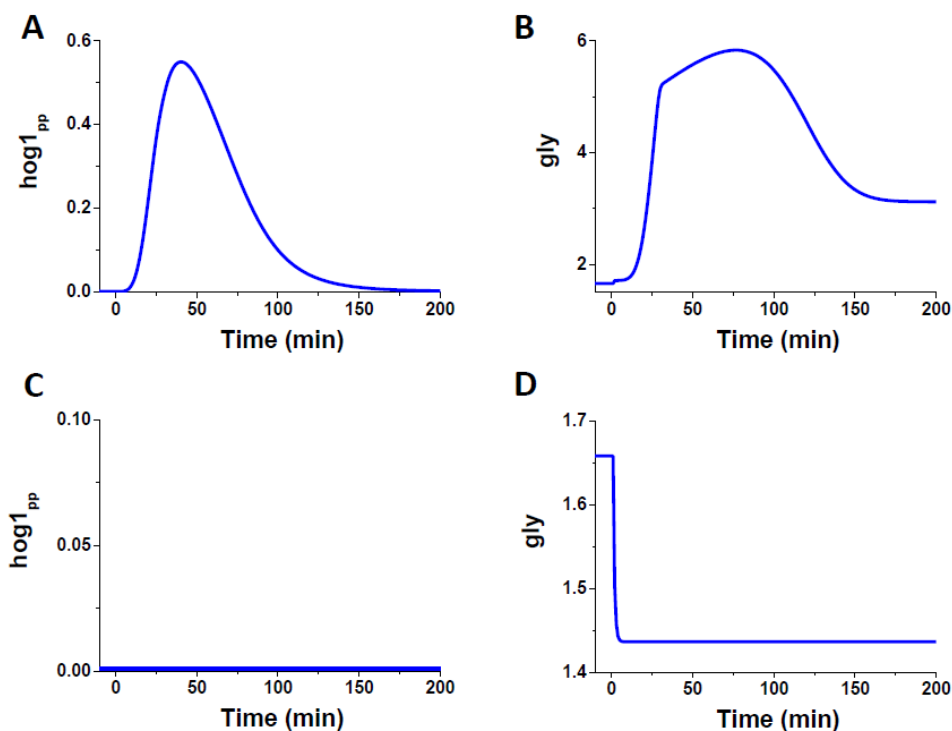


*Figure 5.19. Theoretical investigation of the adaptation of *C. glabrata* BG2 strains to the modest hyper- and the hypo-osmotic stress conditions.*

*A comparative analysis of the model predictions for the adaptation properties of *C. glabrata* BG2 strains to the mild hyper- (A, B) and hypo- (C, D) osmotic stress revealed the main differences in the underlying molecular mechanisms of adaptation. Hog1 is phosphorylated only in the case of hyper-osmotic stress (A) and not hypo-osmotic stress (C). The phosphorylated Hog1 leads to the production of glycerol in order to compensate the changes in turgor pressure (B). Under the hypo-osmotic stress glycerol channels open and glycerol is released from the cell to prevent the cell from bursting (D). See Equations (5.48) with parameter set "O15" in Table 7.5.*



### **5.6.1 The model predictions for Sho1 deletion and overexpression**

The proposed model is then applied to study the role of Sho1 receptors in *C. glabrata* adaptation to osmotic stress. First, we investigate the adaptation properties of BG2 Sho1 deletion strains (Figure 5.20A). In this species, the signal is transmitted through the Sln1 branch only [293]. Figure 5.20B shows the developed model predictions for the phosphorylated Hog1 dependence on time. Our model predicts that in the BG2 Sho1 deletion species the adaptation to hyper-osmotic stress takes longer time as indicated by the time required for phosphorylation of Hog1 (Figure 5.20B). Moreover, this figure shows a significant decrease (100 times) in magnitude of Hog1 phosphorylation compared to the BG2 and 2001 strains (Figure 7.19 in Appendix D). The time-course dependence for the magnitude of Hog1 phosphorylation (Figure 5.20B) suggests that the Sho1 branch has a significant contribution to the activation of Hog1 and thereby glycerol production under the hyper-osmotic stress.

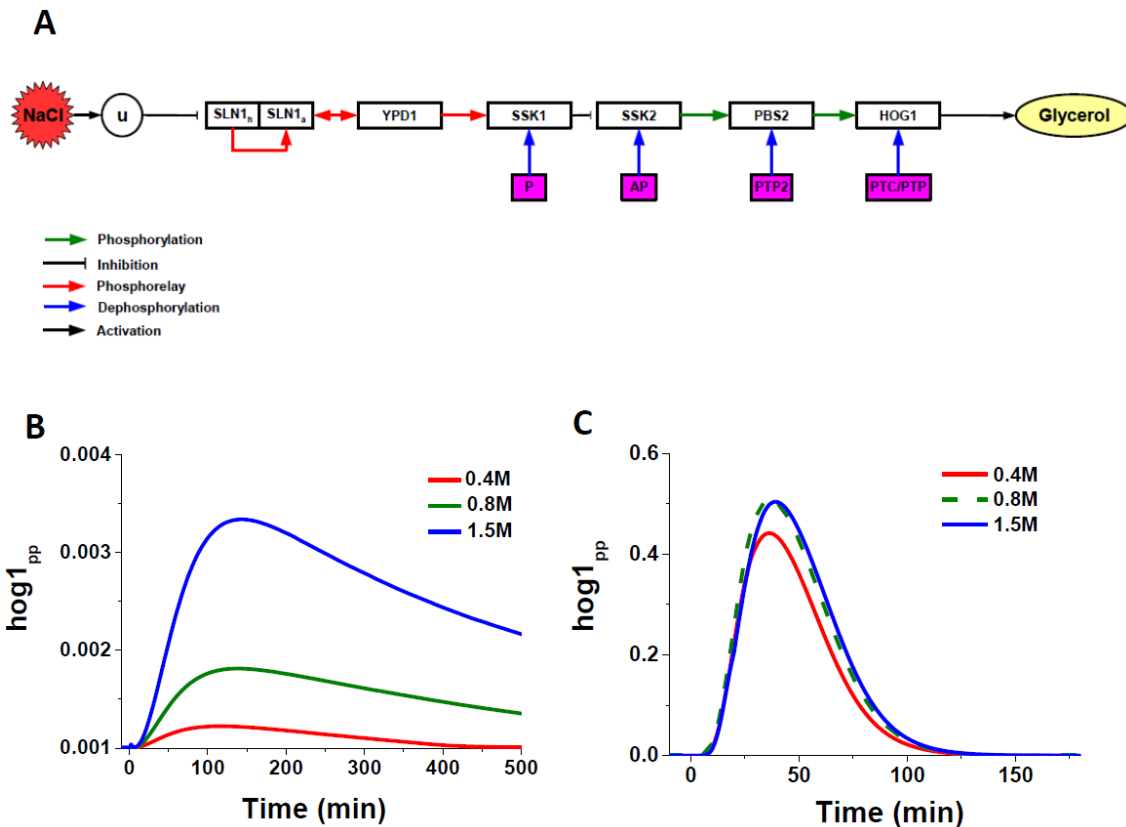


Figure 5.20. The model predictions for *C. glabrata* Sho1 deletion and overexpression.

A. Schematic representation of the signal transduction pathway involved in the activation of glycerol production in Sho1 deleted mutants. B. The model for the Sho1 deletion mutant predicts that the phosphorylation of Hog1 takes longer time compared to the BG2 strains and characterised by lower magnitude of phosphorylated Hog1 species. C. We test our model in the case of Sho1 overexpression in 2001 strain. The model predicts that the level of phosphorylated Hog1 increases noticeably. See Equations (5.48) with parameter set "O15" in Table 7.5, where  $h_i = 0$  in (B) and  $h_i = 0.38$ ,  $x4_i = 0$  in (C).

Next, we test our model for the overexpression of Sho1 receptors (ten times) in *C. glabrata* 2001 species. Our model assumption regarding the decrease in the number of the active receptors during plasmolysis led us to the model predictions for the delay and magnitude decrease of Hog1 phosphorylation in 2001 species obtained in one of the previous sections (Figure 7.19B). The model predictions for Hog1 phosphorylation levels with Sho1 overexpression in 2001 strain are illustrated in Figure 5.20C. This figure shows the experimentally testable predictions of our model, according to which Hog1 phosphorylation

level is increased in contrast to the case without Sho1 overexpression (Figure 5.12B). Our model predicts that in the case of overexpressed Sho1, phosphorylation levels of Hog1 under 0.4M, 0.8M and 1.5M of NaCl are distributed closer to each other.

According to our model assumptions, the level of Hog1 phosphorylation depends on the number of the active receptors. The model predictions for Hog1 phosphorylation in the case of overexpressed Sho1 receptors presented in this subsection would allow to test this assumption experimentally. If the assumption is correct, the overexpression of Sho1 in 2001 strain should lead to the phosphorylated Hog1 dependencies shown in Figure 5.20C and not in Figure 7.20.

### **5.6.2 Potential therapeutical application of the model**

We proposed and analysed a new mathematical model for the yeast adaptation to osmotic stress in the previous sections. Admittedly, the model structure and the parameter values are based on limited experimental data, and may have to be adjusted if and when more data become available. However, if we assume that this model is anywhere close to the reality, it may have some potential therapeutical applications.

*C. glabrata* is a human pathogenic yeast. It was shown that *C. glabrata* species are drug resistant and more tolerant to various extracellular stresses comparing to other yeast [45]. This fact impedes the effective treatment of the pathogens. Current *C. glabrata* treatment includes the use of drugs that have adverse side effects and it was reported that in some cases they are not effective [281,312-314]. In this subsection we make an attempt to suggest potential clinical applications of the developed model.

Previously we showed that the cell is able to adapt to the hyper-osmotic stress signal shown in Figure 5.3. According to the functional diagram shown in Figure 5.1, the yeast cell may decrease its ability to adapt to osmotic stress if the intracellular resource for adaptation (glycerol, glucose) is used up. In this subsection we test the developed model aiming to reach this case. We can do

this by applying the repetitive NaCl signal shown in Figure 5.21, which shows that this signal contains three parts. The first part (0-180 min) is the strong hyper-osmotic stress of 2.5M. The second part (180-370 min) is the hypo-osmotic stress of 0.05M. The last, third part is again the strong hyper-osmotic stress of 2.5M maintained until the end of the assumed experiment (600 min).

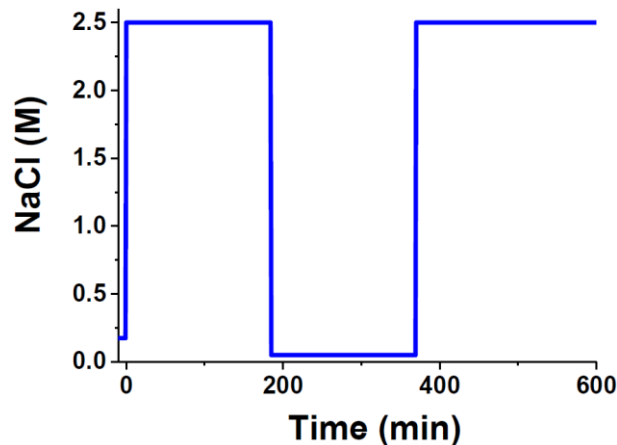


Figure 5.21. Double hyper-and-hypo-osmotic NaCl signal as a function of time. The developed model is tested under 2.5M and 0.05M of NaCl for 600 minutes. The concentration of 2.5M is applied after  $t = 0$  min and maintained during 180 min. In the range 180-370 min the cell is exposed to hypo-osmotic stress of 0.05M and then 2.5M of NaCl is applied again.

Figure 5.22 shows the model predictions for *C. glabrata* BG2 strain in response to the double hyper-and-hypo-osmotic stress (Figure 5.21). It can be seen from Figure 5.22 that under the first hyper-osmotic stress the intracellular resource such as glucose is accumulated (Figure 5.22A), glycerol is produced (Figure 5.22B), and Hog1 is phosphorylated (Figure 5.22C). The volume of the cell initially decreases but then restores (Figure 5.22D). The following hypo-osmotic stress leads to the glycerol efflux. Then, under the second hyper-osmotic stress, the glucose cannot accumulate (Figure 5.22A) due to the exhausted extracellular glucose (Figure 7.21A in Appendix D) and therefore glycerol cannot be increased significantly (Figure 5.22B) even in the presence of high Hog1 phosphorylation (Figure 5.22C). This affects the ability of the cell to restore its volume (Figure 5.22D) and turgor pressure after the second osmotic shock (Figure 7.21B).

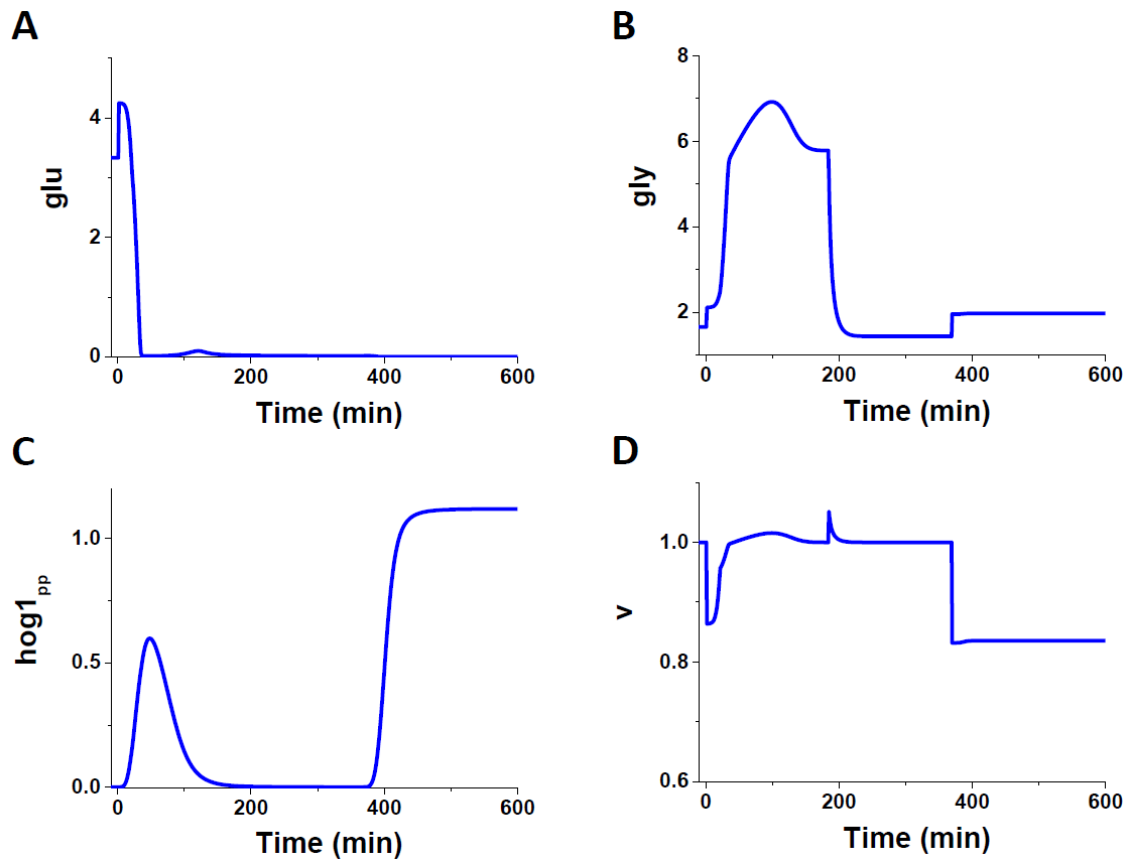


Figure 5.22. The model predictions for the double hyper-and-hypo-osmotic stress.

Under the first hyper-osmotic stress, the intracellular glucose (A), glycerol (B) are produced, Hog1 is phosphorylated (C) and the volume of the cell is restored. The following hypo-osmotic stress leads to the glucose and glycerol exhaustion (A and B). This results in the inability to produce the osmotically active glycerol (B) and restore the cell volume (D) after the second hyper-osmotic shock even in the presence of highly phosphorylated Hog1 (C). See Equations (5.48) with parameter set "O15" in Table 7.5.

We suggest here that when the yeast cell shrinks, it loses its viability, which is consistent with [326]. The model developed in this chapter predicts that the combination of the hyper-, hypo- and then hyper- osmotic stresses increases the vulnerability of *C. glabrata* pathogens.

Next we describe the effect of the non-dimensional concentration of extracellular glucose in equilibrium, denoted by parameter  $glu_{ext}^0$ , that defines the resource (glucose and glycerol) on the successful adaptation to hyper-osmotic stress. First, we test the model when the equilibrium glucose

concentration is increased from  $glu_{ext}^0 = 3.337$  to  $glu_{ext}^0 = 10$ . Figure 7.22 shows that the model predicts that *C. glabrata* is not vulnerable in this case. The glucose is accumulated (Figure 7.22A), glycerol is produced (Figure 7.22B), Hog1 phosphorylation returns to its equilibrium level (Figure 7.22C) and the volume of the cell restores (Figure 7.22D) after the second hyper-osmotic shock. Second, we test our model for the decreased  $glu_{ext}^0 = 0.3337$ . Figure 7.23 shows the model predictions under single hyper-osmotic stress, which is applied at  $t = 0$  and maintained for 600 min. Our model predicts that in this case, the decreased concentration of intracellular glucose in equilibrium leads to the increased vulnerability of the cell even under the single hyper-osmotic shock. Intracellular glucose cannot be accumulated (Figure 7.23A), glycerol production is not enough (Figure 7.23B) to restore the volume of the cell (Figure 7.23D) despite the presence of phosphorylated Hog1 (Figure 7.23C). These results suggest the important role of the equilibrium concentration of external glucose in *C. glabrata* cell vulnerability.

## 5.7 Conclusions

In this chapter we demonstrated the second example of high-level analysis of cellular signalling system in terms of Figure 1.1. We developed a model of the response of *C. glabrata* to osmotic stress based on the Gennemark model for *S. cerevisiae* [47] and using Equations (3.48) from Chapter 3. Our model links the intracellular multisite phosphorylation of Hog1 and glycerol metabolism with the biophysical adaptation of cell to osmotic stress. Due to the close genetic relation between *C. glabrata* and *S. cerevisiae*, the proposed model for *C. glabrata* adaptation to osmotic stress can be compared with the previously published modelling studies for *S. cerevisiae* [47-57].

The model developed in this chapter has the following advantages compared to the previously published models. First, our model includes the biophysical part that describes the volume and turgor pressure regulation. This part was absent in the group of previously published models [51-57]. Second, our model includes more detailed Hog1 activation module (Figure 5.9) compared to [47,48]. It is important to have the detailed Hog1 activation module because it

allows to test the model under various mutations in the MAPK pathways. Third, in our model we introduced the biochemical reactions rather than control functions that were used in the Gennemark model [47]. This seems to be more physiologically plausible. Fourth, the model developed in this chapter correctly describes the behaviour of the cell under the hypo-osmotic stress (Figure 5.10), where the cell should rapidly export glycerol in order to prevent the cell from bursting, which is in line with [317]. The model also demonstrates the recovery of both Hog1 phosphorylation level and the turgor pressure to their equilibrium level (Figure 5.10), which was not observed in the Gennemark model [47].

The detailed part of the model that includes the detailed MAPK signalling and multisite phosphorylation-regulated Hog1 activation allowed us to test the developed model and make the predictions of *C. glabrata* adaptation to osmotic stress for BG2 and 2001 strains. The predictions of our model for Hog1 phosphorylation in the *C. glabrata* BG2 strain are consistent with the experimental data obtained by Professor Ken Haynes' group (Figure 5.14).

The proposed model was applied to study the difference in the mechanisms of *C. glabrata* 2001 and BG2 strains adaptation to osmotic stress. Our model predicts the experimentally testable delay in *C. glabrata* Hog1 phosphorylation in both strains under the higher concentrations of NaCl, which was experimentally established in *S. cerevisiae* [316], as well as a decrease in the magnitude of phosphorylated Hog1 for 2001 strains under 1.5M of NaCl (Figure 5.12E). The developed model suggests a new mechanism of the yeast adaptation to osmotic stress that can explain this decrease in magnitude. According to the introduced assumption, the decrease in Hog1 magnitude phosphorylation is due to the loss of some transmembrane receptors activity under the plasmolysis (Figure 5.12F). The role of Sho1 mechanoreceptors in the adaptation to osmotic stress was also studied in this chapter by employing the developed model. Our model predicts that Sho1 has a significant role in the adaptation of *C. glabrata* to osmotic stress (Figure 5.20B), and that overexpression of Sho1 leads to an increase of phosphorylated Hog1 magnitude (Figure 5.20C).

Using the predictive power of the developed model we tested the model under the double hyper-and-hypo-osmotic stress signal shown in Figure 5.21. Our model predicts that, if the strong hyper-osmotic is followed by the hypo-osmotic and then the strong hyper-osmotic shock again, the cell uses up its resource such as glucose (Figure 5.22A) and glycerol (Figure 5.22B) for the successful adaptation to the final, maintained hyper-osmotic stress. The lack of these resource in turn leads to the inability of *C. glabrata* to restore its volume (Figure 5.22D) and therefore the turgor pressure. This in turn leads to the conclusion that *C. glabrata* cells become more vulnerable for this type of the osmotic signal. We also showed that when the external glucose concentration in equilibrium is decreased, the cells become more vulnerable for the hyper-osmotic shock. Due to the fact that pathogenic *C. glabrata* are more tolerant to osmotic shock [45], these findings may have a clinical significance.



## 6 Conclusions and further work

### 6.1 Conclusions

In this thesis we applied a Systems Biology approach to study cellular signal transduction. In Chapters 2 and 3 we investigated two basic multisite interactions, namely protein binding and phosphorylation. In Chapters 4 and 5 we performed a higher level analysis (in terms of Figure 1.1) studying STAT-STAT interactions in T cell plasticity and *C. glabrata* adaptation to osmotic stress. In this chapter the main findings of this thesis are summarised.

We studied ligand-dependent regulation of the activity of multisite binding proteins using an example of calcium-dependent protein calmodulin (CaM) in response to rapid change in calcium concentration in Chapter 2 of this thesis. Two physiological cases were investigated: i) when the ligand concentration significantly exceeded protein concentration [105,106] and ii) when the total amount of ligand is comparable with the protein concentration [107]. For these two cases, we built mathematical models and studied the dynamics of the concentrations of individual conformations with variable number of bound ligands. We identified that in both cases the concentration of intermediate conformations as a function of time demonstrates bell shapes (Figures 2.7, 2.8 and 2.11), whereas the concentrations of the apo- and fully saturated forms represent inhibitory and activatory monotonic shapes respectively (Figures 2.4 and 2.11). The difference in model predictions for the above mentioned cases is that in "ii" as the protein concentration rises, free ligand concentration becomes exhausted (Figure 2.10) in contrast to "i", where the ligand concentration is abundant. The analysis of cooperativity performed for "i" using CaM as an example of molecule with four binding sites, revealed that the model time-dependent predictions for the cases with cooperativity and without cooperativity differ quantitatively rather than qualitatively as shown in Figure 2.9.

We derived the characteristic times and the dynamics for the kinetic responses elicited by a ligand concentration change as a function of ligand concentration and the number of ligand binding sites. The concentration of effector proteins regulated by multisite ligand binding was shown to depend on ligand concentration in a highly nonlinear fashion. The model developed in Chapter 2

shows that not only the number of bound ligands but also the ligand temporal regulation can lead to the intracellular multifunctionality of multisite proteins.

Due to the structure of CaM molecule, for the first time to our knowledge, we considered the independent binding to CaM (consistent with [20]), which is different from the previously published model [93], where the sequential binding of CaM was considered. Therefore our description of calcium binding might be physiologically more meaningful compared to the previously published model [93] and can be used to model other calcium-dependent effector proteins such as TnC and CaN.

The model proposed in Chapter 2 may have applications in understanding the results of experiments studying the dependence of kinetics of ligand binding reactions on hydrostatic pressure [78,89,112]. In these experiments pressure is changed rapidly, which results in the rapid change of reaction constants and transition of the system from initial steady-state to a new steady-state. The equilibrium constants then are calculated by biologists using the obtained experimental data for the kinetic transition processes. However, this approach requires physiologically plausible description of the molecular interactions and equations for the reaction constants. For example, in previous studies [19,93] the equations for the sequential multisite calcium binding were applied to EF-hand proteins [94-97], whereas binding of calcium to the EF-hand proteins is non-sequential [20]. This may result in the incorrect interpretation of the experimental data. Therefore, the developed model may allow for a novel and more accurate interpretation of concentration and pressure jump-dependent kinetic experiments [78,89,112].

Phosphorylation of proteins was studied in Chapter 3. In this chapter we developed a model for single- and multisite phosphorylation. The model offers new features as opposed to the previously published models for single- [23-26,29,152] and multisite phosphorylation [27,153,154,156,189]. For example, it shows the modulation of magnitude of phosphorylated proteins by variation of the parameters (Figures 3.3, 3.5, 3.9). This was achieved by including into consideration the concentration of enzyme-substrate complexes that were neglected in [23]. The proposed model for phosphorylation was applied to

intracellular signalling in the immune system using the examples of STAT3 and IRF-5 as well as erythrocyte regulation of aggregation and deformability. This model is limited to the assumptions used in the model that included consideration of multisite proteins with identical phosphorylation sites, which is not the case in many real proteins.

The comparison of the proposed model predictions for STAT3 with the Goldbeter and Koshland model [23] revealed that the model [23] can be used only in the case when the total concentrations of JAK and SHP-1 are much lower than the total concentration of STAT3. The concentrations of intermediate phosphorylation complexes cannot always be ignored in real biological systems due to the fact that in this case the concentrations of kinases and their substrates may be comparable [29]. Thus, Chapter 3 might offer more accurate model of phosphorylation reaction.

The model for multisite phosphorylation described in Chapter 3 predicts that IRF-5 phosphorylated at different phosphorylation sites has selective activity (Figures 3.4 and 3.5). The distribution of phosphorylated IRF-5 species was investigated for various parametric changes. Our model predicts that this distribution is highly dependent on the parameters of the system, particularly on the ratio of the total AP to IRF-5 concentrations and phosphorylation/dephosphorylation reaction rates. The results obtained in this chapter may be useful for understanding the regulatory role of IRF-5 in the inflammatory diseases including Systemic Lupus Erythematosus potentially caused by the malfunctions in the mechanism of IRF-5 phosphorylation [190].

The model for phosphorylation of EF1 and EF2 proteins proposed in Chapter 3 was used by a team of researchers, including the author of this thesis, in [31] to study the molecular system that controls the aggregation and deformability of the erythrocyte. This model and findings in [31] may have a practical application in understanding erythrocyte disorders and aging.

In Chapters 2 and 3, we used two particular examples of multisite proteins, namely CaM and IRF-5 respectively. However, the results are more general than that. The models proposed in these chapters can be applied to other

multisite proteins if the following conditions are satisfied. First, the protein should have  $n$  sites for binding or phosphorylation. Second, it should have the corresponding type of binding or phosphorylation, for example sequential or independent. In these chapters we derived equations for the independent interactions. Third, we need to know whether the cooperativity is present or not. Fourth, the reaction constants of binding or phosphorylation for individual sites differ within the range of proteins. However, these constants can be obtained if the appropriate equations are applied to describe the experimental data for protein binding or phosphorylation.

In Chapter 4 we extended the model for STAT phosphorylation proposed in Chapter 3 and studied an example of T cell phenotype plasticity in Th1 to Tr1 switching [39] by investigating the mechanisms of intracellular STAT signalling. While in previously published models [40-43] only one JAK-STAT pathway was studied at a time, in Chapter 4 we developed an integrative model that considers the interactions between different JAK-STAT pathways (Figure 4.1). The analysis of the developed model revealed the competitive nature of STAT proteins as well as the cross-regulation in JAK-STAT pathways and showed their impact on the produced cytokines and T cell phenotype switching. In Chapter 4 we proposed a potential mechanism (in terms of Figure 1.1) for the Th1 to Tr1 switching [39]. According to the proposed mechanism, the T cell phenotype switching is due to the relative redistribution of STAT dimer complexes caused by the cytokine-dependent STAT competition. The developed model predicts that the balance between the intracellular STAT species defines the amount of the produced cytokines and thereby T cell phenotypes.

We validated our model using experimental data (Figure 4.4) for IFN- $\gamma$  to IL-10 switching that regulates human Th1/Tr1 responses [244]. The parameters were found by using the MATLAB-integrated genetic algorithm for optimisation. Parameter sensitivity analysis revealed that within 2-fold change both the cytokine and STAT switching are observed in 78% cases (Figure 4.8). Therefore, we can assume that our model predictions are reasonably robust within this diapason of parameters. Next, we investigated how various malfunctions, which are modelled by parameter alterations, may lead to

pathological states. For example, we showed that inappropriate regulation of IL-2 receptor system may result in the disturbed IFN- $\gamma$  to IL-10 switching (Figure 4.12C), which may mediate autoimmune and IBD states, consistent with [262]. The analysis of our model in the context of possible immune pathologies may offer new strategies for their clinical treatment. In particular, the proposed model predicts that the reduction of the uncontrolled inflammation could be achieved by enhancing the role of competing STAT3 pathway. Our model also shows that the increased IL-6 leads to the lack of switching in phosphorylated STAT proteins and produced cytokines, whereas the switching is stronger for the reduced IL-6 (Figure 4.13).

Using the systems approach described in Introduction of this thesis we analysed the system of interacting STATs (Figure 4.1). This analysis predicts that there is also a competition between the modules formed by the competing STATs, namely STAT3-STAT5 and STAT3-STAT4 in our example. This competition is controlled by other cytokines, for example IL-21 in our system (Figure 4.16).

The proposed model, with necessary adjustments such as parameter variations, can be applicable to a number of various STAT signalling circuits, for example, to the Th1/Th2 [277], Treg/Th17 or Th17/Th2 [278] phenotype switching in the following way. The model for pro-inflammatory IFN- $\gamma$  producing Th1 and anti-inflammatory IL-10 producing Tr1 cells can be extended to pro-inflammatory IL-17 producing Th17 and anti-inflammatory IL-4 producing Th2 as well as anti-inflammatory IL-10 producing Treg cells.

In Chapter 5 of this thesis we introduced a new model for *C. glabrata* adaptation to osmotic shock [33]. The model links the cellular adaptation to osmotic stress with intracellular molecular interactions such as multisite phosphorylation of Hog1 in MAPK pathway, phosphorelay system and glycerol metabolism (Figure 5.9). Previously published models for Hog1 activation in yeast adaptation to osmotic stress lack the systems description as it is shown in Figure 1.1. For example, in [51-57] the biophysical part is absent, in [47,48] the model of Hog1 activation pathway is not detailed and all the above mentioned models did not describe adaptation to hypo-osmotic stress.

The detailed Hog1 pathway description in our model allowed testing the model for the adaptation of BG2 and 2001 strains of *C. glabrata* to both hypo- and hyper-osmotic stress conditions and demonstrating the differences in these two strains adaptation to osmotic stress. Our model demonstrates the time delay accompanied by a decrease in magnitude of Hog1 phosphorylation in 2001 strains under 1.5M concentration of NaCl (Figure 5.12E). Description of this effect was possible when we introduced an experimentally testable assumption that when the cell shrinks under hyper-osmotic stress, some transmembrane receptors lose their activity and this leads to the decrease in Hog1 magnitude phosphorylation (Figure 5.12F). Our model predicts that the overexpression of Sho1 leads to an increase of phosphorylated Hog1 magnitude in 2001 strain (Figure 5.20C).

The understanding of the possible mechanism of yeast adaptation to osmotic stress allowed us to propose potentially useful clinical applications of the model developed in Chapter 5. The model predicts that in case of the strong hyper-osmotic followed by the hypo-osmotic and then the strong hyper-osmotic shock again (Figure 5.21), the cell uses up its resource for adaptation such as intracellular glucose and glycerol and is not able to restore its volume and turgor pressure and therefore adapt to the hyper-osmotic stress (Figure 5.22). The lack of adaptation in turn leads to the increased vulnerability of *C. glabrata*. This effect can be amplified if hyper-osmotic stress is combined with the decreased external glucose (Figure 7.23).

## 6.2 Further work

The mathematical framework proposed in this thesis has certain limitations that could be addressed in further work. We consider these limitations in application to each chapter of this thesis.

In Chapters 2 and 3 we considered multisite protein interactions assuming that the cooperativity is absent. We made this assumption due to the findings in Chapter 2 that the cooperativity has quantitative rather than qualitative effect on the model predictions for the concentration of individual multisite protein

conformations (Figure 2.9). In order to provide more realistic description of multisite binding and phosphorylation, in further work the cooperativity will be included into consideration.

One of the limitations of the model proposed in Chapter 4 for STAT-STAT interactions in T cells differentiation and plasticity is that we studied only STAT transcription factors. However the other transcription factors including NFAT, NF- $\kappa$ B, T-bet and GATA3 may also play an important role in T cell phenotype plasticity [327]. Since the focus of this chapter was on STAT signalling effects, we simplified interleukin-receptor interactions by neglecting receptor autophosphorylation and dimerisation. This simplification should not affect the interaction between STAT proteins however the consideration of full receptor system may lead to new effects in the overall system response. In order to study the phenotype switching we considered only cytokine pairings that activate STAT proteins, however it could be more than just two activating cytokines. In Chapter 4 we did not analyse the dynamics of the system. Possible time-course model predictions could add more details to the phenotype switching in the disease development.

Our Systems Biology analysis of STAT proteins in immunity can be further developed to explore new promising therapeutic opportunities for various inflammatory conditions. Other STATs can be included into the model, to understand the mechanism of the other STAT-STAT interactions in the immune system. It would be beneficial to establish the logics of T cell fate determination and plasticity in the immune system depending on environmental conditions (extracellular cytokines).

The model for the yeast adaptation to osmotic stress proposed in Chapter 5 was applied to investigate the adaptation to osmotic stress only. However, our model predictions for the hyper-osmotic stress combined with the glucose starvation (Figure 7.23) showed that the yeast may become more vulnerable in this case. Therefore, the yeast adaptation to the combination of external stress conditions including osmolarity, starvation, pheromone and temperature shock can be investigated in further work. Due to the fact that each of these stresses activates certain transcription factors by preventing the cross-talk between the

pathways [288] and due to the complicated structure of the pathways, the model for the yeast adaptation to various osmotic stress conditions can be developed in terms of "compound control" logics proposed in [328] and explicitly analysed in [329].



## 7 Appendix

### 7.1 Appendix A

#### 7.1.1 Biochemical kinetics

In biological objects the signals are transmitted through different mechanisms, for example molecular ligand binding, changes in proteins structure and protein conformational dynamics [330]. These changes occur as a result of biochemical reactions where the substances transform from one state to another. Due to the fact that the reactions are time-dependent processes and therefore can be fast or slow, all reactions are characterised by the time required for their completion. Now consider the following biochemical reaction:



where  $A$  is substrate and  $B$  is product of the reaction. The rate of this reaction is given by the change in concentration of  $B$  in time:

$$v = \frac{d}{dt}[B] \quad (7.2)$$

where  $[B]$  is the concentration of the product.

Reactions can be reversible and irreversible. Equation (7.1) is irreversible, which means that the substrate  $A$  can transform to the product  $B$  and the reverse transition is not possible. However in some cases the reverse reaction can also occur. An example of the reversible (both direction) reaction is given by:



Chemical kinetics [60,61] have been studied by mathematical modelling to describe the reaction rates. There are several mathematical approaches to deliver this. One of the mathematical models for the kinetics of biochemical reactions is the law of mass action. It assumes that the volume and the temperature, under which the reactions occur, are constant during the time of the reaction. To complete the biochemical reaction, the reacting particles should collide and have sufficient energy to interact. The law of mass action suggests

that the rate of the reaction is proportional to the concentrations of the reagents and the reaction constants. For the following biochemical reaction



the law of mass action gives the following equation for the reaction rate:

$$v = \frac{d[B]}{dt} = k \prod_{i=1}^n [A_i]^{c_i}, \quad (7.5)$$

where  $\sum_{i=1}^n c_i$  is the order of the reaction,  $k$  is the rate constant, which represents the probability of the molecules collision.

Now consider the following biochemical equation:



where  $c_i \neq b_i$ ,  $i = 1 \dots n$  and  $b_i \neq 0$ .

The reaction rate is given by:

$$v = k \prod_{i=1}^n [A_i]^{c_i}, \quad (7.7)$$

however, in contrast to Equation (7.4),  $A_i$  do not disappear in the reaction (7.6) as they are presented in both left and right parts of the equation by different numbers of molecules. The rate of change in concentrations of  $A_i$  is given by:

$$\frac{d[A_i]}{dt} = (b_i - c_i) \cdot v = (b_i - c_i) \cdot k \prod_{i=1}^n [A_i]^{c_i}. \quad (7.8)$$

Equation (7.8) shows that when  $b_i > c_i$  then  $A_i$  is produced, while when  $b_i < c_i$ ,  $A_i$  is consumed in the reaction. The difference  $b_i - c_i$  is called the stoichiometric coefficient.

In the case when the reaction rate is zero, there is a chemical equilibrium. This implies that the formation of the product from the substrate is balanced by the

backwards transformation to substrate from the product. For the reaction (7.3) we have:

$$v = \frac{d[B]}{dt} = 0, \quad (7.9)$$

and since  $\frac{d[B]}{dt} = k^+[A] - k^-[B]$ , this gives the equilibrium constant:

$$K = \frac{k^+}{k^-} = \frac{[B]}{[A]} \quad (7.10)$$

The equilibrium constant in Equation (7.10) characterizes the extent, to which reactants are converted to products by this reaction, and not the reaction speed [331].

### 7.1.2 Molecular binding

Molecular binding describes the interaction between reacting molecules that lead to the formation of a stable complex. The biochemical reaction for the molecular binding can be written as follows:



where  $C$  is the molecular complex. The reaction rate in Equation (7.11) is given by:

$$v = \frac{d[C]}{dt} = k^+[A][B] - k^-[C], \quad (7.12)$$

The total concentration of  $A$ , denoted by  $[A]$ , is conserved in this reaction:

$$A_T = [A] + [C], \quad (7.13)$$

where  $A_T$  is the total constant concentration of  $A$ .

In equilibrium, Equations (7.12) and (7.13) give the concentration of  $C$ :

$$[C] = A_T \frac{[B]}{K_d + [B]} \quad (7.14)$$

where  $K_d = \frac{k^-}{k^+}$  is called the dissociation constant, which represents the inverse of  $K_A = \frac{k^+}{k^-}$ , which is called the association constant.

The following reaction describes the case where there are multiple binding sites in molecule B :



where  $X_i^0$  is the  $i$ th binding site of the multisite protein B in unbound state,  $X_i^1$  is the  $i$ th binding site of the multisite protein being occupied,  $k_i^+$  and  $k_i^-$  are the association and dissociation constants, respectively.

Cooperative binding is a special case of molecular interactions where the association and dissociation constants of the binding to one site of a molecule depend on the state of other sites. There are several approaches of modelling the Equation (7.15).

Studying oxygen binding to haemoglobin, Hill was looking for an equation that would describe haemoglobin saturation curve and satisfy the experimental observations [9]. He suggested the following empirical formula for the probability of a molecular binding of protein  $X_i$  with ligand A :

$$p = \frac{[A]^n}{K_d^n + [A]^n} \quad (7.16)$$

where  $K_d$  is the dissociation constant and  $n$  is the Hill coefficient [9]. The Hill coefficient represents the degree of cooperativity rather than the number of bound sites and quantitatively describes the cooperativity dependence on the state of other sites. Despite the fact that Equation (7.16) agreed with the experiments [9], this phenomenological equation could not explain the underlying biological mechanisms of molecular binding since Hill coefficient is a value that is found in order to fit the experimental data rather than based on physiological assumptions [332].

Later, Adair experimentally tested Hill's equation and found that it was qualitatively consistent with experiments for  $n > 1$ , as it was stated in Adair's original work [10]. However Hill's theory was not confirmed quantitatively. Adair demonstrated that there are four binding sites of haemoglobin for oxygen and assumed that haemoglobin is built up in stages. Assuming the ideal solution where all components obey the mass law, he deduced the following formula for the probability of the building up of the four oxygen molecules:

$$p = \frac{1}{4} \cdot \frac{K_1 \cdot [A] + 2 \cdot K_2 \cdot [A]^2 + 3 \cdot K_3 \cdot [A]^3 + 4 \cdot K_4 \cdot [A]^4}{1 + K_1 \cdot [A] + K_2 \cdot [A]^2 + K_3 \cdot [A]^3 + K_4 \cdot [A]^4}, \text{ or in general form, for the}$$

molecule with  $n$  binding sites:

$$p = \frac{\frac{1}{n} \cdot \sum_{i=1}^n i \cdot K_i \cdot [A]^i}{1 + \sum_{i=1}^n K_i \cdot [A]^i}, \quad (7.17)$$

where  $n$  is the number of binding sites and  $K_i$  are the corresponding association constants [10]. Equation (7.17), suggested by Adair, is biologically more meaningful than Equation (7.16) due to the fact that  $n$  in Equation (7.17) describes the number of binding sites of multisite molecule and not a phenomenological constant.

In order to deliver a deeper understanding of the underlying biophysical mechanism of molecular binding of oxygen binding to haemoglobin, Pauling in his original work [11] developed Adair's model [10] by deriving an equation based on the structure of haemoglobin module. Pauling assumed in his model [11] that the haemoglobin molecule contains four equivalent hemes connected with others in such a way that the interactions are equal for the connected pairs of hemes and suggested the following equation for the probability of binding:

$$p = \frac{K[A] + 3\alpha K^2[A]^2 + 3\alpha^3 K^3[A]^3 + \alpha^6 K^4[A]^4}{1 + 4K[A] + 6\alpha K^2[A]^2 + 4\alpha^3 K^3[A]^3 + \alpha^6 K^4[A]^4}, \quad (7.18)$$

where  $K$  is such that  $RT \ln K$  is the free energy change when oxygen is added to the heme,  $R$  is the universal gas constant,  $T$  is the thermodynamic temperature in SI unit kelvins, and  $\alpha$  is such that  $RT \ln \alpha$  is the additional free energy that is required to stabilize two groups of interacting hemes [11].

Another attempt to develop the Adair's equation was performed by Klotz [12]. He assumed that the ligand molecules bind sequentially and introduced description of a model of cooperative binding by using the mass-action law [333]. This implies that the second site can be bound by ligand only if the first site is already bound. The Klotz equation for the probability that all the sites of the protein are bound is given by:

$$p = \frac{\sum_{i=1}^n i \cdot \left( \prod_{j=1}^i K_j \right) \cdot [A]^i}{1 + \sum_{i=1}^n \left( \prod_{j=1}^i K_j \right) \cdot [A]^i}, \quad (7.19)$$

where  $K_j$  ( $j=1, \dots, n$ ) are individual binding constants. The advantage of Equation (7.19) is that it reveals the interaction type in each of the individual steps of molecular binding [12].

The first realistic schemes of reactions involved in multisite molecular binding were suggested by Weiss [13]. He considered both sequential and independent binding. For the sequential binding Weiss assumed that the ligand molecules stack on top of each other in order to bind their binding sites and derived the following equation:

$$p = \frac{\frac{[A]^n}{\prod_{j=1}^n K_j}}{1 + \sum_{i=1}^n \frac{[A]^i}{\prod_{j=1}^i K_j}}, \quad (7.20)$$

where  $K_j$  ( $j=1, \dots, n$ ) are the individual dissociation constants.

Considering the independent binding, Weiss assumed that the protein has multiple ligand binding sites available to the ligand and that the sites can be occupied independently of each other. In this case, the probability that all the sites of the protein are bound can be written as follows:

$$p = \frac{[A]^n}{\prod_{j=1}^n K_j} \quad (7.21)$$

$$1 + \sum_{i=1}^n \frac{n!}{(n-i)!i!} \frac{[A]^i}{\prod_{j=1}^i K_j}$$

### 7.1.3 Enzyme kinetics

Enzyme kinetics [334] focuses on the regulation of chemical reactions catalysed by enzymes. The enzymes can either activate (speed up) or inhibit (slow down) the reaction. There are several ways to describe the enzyme kinetics. The most widely used is Michaelis-Menten model [335].

The basic enzymatic reaction can be described by the following biochemical equation:



where E is the enzyme, S is the substrate, ES is the enzyme-substrate complex and P is the product of the reaction.

According to the law of mass action, the rate of this reaction is given by:

$$v = \frac{d[P]}{dt} = k_c [ES]. \quad (7.23)$$

The total concentration of the enzyme is constant and can be described by the following equation:

$$E_T = [E] + [ES]. \quad (7.24)$$

In their work Michaelis and Menten [335] suggested that the substrate S is in instantaneous equilibrium with the complex ES, which implies:

$$\frac{d[S]}{dt} = -k_f [E][S] + k_r [ES] = 0. \quad (7.25)$$

Using Equations (7.24) and (7.25) we can write for the concentration of the enzyme-substrate complex:

$$[ES] = E_T \frac{[S]}{K_d + [S]}, \quad (7.26)$$

where  $K_d = \frac{k_r}{k_f}$  is the dissociation constant.

The rate of reaction (7.23) in this case can be described by the following equation:

$$v = \frac{d[P]}{dt} = V_{max} \frac{[S]}{K_d + [S]}, \quad (7.27)$$

where  $V_{max} = k_c E_T$ .

In contrast to the Michaelis-Menten model, Briggs and Haldane assumed that the concentration of complex  $[ES]$  reaches equilibrium in a negligible time and maintains the constant concentration within the overall time of the reaction [62]. This approach is also known as the Quasi Steady State Assumption (QSSA). According to the QSSA, the rate of ES complex formation is zero:

$$\frac{d[ES]}{dt} = k_f [E][S] - (k_r + k_c)[ES] = 0. \quad (7.28)$$

Using Equations (7.24) and (7.28) it can be written for the concentration of the enzyme-substrate complex:

$$[ES] = E_T \frac{[S]}{K_m + [S]}, \quad (7.29)$$

where  $K_m = \frac{k_r + k_c}{k_f}$  is the Michaelis constant.



The rate of reaction (7.23) in this case can be written as follows:

$$v = \frac{d[P]}{dt} = V_{max} \frac{[S]}{K_m + [S]}, \quad (7.30)$$

where  $V_{max} = k_c E_T$ .

It can be seen that Equation (7.30) transforms to Equation (7.27) when  $k_c \ll k_f, k_r$ . The Michaelis constant  $K_m$  in Equation (7.30) represents the substrate concentration, at which the reaction rate  $v$  is half of the maximum reaction rate  $V_{max}$ . In experiments the reaction rate is measured within a short period of time. When the concentration of  $[ES]$  rapidly approaches a steady-state, it is assumed that during this period the enzyme-substrate complex is already formed (due to the fact that  $[ES]$  is in its steady-state) but the concentration of the substrate did not change. The Michaelis constant  $K_m$  can then be found after plotting the reaction rate against the substrate concentration.

## 7.2 Appendix B

### 7.2.1 Derivation of Equation (2.6)

We can write from Equations (2.5):

$$\frac{dL_i^0(U, t)}{dt} = k_i^- \cdot L_T - L_i^0(U, t) \cdot (k_i^+ \cdot U + k_i^-). \quad (7.31)$$

Before  $t=0$  the system is in equilibrium, which implies  $U = U_0$ . In this case the

steady-state solutions are  $L_i^0(U_0) = L_T \frac{K_i}{K_i + U_0}$  and  $L_i^1(U_0) = L_T \frac{U_0}{K_i + U_0}$ . The

ligand jumps from  $U_0$  to  $U_1$  at  $t=0$ , which implies  $U = U_1$ . We find the general

solution for  $L_i^0(U_1, t)$  in Equation (7.31):

$$L_i^0(U_1, t) = L_T \cdot \frac{K_i}{K_i + U_1} - C_3 \cdot \exp\left(-\frac{t}{\tau(U_1)}\right), \quad (7.32)$$

where  $\tau(U_1) = \frac{K_i}{k_i^- \cdot (U_1 + K_i)}$ ,  $K_i = \frac{k_i^-}{k_i^+}$  and  $C_3$  is a constant.

To find  $C_3$  we use the steady-state solutions  $L_i^0(U_0) = L_T \frac{K_i}{K_i + U_0}$  and

$L_i^1(U_0) = L_T \frac{U_0}{K_i + U_0}$  as initial conditions for  $t = 0$ :

$$C_3 = L_T \cdot \left( \frac{K_i}{K_i + U_1} - \frac{K_i}{K_i + U_0} \right). \quad (7.33)$$

A particular solution for the system of differential Equations (2.5) in response to the ligand concentration shift from  $U_0$  to  $U_1$  is given by:

$$L_i^0(U, t) = L_T \cdot \left( \frac{K_i}{K_i + U_1} - \left( \frac{K_i}{K_i + U_1} - \frac{K_i}{K_i + U_0} \right) \cdot \exp\left(-\frac{t}{\tau(U_1)}\right) \right), \quad (7.34)$$

$$L_i^1(U, t) = L_T \cdot \left( \frac{U_1}{K_i + U_1} - \left( \frac{U_1}{K_i + U_1} - \frac{U_0}{K_i + U_0} \right) \cdot \exp\left(-\frac{t}{\tau(U_1)}\right) \right).$$

### 7.2.2 Derivation of Equation (2.45)

To find steady-state solutions of System (2.44) we can write from this system:

$$-k^+ \cdot L^0(U_T) \cdot (U_T - L_T + L^0(U_T)) + k^- \cdot (L_T - L^0(U_T)) = 0. \quad (7.35)$$

Before  $t = 0$  the system is in equilibrium:  $U = U_{T0}$ . There are two roots of Equation (7.35):

$$L^0(U_{T0}) = \frac{K}{2} \cdot \left( \frac{L_T}{K} - \frac{U_{T0}}{K} - 1 \pm \sqrt{\left( \frac{U_{T0}}{K} - \frac{L_T}{K} \right)^2 + 2 \cdot \left( \frac{U_{T0}}{K} + \frac{L_T}{K} \right) + 1} \right). \quad (7.36)$$

As long as we need only positive solutions, we need to solve the following inequality:

$$\frac{K}{2} \cdot \left( \frac{L_T}{K} - \frac{U_{T0}}{K} - 1 \pm \sqrt{\left( \frac{U_{T0}}{K} - \frac{L_T}{K} \right)^2 + 2 \cdot \left( \frac{U_{T0}}{K} + \frac{L_T}{K} \right) + 1} \right) \geq 0. \quad (7.37)$$

Inequality (7.37) can be rewritten in the following way:

$$\left(\frac{L_T}{K} - \frac{U_{T0}}{K} - 1\right) \pm \sqrt{\left(\frac{L_T}{K} - \frac{U_{T0}}{K} - 1\right)^2 + 4 \cdot \frac{L_T}{K}} \geq 0. \quad (7.38)$$

Since  $4 \cdot \frac{L_T}{K} > 0$  there is only one positive root of Equation (7.35):

$$\left(\frac{L_T}{K} - \frac{U_{T0}}{K} - 1\right) + \sqrt{\left(\frac{L_T}{K} - \frac{U_{T0}}{K} - 1\right)^2 + 4 \cdot \frac{L_T}{K}} > 0. \quad (7.39)$$

### 7.2.3 Derivation of Equation (2.46)

The total ligand concentration jumps from  $U_{T0}$  to  $U_{T1}$  at  $t=0$ :  $U_T = U_{T1}$ . We find the general solution for  $L^0(U_{T1}, t)$  in Equations (2.44):

$$\int \frac{dL^0(U_{T1}, t)}{-k^+ \cdot L^0(U_{T1}, t)^2 - (k^+ \cdot (U_{T1} - L_T) + k^-) \cdot L^0(U_{T1}, t) + k^- \cdot L_T} = \int dt. \quad (7.40)$$

The integral  $\int \frac{dx}{\tilde{a}x^2 + \tilde{b}x + \tilde{c}} = \frac{1}{\sqrt{\tilde{b}^2 - 4\tilde{a}\tilde{c}}} \cdot \ln \left| \frac{2\tilde{a}x + \tilde{b} - \sqrt{\tilde{b}^2 - 4\tilde{a}\tilde{c}}}{2\tilde{a}x + \tilde{b} + \sqrt{\tilde{b}^2 - 4\tilde{a}\tilde{c}}} \right| + C_0$  if  $\tilde{b}^2 - 4\tilde{a}\tilde{c} > 0$ .

In our case  $\tilde{b}^2 - 4\tilde{a}\tilde{c} > 0$ , where  $\tilde{a} = -k^+$ ,  $\tilde{b} = -(k^+ \cdot (U_{T1} - L_T) + k^-)$  and  $\tilde{c} = k^- \cdot L_T$ .

Thus, we can take the integral in Equation (7.40) in the following way:

$$\begin{aligned} & \left| \frac{-2 \cdot k_i^+ \cdot L_i^0(U_{T1}, t) - (k_i^+ \cdot (U_{T1} - L_T) + k_i^-) - \sqrt{(k_i^+ \cdot (U_{T1} - L_T) + k_i^-)^2 + 4 \cdot k_i^+ \cdot k_i^- \cdot L_T}}{-2 \cdot k_i^+ \cdot L_i^0(U_{T1}, t) - (k_i^+ \cdot (U_{T1} - L_T) + k_i^-) + \sqrt{(k_i^+ \cdot (U_{T1} - L_T) + k_i^-)^2 + 4 \cdot k_i^+ \cdot k_i^- \cdot L_T}} \right| = \\ & = C \cdot \exp\left(t \cdot \sqrt{(k_i^+ \cdot (U_{T1} - L_T) + k_i^-)^2 + 4 \cdot k_i^+ \cdot k_i^- \cdot L_T}\right), \end{aligned} \quad (7.41)$$

where  $C > 0$  is a constant.

Since

$$-2 \cdot k^+ \cdot L^0(U_{T1}, t) - (k^+ \cdot (U_{T1} - L_T) + k^-) - \sqrt{(k^+ \cdot (U_{T1} - L_T) + k^-)^2 + 4 \cdot k^+ \cdot k^- \cdot L_T} < 0 \quad \text{in}$$

Equation (7.41) we consider the denominator only:

$$-2 \cdot k^+ \cdot L^0(U_{T1}, t) - (k^+ \cdot (U_{T1} - L_T) + k^-) + \sqrt{(k^+ \cdot (U_{T1} - L_T) + k^-)^2 + 4 \cdot k^+ \cdot k^- \cdot L_T} \quad (7.42)$$

There are two steady-states for  $L^0(U_{T1}, t)$ :  $L^0(U_{T0}, 0)$  and  $L^0(U_{T1}, \infty)$ , where  $L^0(U_{T0}, 0) > L^0(U_{T1}, \infty)$ .

For the second steady-state the denominator (7.42) is 0. Since the denominator is a decreasing function and starts with 0, the denominator is less than 0 for  $L^0(U_{T1}, t) \in [L^0(U_{T1}, \infty), L^0(U_{T1}, 0)]$ . Thus, the equation in the module in (7.41) is positive:

$$\begin{aligned} & \frac{-2 \cdot k^+ \cdot L^0(U_{T1}, t) - (k^+ \cdot (U_{T1} - L_T) + k^-) - \sqrt{(k^+ \cdot (U_{T1} - L_T) + k^-)^2 + 4 \cdot k^+ \cdot k^- \cdot L_T}}{-2 \cdot k^+ \cdot L^0(U_{T1}, t) - (k^+ \cdot (U_{T1} - L_T) + k^-) + \sqrt{(k^+ \cdot (U_{T1} - L_T) + k^-)^2 + 4 \cdot k^+ \cdot k^- \cdot L_T}} = \\ & = C \cdot \exp\left(t \cdot \sqrt{(k^+ \cdot (U_{T1} - L_T) + k^-)^2 + 4 \cdot k^+ \cdot k^- \cdot L_T}\right), \end{aligned} \quad (7.43)$$

The general solution for  $L^0$  is as follows:

$$\frac{L^0(U_{T1}, \eta)}{L_T} = \frac{K}{2 \cdot L_T} \cdot \left( \frac{L_T}{K} - \frac{U_{T1}}{K} - 1 + F(U_{T1}) \cdot \frac{C \cdot \exp(\eta \cdot F(U_{T1})) + 1}{C \cdot \exp(\eta \cdot F(U_{T1})) - 1} \right), \quad (7.44)$$

where  $\eta = t \cdot k^-$ .

Now we need to find  $C$  when  $t = 0$ :

$$C = \frac{F(U_{T0}) + F(U_{T1}) + \frac{U_{T1}}{K} - \frac{U_{T0}}{K}}{F(U_{T0}) - F(U_{T1}) + \frac{U_{T1}}{K} - \frac{U_{T0}}{K}}. \quad (7.45)$$

#### 7.2.4 Derivation of Equation (2.57)

Differentiating Equation (2.52) with respect to  $t$  and solving for  $dN_m/dt = 0$  yields the time  $\tau_m^{max}$  when the concentration of multisite protein conformations,  $N_m$ , bound to  $m$  ligand molecules is maximal:

$$\frac{d\left(L_T \cdot (p^1(U_T, t))^m \cdot (p^0(U_T, t))^{n-m}\right)}{dt} = 0. \quad (7.46)$$

There are three solutions of Equation (7.46):

$$\begin{aligned}
1) \tau_m^{max} &= \frac{\ln \left( \frac{1 + \frac{U_{T1}}{K} + F(U_{T1}) + \frac{L_T}{K} \cdot n}{C(U_{T1}) \cdot \left( 1 + \frac{U_{T1}}{K} - F(U_{T1}) + \frac{L_T}{K} \cdot n \right)} \right)}{F(U_{T1})}, \\
2) \tau_m^{max} &= \frac{\ln \left( \frac{1 + \frac{U_{T1}}{K} + F(U_{T1}) - \frac{L_T}{K} \cdot n}{C(U_{T1}) \cdot \left( 1 + \frac{U_{T1}}{K} - F(U_{T1}) - \frac{L_T}{K} \cdot n \right)} \right)}{F(U_{T1})}, \\
3) \tau_m^{max} &= \frac{\ln \left( \frac{1 + \frac{U_{T1}}{K} + F(U_{T1}) + \frac{L_T}{K} \cdot (n - 2m)}{C(U_{T1}) \cdot \left( 1 + \frac{U_{T1}}{K} - F(U_{T1}) + \frac{L_T}{K} \cdot (n - 2m) \right)} \right)}{F(U_{T1})},
\end{aligned} \tag{7.47}$$

where  $\tau_m^{max} = k^- \cdot t$ .

Consider the first solution  $\tau_m^{max} = \frac{\ln \left( \frac{1 + \frac{U_{T1}}{K} + F(U_{T1}) + \frac{L_T}{K} \cdot n}{C(U_{T1}) \cdot \left( 1 + \frac{U_{T1}}{K} - F(U_{T1}) + \frac{L_T}{K} \cdot n \right)} \right)}{F(U_{T1})}$  in

Equations (7.47). We need only real positive solutions, which implies

$$\frac{1 + \frac{U_{T1}}{K} + F(U_{T1}) + \frac{L_T}{K} \cdot n}{C(U_{T1}) \cdot \left( 1 + \frac{U_{T1}}{K} - F(U_{T1}) + \frac{L_T}{K} \cdot n \right)} > 1.$$

The expression in the logarithm can be

written as follows:

$$\frac{1 + \frac{U_{T1}}{K} + F(U_{T1}) + \frac{L_T}{K} \cdot n}{C(U_{T1}) \cdot \left(1 + \frac{U_{T1}}{K} - F(U_{T1}) + \frac{L_T}{K} \cdot n\right)} > 1,$$

$$\frac{1 + \frac{U_{T1}}{K} + F(U_{T1}) + \frac{L_T}{K} \cdot n}{1 + \frac{U_{T1}}{K} - F(U_{T1}) + \frac{L_T}{K} \cdot n} > C(U_{T1}), \text{ since } C(U_{T1}) > 0$$

$$\frac{1 + \frac{U_{T1}}{K} + F(U_{T1}) + \frac{L_T}{K} \cdot n}{1 + \frac{U_{T1}}{K} - F(U_{T1}) + \frac{L_T}{K} \cdot n} > \frac{F(U_{T0}) + F(U_{T1}) + \frac{U_{T1}}{K} - \frac{U_{T0}}{K}}{F(U_{T0}) - F(U_{T1}) + \frac{U_{T1}}{K} - \frac{U_{T0}}{K}},$$

$$1 + \frac{2 \cdot F(U_{T1})}{1 + \frac{U_{T1}}{K} - F(U_{T1}) + \frac{L_T}{K} \cdot n} > 1 + \frac{2 \cdot F(U_{T1})}{F(U_{T0}) - F(U_{T1}) + \frac{U_{T1}}{K} - \frac{U_{T0}}{K}},$$

$$\frac{1}{1 + \frac{U_{T1}}{K} - F(U_{T1}) + \frac{L_T}{K} \cdot n} > \frac{1}{F(U_{T0}) - F(U_{T1}) + \frac{U_{T1}}{K} - \frac{U_{T0}}{K}}. \quad (7.48)$$

Now compare the denominators (here the symbol " $\vee$ " stands for comparison) in inequality (7.48):

$$1 + \frac{U_{T1}}{K} - F(U_{T1}) + \frac{L_T}{K} \cdot n \vee F(U_{T0}) - F(U_{T1}) + \frac{U_{T1}}{K} - \frac{U_{T0}}{K}, \quad (7.49)$$

$$\frac{U_{T0}}{K} + \frac{L_T}{K} \cdot n + 1 > \sqrt{\left(\frac{U_{T0}}{K} + \frac{L_T}{K} \cdot n + 1\right)^2 - 4 \cdot \frac{U_{T0}}{K} \cdot \frac{n \cdot L_T}{K}}.$$

Thus inequality (7.48) is not true:

$$\frac{1}{1 + \frac{U_{T1}}{K} - F(U_{T1}) + \frac{L_T}{K} \cdot n} < \frac{1}{F(U_{T0}) - F(U_{T1}) + \frac{U_{T1}}{K} - \frac{U_{T0}}{K}},$$

$$\frac{1 + \frac{U_{T1}}{K} + F(U_{T1}) + \frac{L_T}{K} \cdot n}{C(U_{T1}) \cdot \left(1 + \frac{U_{T1}}{K} - F(U_{T1}) + \frac{L_T}{K} \cdot n\right)} < 1, \quad (7.50)$$

$$\tau_m^{max} < 0.$$

Thus, the first solution in Equations (7.47) is not useful in our case.

Now consider the second solution in Equation (7.47). The expression in the logarithm can be written as follows:

$$\frac{\frac{U_{T1}}{K} - \frac{L_T}{K} \cdot n + 1 + \sqrt{\left(\frac{U_{T1}}{K} - \frac{n \cdot L_T}{K} + 1\right)^2 + 4 \cdot \frac{U_{T1}}{K}}}{C(U_{T1}) \cdot \left(\frac{U_{T1}}{K} - \frac{L_T}{K} \cdot n + 1 - \sqrt{\left(\frac{U_{T1}}{K} - \frac{n \cdot L_T}{K} + 1\right)^2 + 4 \cdot \frac{U_{T1}}{K}}\right)} < 0, \quad (7.51)$$

which implies that there are only complex solutions. The second solution in Equations (7.47) is also not useful.

Now consider the third solution in Equation (7.47). We cannot guarantee the sign in the logarithmic function but there are positive asymptotes when

$$1 + \frac{U_{T1}}{K} - F(U_{T1}) + \frac{L_T}{K} \cdot (n - 2m) = 0 \text{ for intermediate } (m \in [1, n-1]) \text{ species:}$$

$$\frac{U_{T1}}{K} = m \cdot \left(\frac{L_T}{K} + \frac{1}{n-m}\right). \quad (7.52)$$

## 7.2.5 Derivation of Equation (2.59)

For the apo form Equation (2.52) can be written as follows:

$$N_0(U_T, t) = \frac{1}{2} \cdot (N_0(U_T, 0) + N_0(U_T, \infty)). \quad (7.53)$$

Equation (7.53) can be written as follows:

$$\begin{aligned} & \left( \frac{n \cdot L_T}{K} - \frac{U_{T1}}{K} - 1 + F(U_{T1}) \cdot \frac{C(U_T) \cdot \exp(\eta \cdot F(U_{T1})) + 1}{C(U_T) \cdot \exp(\eta \cdot F(U_{T1})) - 1} \right)^n = \\ & = \frac{1}{2} \left( \left( \frac{n \cdot L_T}{K} - \frac{U_{T1}}{K} - 1 + F(U_{T1}) \cdot \frac{C(U_T) + 1}{C(U_T) - 1} \right)^n + \left( \frac{n \cdot L_T}{K} - \frac{U_{T1}}{K} - 1 + F(U_{T1}) \right)^n \right). \end{aligned} \quad (7.54)$$

### 7.2.6 Derivation of Equation (2.60)

For the saturated form Equation (2.52) is:

$$N_n(U_T, t) = \frac{1}{2} \cdot (N_n(U_T, 0) + N_n(U_T, \infty)). \quad (7.55)$$

We can rewrite Equation (7.55) in the following way:

$$\begin{aligned} & \left( \frac{n \cdot L_T}{K} + \frac{U_{T1}}{K} + 1 - F(U_{T1}) \cdot \frac{C(U_T) \cdot \exp(\eta \cdot F(U_{T1})) + 1}{C(U_T) \cdot \exp(\eta \cdot F(U_{T1})) - 1} \right)^n = \\ & = \frac{1}{2} \left( \left( \frac{n \cdot L_T}{K} + \frac{U_{T1}}{K} + 1 - F(U_{T1}) \cdot \frac{C(U_T) + 1}{C(U_T) - 1} \right)^n + \left( \frac{n \cdot L_T}{K} + \frac{U_{T1}}{K} + 1 - F(U_{T1}) \right)^n \right). \end{aligned} \quad (7.56)$$

## 7.3 Appendix C

Here we present mathematical details of the model for STAT-STAT interactions described in the fifth chapter of this thesis. We derive the equations employed in the STAT3-STAT5 (Figure 4.3), STAT3-STAT4 (Figure 4.14A) and combined STAT3-STAT4-STAT5 (Figure 4.15A) circuits. Table 7.1 shows the short names and abbreviations used.

*Table 7.1. Abbreviations used in the STAT phosphorylation model.*

Abbreviation	Meaning
I2	IL-2
RJ2	IL-2 Receptor complex with JAK
I2RJ2	IL-2 Receptor:JAK complex with bound IL-2
RpJ2	Phosphorylated IL-2 Receptor:JAK complex
P2	SHP-1 phosphatase



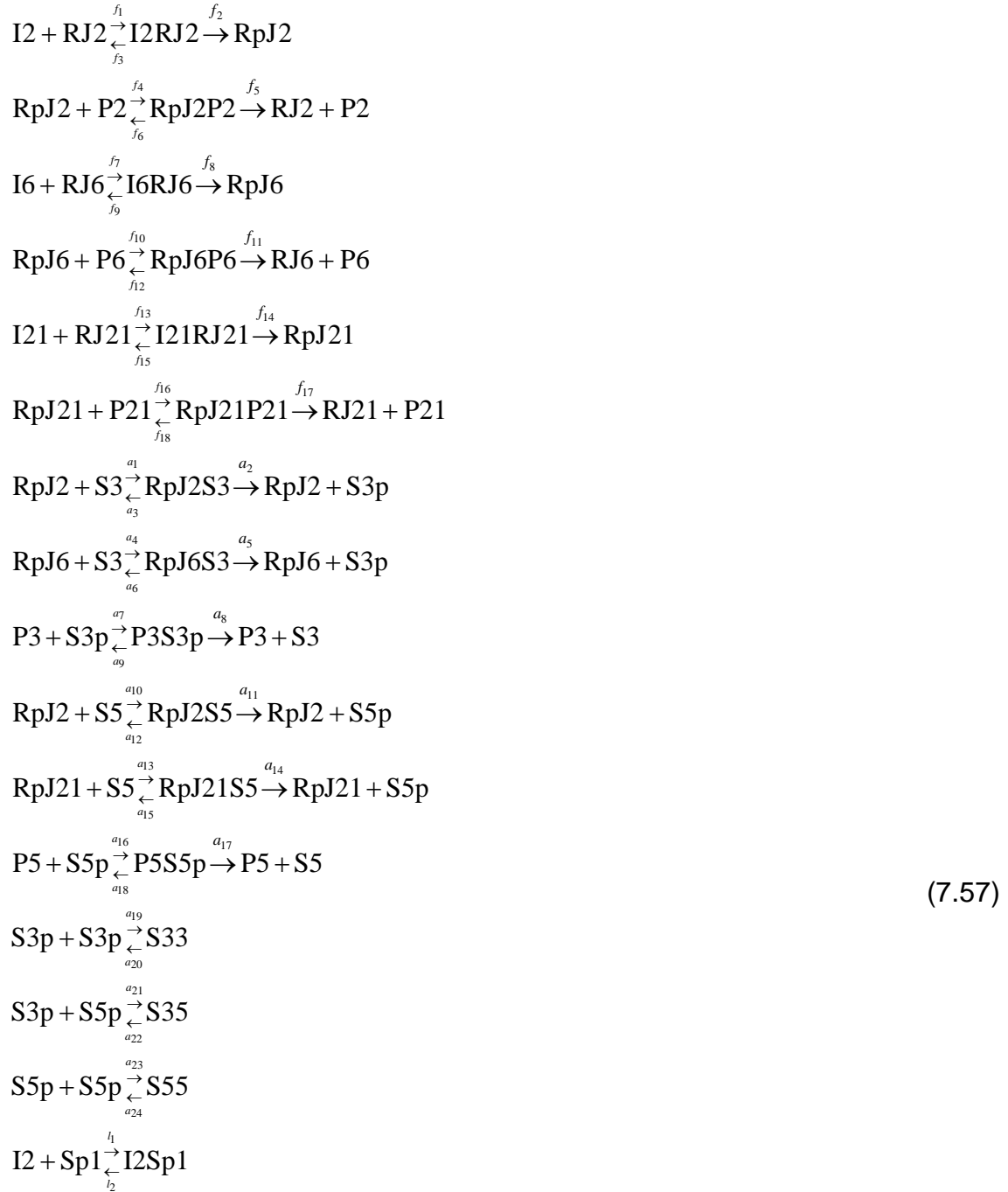
RpJ2P2	Phosphorylated IL-2 Receptor:JAK complex with SHP-1
I6	IL-6
RJ6	IL-6 Receptor:JAK complex
I6RJ6	IL-6 Receptor:JAK complex with bound IL-6
RpJ6	Phosphorylated IL-6 Receptor:JAK complex
P6	SHP-2 phosphatase
RpJ6P6	Phosphorylated IL-6 Receptor:JAK complex with SHP-2
I12	IL-12
RJ12	IL-12 Receptor:JAK complex
I12RJ12	IL-12 Receptor:JAK complex with bound IL-12
RpJ12	Phosphorylated IL-12 Receptor:JAK complex
P12	JAK phosphatase
RpJ12P12	Phosphorylated IL-12 Receptor:JAK complex with P12 phosphatase
I35	IL-35
RJ35	IL-35 Receptor:JAK complex
I35RJ35	IL-35 Receptor:JAK complex with bound IL-35
RpJ35	Phosphorylated IL-35 Receptor:JAK complex
P35	JAK phosphatase
RpJ35P35	Phosphorylated IL-35 Receptor:JAK complex with P35 phosphatase
I21	IL-21
RJ21	IL-21 Receptor:JAK complex
I21RJ21	IL-21 Receptor:JAK complex with bound IL-21
RpJ21	Phosphorylated IL-21 Receptor:JAK complex
P21	JAK phosphatase
RpJ21P21	Phosphorylated IL-21 Receptor:JAK complex with P21 phosphatase
S3	STAT3
RpJ2S3	Phosphorylated IL-2 Receptor:JAK complex with STAT3
RpJ6S3	Phosphorylated IL-6 Receptor:JAK complex with STAT3
S3p	Phosphorylated STAT3
P3	SHP-1 phosphatase
P3S3p	Phosphorylated STAT3 complex with SHP-1

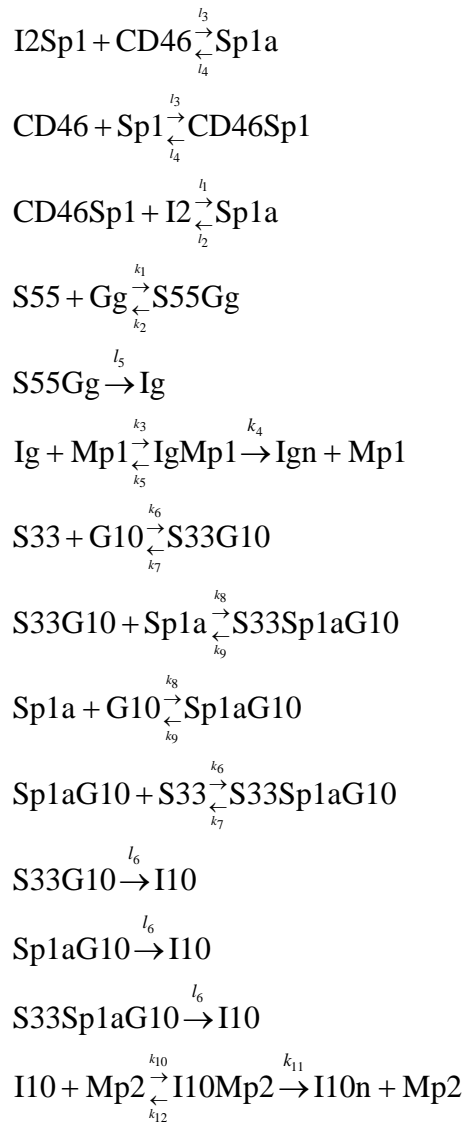
S4	STAT4
S4p	Phosphorylated STAT4
RpJ12S4	Phosphorylated IL-12 Receptor:JAK complex with STAT4
RpJ35S4	Phosphorylated IL-35 Receptor:JAK complex with STAT4
P4	PTP phosphatase
P4S4p	Phosphorylated STAT4 complex with PTP phosphatase
S5	STAT5
S5p	Phosphorylated STAT5
RpJ2S5	Phosphorylated IL-2 Receptor:JAK complex with STAT5
RpJ21S5	Phosphorylated IL-21 Receptor:JAK complex with STAT5
P5	SHP-2 phosphatase
P5S5p	Phosphorylated STAT5 complex with SHP-2 phosphatase
S33	STAT3:STAT3 homodimer
S34	STAT3:STAT4 heterodimer
S44	STAT4:STAT4 homodimer
S35	STAT3:STAT5 heterodimer
S55	STAT5:STAT5 homodimer
Gg	Gene responsible for IFN- $\gamma$ production
S44Gg	IFN- $\gamma$ gene complex with STAT4:STAT4 homodimer
S55Gg	IFN- $\gamma$ gene complex with STAT5:STAT5 homodimer
S44S55Gg	IFN- $\gamma$ gene complex with STAT4:STAT4 and STAT5:STAT5
Ig	IFN- $\gamma$
Mp1	Metalloprotease that cleaves IFN- $\gamma$
IgMp1	Metalloprotease complex with IFN- $\gamma$ gene
Ign	Non-active IFN- $\gamma$
G10	IL-10 gene
S33G10	IL-10 gene complex with STAT3:STAT3 homodimer
Sp1	SP1 transcription factor
Sp1a	SP1 transcription factor in active form
S33Sp1aG10	IL-10 gene complex with STAT3:STAT3 and Sp1a
Sp1aG10	Complex of Sp1a with IL-10 gene
Mp2	Metalloprotease that cleaves IL-10

I10Mp2	Metalloprotease complex with IL-10 gene
I10n	Non-active IL-10

## 7.4 Model for the STAT3-STAT5 circuit

The biochemical reactions involved in the STAT3-STAT5 circuit (Figure 4.3) are given by:





All values here represent concentrations and reaction constants and thereby are real positive numbers.

The system of reactions (7.57) can be divided into three major subsystems of interactions: i) Cytokine-receptor interactions, ii) STAT phosphorylation and dimerisation, iii) Cytokine production.

#### 7.4.1 Cytokine-receptor interactions

In the most general case the reactions can be written as follows:



where  $C$  is cytokine,  $RJ$  is Receptor:JAK complex,  $P$  is phosphatase and small  $p$  denotes phosphorylated state.

The ODEs for the system (7.58):

$$\begin{aligned}\frac{d}{dt}[CRJ] &= q_1[C][RJ] - (q_2 + q_3)[CRJ], \\ \frac{d}{dt}[RpJ] &= q_2[CRJ] - q_4[RpJ][P] + q_6[RpJP], \\ \frac{d}{dt}[RpJP] &= q_4[RpJ][P] - (q_5 + q_6)[RpJP].\end{aligned}\tag{7.59}$$

Corresponding conservation equations:

$$\begin{aligned}R_T &= [RJ] + [CRJ] + [RpJ] + [RpJP], \\ P_T &= [P] + [RpJP],\end{aligned}\tag{7.60}$$

where  $R_T$  and  $P_T$  are the total amounts of receptors and phosphatase, respectively. Here we neglect STAT-receptor interactions since STAT proteins do not have a significant impact on receptor dephosphorylation.

Equations (7.60) can be written as follows:

$$\begin{aligned}R_T &= \alpha + \beta + \gamma + \omega, \\ P_T &= p + \omega,\end{aligned}\tag{7.61}$$

where  $\alpha = [RJ]$ ,  $\beta = [CRJ]$ ,  $\gamma = [RpJ]$ ,  $\omega = [RpJP]$ ,  $p = [P]$ ,  $c = [C]$ .

The ODEs (7.59) can be rewritten in the following way:

$$\begin{aligned}\frac{d}{dt}\beta &= q_1c\alpha - (q_2 + q_3)\beta, \\ \frac{d}{dt}\gamma &= q_2\beta - q_4\gamma p + q_6\omega, \\ \frac{d}{dt}\omega &= q_4\gamma p - (q_5 + q_6)\omega.\end{aligned}\tag{7.62}$$

We need to find steady-state solutions of Equations (7.62):

$$\begin{aligned}
0 &= q_1 c \alpha - (q_2 + q_3) \beta, \\
0 &= q_2 \beta - q_4 \gamma p + q_6 \omega, \\
0 &= q_4 \gamma p - (q_5 + q_6) \omega, \\
R_T &= \alpha + \beta + \gamma + \omega, \\
P_T &= p + \omega.
\end{aligned} \tag{7.63}$$

We found the concentrations of the complexes:

$$\begin{aligned}
\omega &= P_T \frac{\gamma}{\frac{q_5 + q_6}{q_4} + \gamma} = \frac{P_T \gamma}{Q_2 + \gamma}, \\
\beta &= \frac{q_5}{q_2} \omega = \frac{q_5}{q_2} \frac{P_T \gamma}{Q_2 + \gamma} = \frac{P_T \gamma}{Q_3 (Q_2 + \gamma)}, \\
\alpha &= \frac{q_2 + q_3}{q_1} \frac{\beta}{c} = \frac{Q_1 P_T \gamma}{c Q_3 (Q_2 + \gamma)},
\end{aligned} \tag{7.64}$$

where  $Q_1 = \frac{q_2 + q_3}{q_1}$  and  $Q_2 = \frac{q_5 + q_6}{q_4}$  are Michaelis constants for phosphorylation and dephosphorylation, respectively, and  $Q_3 = \frac{q_2}{q_5}$ .

We can write the following equation using the conservation Equation for the receptor (7.61):

$$R_T = \gamma + \frac{P_T \gamma}{Q_2 + \gamma} \left( \frac{Q_1}{c Q_3} + \frac{1}{Q_3} + 1 \right). \tag{7.65}$$

As a result we obtain a quadratic equation:

$$0 = \gamma^2 + \gamma \chi - \delta, \tag{7.66}$$

where  $\chi = Q_2 - R_T + P_T \left( \frac{Q_1}{c Q_3} + \frac{1}{Q_3} + 1 \right)$ ,  $\delta = R_T Q_2$ .

The solution of Equation (7.66) is:

$$\gamma = -\frac{\chi}{2} + \frac{\sqrt{\chi^2 + 4\delta}}{2} \tag{7.67}$$

Equation (7.67) can be rewritten as follows:

$$\gamma = \frac{1}{2} \left( \sqrt{\left( \lambda + \frac{\rho}{c} \right)^2 + 4\delta} - \lambda - \frac{\rho}{c} \right), \quad (7.68)$$

where  $\lambda = Q_2 - R_T + P_T \left( \frac{1}{Q_3} + 1 \right)$  and  $\rho = \frac{P_T Q_1}{Q_3}$ .

Using Equation (7.68) we can now write for  $[RpJ2]$ ,  $[RpJ6]$  and  $[RpJ21]$  in non-dimensional form respectively:

$$\begin{aligned} [w2] &= -\frac{M_2 - r2_t + p2_t \left( \frac{M_1}{n_1 [i2]} + \frac{1}{n_1} + 1 \right)}{2} + \\ &+ \frac{\sqrt{\left( M_2 - r2_t + p2_t \left( \frac{M_1}{n_1 [i2]} + \frac{1}{n_1} + 1 \right) \right)^2 + 4r2_t M_2}}{2}, \\ [w6] &= -\frac{M_4 - r6_t + p6_t \left( \frac{M_3}{n_2 [i6]} + \frac{1}{n_2} + 1 \right)}{2} + \\ &+ \frac{\sqrt{\left( M_4 - r6_t + p6_t \left( \frac{M_3}{n_2 [i6]} + \frac{1}{n_2} + 1 \right) \right)^2 + 4r6_t M_4}}{2}, \\ [w21] &= -\frac{M_6 - r21_t + p21_t \left( \frac{M_5}{n_3 [i21]} + \frac{1}{n_3} + 1 \right)}{2} + \\ &+ \frac{\sqrt{\left( M_6 - r21_t + p21_t \left( \frac{M_5}{n_3 [i21]} + \frac{1}{n_3} + 1 \right) \right)^2 + 4r21_t M_6}}{2}, \end{aligned} \quad (7.69)$$

where

$$\begin{aligned} [i2] &= \frac{[I2]}{S3_T}, [w2] = \frac{[RpJ2]}{S3_T}, r2_t = \frac{R2_T}{S3_T}, p2_t = \frac{P2_T}{S3_T}, M_1 = \frac{f_2 + f_3}{f_1 S3_T}, M_2 = \frac{f_5 + f_6}{f_4 S3_T}, n_1 = \frac{f_2}{f_5}, [i6] = \frac{[I6]}{S3_T}, \\ [w6] &= \frac{[RpJ6]}{S3_T}, r6_t = \frac{R6_T}{S3_T}, p6_t = \frac{P6_T}{S3_T}, M_3 = \frac{f_8 + f_9}{f_7 S3_T}, M_4 = \frac{f_{11} + f_{12}}{f_{10} S3_T}, n_2 = \frac{f_8}{f_{11}}, [i21] = \frac{[I21]}{S3_T}, \\ [w21] &= \frac{[RpJ21]}{S3_T}, r21_t = \frac{R21_T}{S3_T}, p21_t = \frac{P21_T}{S3_T}, M_5 = \frac{f_{14} + f_{15}}{f_{13} S3_T}, M_6 = \frac{f_{17} + f_{18}}{f_{16} S3_T}, n_3 = \frac{f_{14}}{f_{17}}. \end{aligned}$$

#### 7.4.2 STAT phosphorylation and dimerisation

The ODEs describing biochemical reactions in the STAT subsystem:

$$\begin{aligned}
\frac{d}{dt}[RpJ2S3] &= a_1[RpJ2][S3] - (a_2 + a_3)[RpJ2S3], \\
\frac{d}{dt}[RpJ6S3] &= a_4[RpJ6][S3] - (a_5 + a_6)[RpJ6S3], \\
\frac{d}{dt}[S3p] &= a_2[RpJ2S3] + a_5[RpJ6S3] - a_7[P3][S3p] + a_9[P3S3p] - \\
&\quad - 2a_{19}[S3p]^2 + 2a_{20}[S33] - a_{21}[S3p][S5p] + a_{22}[S35], \\
\frac{d}{dt}[P3S3p] &= a_7[P3][S3p] - (a_8 + a_9)[P3S3p], \\
\frac{d}{dt}[RpJ2S5] &= a_{10}[RpJ2][S5] - (a_{11} + a_{12})[RpJ2S5], \\
\frac{d}{dt}[RpJ21S5] &= a_{13}[RpJ21][S5] - (a_{14} + a_{15})[RpJ21S5], \\
\frac{d}{dt}[S5p] &= a_{11}[RpJ2S5] + a_{14}[RpJ21S5] - a_{16}[P5][S5p] + a_{18}[P5S5p] - \\
&\quad - a_{21}[S3p][S5p] + a_{22}[S35] - 2a_{23}[S5p]^2 + 2a_{24}[S55], \\
\frac{d}{dt}[P5S5p] &= a_{16}[P5][S5p] - (a_{17} + a_{18})[P5S5p], \\
\frac{d}{dt}[S33] &= a_{19}[S3p]^2 - a_{20}[S33], \\
\frac{d}{dt}[S35] &= a_{21}[S3p][S5p] - a_{22}[S35], \\
\frac{d}{dt}[S55] &= a_{23}[S5p]^2 - a_{24}[S55].
\end{aligned} \tag{7.70}$$

Conservation equations (here we neglect STAT-gene interactions due to the fact that the amount of genes activating certain cytokine production is low comparing to STAT):

$$\begin{aligned}
S3_T &= [S3] + [S3p] + 2[S33] + [S35] + [RpJ2S3] + [RpJ6S3] + [P3S3p], \\
S5_T &= [S5] + [S5p] + 2[S55] + [S35] + [RpJ2S5] + [RpJ21S5] + [P5S5p], \\
P3_T &= [P3] + [P3S3p], \\
P5_T &= [P5] + [P5S5p].
\end{aligned} \tag{7.71}$$

Then we can normalise Equations (7.71) to  $S3_T$ :



$$\begin{aligned}
1 &= [s3] + [s3p] + 2[s33] + [s35] + [w2s3] + [w6s3] + [p3s3p], \\
s5_t &= [s5] + [s5p] + 2[s55] + [s35] + [w2s5] + [w21s5] + [p5s5p], \\
p3_t &= [p3] + [p3s3p], \\
p5_t &= [p5] + [p5s5p],
\end{aligned} \tag{7.72}$$

where

$$\begin{aligned}
[s3] &= \frac{[S3]}{S3_T}, [s3p] = \frac{[S3p]}{S3_T}, [w2s3] = \frac{[RpJ2S3]}{S3_T}, [w6s3] = \frac{[RpJ6S3]}{S3_T}, [p3s3p] = \frac{[P3S3p]}{S3_T}, s5_t = \frac{S5_T}{S3_T}, \\
[s5] &= \frac{[S5]}{S3_T}, [s5p] = \frac{[S5p]}{S3_T}, [w2s5] = \frac{[RpJ2S5]}{S3_T}, [w21s5] = \frac{[RpJ21S5]}{S3_T}, [p5s5p] = \frac{[P5S5p]}{S3_T}, \\
[s33] &= \frac{[S33]}{S3_T}, [s35] = \frac{[S35]}{S3_T}, [s55] = \frac{[S55]}{S3_T}, [p3] = \frac{[P3]}{S3_T}, [p5] = \frac{[P5]}{S3_T}, p3_t = \frac{P3_T}{S3_T}, p5_t = \frac{P5_T}{S3_T}.
\end{aligned}$$

The ODEs (7.70) can be written in non-dimensional form as follows:

$$\begin{aligned}
\frac{d}{d\tau} [w2s3] &= m_1 [w2][s3] - [w2s3], \\
\frac{d}{d\tau} [w6s3] &= m_3 [w6][s3] - (m_4 + m_5)[w6s3], \\
\frac{d}{d\tau} [s3p] &= m_2 [w2s3] + m_4 [w6s3] - m_6 [p3][s3p] + m_8 [p3s3p] - \\
&\quad - 2m_{18} [s3p]^2 + 2m_{19} [s33] - m_{20} [s3p][s5p] + m_{21} [s35], \\
\frac{d}{d\tau} [p3s3p] &= m_6 [p3][s3p] - (m_7 + m_8)[p3s3p], \\
\frac{d}{d\tau} [w2s5] &= m_9 [w2][s5] - (m_{10} + m_{11})[w2s5], \\
\frac{d}{d\tau} [w21s5] &= m_{12} [w21][s5] - (m_{13} + m_{14})[w21s5], \\
\frac{d}{d\tau} [s5p] &= m_{10} [w2s5] + m_{13} [w21s5] - m_{15} [p5][s5p] + m_{17} [p5s5p] - \\
&\quad - m_{20} [s3p][s5p] + m_{21} [s35] - 2m_{22} [s5p]^2 + 2m_{23} [s55], \\
\frac{d}{d\tau} [p5s5p] &= m_{15} [p5][s5p] - (m_{16} + m_{17})[p5s5p], \\
\frac{d}{d\tau} [s33] &= m_{18} [s3p]^2 - m_{19} [s33], \\
\frac{d}{d\tau} [s35] &= m_{20} [s3p][s5p] - m_{21} [s35], \\
\frac{d}{d\tau} [s55] &= m_{22} [s5p]^2 - m_{23} [s55],
\end{aligned} \tag{7.73}$$

where

$$\begin{aligned}\tau &= t(a_2 + a_3), m_1 = \frac{a_1}{a_2 + a_3} S3_T, m_2 = \frac{a_2}{a_2 + a_3}, m_3 = \frac{a_4}{a_2 + a_3} S3_T, m_4 = \frac{a_5}{a_2 + a_3}, m_5 = \frac{a_6}{a_2 + a_3}, \\ m_6 &= \frac{a_7}{a_2 + a_3} S3_T, m_7 = \frac{a_8}{a_2 + a_3}, m_8 = \frac{a_9}{a_2 + a_3}, m_9 = \frac{a_{10}}{a_2 + a_3} S3_T, m_{10} = \frac{a_{11}}{a_2 + a_3}, m_{11} = \frac{a_{12}}{a_2 + a_3}, \\ m_{12} &= \frac{a_{13}}{a_2 + a_3} S3_T, m_{13} = \frac{a_{14}}{a_2 + a_3}, m_{14} = \frac{a_{15}}{a_2 + a_3}, m_{15} = \frac{a_{16}}{a_2 + a_3} S3_T, m_{16} = \frac{a_{17}}{a_2 + a_3}, m_{17} = \frac{a_{18}}{a_2 + a_3}, \\ m_{18} &= \frac{a_{19}}{a_2 + a_3} S3_T, m_{19} = \frac{a_{20}}{a_2 + a_3}, m_{20} = \frac{a_{21}}{a_2 + a_3} S3_T, m_{21} = \frac{a_{22}}{a_2 + a_3}, m_{22} = \frac{a_{23}}{a_2 + a_3} S3_T, m_{23} = \frac{a_{24}}{a_2 + a_3}.\end{aligned}$$

We need to find steady-state solutions of Equations (7.73):

$$\begin{aligned}0 &= m_1 [w2][s3] - [w2s3], \\ 0 &= m_3 [w6][s3] - (m_4 + m_5) [w6s3], \\ \frac{d}{d\tau} [s3p] &= m_2 [w2s3] + m_4 [w6s3] - m_6 [p3][s3p] + m_8 [p3s3p] - \\ &\quad - 2m_{18} [s3p]^2 + 2m_{19} [s33] - m_{20} [s3p][s5p] + m_{21} [s35], \\ 0 &= m_6 [p3][s3p] - (m_7 + m_8) [p3s3p], \\ 0 &= m_9 [w2][s5] - (m_{10} + m_{11}) [w2s5], \\ 0 &= m_{12} [w21][s5] - (m_{13} + m_{14}) [w21s5], \\ \frac{d}{d\tau} [s5p] &= m_{10} [w2s5] + m_{13} [w21s5] - m_{15} [p5][s5p] + m_{17} [p5s5p] - \\ &\quad - m_{20} [s3p][s5p] + m_{21} [s35] - 2m_{22} [s5p]^2 + 2m_{23} [s55], \\ 0 &= m_{15} [p5][s5p] - (m_{16} + m_{17}) [p5s5p], \\ 0 &= m_{18} [s3p]^2 - m_{19} [s33], \\ 0 &= m_{20} [s3p][s5p] - m_{21} [s35], \\ 0 &= m_{22} [s5p]^2 - m_{23} [s55].\end{aligned}\tag{7.74}$$

Equations (7.74) can be simplified as follows:

$$\begin{aligned}
0 &= m_1 [w2][s3] - [w2s3], \\
0 &= m_3 [w6][s3] - (m_4 + m_5) [w6s3], \\
\frac{d}{d\tau} [s3p] &= m_2 [w2s3] + m_4 [w6s3] - m_7 [p3s3p], \\
0 &= m_6 [p3][s3p] - (m_7 + m_8) [p3s3p], \\
0 &= m_9 [w2][s5] - (m_{10} + m_{11}) [w2s5], \\
0 &= m_{12} [w21][s5] - (m_{13} + m_{14}) [w21s5], \\
\frac{d}{d\tau} [s5p] &= m_{10} [w2s5] + m_{13} [w21s5] - m_{16} [p5s5p], \\
0 &= m_{15} [p5][s5p] - (m_{16} + m_{17}) [p5s5p], \\
0 &= m_{18} [s3p]^2 - m_{19} [s33], \\
0 &= m_{20} [s3p][s5p] - m_{21} [s35], \\
0 &= m_{22} [s5p]^2 - m_{23} [s55].
\end{aligned} \tag{7.75}$$

Then using conservation Equations (7.72) and System (7.75) we obtain:

$$\begin{aligned}
\frac{d}{d\tau} [s3p] &= m_2 [w2s3] + m_4 [w6s3] - m_7 [p3s3p], \\
\frac{d}{d\tau} [s5p] &= m_{10} [w2s5] + m_{13} [w21s5] - m_{16} [p5s5p],
\end{aligned} \tag{7.76}$$

where

$$\begin{aligned}
[p3s3p] &= p3_t \frac{[s3p]}{\frac{m_7 + m_8}{m_6} + [s3p]}, \\
[p5s5p] &= p5_t \frac{[s5p]}{\frac{m_{16} + m_{17}}{m_{15}} + [s5p]}, \\
[s33] &= \frac{m_{18}}{m_{19}} [s3p]^2, \\
[s35] &= \frac{m_{20}}{m_{21}} [s3p][s5p], \\
[s55] &= \frac{m_{22}}{m_{23}} [s5p]^2, \\
[w2s3] &= m_1 [w2][s3], \\
[w6s3] &= \frac{m_3}{m_4 + m_5} [w6][s3], \\
[w2s5] &= \frac{m_9}{m_{10} + m_{11}} [w2][s5], \\
[w21s5] &= \frac{m_{12}}{m_{13} + m_{14}} [w21][s5], \\
[s3] &= \frac{1 - [s3p] - 2[s33] - [s35] - [p3s3p]}{1 + m_1 [w2] + \frac{m_3}{m_4 + m_5} [w6]}, \\
[s5] &= \frac{s5_t - [s5p] - 2[s55] - [s35] - [p5s5p]}{1 + \frac{m_9}{m_{10} + m_{11}} [w2] + \frac{m_{12}}{m_{13} + m_{14}} [w21]}.
\end{aligned} \tag{7.77}$$

We can rewrite Equations (7.77):

$$\begin{aligned}
[p3s3p] &= p3_t \frac{[s3p]}{M_9 + [s3p]}, \\
[p5s5p] &= p5_t \frac{[s5p]}{M_{12} + [s5p]}, \\
[s33] &= \frac{[s3p]^2}{M_{13}}, \\
[s35] &= \frac{[s3p][s5p]}{M_{14}}, \\
[s55] &= \frac{[s5p]^2}{M_{15}}, \\
[w2s3] &= \frac{[w2][s3]}{M_7}, \\
[w6s3] &= \frac{[w6][s3]}{M_8}, \\
[w2s5] &= \frac{[w2][s5]}{M_{10}}, \\
[w21s5] &= \frac{[w21][s5]}{M_{11}}, \\
[s3] &= \frac{1 - [s3p] - 2[s33] - [s35] - [p3s3p]}{1 + \frac{[w2]}{M_7} + \frac{[w6]}{M_8}}, \\
[s5] &= \frac{s5_t - [s5p] - 2[s55] - [s35] - [p5s5p]}{1 + \frac{[w2]}{M_{10}} + \frac{[w21]}{M_{11}}},
\end{aligned} \tag{7.78}$$

where we denote Michaelis constants

$$\begin{aligned}
M_7 &= \frac{a_2 + a_3}{a_1 S_{3T}}, M_8 = \frac{a_5 + a_6}{a_4 S_{3T}}, M_9 = \frac{a_8 + a_9}{a_7 S_{3T}}, M_{10} = \frac{a_{11} + a_{12}}{a_{10} S_{3T}}, M_{11} = \frac{a_{14} + a_{15}}{a_{13} S_{3T}}, M_{12} = \frac{a_{17} + a_{18}}{a_{16} S_{3T}}, \\
M_{13} &= \frac{a_{20}}{a_{19} S_{3T}}, M_{14} = \frac{a_{22}}{a_{21} S_{3T}}, M_{15} = \frac{a_{24}}{a_{23} S_{3T}}.
\end{aligned}$$

We look for steady-state solutions of System (7.76):

$$\begin{aligned}
0 &= m_2 [w2s3] + m_4 [w6s3] - m_7 [p3s3p], \\
0 &= m_{10} [w2s5] + m_{13} [w21s5] - m_{16} [p5s5p].
\end{aligned} \tag{7.79}$$

We can rewrite Equations (7.79) as follows:

$$\begin{aligned}
0 &= n_4 [w2s3] + n_5 [w6s3] - [p3s3p], \\
0 &= n_6 [w2s5] + n_7 [w21s5] - [p5s5p],
\end{aligned} \tag{7.80}$$

where  $n_4 = \frac{a_2}{a_8}, n_5 = \frac{a_5}{a_8}, n_6 = \frac{a_{11}}{a_{17}}, n_7 = \frac{a_{14}}{a_{17}}$ .

System (7.80) can be rewritten after substituting solutions from Equation (7.78):

$$0 = [s3p] + 2 \frac{[s3p]^2}{M_{13}} + \frac{[s3p][s5p]}{M_{14}} + p3_t \frac{[s3p]}{M_9 + [s3p]} \left( 1 + \frac{M_7 M_8 + M_8 [w2] + M_7 [w6]}{n_4 M_8 [w2] + n_5 M_7 [w6]} \right) - 1, \quad (7.81)$$

$$0 = [s5p] + 2 \frac{[s5p]^2}{M_{15}} + \frac{[s3p][s5p]}{M_{14}} + p5_t \frac{[s5p]}{M_{12} + [s5p]} \left( 1 + \frac{M_{10} M_{11} + M_{11} [w2] + M_{10} [w21]}{n_6 M_{11} [w2] + n_7 M_{10} [w21]} \right) - s5_t,$$

We solve System (7.81) for  $[s3p]$  and  $[s5p]$  numerically.

### 7.4.3 Cytokine production

In general case, transcription factor T can activate gene G by forming a complex with the gene TG:



The ODEs for Equation (7.82):

$$\begin{aligned} \frac{d}{dt}[G] &= -h_1[T][G] + h_2[TG], \\ \frac{d}{dt}[TG] &= h_1[T][G] - h_2[TG]. \end{aligned} \quad (7.83)$$

Conservation equation that follows from Equations (7.83):

$$G_T = [G] + [TG], \quad (7.84)$$

where  $G_T$  is the total concentration of the gene.

Equation (7.84) can be written as follows:

$$G_T = \lambda + \theta, \quad (7.85)$$

where  $\lambda = [G], \theta = [TG]$ .

The ODEs (7.83) can be rewritten in the following way:

$$\begin{aligned}\frac{d}{dt}\lambda &= -h_1T\lambda + h_2\theta, \\ \frac{d}{dt}\theta &= h_1T\lambda - h_2\theta,\end{aligned}\tag{7.86}$$

where  $T = [T]$ .

We need to find steady-state solutions of Equation (7.86):

$$\begin{aligned}0 &= h_1T\lambda - h_2\theta, \\ G_T &= \lambda + \theta.\end{aligned}\tag{7.87}$$

We can find  $\theta$  from Equations (7.87):

$$\theta = G_T \frac{T}{Qh + T},\tag{7.88}$$

where  $Qh = \frac{h_2}{h_1}$  is a Michaelis constant.

In the most general case the reactions of the activation of a gene G by two transcription factors T1 and T2 are:



The ODEs for System (7.89):

$$\begin{aligned}\frac{d}{dt}[G] &= -b_1[T1][G] + b_2[T1G] - b_3[T2][G] + b_4[T2G], \\ \frac{d}{dt}[T1G] &= b_1[T1][G] - b_2[T1G] - b_3[T1G][T2] + b_4[T1T2G], \\ \frac{d}{dt}[T2G] &= b_3[T2][G] - b_4[T2G] - b_1[T2G][T1] + b_2[T1T2G], \\ \frac{d}{dt}[T1T2G] &= b_3[T1G][T2] - b_4[T1T2G] + b_1[T2G][T1] - b_2[T1T2G].\end{aligned}\tag{7.90}$$

Conservation equation that follows from Equations (7.90):

$$G_T = [G] + [T1G] + [T2G] + [T1T2G], \quad (7.91)$$

where  $G_T$  is the total amount of the gene.

Equation (7.91) can be written as follows:

$$G_T = \psi + \xi + \varphi + \nu, \quad (7.92)$$

where  $\psi = [G], \xi = [T1G], \varphi = [T2G], \nu = [T1T2G]$ .

The ODEs (7.90) can be rewritten in the following way:

$$\begin{aligned} \frac{d}{dt} \psi &= -b_1 T1 \psi + b_2 \xi - b_3 T2 \psi + b_4 \varphi, \\ \frac{d}{dt} \xi &= b_1 T1 \psi - b_2 \xi - b_3 \xi T2 + b_4 \nu, \\ \frac{d}{dt} \varphi &= b_3 T2 \psi - b_4 \varphi - b_1 \varphi T1 + b_2 \nu, \\ \frac{d}{dt} \nu &= b_3 \xi T2 - b_4 \nu + b_1 \varphi T1 - b_2 \nu, \end{aligned} \quad (7.93)$$

where  $T1 = [T1], T2 = [T2]$ .

We find steady-state solutions of Equations (7.93):

$$\begin{aligned} 0 &= b_1 T1 \psi - b_2 \xi - b_3 \xi T2 + b_4 \nu, \\ 0 &= b_3 T2 \psi - b_4 \varphi - b_1 \varphi T1 + b_2 \nu, \\ 0 &= b_3 \xi T2 - b_4 \nu + b_1 \varphi T1 - b_2 \nu, \\ G_T &= \psi + \xi + \varphi + \nu. \end{aligned} \quad (7.94)$$

Next, we find concentrations of the complexes:



$$\xi = G_T \frac{\frac{b_4 T_1}{b_3}}{\left(\frac{b_2}{b_1} + T_1\right) \left(\frac{b_4}{b_3} + T_2\right)} = G_T \frac{Qb_2 T_1}{(Qb_1 + T_1)(Qb_2 + T_2)},$$

$$\varphi = G_T \frac{\frac{b_2 T_2}{b_1}}{\left(\frac{b_2}{b_1} + T_1\right) \left(\frac{b_4}{b_3} + T_2\right)} = G_T \frac{Qb_1 T_2}{(Qb_1 + T_1)(Qb_2 + T_2)}, \quad (7.95)$$

$$\nu = G_T \frac{T_1 T_2}{\left(\frac{b_2}{b_1} + T_1\right) \left(\frac{b_4}{b_3} + T_2\right)} = G_T \frac{T_1 T_2}{(Qb_1 + T_1)(Qb_2 + T_2)},$$

where  $Qb_1 = \frac{b_2}{b_1}$ ,  $Qb_2 = \frac{b_4}{b_3}$  are Michaelis constants.

If a protein is activated by the first and the second transcription factors at the same time then its concentration is proportional to the concentration  $\nu$  only:

$$\nu = G_T \frac{T_1}{Qb_1 + T_1} \cdot \frac{T_2}{Qb_2 + T_2}, \quad (7.96)$$

which is a probability of the two transcription factors to be bound to the same gene.

If a protein is activated by the first or the second transcription factors then it is proportional to the sum of concentrations  $\xi + \varphi + \nu$ :

$$\xi + \varphi + \nu = G_T \frac{Qb_2 T_1 + Qb_1 T_2 + T_1 T_2}{(Qb_1 + T_1)(Qb_2 + T_2)},$$

$$\xi + \varphi + \nu = G_T \frac{Qb_2 T_1 + Qb_1 T_2 + T_1 T_2 + T_1 T_2 - T_1 T_2}{(Qb_1 + T_1)(Qb_2 + T_2)},$$

$$\xi + \varphi + \nu = G_T \frac{T_1(Qb_2 + T_2) + T_2(Qb_1 + T_1) - T_1 T_2}{(Qb_1 + T_1)(Qb_2 + T_2)}, \quad (7.97)$$

$$\xi + \varphi + \nu = G_T \left( \frac{T_1}{Qb_1 + T_1} + \frac{T_2}{Qb_2 + T_2} - \frac{T_1 T_2}{(Qb_1 + T_1)(Qb_2 + T_2)} \right),$$

$$\xi + \varphi + \nu = G_T \left( \frac{T_1}{Qb_1 + T_1} + \frac{T_2}{Qb_2 + T_2} - \frac{T_1}{Qb_1 + T_1} \frac{T_2}{Qb_2 + T_2} \right),$$

which is a probability of either of the two transcription factors to be bound to the same gene.

## CD46

The full mechanism of how CD46 enhances IL-10 production is still not clear. We assume here that the mechanism of reactions is similar to the one described in Equation (7.89). Thus it can be written for the concentration of SP1 in non-dimensional form according to Equation (7.96):

$$[sp1a] = sp1_t \frac{[i2]}{M_{16} + [i2]} \cdot \frac{[cd46]}{M_{17} + [cd46]}, \quad (7.98)$$

where  $[sp1a] = \frac{[SP1a]}{S3_T}$ ,  $sp1_t = \frac{SP1_T}{S3_T}$ ,  $[cd46] = \frac{[CD46]}{S3_T}$ ,  $M_{16} = \frac{l_2}{l_1 S3_T}$ , and

$$M_{17} = \frac{l_4}{l_3 S3_T}.$$

We assume here that the gene interaction with the transcription factor and its subsequent expression lead to the mRNA translation and certain cytokine secretion. The produced cytokine then can be degraded by a metalloprotease. In this case the biochemical reactions can be written as follows:



where TG is the transcription factor complex with gene, C is the active cytokine, Mp is the metalloprotease, CMp is cytokine-metalloprotease complex and Cn is a non-active cytokine.

The ODEs for the reactions in System (7.99):

$$\begin{aligned} \frac{d}{dt}[C] &= KP[TG] - u_1[C][Mp] + u_3[CMp], \\ \frac{d}{dt}[CMp] &= u_1[C][Mp] - (u_2 + u_3)[CMp], \\ \frac{d}{dt}[Mp] &= -u_1[C][Mp] + (u_2 + u_3)[CMp]. \end{aligned} \quad (7.100)$$

Conservation equation that follows from Equations (7.100):

$$Mp_T = [Mp] + [CMp] \quad (7.101)$$

We find steady-state solutions of System (7.100):

$$\begin{aligned} 0 &= KP[TG] - u_1[C][Mp] + u_3[CMp], \\ 0 &= u_1[C][Mp] - (u_2 + u_3)[CMp]. \end{aligned} \quad (7.102)$$

Thus we obtain a system of equations:

$$\begin{aligned} 0 &= KP\vartheta - u_2\sigma, \\ 0 &= u_1C\zeta - (u_2 + u_3)\sigma, \\ Mp_T &= \zeta + \sigma, \end{aligned} \quad (7.103)$$

where  $\vartheta = [TG]$ ,  $C = [C]$ ,  $\zeta = [Mp]$ ,  $\sigma = [CMp]$ .

We can find  $\sigma$  from this system of Equations (7.103):

$$\sigma = Mp_T \frac{C}{Qu + C}, \quad (7.104)$$

where  $Qu = \frac{u_2 + u_3}{u_1}$  is a Michaelis constant.

We next substitute  $\sigma$  from equation (7.104) to the first equation in System (7.103):

$$\begin{aligned} 0 &= KP\vartheta - u_2 Mp_T \frac{C}{Qu + C}, \\ C &= \frac{KP\vartheta Qu}{u_2 Mp_T - KP\vartheta}, \\ C &= \frac{Qu}{\frac{u_2 Mp_T}{KP\vartheta} - 1}. \end{aligned} \quad (7.105)$$

Since  $C$  should be positive and the maximum value for  $\frac{Mp_T}{\vartheta}$  is 1,  $KP < u_2$ , which implies that the rate of the cytokine production should be less than its maximum rate of the degradation by metalloprotease.

Equation (7.105) can be written as follows:

$$C = \frac{Qu}{\frac{Mp_T}{Qp\vartheta} - 1}, \quad (7.106)$$

where  $Qp = \frac{KP}{u_2}$ ,  $Qp < 1$ .

When the cytokine production is up-regulated by one transcription factor only,  $\vartheta = \theta$  from Equation (7.88) and thus it can be written:

$$C = \frac{Qu}{\frac{Mp_T}{QpG_T \frac{T}{Qh+T}} - 1}. \quad (7.107)$$

If the cytokine production is up-regulated by two transcription factors at the same time,  $\vartheta = \nu$  as shown in Equation (7.96), it can be written:

$$C = \frac{Qu}{\frac{Mp_T}{QpG_T \frac{T1}{Qb_1+T1} \frac{T2}{Qb_2+T2}} - 1}. \quad (7.108)$$

If the cytokine production is up-regulated by either of the two transcription factors,  $\vartheta = \xi + \varphi + \nu$  as shown in Equation (7.97), and thus it can be written:

$$C = \frac{Qu}{\frac{Mp_T}{QpG_T \left( \frac{T1}{Qb_1+T1} + \frac{T2}{Qb_2+T2} - \frac{T1}{Qb_1+T1} \frac{T2}{Qb_2+T2} \right)} - 1}. \quad (7.109)$$

### IFN- $\gamma$ and IL-10 production

Since IFN- $\gamma$  is activated by STAT55 only (Figure 4.3) we can write using Equation (7.107):

$$[ig] = \frac{M_{18}}{n_8 g g_t \frac{[s55]}{M_{19} + [s55]} - 1}, \quad (7.110)$$

where  $[ig] = \frac{[Ig]}{S3_T}$ ,  $mp1_t = \frac{Mp1_T}{S3_T}$ ,  $gg_t = \frac{Gg_T}{S3_T}$ ,  $M_{18} = \frac{k_4 + k_5}{k_3 S3_T}$ ,  $M_{19} = \frac{k_2}{k_1 S3_T}$ ,  $n_8 = \frac{l_5}{k_4}$ ,  $n_8 < 1$ .

IL-10 gene can be activated by either STAT33 or CD46. Thus it can be written according to Equation (7.109):

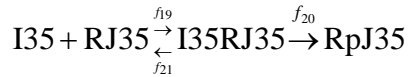
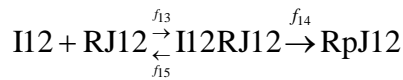
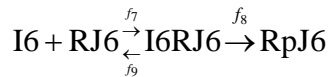
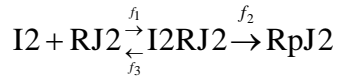
$$[i10] = \frac{M_{20}}{mp2_t} \frac{1}{n_9 g 10_t \left( \frac{[s33]}{M_{21} + [s33]} + \frac{[sp1a]}{M_{22} + [sp1a]} - \frac{[s33]}{M_{21} + [s33]} \frac{[sp1a]}{M_{22} + [sp1a]} \right)^{-1}}, \quad (7.111)$$

where

$$mp2_t = \frac{Mp2_t}{S3_T}, g10_t = \frac{G10_t}{S3_T}, M_{20} = \frac{k_{11} + k_{12}}{k_{10} S3_T}, M_{21} = \frac{k_7}{k_6 S3_T}, M_{22} = \frac{k_9}{k_8 S3_T}, n_9 = \frac{l_6}{k_{11}}, n_9 < 1.$$

## 7.5 Model for the STAT3-STAT4 circuit

The biochemical reactions involved in the circuit (Figure 4.14A) are as follows:



$$\text{RpJ35} + \text{P35} \begin{array}{c} \xrightarrow{f_{22}} \\ \xleftarrow{f_{24}} \end{array} \text{RpJ35P35} \xrightarrow{f_{23}} \text{RJ35} + \text{P35}$$

$$\text{RpJ2} + \text{S3} \begin{array}{c} \xrightarrow{a_1} \\ \xleftarrow{a_3} \end{array} \text{RpJ2S3} \xrightarrow{a_2} \text{RpJ2} + \text{S3p}$$

$$\text{RpJ6} + \text{S3} \begin{array}{c} \xrightarrow{a_4} \\ \xleftarrow{a_6} \end{array} \text{RpJ6S3} \xrightarrow{a_5} \text{RpJ6} + \text{S3p}$$

$$\text{P3} + \text{S3p} \begin{array}{c} \xrightarrow{a_7} \\ \xleftarrow{a_9} \end{array} \text{P3S3p} \xrightarrow{a_8} \text{P3} + \text{S3}$$

$$\text{RpJ12} + \text{S4} \begin{array}{c} \xrightarrow{a_{10}} \\ \xleftarrow{a_{12}} \end{array} \text{RpJ12S4} \xrightarrow{a_{11}} \text{RpJ12} + \text{S4p}$$

$$\text{RpJ35} + \text{S4} \begin{array}{c} \xrightarrow{a_{13}} \\ \xleftarrow{a_{15}} \end{array} \text{RpJ35S4} \xrightarrow{a_{14}} \text{RpJ35} + \text{S4p}$$

$$\text{P4} + \text{S4p} \begin{array}{c} \xrightarrow{a_{16}} \\ \xleftarrow{a_{18}} \end{array} \text{P4S4p} \xrightarrow{a_{17}} \text{P4} + \text{S4}$$

$$\text{S3p} + \text{S3p} \begin{array}{c} \xrightarrow{a_{19}} \\ \xleftarrow{a_{20}} \end{array} \text{S33}$$

$$\text{S3p} + \text{S4p} \begin{array}{c} \xrightarrow{a_{21}} \\ \xleftarrow{a_{22}} \end{array} \text{S34}$$

$$\text{S4p} + \text{S4p} \begin{array}{c} \xrightarrow{a_{23}} \\ \xleftarrow{a_{24}} \end{array} \text{S44}$$

$$\text{I2} + \text{Sp1} \begin{array}{c} \xrightarrow{l_1} \\ \xleftarrow{l_2} \end{array} \text{I2Sp1}$$

$$\text{I2Sp1} + \text{CD46} \begin{array}{c} \xrightarrow{l_3} \\ \xleftarrow{l_4} \end{array} \text{Sp1a}$$

$$\text{CD46} + \text{Sp1} \begin{array}{c} \xrightarrow{l_3} \\ \xleftarrow{l_4} \end{array} \text{CD46Sp1}$$

$$\text{CD46Sp1} + \text{I2} \begin{array}{c} \xrightarrow{l_1} \\ \xleftarrow{l_2} \end{array} \text{Sp1a}$$

$$\text{S44} + \text{Gg} \begin{array}{c} \xrightarrow{k_1} \\ \xleftarrow{k_2} \end{array} \text{S44Gg}$$

$$\text{S44Gg} \xrightarrow{l_5} \text{Ig}$$

$$\text{Ig} + \text{Mp1} \begin{array}{c} \xrightarrow{k_3} \\ \xleftarrow{k_5} \end{array} \text{IgMp1} \xrightarrow{k_4} \text{Ign} + \text{Mp1}$$

$$\text{S33} + \text{G10} \begin{array}{c} \xrightarrow{k_6} \\ \xleftarrow{k_7} \end{array} \text{S33G10}$$

(7.112)

$$S33G10 + Sp1a \begin{matrix} \xrightarrow{k_8} \\ \leftarrow k_9 \end{matrix} S33Sp1aG10$$

$$Sp1a + G10 \begin{matrix} \xrightarrow{k_8} \\ \leftarrow k_9 \end{matrix} Sp1aG10$$

$$Sp1aG10 + S33 \begin{matrix} \xrightarrow{k_6} \\ \leftarrow k_7 \end{matrix} S33Sp1aG10$$

$$S33G10 \xrightarrow{l_6} I10$$

$$Sp1aG10 \xrightarrow{l_6} I10$$

$$S33Sp1aG10 \xrightarrow{l_6} I10$$

$$I10 + Mp2 \begin{matrix} \xrightarrow{k_{10}} \\ \leftarrow k_{12} \end{matrix} I10Mp2 \xrightarrow{k_{11}} I10n + Mp2$$

### 7.5.1 Cytokine-receptor interactions

According to Equations (1.12) we can write for  $[RpJ2]$ ,  $[RpJ6]$ ,  $[RpJ12]$  and  $[RpJ35]$  in non-dimensional form respectively:

$$[w2] = -\frac{M_2 - r2_t + p2_t \left( \frac{M_1}{n_1[i2]} + \frac{1}{n_1} + 1 \right)}{2} + \frac{\sqrt{\left( M_2 - r2_t + p2_t \left( \frac{M_1}{n_1[i2]} + \frac{1}{n_1} + 1 \right) \right)^2 + 4r2_t M_2}}{2},$$

$$[w6] = -\frac{M_4 - r6_t + p6_t \left( \frac{M_3}{n_2[i6]} + \frac{1}{n_2} + 1 \right)}{2} + \frac{\sqrt{\left( M_4 - r6_t + p6_t \left( \frac{M_3}{n_2[i6]} + \frac{1}{n_2} + 1 \right) \right)^2 + 4r6_t M_4}}{2},$$

$$\begin{aligned}
[w12] &= -\frac{M_6 - r12_t + p12_t \left( \frac{M_5}{n_3 [i12]} + \frac{1}{n_3} + 1 \right)}{2} + \\
&+ \frac{\sqrt{\left( M_6 - r12_t + p12_t \left( \frac{M_5}{n_3 [i12]} + \frac{1}{n_3} + 1 \right) \right)^2 + 4r12_t M_6}}{2}, \\
[w35] &= -\frac{M_8 - r35_t + p35_t \left( \frac{M_7}{n_4 [i35]} + \frac{1}{n_4} + 1 \right)}{2} + \\
&+ \frac{\sqrt{\left( M_8 - r35_t + p35_t \left( \frac{M_7}{n_4 [i35]} + \frac{1}{n_4} + 1 \right) \right)^2 + 4r35_t M_8}}{2},
\end{aligned} \tag{7.113}$$

where

$$\begin{aligned}
[i2] &= \frac{[I2]}{S3_t}, [w2] = \frac{[RpJ2]}{S3_T}, r2_t = \frac{R2_T}{S3_T}, p2_t = \frac{P2_T}{S3_T}, M_1 = \frac{f_2 + f_3}{f_1 S3_T}, M_2 = \frac{f_5 + f_6}{f_4 S3_T}, n_1 = \frac{f_2}{f_5}, [i6] = \frac{[I6]}{S3_T}, \\
[w6] &= \frac{[RpJ6]}{S3_T}, r6_t = \frac{R6_T}{S3_T}, p6_t = \frac{P6_T}{S3_T}, M_3 = \frac{f_8 + f_9}{f_7 S3_T}, M_4 = \frac{f_{11} + f_{12}}{f_{10} S3_T}, n_2 = \frac{f_8}{f_{11}}, [i12] = \frac{[I12]}{S3_T}, \\
[w12] &= \frac{[RpJ12]}{S3_T}, r12_t = \frac{R12_T}{S3_T}, p12_t = \frac{P12_T}{S3_T}, M_5 = \frac{f_{14} + f_{15}}{f_{13} S3_T}, M_6 = \frac{f_{17} + f_{18}}{f_{16} S3_T}, n_3 = \frac{f_{14}}{f_{17}}, \\
[i35] &= \frac{[I35]}{S3_T}, [w35] = \frac{[RpJ35]}{S3_T}, r35_t = \frac{R35_T}{S3_T}, p35_t = \frac{P35_T}{S3_T}, M_7 = \frac{f_{20} + f_{21}}{f_{19} S3_T}, M_8 = \frac{f_{23} + f_{24}}{f_{22} S3_T}, n_4 = \frac{f_{20}}{f_{23}}.
\end{aligned}$$

## 7.5.2 STAT phosphorylation and subsequent dimerisation

ODEs for the STAT phosphorylation and dimerisation module are given by:



$$\begin{aligned}
\frac{d}{dt}[RpJ2S3] &= a_1[RpJ2][S3] - (a_2 + a_3)[RpJ2S3], \\
\frac{d}{dt}[RpJ6S3] &= a_4[RpJ6][S3] - (a_5 + a_6)[RpJ6S3], \\
\frac{d}{dt}[S3p] &= a_2[RpJ2S3] + a_5[RpJ6S3] - a_7[P3][S3p] + a_9[P3S3p] - \\
&\quad - 2a_{19}[S3p]^2 + 2a_{20}[S33] - a_{21}[S3p][S5p] + a_{22}[S35], \\
\frac{d}{dt}[P3S3p] &= a_7[P3][S3p] - (a_8 + a_9)[P3S3p], \\
\frac{d}{dt}[RpJ12S4] &= a_{10}[RpJ12][S4] - (a_{11} + a_{12})[RpJ12S4], \\
\frac{d}{dt}[RpJ35S4] &= a_{13}[RpJ35][S4] - (a_{14} + a_{15})[RpJ35S4], \\
\frac{d}{dt}[S4p] &= a_{11}[RpJ12S4] + a_{14}[RpJ35S4] - a_{16}[P4][S4p] + a_{18}[P4S4p] - \\
&\quad - a_{21}[S3p][S4p] + a_{22}[S34] - 2a_{23}[S4p]^2 + 2a_{24}[S44], \\
\frac{d}{dt}[P4S4p] &= a_{16}[P4][S4p] - (a_{17} + a_{18})[P4S4p], \\
\frac{d}{dt}[S33] &= a_{19}[S3p]^2 - a_{20}[S33], \\
\frac{d}{dt}[S34] &= a_{21}[S3p][S4p] - a_{22}[S34], \\
\frac{d}{dt}[S44] &= a_{23}[S4p]^2 - a_{24}[S44].
\end{aligned} \tag{7.114}$$

Conservation equations (here we neglect STAT-gene interactions):

$$\begin{aligned}
S3_T &= [S3] + [S3p] + 2[S33] + [S34] + [RpJ2S3] + [RpJ6S3] + [P3S3p], \\
S4_T &= [S4] + [S4p] + 2[S44] + [S34] + [RpJ12S4] + [RpJ35S4] + [P4S4p], \\
P3_T &= [P3] + [P3S3p], \\
P4_T &= [P4] + [P4S4p].
\end{aligned} \tag{7.115}$$

Conservation Equations (7.115) in non-dimensional form:

$$\begin{aligned}
1 &= [s3] + [s3p] + 2[s33] + [s34] + [w2s3] + [w6s3] + [p3s3p], \\
s4_t &= [s4] + [s4p] + 2[s44] + [s34] + [w12s4] + [w35s4] + [p4s4p], \\
p3_t &= [p3] + [p3s3p], \\
p4_t &= [p4] + [p4s4p],
\end{aligned} \tag{7.116}$$

where

$$\begin{aligned}
[s3] &= \frac{[S3]}{S3_T}, [s3p] = \frac{[S3p]}{S3_T}, [w2s3] = \frac{[RpJ2S3]}{S3_T}, [w6s3] = \frac{[RpJ6S3]}{S3_T}, [p3s3p] = \frac{[P3S3p]}{S3_T}, s4_t = \frac{S4_T}{S3_T}, \\
[s4] &= \frac{[S4]}{S3_T}, [s4p] = \frac{[S4p]}{S3_T}, [w12s4] = \frac{[RpJ12S4]}{S3_T}, [w35s4] = \frac{[RpJ35S4]}{S3_T}, [p4s4p] = \frac{[P4S4p]}{S3_T}, \\
[s33] &= \frac{[S33]}{S3_T}, [s34] = \frac{[S34]}{S3_T}, [s44] = \frac{[S44]}{S3_T}, [p3] = \frac{[P3]}{S3_T}, [p4] = \frac{[P4]}{S3_T}, p3_t = \frac{P3_T}{S3_T}, p4_t = \frac{P4_T}{S3_T}.
\end{aligned}$$

ODEs (7.114) in non-dimensional form can be written as follows:

$$\begin{aligned}
\frac{d}{d\tau}[w2s3] &= m_1[w2][s3] - [w2s3] \\
\frac{d}{d\tau}[w6s3] &= m_3[w6][s3] - (m_4 + m_5)[w6s3] \\
\frac{d}{d\tau}[s3p] &= m_2[w2s3] + m_4[w6s3] - m_6[p3][s3p] + m_8[p3s3p] - \\
&\quad - 2m_{18}[s3p]^2 + 2m_{19}[s33] - m_{20}[s3p][s4p] + m_{21}[s34] \\
\frac{d}{d\tau}[p3s3p] &= m_6[p3][s3p] - (m_7 + m_8)[p3s3p] \\
\frac{d}{d\tau}[w12s4] &= m_9[w12][s4] - (m_{10} + m_{11})[w12s4] \\
\frac{d}{d\tau}[w35s4] &= m_{12}[w35][s4] - (m_{13} + m_{14})[w35s4] \\
\frac{d}{d\tau}[s4p] &= m_{10}[w12s4] + m_{13}[w35s4] - m_{15}[p4][s4p] + m_{17}[p4s4p] - \\
&\quad - m_{20}[s3p][s4p] + m_{21}[s34] - 2m_{22}[s4p]^2 + 2m_{23}[s44] \\
\frac{d}{d\tau}[p4s4p] &= m_{15}[p4][s4p] - (m_{16} + m_{17})[p4s4p] \\
\frac{d}{d\tau}[s33] &= m_{18}[s3p]^2 - m_{19}[s33] \\
\frac{d}{d\tau}[s34] &= m_{20}[s3p][s4p] - m_{21}[s34] \\
\frac{d}{d\tau}[s44] &= m_{22}[s4p]^2 - m_{23}[s44]
\end{aligned} \tag{7.117}$$

where

$$\begin{aligned}
\tau &= t(a_2 + a_3), m_1 = \frac{a_1}{a_2 + a_3} S3_T, m_2 = \frac{a_2}{a_2 + a_3}, m_3 = \frac{a_4}{a_2 + a_3} S3_T, m_4 = \frac{a_5}{a_2 + a_3}, m_5 = \frac{a_6}{a_2 + a_3}, \\
m_6 &= \frac{a_7}{a_2 + a_3} S3_T, m_7 = \frac{a_8}{a_2 + a_3}, m_8 = \frac{a_9}{a_2 + a_3}, m_9 = \frac{a_{10}}{a_2 + a_3} S3_T, m_{10} = \frac{a_{11}}{a_2 + a_3}, m_{11} = \frac{a_{12}}{a_2 + a_3}, \\
m_{12} &= \frac{a_{13}}{a_2 + a_3} S3_T, m_{13} = \frac{a_{14}}{a_2 + a_3}, m_{14} = \frac{a_{15}}{a_2 + a_3}, m_{15} = \frac{a_{16}}{a_2 + a_3} S3_T, m_{16} = \frac{a_{17}}{a_2 + a_3}, m_{17} = \frac{a_{18}}{a_2 + a_3}, \\
m_{18} &= \frac{a_{19}}{a_2 + a_3} S3_T, m_{19} = \frac{a_{20}}{a_2 + a_3}, m_{20} = \frac{a_{21}}{a_2 + a_3} S3_T, m_{21} = \frac{a_{22}}{a_2 + a_3}, m_{22} = \frac{a_{23}}{a_2 + a_3} S3_T, m_{23} = \frac{a_{24}}{a_2 + a_3}.
\end{aligned}$$

We need to find steady-state solution of System (7.117):

$$\begin{aligned}
0 &= m_1 [w2][s3] - [w2s3] \\
0 &= m_3 [w6][s3] - (m_4 + m_5)[w6s3] \\
\frac{d}{d\tau} [s3p] &= m_2 [w2s3] + m_4 [w6s3] - m_6 [p3][s3p] + m_8 [p3s3p] - \\
&\quad -2m_{18} [s3p]^2 + 2m_{19} [s33] - m_{20} [s3p][s4p] + m_{21} [s34] \\
0 &= m_6 [p3][s3p] - (m_7 + m_8)[p3s3p] \\
0 &= m_9 [w12][s4] - (m_{10} + m_{11})[w12s4] \\
0 &= m_{12} [w35][s4] - (m_{13} + m_{14})[w35s4] \\
\frac{d}{d\tau} [s4p] &= m_{10} [w12s4] + m_{13} [w35s4] - m_{15} [p4][s4p] + m_{17} [p4s4p] - \\
&\quad -m_{20} [s3p][s4p] + m_{21} [s34] - 2m_{22} [s4p]^2 + 2m_{23} [s44] \\
0 &= m_{15} [p4][s4p] - (m_{16} + m_{17})[p4s4p] \\
0 &= m_{18} [s3p]^2 - m_{19} [s33] \\
0 &= m_{20} [s3p][s4p] - m_{21} [s34] \\
0 &= m_{22} [s4p]^2 - m_{23} [s44]
\end{aligned} \tag{7.118}$$

We can simplify System (7.118):

$$\begin{aligned}
0 &= m_1 [w2][s3] - [w2s3] \\
0 &= m_3 [w6][s3] - (m_4 + m_5)[w6s3] \\
\frac{d}{d\tau} [s3p] &= m_2 [w2s3] + m_4 [w6s3] - m_7 [p3s3p] \\
0 &= m_6 [p3][s3p] - (m_7 + m_8)[p3s3p] \\
0 &= m_9 [w12][s4] - (m_{10} + m_{11})[w12s4] \\
0 &= m_{12} [w35][s4] - (m_{13} + m_{14})[w35s4] \\
\frac{d}{d\tau} [s4p] &= m_{10} [w12s4] + m_{13} [w35s4] - m_{16} [p4s4p] \\
0 &= m_{15} [p4][s4p] - (m_{16} + m_{17})[p4s4p] \\
0 &= m_{18} [s3p]^2 - m_{19} [s33] \\
0 &= m_{20} [s3p][s4p] - m_{21} [s34] \\
0 &= m_{22} [s4p]^2 - m_{23} [s44]
\end{aligned} \tag{7.119}$$

Then using conservation Equations (7.116) and System (7.119) we obtain:

$$\begin{aligned}
\frac{d}{d\tau} [s3p] &= m_2 [w2s3] + m_4 [w6s3] - m_7 [p3s3p], \\
\frac{d}{d\tau} [s4p] &= m_{10} [w12s4] + m_{13} [w35s4] - m_{16} [p4s4p],
\end{aligned} \tag{7.120}$$

where

$$[p3s3p] = p3_t \frac{[s3p]}{\frac{m_7 + m_8}{m_6} + [s3p]}$$

$$[p4s4p] = p4_t \frac{[s4p]}{\frac{m_{16} + m_{17}}{m_{15}} + [s4p]}$$

$$[s33] = \frac{m_{18}}{m_{19}} [s3p]^2$$

$$[s34] = \frac{m_{20}}{m_{21}} [s3p][s4p]$$

$$[s44] = \frac{m_{22}}{m_{23}} [s4p]^2$$

$$[w2s3] = m_1 [w2][s3]$$

$$[w6s3] = \frac{m_3}{m_4 + m_5} [w6][s3]$$

$$[w12s4] = \frac{m_9}{m_{10} + m_{11}} [w12][s4]$$

$$[w35s4] = \frac{m_{12}}{m_{13} + m_{14}} [w35][s4]$$

$$[s3] = \frac{1 - [s3p] - 2[s33] - [s34] - [p3s3p]}{1 + m_1 [w2] + \frac{m_3}{m_4 + m_5} [w6]}$$

$$[s4] = \frac{s4_t - [s4p] - 2[s44] - [s34] - [p4s4p]}{1 + \frac{m_9}{m_{10} + m_{11}} [w12] + \frac{m_{12}}{m_{13} + m_{14}} [w35]}$$

Or we can rewrite it as follows:

$$\begin{aligned}
[p3s3p] &= p3_t \frac{[s3p]}{M_{11} + [s3p]} \\
[p4s4p] &= p4_t \frac{[s4p]}{M_{14} + [s4p]} \\
[s33] &= \frac{[s3p]^2}{M_{15}} \\
[s34] &= \frac{[s3p][s4p]}{M_{16}} \\
[s44] &= \frac{[s4p]^2}{M_{17}} \\
[w2s3] &= \frac{[w2][s3]}{M_9} \\
[w6s3] &= \frac{[w6][s3]}{M_{10}} \\
[w12s4] &= \frac{[w12][s4]}{M_{12}} \\
[w35s4] &= \frac{[w35][s4]}{M_{13}} \\
[s3] &= \frac{1 - [s3p] - 2[s33] - [s34] - [p3s3p]}{1 + \frac{[w2]}{M_9} + \frac{[w6]}{M_{10}}} \\
[s4] &= \frac{s4_t - [s4p] - 2[s44] - [s34] - [p4s4p]}{1 + \frac{[w12]}{M_{12}} + \frac{[w35]}{M_{13}}}
\end{aligned} \tag{7.121}$$

where we denote Michaelis constants

$$\begin{aligned}
M_9 &= \frac{a_2 + a_3}{a_1 S_{3T}}, M_{10} = \frac{a_5 + a_6}{a_4 S_{3T}}, M_{11} = \frac{a_8 + a_9}{a_7 S_{3T}}, M_{12} = \frac{a_{11} + a_{12}}{a_{10} S_{3T}}, M_{13} = \frac{a_{14} + a_{15}}{a_{13} S_{3T}}, \\
M_{14} &= \frac{a_{17} + a_{18}}{a_{16} S_{3T}}, M_{15} = \frac{a_{20}}{a_{19} S_{3T}}, M_{16} = \frac{a_{22}}{a_{21} S_{3T}}, M_{17} = \frac{a_{24}}{a_{23} S_{3T}}.
\end{aligned}$$

When considering steady-state solutions of System (7.120) we can write:

$$\begin{aligned}
0 &= m_2 [w2s3] + m_4 [w6s3] - m_7 [p3s3p], \\
0 &= m_{10} [w12s4] + m_{13} [w35s4] - m_{16} [p4s4p].
\end{aligned} \tag{7.122}$$

Or we can rewrite Equations (7.122) as follows:

$$\begin{aligned}
0 &= n_5 [w2s3] + n_6 [w6s3] - [p3s3p], \\
0 &= n_7 [w12s4] + n_8 [w35s4] - [p4s4p],
\end{aligned} \tag{7.123}$$

where  $n_5 = \frac{a_2}{a_8}, n_6 = \frac{a_5}{a_8}, n_7 = \frac{a_{11}}{a_{17}}, n_8 = \frac{a_{14}}{a_{17}}$ .

We can rewrite System (7.123) substituting Equations (7.121):

$$0 = [s3p] + 2 \frac{[s3p]^2}{M_{15}} + \frac{[s3p][s4p]}{M_{16}} + p3_t \frac{[s3p]}{M_{11} + [s3p]} \left( 1 + \frac{M_9 M_{10} + M_{10} [w2] + M_9 [w6]}{n_5 M_{10} [w2] + n_6 M_9 [w6]} \right) - 1, \quad (7.124)$$

$$0 = [s4p] + 2 \frac{[s4p]^2}{M_{17}} + \frac{[s3p][s4p]}{M_{16}} + p4_t \frac{[s4p]}{M_{14} + [s4p]} \left( 1 + \frac{M_{12} M_{13} + M_{13} [w12] + M_{12} [w35]}{n_7 M_{13} [w12] + n_8 M_{12} [w35]} \right) - s4_t,$$

We find  $[s3p]$  and  $[s4p]$  in System (7.124) numerically.

#### CD46

It can be written for SP1 in non-dimensional form according to Equation (7.96):

$$[sp1a] = sp1_t \frac{[i2]}{M_{18} + [i2]} \frac{[cd46]}{M_{19} + [cd46]}, \quad (7.125)$$

where  $[sp1a] = \frac{[SP1a]}{S3_T}$ ,  $sp1_t = \frac{SP1_T}{S3_T}$ ,  $[cd46] = \frac{[CD46]}{S3_T}$ ,  $M_{18} = \frac{l_2}{l_1 S3_T}$ , and

$$M_{19} = \frac{l_4}{l_3 S3_t}.$$

### 7.5.3 IFN- $\gamma$ and IL-10 production

Since IFN- $\gamma$  is activated in this module by STAT44 only (Figure 4.14A) we can write using Equation (7.107):

$$[ig] = \frac{M_{20}}{\frac{mp1_t}{n_9 gg_t \frac{[s44]}{M_{21} + [s44]} - 1}}, \quad (7.126)$$

where  $[ig] = \frac{[Ig]}{S3_T}$ ,  $mp1_t = \frac{Mp1_T}{S3_T}$ ,  $gg_t = \frac{Gg_T}{S3_T}$ ,  $M_{20} = \frac{k_4 + k_5}{k_3 S3_T}$ ,  $M_{21} = \frac{k_2}{k_1 S3_T}$ ,  $n_9 = \frac{l_5}{k_4}$ ,  $n_9 < 1$ .

According to Equation (7.109) we can write:

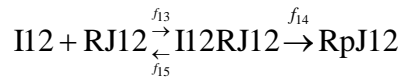
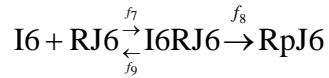
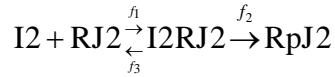
$$[i10] = \frac{M_{22}}{mp2_t} \cdot \frac{1}{n_{10}g10_t \left( \frac{[s33]}{M_{23} + [s33]} + \frac{[sp1a]}{M_{24} + [sp1a]} - \frac{[s33]}{M_{23} + [s33]} \frac{[sp1a]}{M_{24} + [sp1a]} \right)^{-1}}, \quad (7.127)$$

where

$$mp2_t = \frac{Mp2_T}{S3_T}, g10_t = \frac{G10_T}{S3_T}, M_{22} = \frac{k_{11} + k_{12}}{k_{10}S3_T}, M_{23} = \frac{k_7}{k_6S3_T}, M_{24} = \frac{k_9}{k_8S3_T}, n_{10} = \frac{l_6}{k_{11}}, n_{10} < 1.$$

## 7.6 Combined STAT3-STAT4-STAT5 model

The reactions involved in STAT3-STAT4-STAT5 circuit (Figure 4.15A):



$$\text{RpJ12} + \text{P12} \begin{array}{c} \xrightarrow{f_{16}} \\ \xrightarrow{f_{17}} \\ \xleftarrow{f_{18}} \end{array} \text{RpJ12P12} \rightarrow \text{RJ12} + \text{P12}$$

$$\text{I35} + \text{RJ35} \begin{array}{c} \xrightarrow{f_{19}} \\ \xleftarrow{f_{21}} \end{array} \text{I35RJ35} \xrightarrow{f_{20}} \text{RpJ35}$$

$$\text{RpJ35} + \text{P35} \begin{array}{c} \xrightarrow{f_{22}} \\ \xleftarrow{f_{24}} \end{array} \text{RpJ35P35} \xrightarrow{f_{23}} \text{RJ35} + \text{P35}$$

$$\text{I21} + \text{RJ21} \begin{array}{c} \xrightarrow{f_{25}} \\ \xleftarrow{f_{27}} \end{array} \text{I21RJ21} \xrightarrow{f_{26}} \text{RpJ21}$$

$$\text{RpJ21} + \text{P21} \begin{array}{c} \xrightarrow{f_{28}} \\ \xleftarrow{f_{30}} \end{array} \text{RpJ21P21} \xrightarrow{f_{29}} \text{RJ21} + \text{P21}$$

$$\text{RpJ2} + \text{S3} \begin{array}{c} \xrightarrow{a_1} \\ \xleftarrow{a_3} \end{array} \text{RpJ2S3} \xrightarrow{a_2} \text{RpJ2} + \text{S3p}$$

$$\text{RpJ6} + \text{S3} \begin{array}{c} \xrightarrow{a_4} \\ \xleftarrow{a_6} \end{array} \text{RpJ6S3} \xrightarrow{a_5} \text{RpJ6} + \text{S3p}$$

$$\text{P3} + \text{S3p} \begin{array}{c} \xrightarrow{a_7} \\ \xleftarrow{a_9} \end{array} \text{P3S3p} \xrightarrow{a_8} \text{P3} + \text{S3}$$

$$\text{RpJ12} + \text{S4} \begin{array}{c} \xrightarrow{a_{10}} \\ \xleftarrow{a_{12}} \end{array} \text{RpJ12S4} \xrightarrow{a_{11}} \text{RpJ12} + \text{S4p}$$

$$\text{RpJ35} + \text{S4} \begin{array}{c} \xrightarrow{a_{13}} \\ \xleftarrow{a_{15}} \end{array} \text{RpJ35S4} \xrightarrow{a_{14}} \text{RpJ35} + \text{S4p}$$

$$\text{P4} + \text{S4p} \begin{array}{c} \xrightarrow{a_{16}} \\ \xleftarrow{a_{18}} \end{array} \text{P4S4p} \xrightarrow{a_{17}} \text{P4} + \text{S4}$$

$$\text{RpJ2} + \text{S5} \begin{array}{c} \xrightarrow{a_{19}} \\ \xleftarrow{a_{21}} \end{array} \text{RpJ2S5} \xrightarrow{a_{20}} \text{RpJ2} + \text{S5p}$$

$$\text{RpJ21} + \text{S5} \begin{array}{c} \xrightarrow{a_{22}} \\ \xleftarrow{a_{24}} \end{array} \text{RpJ21S5} \xrightarrow{a_{23}} \text{RpJ21} + \text{S5p}$$

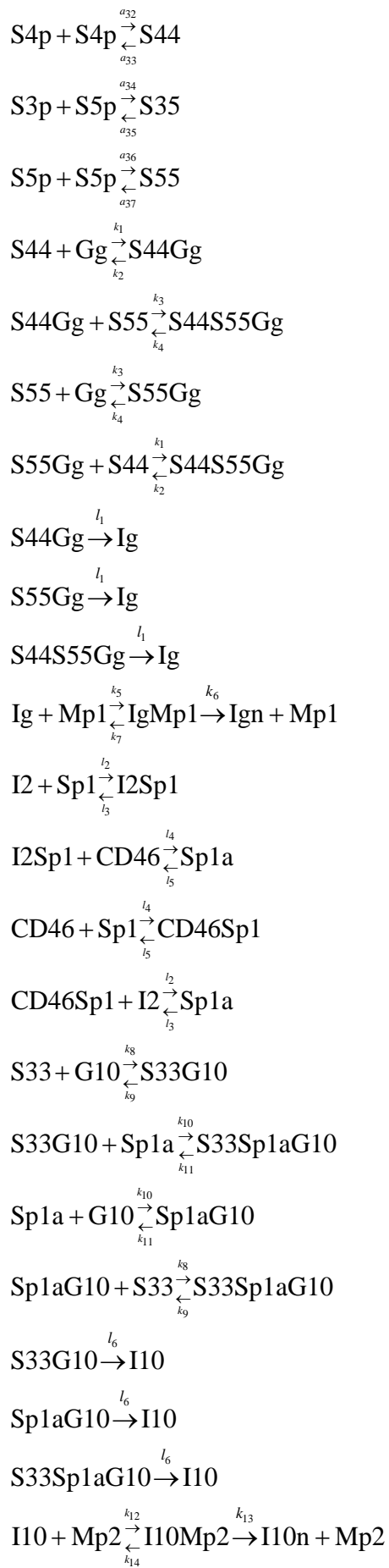
$$\text{P5} + \text{S5p} \begin{array}{c} \xrightarrow{a_{25}} \\ \xleftarrow{a_{27}} \end{array} \text{P5S5p} \xrightarrow{a_{26}} \text{P5} + \text{S5}$$

$$\text{S3p} + \text{S3p} \begin{array}{c} \xrightarrow{a_{28}} \\ \xleftarrow{a_{29}} \end{array} \text{S33}$$

$$\text{S3p} + \text{S4p} \begin{array}{c} \xrightarrow{a_{30}} \\ \xleftarrow{a_{31}} \end{array} \text{S34}$$

(7.128)





### 7.6.1 Cytokine-receptor interactions

According to Equation (7.68) we can write for  $[RpJ2]$ ,  $[RpJ6]$ ,  $[RpJ12]$ ,

$[RpJ35]$  and  $[RpJ21]$  in non-dimensional form respectively:

$$\begin{aligned}
 [w2] &= -\frac{M_2 - r2_t + p2_t \left( \frac{M_1}{n_1[i2]} + \frac{1}{n_1} + 1 \right)}{2} + \\
 &\quad + \frac{\sqrt{\left( M_2 - r2_t + p2_t \left( \frac{M_1}{n_1[i2]} + \frac{1}{n_1} + 1 \right) \right)^2 + 4r2_t M_2}}{2}, \\
 [w6] &= -\frac{M_4 - r6_t + p6_t \left( \frac{M_3}{n_2[i6]} + \frac{1}{n_2} + 1 \right)}{2} + \\
 &\quad + \frac{\sqrt{\left( M_4 - r6_t + p6_t \left( \frac{M_3}{n_2[i6]} + \frac{1}{n_2} + 1 \right) \right)^2 + 4r6_t M_4}}{2}, \\
 [w12] &= -\frac{M_6 - r12_t + p12_t \left( \frac{M_5}{n_3[i12]} + \frac{1}{n_3} + 1 \right)}{2} + \\
 &\quad + \frac{\sqrt{\left( M_6 - r12_t + p12_t \left( \frac{M_5}{n_3[i12]} + \frac{1}{n_3} + 1 \right) \right)^2 + 4r12_t M_6}}{2}, \\
 [w35] &= -\frac{M_8 - r35_t + p35_t \left( \frac{M_7}{n_4[i35]} + \frac{1}{n_4} + 1 \right)}{2} + \\
 &\quad + \frac{\sqrt{\left( M_8 - r35_t + p35_t \left( \frac{M_7}{n_4[i35]} + \frac{1}{n_4} + 1 \right) \right)^2 + 4r35_t M_8}}{2}, \\
 [w21] &= -\frac{M_{10} - r21_t + p21_t \left( \frac{M_9}{n_5[i21]} + \frac{1}{n_5} + 1 \right)}{2} + \\
 &\quad + \frac{\sqrt{\left( M_{10} - r21_t + p21_t \left( \frac{M_9}{n_5[i21]} + \frac{1}{n_5} + 1 \right) \right)^2 + 4r21_t M_{10}}}{2},
 \end{aligned} \tag{7.129}$$

where

$$\begin{aligned}
[i2] &= \frac{[I2]}{S3_T}, [w2] = \frac{[RpJ2]}{S3_T}, r2_t = \frac{R2_T}{S3_T}, p2_t = \frac{P2_T}{S3_T}, M_1 = \frac{f_2 + f_3}{f_1 S3_T}, M_2 = \frac{f_5 + f_6}{f_4 S3_T}, n_1 = \frac{f_2}{f_5}, [i6] = \frac{[I6]}{S3_T}, \\
[w6] &= \frac{[RpJ6]}{S3_T}, r6_t = \frac{R6_T}{S3_T}, p6_t = \frac{P6_T}{S3_T}, M_3 = \frac{f_8 + f_9}{f_7 S3_T}, M_4 = \frac{f_{11} + f_{12}}{f_{10} S3_T}, n_2 = \frac{f_8}{f_{11}}, [i12] = \frac{[I12]}{S3_T}, \\
[w12] &= \frac{[RpJ12]}{S3_T}, r12_t = \frac{R12_T}{S3_T}, p12_t = \frac{P12_T}{S3_T}, M_5 = \frac{f_{14} + f_{15}}{f_{13} S3_T}, M_6 = \frac{f_{17} + f_{18}}{f_{16} S3_T}, n_3 = \frac{f_{14}}{f_{17}}, [i35] = \frac{[I35]}{S3_T}, \\
[w35] &= \frac{[RpJ35]}{S3_T}, r35_t = \frac{R35_T}{S3_T}, p35_t = \frac{P35_T}{S3_T}, M_7 = \frac{f_{20} + f_{21}}{f_{19} S3_T}, M_8 = \frac{f_{23} + f_{24}}{f_{22} S3_T}, n_4 = \frac{f_{20}}{f_{23}}, \\
[i21] &= \frac{[I21]}{S3_T}, [w21] = \frac{[RpJ21]}{S3_T}, r21_t = \frac{R21_T}{S3_T}, p21_t = \frac{P21_T}{S3_T}, M_9 = \frac{f_{26} + f_{27}}{f_{25} S3_T}, M_{10} = \frac{f_{29} + f_{30}}{f_{28} S3_T}, n_5 = \frac{f_{26}}{f_{29}}.
\end{aligned}$$

## 7.6.2 STAT phosphorylation and dimerisation

ODEs for the STAT module are given by:

$$\begin{aligned}
\frac{d}{dt}[RpJ2S3] &= a_1 [RpJ2][S3] - (a_2 + a_3)[RpJ2S3], \\
\frac{d}{dt}[RpJ6S3] &= a_4 [RpJ6][S3] - (a_5 + a_6)[RpJ6S3], \\
\frac{d}{dt}[S3p] &= a_2 [RpJ2S3] + a_5 [RpJ6S3] - a_7 [P3][S3p] + a_9 [P3S3p] - \\
&\quad - 2a_{28} [S3p]^2 + 2a_{29} [S33] - a_{30} [S3p][S4p] + a_{31} [S34] - \\
&\quad - a_{34} [S3p][S5p] + a_{35} [S35], \\
\frac{d}{dt}[P3S3p] &= a_7 [P3][S3p] - (a_8 + a_9)[P3S3p],
\end{aligned}$$

$$\begin{aligned}
\frac{d}{dt}[RpJ12S4] &= a_{10}[RpJ12][S4] - (a_{11} + a_{12})[RpJ12S4], \\
\frac{d}{dt}[RpJ35S4] &= a_{13}[RpJ35][S4] - (a_{14} + a_{15})[RpJ35S4], \\
\frac{d}{dt}[S4p] &= a_{11}[RpJ12S4] + a_{14}[RpJ35S4] - a_{16}[P4][S4p] + a_{18}[P4S4p] - \\
&\quad - a_{30}[S3p][S4p] + a_{31}[S34] - 2a_{32}[S4p]^2 + 2a_{33}[S44], \\
\frac{d}{dt}[P4S4p] &= a_{16}[P4][S4p] - (a_{17} + a_{18})[P4S4p], \\
\frac{d}{dt}[RpJ2S5] &= a_{19}[RpJ2][S5] - (a_{20} + a_{21})[RpJ2S5], \\
\frac{d}{dt}[RpJ21S5] &= a_{22}[RpJ21][S5] - (a_{23} + a_{24})[RpJ21S5], \\
\frac{d}{dt}[S5p] &= a_{20}[RpJ2S5] + a_{23}[RpJ21S5] - a_{25}[P5][S5p] + a_{27}[P5S5p] - \\
&\quad - a_{34}[S3p][S5p] + a_{35}[S35] - 2a_{36}[S5p]^2 + 2a_{37}[S55], \\
\frac{d}{dt}[P5S5p] &= a_{25}[P5][S5p] - (a_{26} + a_{27})[P5S5p], \\
\frac{d}{dt}[S33] &= a_{28}[S3p]^2 - a_{29}[S33], \\
\frac{d}{dt}[S34] &= a_{30}[S3p][S4p] - a_{31}[S34], \\
\frac{d}{dt}[S44] &= a_{32}[S4p]^2 - a_{33}[S44], \\
\frac{d}{dt}[S35] &= a_{34}[S3p][S5p] - a_{35}[S35], \\
\frac{d}{dt}[S55] &= a_{36}[S5p]^2 - a_{37}[S55].
\end{aligned} \tag{7.130}$$

Conservation equations (here we neglect STAT-gene interactions):

$$\begin{aligned}
S3_T &= [S3] + [S3p] + 2[S33] + [S34] + [S35] + [RpJ2S3] + [RpJ6S3] + [P3S3p], \\
S4_T &= [S4] + [S4p] + 2[S44] + [S34] + [RpJ12S4] + [RpJ35S4] + [P4S4p], \\
S5_T &= [S5] + [S5p] + 2[S55] + [S35] + [RpJ2S5] + [RpJ21S5] + [P5S5p], \\
P3_T &= [P3] + [P3S3p], \\
P4_T &= [P4] + [P4S4p], \\
P5_T &= [P5] + [P5S5p].
\end{aligned} \tag{7.131}$$

Conservation Equations (7.131) in non-dimensional form:

$$\begin{aligned}
1 &= [s3] + [s3p] + 2[s33] + [s34] + [s35] + [w2s3] + [w6s3] + [p3s3p], \\
s4_t &= [s4] + [s4p] + 2[s44] + [s34] + [w12s4] + [w35s4] + [p4s4p], \\
s5_t &= [s5] + [s5p] + 2[s55] + [s35] + [w2s5] + [w21s5] + [p5s5p], \\
p3_t &= [p3] + [p3s3p], \\
p4_t &= [p4] + [p4s4p], \\
p5_t &= [p5] + [p5s5p],
\end{aligned} \tag{7.132}$$

where

$$\begin{aligned}
[s3] &= \frac{[S3]}{S3_T}, [s3p] = \frac{[S3p]}{S3_T}, [w2s3] = \frac{[RpJ2S3]}{S3_T}, [w6s3] = \frac{[RpJ6S3]}{S3_T}, [p3s3p] = \frac{[P3S3p]}{S3_T}, s4_t = \frac{S4_t}{S3_T}, \\
[s4] &= \frac{[S4]}{S3_T}, [s4p] = \frac{[S4p]}{S3_T}, [w12s4] = \frac{[RpJ12S4]}{S3_T}, [w35s4] = \frac{[RpJ35S4]}{S3_T}, [p4s4p] = \frac{[P4S4p]}{S3_T}, \\
s5_t &= \frac{S5_t}{S3_T}, [s5] = \frac{[S5]}{S3_T}, [s5p] = \frac{[S5p]}{S3_T}, [w2s5] = \frac{[RpJ2S5]}{S3_T}, [w21s5] = \frac{[RpJ21S5]}{S3_T}, [p5s5p] = \frac{[P5S5p]}{S3_T}, \\
[s33] &= \frac{[S33]}{S3_T}, [s34] = \frac{[S34]}{S3_T}, [s44] = \frac{[S44]}{S3_T}, [s35] = \frac{[S35]}{S3_T}, [s55] = \frac{[S55]}{S3_T}, [p3] = \frac{[P3]}{S3_T}, [p4] = \frac{[P4]}{S3_T}, \\
[p5] &= \frac{[P5]}{S3_T}, p3_t = \frac{P3_t}{S3_T}, p4_t = \frac{P4_t}{S3_T}, p5_t = \frac{P5_t}{S3_T}.
\end{aligned}$$

ODEs (7.130) in non-dimensional form are given by:

$$\begin{aligned}
\frac{d}{d\tau}[w2s3] &= m_1[w2][s3] - [w2s3] \\
\frac{d}{d\tau}[w6s3] &= m_3[w6][s3] - (m_4 + m_5)[w6s3] \\
\frac{d}{d\tau}[s3p] &= m_2[w2s3] + m_4[w6s3] - m_6[p3][s3p] + m_8[p3s3p] - \\
&\quad -2m_{27}[s3p]^2 + 2m_{28}[s33] - m_{29}[s3p][s4p] + m_{30}[s34] - \\
&\quad -m_{33}[s3p][s5p] + m_{34}[s35] \\
\frac{d}{d\tau}[p3s3p] &= m_6[p3][s3p] - (m_7 + m_8)[p3s3p] \\
\frac{d}{d\tau}[w12s4] &= m_9[w12][s4] - (m_{10} + m_{11})[w12s4] \\
\frac{d}{d\tau}[w35s4] &= m_{12}[w35][s4] - (m_{13} + m_{14})[w35s4] \\
\frac{d}{d\tau}[s4p] &= m_{10}[w12s4] + m_{13}[w35s4] - m_{15}[p4][s4p] + \\
&\quad + m_{17}[p4s4p] - m_{29}[s3p][s4p] + \\
&\quad + m_{30}[s34] - 2m_{31}[s4p]^2 + 2m_{32}[s44] \\
\frac{d}{d\tau}[p4s4p] &= m_{15}[p4][s4p] - (m_{16} + m_{17})[p4s4p] \\
\frac{d}{d\tau}[w2s5] &= m_{18}[w2][s5] - (m_{19} + m_{20})[w2s5] \\
\frac{d}{d\tau}[w21s5] &= m_{21}[w21][s5] - (m_{22} + m_{23})[w21s5] \\
\frac{d}{d\tau}[s5p] &= m_{19}[w2s5] + m_{22}[w21s5] - m_{24}[p5][s5p] + m_{26}[p5s5p] - \\
&\quad -m_{33}[s3p][s5p] + m_{34}[s35] - 2m_{35}[s5p]^2 + 2m_{36}[s55] \\
\frac{d}{d\tau}[p5s5p] &= m_{24}[p5][s5p] - (m_{25} + m_{26})[p5s5p] \\
\frac{d}{d\tau}[s33] &= m_{27}[s3p]^2 - m_{28}[s33] \\
\frac{d}{d\tau}[s34] &= m_{29}[s3p][s4p] - m_{30}[s34] \\
\frac{d}{d\tau}[s44] &= m_{31}[s4p]^2 - m_{32}[s44] \\
\frac{d}{d\tau}[s35] &= m_{33}[s3p][s5p] - m_{34}[s35] \\
\frac{d}{d\tau}[s55] &= m_{35}[s5p]^2 - m_{36}[s55]
\end{aligned} \tag{7.133}$$

where

$$\begin{aligned}
\tau = t(a_2 + a_3), m_1 &= \frac{a_1}{a_2 + a_3} S3, m_2 = \frac{a_2}{a_2 + a_3}, m_3 = \frac{a_4}{a_2 + a_3} S3, m_4 = \frac{a_5}{a_2 + a_3}, m_5 = \frac{a_6}{a_2 + a_3}, m_6 = \frac{a_7}{a_2 + a_3} S3, \\
m_7 &= \frac{a_8}{a_2 + a_3}, m_8 = \frac{a_9}{a_2 + a_3}, m_9 = \frac{a_{10}}{a_2 + a_3} S3, m_{10} = \frac{a_{11}}{a_2 + a_3}, m_{11} = \frac{a_{12}}{a_2 + a_3}, m_{12} = \frac{a_{13}}{a_2 + a_3} S3, m_{13} = \frac{a_{14}}{a_2 + a_3}, \\
m_{14} &= \frac{a_{15}}{a_2 + a_3}, m_{15} = \frac{a_{16}}{a_2 + a_3} S3, m_{16} = \frac{a_{17}}{a_2 + a_3}, m_{17} = \frac{a_{18}}{a_2 + a_3}, m_{18} = \frac{a_{19}}{a_2 + a_3} S3, m_{19} = \frac{a_{20}}{a_2 + a_3}, m_{20} = \frac{a_{21}}{a_2 + a_3}, \\
m_{21} &= \frac{a_{22}}{a_2 + a_3} S3, m_{22} = \frac{a_{23}}{a_2 + a_3}, m_{23} = \frac{a_{24}}{a_2 + a_3}, m_{24} = \frac{a_{25}}{a_2 + a_3} S3, m_{25} = \frac{a_{26}}{a_2 + a_3}, m_{26} = \frac{a_{27}}{a_2 + a_3}, \\
m_{27} &= \frac{a_{28}}{a_2 + a_3} S3, m_{28} = \frac{a_{29}}{a_2 + a_3}, m_{29} = \frac{a_{30}}{a_2 + a_3} S3, m_{30} = \frac{a_{31}}{a_2 + a_3}, m_{31} = \frac{a_{32}}{a_2 + a_3} S3, m_{32} = \frac{a_{33}}{a_2 + a_3}, \\
m_{33} &= \frac{a_{34}}{a_2 + a_3} S3, m_{34} = \frac{a_{35}}{a_2 + a_3}, m_{35} = \frac{a_{36}}{a_2 + a_3} S3, m_{36} = \frac{a_{37}}{a_2 + a_3}.
\end{aligned}$$

We need to find a steady-state solution of System (7.133):

$$\begin{aligned}
0 &= m_1[w2][s3] - [w2s3] \\
0 &= m_3[w6][s3] - (m_4 + m_5)[w6s3] \\
\frac{d}{d\tau}[s3p] &= m_2[w2s3] + m_4[w6s3] - m_6[p3][s3p] + m_8[p3s3p] - 2m_{27}[s3p]^2 + \\
&\quad + 2m_{28}[s33] - m_{29}[s3p][s4p] + m_{30}[s34] - \\
&\quad - m_{33}[s3p][s5p] + m_{34}[s35] \\
0 &= m_6[p3][s3p] - (m_7 + m_8)[p3s3p] \\
0 &= m_9[w12][s4] - (m_{10} + m_{11})[w12s4] \\
0 &= m_{12}[w35][s4] - (m_{13} + m_{14})[w35s4] \\
\frac{d}{d\tau}[s4p] &= m_{10}[w12s4] + m_{13}[w35s4] - m_{15}[p4][s4p] + m_{17}[p4s4p] - m_{29}[s3p][s4p] + \\
&\quad + m_{30}[s34] - 2m_{31}[s4p]^2 + 2m_{32}[s44] \\
0 &= m_{15}[p4][s4p] - (m_{16} + m_{17})[p4s4p] \\
0 &= m_{18}[w2][s5] - (m_{19} + m_{20})[w2s5] \\
0 &= m_{21}[w21][s5] - (m_{22} + m_{23})[w21s5] \\
\frac{d}{d\tau}[s5p] &= m_{19}[w2s5] + m_{22}[w21s5] - m_{24}[p5][s5p] + m_{26}[p5s5p] - \\
&\quad - m_{33}[s3p][s5p] + m_{34}[s35] - 2m_{35}[s5p]^2 + 2m_{36}[s55] \\
0 &= m_{24}[p5][s5p] - (m_{25} + m_{26})[p5s5p] \tag{7.134} \\
0 &= m_{27}[s3p]^2 - m_{28}[s33] \\
0 &= m_{29}[s3p][s4p] - m_{30}[s34] \\
0 &= m_{31}[s4p]^2 - m_{32}[s44] \\
0 &= m_{33}[s3p][s5p] - m_{34}[s35] \\
0 &= m_{35}[s5p]^2 - m_{36}[s55]
\end{aligned}$$

We can simplify System (7.134):

$$\begin{aligned}
0 &= m_1 [w2][s3] - [w2s3] \\
0 &= m_3 [w6][s3] - (m_4 + m_5)[w6s3] \\
\frac{d}{d\tau} [s3p] &= m_2 [w2s3] + m_4 [w6s3] - m_7 [p3s3p] \\
0 &= m_6 [p3][s3p] - (m_7 + m_8)[p3s3p] \\
0 &= m_9 [w12][s4] - (m_{10} + m_{11})[w12s4] \\
0 &= m_{12} [w35][s4] - (m_{13} + m_{14})[w35s4] \\
\frac{d}{d\tau} [s4p] &= m_{10} [w12s4] + m_{13} [w35s4] - m_{16} [p4s4p] \\
0 &= m_{15} [p4][s4p] - (m_{16} + m_{17})[p4s4p] \\
0 &= m_{18} [w2][s5] - (m_{19} + m_{20})[w2s5] \\
0 &= m_{21} [w21][s5] - (m_{22} + m_{23})[w21s5] \\
\frac{d}{d\tau} [s5p] &= m_{19} [w2s5] + m_{22} [w21s5] - m_{25} [p5s5p] \\
0 &= m_{24} [p5][s5p] - (m_{25} + m_{26})[p5s5p] \\
0 &= m_{27} [s3p]^2 - m_{28} [s33] \\
0 &= m_{29} [s3p][s4p] - m_{30} [s34] \\
0 &= m_{31} [s4p]^2 - m_{32} [s44] \\
0 &= m_{33} [s3p][s5p] - m_{34} [s35] \\
0 &= m_{35} [s5p]^2 - m_{36} [s55]
\end{aligned} \tag{7.135}$$

Then using conservation Equations (7.132) and System (7.135) we obtain:

$$\begin{aligned}
\frac{d}{d\tau} [s3p] &= m_2 [w2s3] + m_4 [w6s3] - m_7 [p3s3p] \\
\frac{d}{d\tau} [s4p] &= m_{10} [w12s4] + m_{13} [w35s4] - m_{16} [p4s4p] \\
\frac{d}{d\tau} [s5p] &= m_{19} [w2s5] + m_{22} [w21s5] - m_{25} [p5s5p]
\end{aligned} \tag{7.136}$$

where



$$[p3s3p] = p3_t \frac{[s3p]}{\frac{m_7 + m_8}{m_6} + [s3p]}$$

$$[p4s4p] = p4_t \frac{[s4p]}{\frac{m_{16} + m_{17}}{m_{15}} + [s4p]}$$

$$[p5s5p] = p5_t \frac{[s5p]}{\frac{m_{25} + m_{26}}{m_{24}} + [s5p]}$$

$$[s33] = \frac{m_{27}}{m_{28}} [s3p]^2$$

$$[s34] = \frac{m_{29}}{m_{30}} [s3p][s4p]$$

$$[s44] = \frac{m_{31}}{m_{32}} [s4p]^2$$

$$[s35] = \frac{m_{33}}{m_{34}} [s3p][s5p]$$

$$[s55] = \frac{m_{35}}{m_{36}} [s5p]^2$$

$$[w2s3] = m_1 [w2][s3]$$

$$[w6s3] = \frac{m_3}{m_4 + m_5} [w6][s3]$$

$$[w12s4] = \frac{m_9}{m_{10} + m_{11}} [w12][s4]$$

$$[w35s4] = \frac{m_{12}}{m_{13} + m_{14}} [w35][s4]$$

$$[w2s5] = \frac{m_{18}}{m_{19} + m_{20}} [w2][s5]$$

$$[w21s5] = \frac{m_{21}}{m_{22} + m_{23}} [w21][s5]$$

$$[s3] = \frac{1 - [s3p] - 2[s33] - [s34] - [s35] - [p3s3p]}{1 + m_1 [w2] + \frac{m_3}{m_4 + m_5} [w6]}$$

$$[s4] = \frac{s4_t - [s4p] - 2[s44] - [s34] - [p4s4p]}{1 + \frac{m_9}{m_{10} + m_{11}} [w12] + \frac{m_{12}}{m_{13} + m_{14}} [w35]}$$

$$[s5] = \frac{s5_t - [s5p] - 2[s55] - [s35] - [p5s5p]}{1 + \frac{m_{18}}{m_{19} + m_{20}} [w2] + \frac{m_{21}}{m_{22} + m_{23}} [w21]}$$

Or we can rewrite it in the following way:

$$\begin{aligned}
[p3s3p] &= p3_t \frac{[s3p]}{M_{13} + [s3p]} \\
[p4s4p] &= p4_t \frac{[s4p]}{M_{16} + [s4p]} \\
[p5s5p] &= p5_t \frac{[s5p]}{M_{19} + [s5p]} \\
[s33] &= \frac{[s3p]^2}{M_{20}} \\
[s34] &= \frac{[s3p][s4p]}{M_{21}} \\
[s44] &= \frac{[s4p]^2}{M_{22}} \\
[s35] &= \frac{[s3p][s5p]}{M_{23}} \\
[s55] &= \frac{[s5p]^2}{M_{24}} \\
[w2s3] &= \frac{[w2][s3]}{M_{11}} \\
[w6s3] &= \frac{[w6][s3]}{M_{12}} \\
[w12s4] &= \frac{[w12][s4]}{M_{14}} \\
[w35s4] &= \frac{[w35][s4]}{M_{15}} \\
[w2s5] &= \frac{[w2][s5]}{M_{17}} \\
[w21s5] &= \frac{[w21][s5]}{M_{18}} \\
[s3] &= \frac{1 - [s3p] - 2[s33] - [s34] - [s35] - [p3s3p]}{1 + \frac{[w2]}{M_{11}} + \frac{[w6]}{M_{12}}} \\
[s4] &= \frac{s4_t - [s4p] - 2[s44] - [s34] - [p4s4p]}{1 + \frac{[w12]}{M_{14}} + \frac{[w35]}{M_{15}}} \\
[s5] &= \frac{s5_t - [s5p] - 2[s55] - [s35] - [p5s5p]}{1 + \frac{[w2]}{M_{17}} + \frac{[w21]}{M_{18}}}
\end{aligned} \tag{7.137}$$

where we denote Michaelis constants

$$\begin{aligned}
M_{11} &= \frac{a_2 + a_3}{a_1 S 3_T}, M_{12} = \frac{a_5 + a_6}{a_4 S 3_T}, M_{13} = \frac{a_8 + a_9}{a_7 S 3_T}, M_{14} = \frac{a_{11} + a_{12}}{a_{10} S 3_T}, M_{15} = \frac{a_{14} + a_{15}}{a_{13} S 3_T}, M_{16} = \frac{a_{17} + a_{18}}{a_{16} S 3_T}, \\
M_{17} &= \frac{a_{20} + a_{21}}{a_{19} S 3_T}, M_{18} = \frac{a_{23} + a_{24}}{a_{22} S 3_T}, M_{19} = \frac{a_{26} + a_{27}}{a_{25} S 3_T}, M_{20} = \frac{a_{29}}{a_{28} S 3_T}, M_{21} = \frac{a_{31}}{a_{30} S 3_T}, M_{22} = \frac{a_{33}}{a_{32} S 3_T}, \\
M_{23} &= \frac{a_{35}}{a_{34} S 3_T}, M_{24} = \frac{a_{37}}{a_{36} S 3_T}.
\end{aligned}$$

We look for steady-state solutions of System (7.136):

$$\begin{aligned}
0 &= m_2 [w 2 s 3] + m_4 [w 6 s 3] - m_7 [p 3 s 3 p], \\
0 &= m_{10} [w 12 s 4] + m_{13} [w 35 s 4] - m_{16} [p 4 s 4 p], \\
0 &= m_{19} [w 2 s 5] + m_{22} [w 21 s 5] - m_{25} [p 5 s 5 p].
\end{aligned} \tag{7.138}$$

We can rewrite Equations (7.138) as follows:

$$\begin{aligned}
0 &= n_6 [w 2 s 3] + n_7 [w 6 s 3] - [p 3 s 3 p], \\
0 &= n_8 [w 12 s 4] + n_9 [w 35 s 4] - [p 4 s 4 p], \\
0 &= n_{10} [w 2 s 5] + n_{11} [w 21 s 5] - [p 5 s 5 p].
\end{aligned} \tag{7.139}$$

$$\text{where } n_6 = \frac{a_2}{a_8}, n_7 = \frac{a_5}{a_8}, n_8 = \frac{a_{11}}{a_{17}}, n_9 = \frac{a_{14}}{a_{17}}, n_{10} = \frac{a_{20}}{a_{26}}, n_{11} = \frac{a_{23}}{a_{26}}.$$

We can rewrite System (7.139) substituting Equations (7.137):

$$\left\{ \begin{aligned}
0 &= [s 3 p] + 2 \frac{[s 3 p]^2}{M_{20}} + \frac{[s 3 p][s 4 p]}{M_{21}} + \frac{[s 3 p][s 5 p]}{M_{23}} + \\
&\quad + p 3_t \frac{[s 3 p]}{M_{13} + [s 3 p]} \left( 1 + \frac{M_{11} M_{12} + M_{12} [w 2] + M_{11} [w 6]}{n_6 M_{12} [w 2] + n_7 M_{11} [w 6]} \right) - 1, \\
0 &= [s 4 p] + 2 \frac{[s 4 p]^2}{M_{22}} + \frac{[s 3 p][s 4 p]}{M_{21}} + \\
&\quad + p 4_t \frac{[s 4 p]}{M_{16} + [s 4 p]} \left( 1 + \frac{M_{14} M_{15} + M_{15} [w 12] + M_{14} [w 35]}{n_8 M_{15} [w 12] + n_9 M_{14} [w 35]} \right) - s 4_t, \\
0 &= [s 5 p] + 2 \frac{[s 5 p]^2}{M_{24}} + \frac{[s 3 p][s 5 p]}{M_{23}} + \\
&\quad + p 5_t \frac{[s 5 p]}{M_{19} + [s 5 p]} \left( 1 + \frac{M_{17} M_{18} + M_{18} [w 2] + M_{17} [w 21]}{n_{10} M_{18} [w 2] + n_{11} M_{17} [w 21]} \right) - s 5_t,
\end{aligned} \right. \tag{7.140}$$

We find  $[s 3 p]$ ,  $[s 4 p]$  and  $[s 5 p]$  in System (7.140) numerically.

## CD46

It can be written for SP1 in non-dimensional form according to Equation (7.96):

$$[sp1a] = sp1_t \frac{[i2]}{M_{25} + [i2]} \frac{[cd46]}{M_{26} + [cd46]}, \quad (7.141)$$

where  $[sp1a] = \frac{[SP1a]}{S3_T}$ ,  $sp1_t = \frac{SP1_T}{S3_T}$ ,  $[cd46] = \frac{[CD46]}{S3_T}$ ,  $M_{25} = \frac{l_3}{l_2 S3_T}$ , and

$$M_{26} = \frac{l_5}{l_4 S3_T}.$$

### 7.6.3 IFN- $\gamma$ and IL-10 production

Since IFN- $\gamma$  gene is activated by either STAT44 or STAT55, it can be written according to Equation (7.109):

$$[ig] = \frac{M_{27}}{mp1_t} \frac{1}{n_{12} gg_t \left( \frac{[s44]}{M_{28} + [s44]} + \frac{[s55]}{M_{29} + [s55]} - \frac{[s44]}{M_{28} + [s44]} \frac{[s55]}{M_{29} + [s55]} \right)^{-1}}, \quad (7.142)$$

where

$$[ig] = \frac{[Ig]}{S3_T}, mp1_t = \frac{Mp1_T}{S3_T}, gg_t = \frac{Gg_T}{S3_T}, M_{27} = \frac{k_6 + k_7}{k_5 S3_T}, M_{28} = \frac{k_2}{k_1 S3_T}, KM_{29} = \frac{k_4}{k_3 S3_T}, n_{12} = \frac{l_1}{k_6},$$

and  $n_{12} < 1$ .

The production of IL-10 can be activated by either STAT33 or SP1 through CD46. Thus, according to Equation (7.109), it can be written:

$$[i10] = \frac{M_{30}}{mp2_t} \frac{1}{n_{13} g10_t \left( \frac{[s33]}{M_{31} + [s33]} + \frac{[sp1a]}{M_{32} + [sp1a]} - \frac{[s33]}{M_{31} + [s33]} \frac{[sp1a]}{M_{32} + [sp1a]} \right)^{-1}}, \quad (7.143)$$

where

$$mp2_t = \frac{Mp2_T}{S3_T}, g10_t = \frac{G10_T}{S3_T}, M_{30} = \frac{k_{13} + k_{14}}{k_{12} S3_T}, M_{31} = \frac{k_9}{k_8 S3_T}, M_{32} = \frac{k_{11}}{k_{10} S3_T}, n_{13} = \frac{l_6}{k_{13}},$$

where  $n_{13} < 1$ .

## 7.7 Parametric analysis

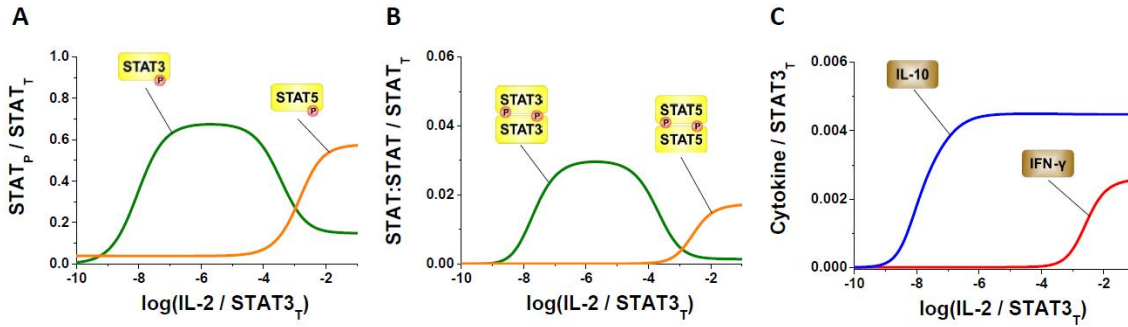


Figure 7.1. The model predictions for the swapped parameters. A. STAT monomers. B. STAT homodimers. C. Cytokines.

Table 7.2. Nominal, optimised parameters and squared error SM.

Par	Nom	O1	O2	O3	O4	O5	O6	O7	O8	O9	O10	O11	O12	O13	O14	O15
r2 <sub>1</sub>	0.003	0.003509	0.002832	0.0027	0.000642	0.019794	0.00045	0.019193	0.007935	0.001365	0.0004	0.027443	0.017109	0.004116	0.001955	0.000483
p2 <sub>1</sub>	0.003	0.027889	0.005466	0.0027	0.003567	0.003013	0.00236	0.000391	0.001873	0.003381	0.000954	0.018632	0.006114	0.002781	0.001408	0.00091
M <sub>1</sub>	0.1	0.025534	0.47271	0.1333	0.040663	0.3277	0.026149	0.40489	0.20611	0.033704	0.015943	0.72946	0.056363	0.13378	0.021674	0.019028
M <sub>2</sub>	4.00E-05	0.000204	0.000161	4.25E-05	0.000197	7.32E-05	0.000283	1.62E-05	0.000343	3.83E-05	0.000223	7.22E-05	5.12E-05	6.21E-05	3.20E-05	9.20E-05
n <sub>1</sub>	120	134.51	644.3	118.42	72.739	103.68	560.59	820.37	200.61	862.9	283.75	105.73	274.74	34.881	230.86	14.268
s5 <sub>1</sub>	0.025	0.024774	0.1077	0.0247	0.002822	0.023708	0.013273	0.018098	0.11675	0.00651	0.004803	0.23769	0.12053	0.023753	0.015575	0.010874
p3 <sub>1</sub>	2.6	0.89728	1.2949	2.5924	24.163	22.171	7.4742	10.399	5.6766	10.873	4.9583	21.681	19.95	20.225	16.902	7.6764
p5 <sub>1</sub>	0.001	0.001858	0.000861	0.0012	0.000221	0.006268	0.000882	0.00265	0.009407	0.001797	0.000474	0.000497	0.009068	0.000475	0.001185	0.006386
M <sub>7</sub>	4.00E-04	0.001728	4.57E-05	3.63E-04	0.001127	0.000878	4.59E-05	0.001467	0.001375	0.000268	0.001358	0.000201	0.002265	0.000388	8.25E-05	0.000542
M <sub>9</sub>	48	9.6863	44.177	47.714	6.8966	69.877	16.866	6.4433	13.955	20.904	5.4463	8.2154	13.764	10.142	8.9364	6.9836
M <sub>13</sub>	19	43.297	12.157	19.154	26.49	64.47	11.366	3.0619	6.861	29.894	4.2357	58.53	2.3561	28.926	2.0914	54.439
n <sub>4</sub>	0.2	0.2107	1.2957	0.1987	0.83912	1.0389	0.27776	0.65197	0.13579	0.31198	1.6554	0.99071	1.015	0.46062	0.3713	0.94161
n <sub>5</sub>	1.6	9.207	7.6231	1.5589	11.252	0.79439	0.60074	0.68472	1.4609	0.34328	0.43991	3.5845	10.667	1.1144	0.41878	0.22359
M <sub>14</sub>	0.1	0.052263	0.94864	0.1002	0.14521	0.42794	0.74908	0.68789	0.045914	0.23346	0.64129	0.026867	0.19001	0.71674	0.87757	0.22681
M <sub>10</sub>	0.005	0.007492	0.001309	0.0047	0.040772	0.005439	0.006246	0.007474	0.001363	0.002274	0.019538	0.002244	0.00649	0.000814	0.01832	0.001643
M <sub>12</sub>	2.00E+03	3354	558.06	1.96E+03	2941.2	7507.6	643.49	542.99	712.59	1185.3	1028.3	1391.6	248.85	257.14	17278	4567.5
M <sub>15</sub>	0.5	1.3545	1.3625	0.3787	0.073671	0.62091	1.3246	0.04003	0.1918	2.5022	0.36109	1.2976	0.29186	0.50924	0.51241	1.027
n <sub>6</sub>	5.5	2.7485	1.1754	5.5056	33.297	2.4937	1.0916	1.3194	20.942	1.999	1.5219	55	17.825	13.946	0.63868	25.109
n <sub>7</sub>	0.03	0.14378	0.17183	0.0322	0.14479	0.060788	0.007304	0.022957	0.19581	0.031909	0.033886	0.025282	0.13774	0.006371	0.004357	0.019089
Q <sub>6</sub>	0.001	0.000604	0.000987	0.0014	0.001767	0.000368	0.002322	0.001199	0.009353	0.000293	0.001671	0.001688	0.002172	0.001201	0.00045	0.000147
Q <sub>21</sub>	3.40E-11	1.82E-11	3.29E-11	3.42E-11	8.30E-11	6.91E-12	9.33E-11	2.18E-11	2.57E-11	2.05E-11	1.36E-10	9.48E-12	6.35E-11	9.55E-12	4.26E-11	1.97E-11
gg <sub>1</sub>	0.9	0.15956	0.28281	0.8949	5.7607	6.1621	5.1155	0.76901	0.12177	6.8237	5.0325	5.1714	0.71957	0.11343	0.5014	8.0729
mp1 <sub>1</sub>	0.003	0.000362	0.011831	0.0034	0.002017	0.00276	0.000491	0.010081	0.000543	0.001536	0.023098	0.002676	0.01239	0.003733	0.00066	0.019531
M <sub>18</sub>	10	49.794	12.051	9.913	17.075	12.601	2.0105	16.569	1.2898	3.2815	57.245	1.3748	4.9301	27.867	11.032	46.883
M <sub>19</sub>	5	1.0175	1.6903	4.354	7.0324	29.257	1.8676	24.928	4.1342	3.3328	11.128	23.95	1.5233	1.3154	22.729	19.486
n <sub>8</sub>	0.01	0.001766	0.007209	0.0101	0.00607	0.005921	0.003473	0.024054	0.003863	0.053508	0.057119	0.001551	0.001237	0.006047	0.023173	0.031357
g10 <sub>1</sub>	7	6.9815	8.8946	7.2184	63.392	14.123	42.777	11.788	1.5184	2.3453	1.1908	10.022	0.89799	25.713	13.946	13.284
mp2 <sub>1</sub>	0.6	1.2895	0.26955	0.5933	4.5548	3.0464	0.78732	0.29224	0.57425	0.060594	0.20987	0.26053	0.36536	1.293	0.67941	4.3577
M <sub>20</sub>	0.015	0.018369	0.019073	0.0149	0.020308	0.030563	0.003852	0.007404	0.020735	0.019924	0.020195	0.014823	0.055386	0.054662	0.02151	0.074155
M <sub>21</sub>	0.01	0.024239	0.032193	0.0138	0.024077	0.022656	0.003987	0.00449	0.006201	0.002048	0.001389	0.095423	0.03017	0.001637	0.001683	0.019085
M <sub>22</sub>	0.2	0.21423	1.2631	0.1885	0.044434	1.0261	0.035059	0.13186	0.10364	0.051725	0.3348	0.1968	0.5264	0.055339	0.18746	0.20254
n <sub>9</sub>	0.02	0.035162	0.006445	0.0191	0.014896	0.031773	0.00877	0.009492	0.06544	0.005009	0.033464	0.00655	0.030446	0.003868	0.007794	0.021937
cd46	0.7	0.073077	0.1249	0.6826	0.17389	0.23045	0.1164	1.9959	0.98331	2.6895	0.60932	0.14905	0.5349	2.0231	3.279	0.12424
sp1 <sub>1</sub>	33	89.836	37.294	33.142	9.0941	18.309	249.25	22.863	16.009	5.3526	14.461	131.19	204.26	16.788	115.79	14.167
M <sub>16</sub>	9.00E-06	6.77E-05	8.85E-06	8.96E-06	5.10E-06	4.47E-06	7.37E-05	1.21E-05	7.99E-06	1.28E-05	6.40E-06	2.10E-05	1.55E-05	2.26E-05	6.83E-05	9.60E-07
M <sub>17</sub>	0.1	0.017299	0.013423	0.1071	0.93739	0.059451	0.16776	0.11441	0.014937	0.070503	0.027861	0.076081	0.37638	0.29741	0.031363	0.9858
SM	1.19E-06	1.15E-06	9.18E-07	7.34E-07	1.81E-06	1.56E-06	2.13E-06	1.21E-06	2.11E-06	7.96E-07	7.92E-07	2.22E-06	8.70E-07	1.13E-06	1.54E-06	1.31E-06

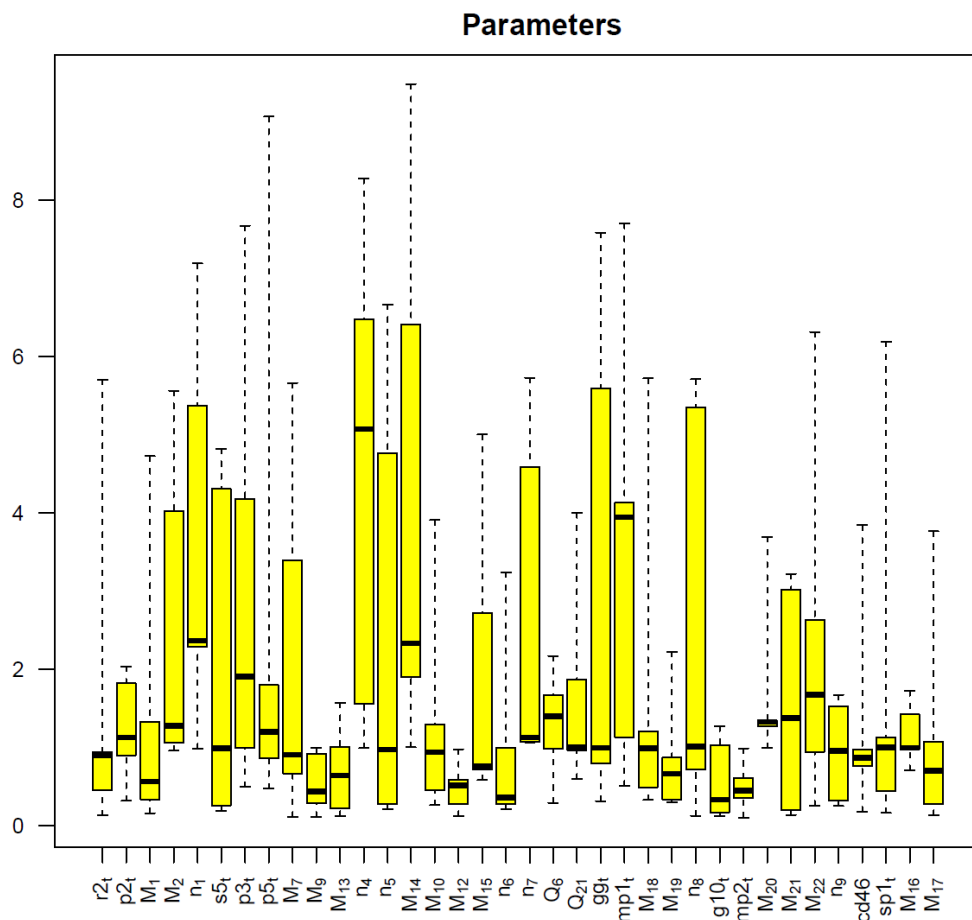


Figure 7.2. The distribution of the optimised parameters. The parameter sets with the closest squared errors  $SM$ , namely "O2", "O3", "O9", "O10" and "O12".

Table 7.3. The percentage of cases when the switching of both cytokine and STAT (C+S+), cytokine and not STAT (C+S-), not cytokine and STAT (C-S+), neither cytokine not STAT (C-S-) occurs for 1-10 fold change of the optimised parameters.

FC	C+S+	C+S-	C-S+	C-S-
1	100	0	0	0
2	77.7	10.7	6.5	5.1
3	44.5	13.8	18.3	23.4
4	28.1	12.7	18.1	41.1
5	16.4	11.6	14.9	57.1
6	11.8	12.8	13.9	61.5
7	5.7	11	11	72.3
8	5	7.7	8.9	78.4
9	4.1	7.2	6.2	82.5
10	2.1	5.6	5.6	86.7

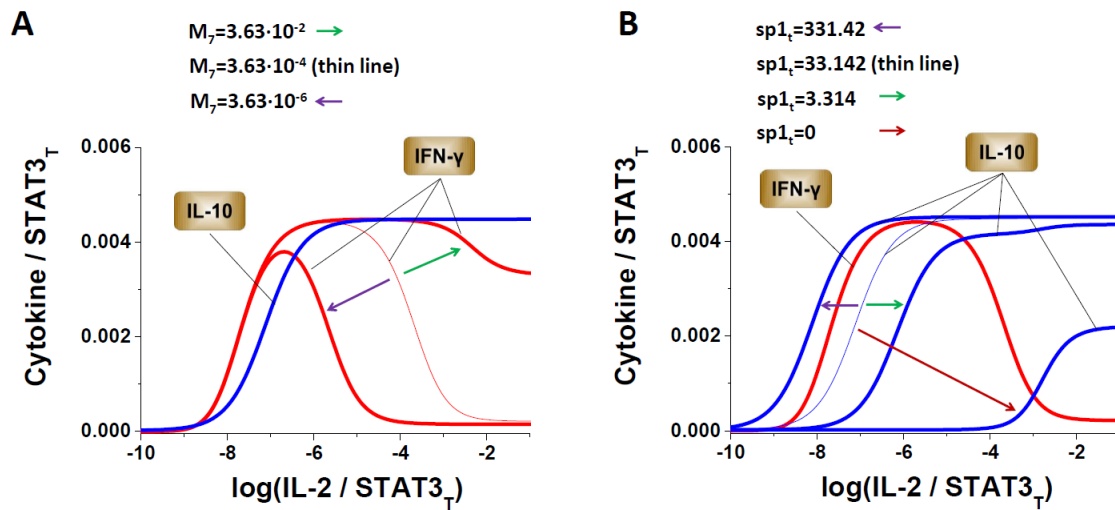


Figure 7.3. The model predictions for the produced IFN- $\gamma$  and IL-10 dependence on the changes in the STAT3 pathway. The influence of STAT3 phosphorylation on the selectivity of IFN- $\gamma$ .

Table 7.4. Parameters in the STAT3-STAT4 subsystem and their correspondence to the parameters in the STAT3-STAT5 subsystem.

Parameters in STAT3-STAT5	Parameters in STAT3-STAT4	Values
$r2_t$	$r2_t$	0.0027
$p2_t$	$p2_t$	0.0027
$M_1$	$M_1$	0.1333
$M_2$	$M_2$	4.25E-05
$n_1$	$n_1$	118.42
$s5_t$	$s4_t$	0.0247
$p3_t$	$p3_t$	2.5924
$p5_t$	$p4_t$	0.0012
$M_7$	$M_9$	3.63E-04
$M_9$	$M_{11}$	47.714
$M_{13}$	$M_{15}$	19.154
$n_4$	$n_5$	0.1987
$n_5$	$n_6$	1.5589
$M_{14}$	$M_{16}$	0.1002
$M_{12}$	$M_{14}$	1.96E+03
$M_{15}$	$M_{17}$	0.3787
$n_6$	$n_7$	5.5056
$n_7$	$n_8$	0.0322
$Q_6$	$Q_6, Q_{12}$	0.0014
$Q_{21}$	$Q_{35}$	3.42E-11
$g6_t$	$g6_t$	0.8949
$mp1_t$	$mp1_t$	0.0034
$M_{18}$	$M_{20}$	9.913
$M_{19}$	$M_{21}$	4.354
$n_8$	$n_9$	0.0101
$g10_t$	$g10_t$	7.2184
$mp2_t$	$mp2_t$	0.5933
$M_{20}$	$M_{22}$	0.0149
$M_{21}$	$M_{23}$	0.0138
$M_{22}$	$M_{24}$	0.1885
$n_9$	$n_{10}$	0.0191
cd46	cd46	0.6826
$sp1_t$	$sp1_t$	33.142
$M_{16}$	$M_{18}$	8.96E-06
$M_{17}$	$M_{19}$	0.1071

## 7.8 Appendix D

In this section the effects of the assumptions introduced to the Gennemark model [47] are presented

### 7.8.1 Gennemark model

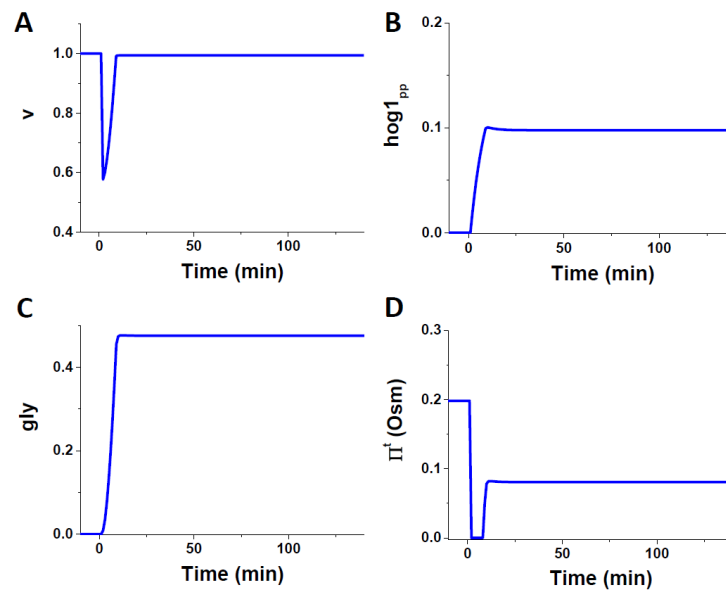


Figure 7.4. The predictions of the Gennemark model in response to the strong hyper-osmotic stress 1M.

A. The volume of the cell. B. Hog1 phosphorylation. C. Glycerol. D. Turgor pressure.



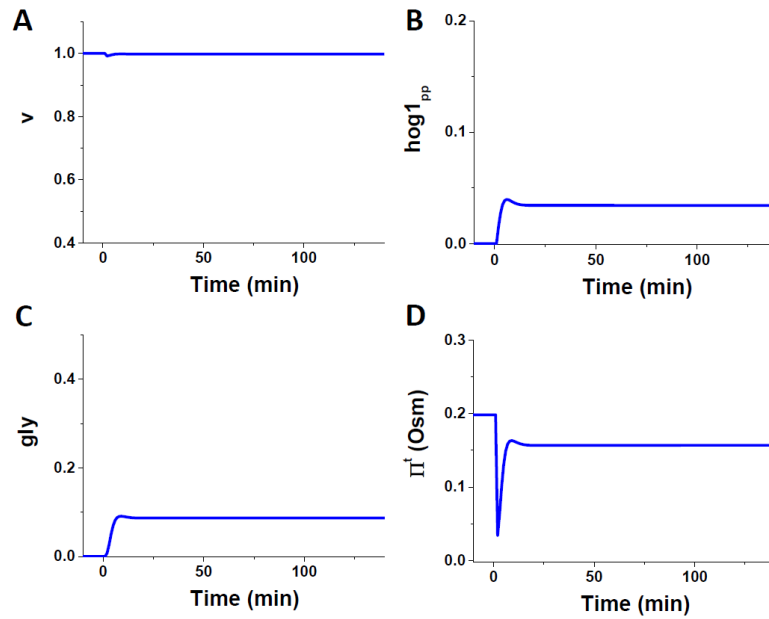


Figure 7.5. The predictions of the Gennemark model in response to the mild hyper-osmotic stress 0.3M.

A. The volume of the cell. B. Hog1 phosphorylation. C. Glycerol. D. Turgor pressure.

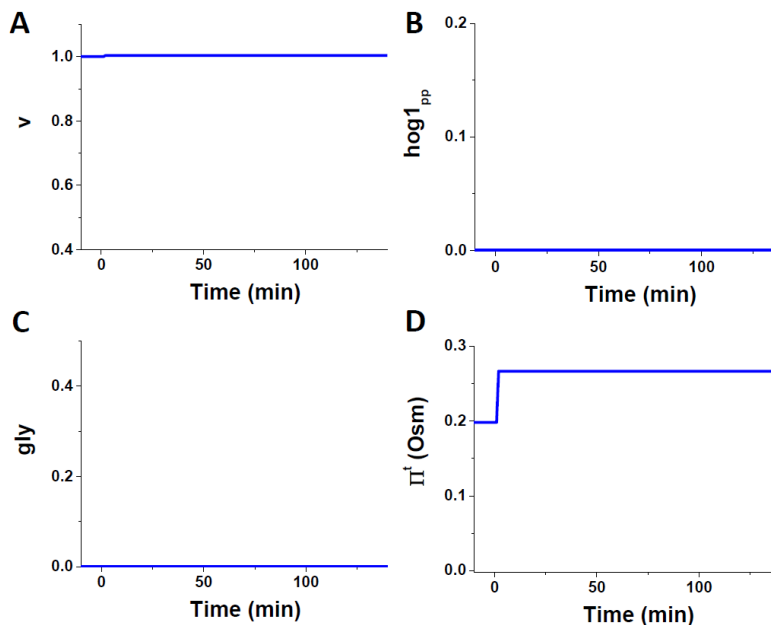


Figure 7.6. The predictions of the Gennemark model in response to the hypo-osmotic stress 0.05M.

A. The volume of the cell. B. Hog1 phosphorylation. C. Glycerol. D. Turgor pressure.

## 7.8.2 Modification 1 of the biophysical part

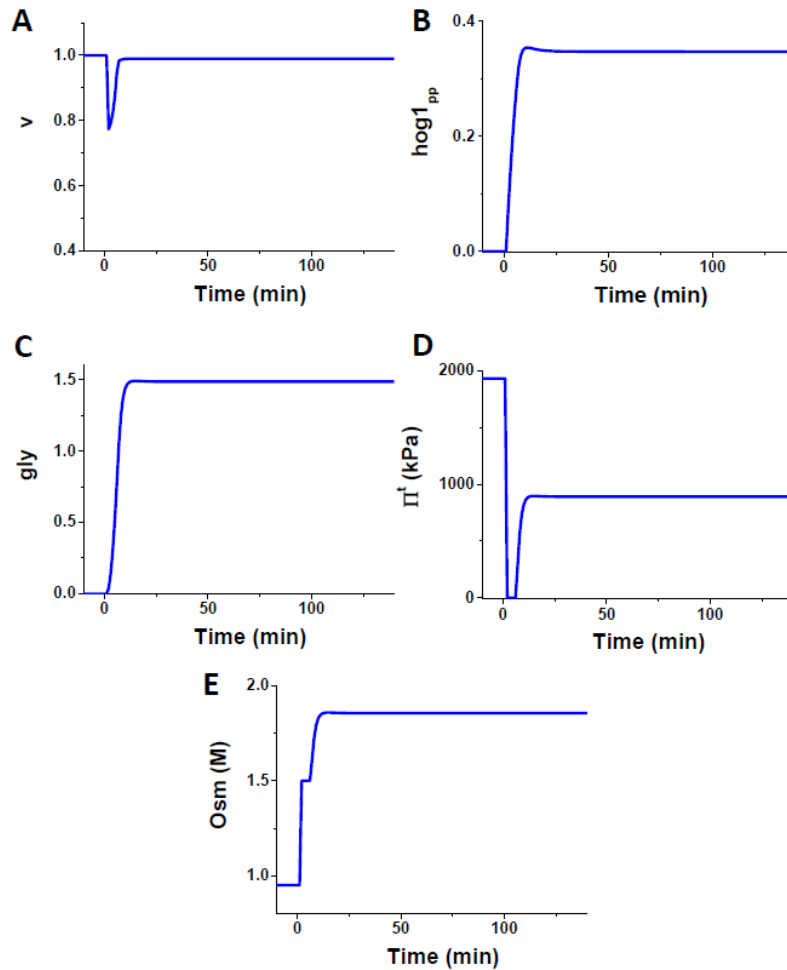


Figure 7.7. The model predictions after the introduction of the modified biophysical part in response to the strong hyper-osmotic stress 1.5M. A. The volume of the cell. B. Hog1 phosphorylation. C. Glycerol. D. Turgor pressure. E. The concentration of osmotically active compounds.

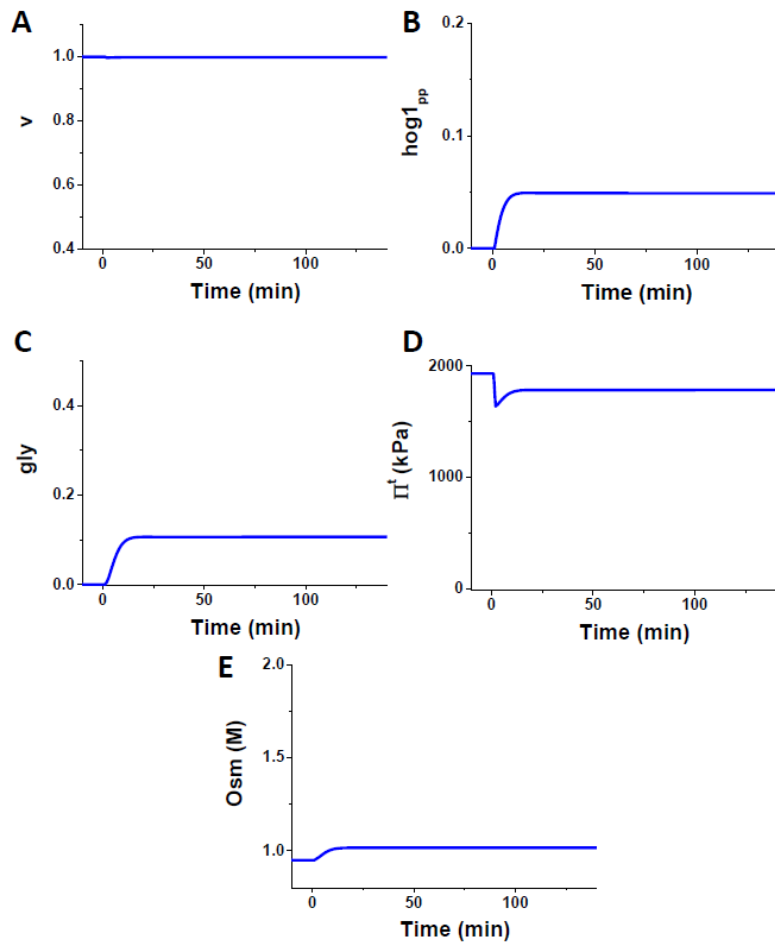


Figure 7.8. The model predictions after the introduction of the modified biophysical part in response to the mild hyper-osmotic stress 0.3M. A. The volume of the cell. B. Hog1 phosphorylation. C. Glycerol. D. Turgor pressure. E. The concentration of osmotically active compounds.

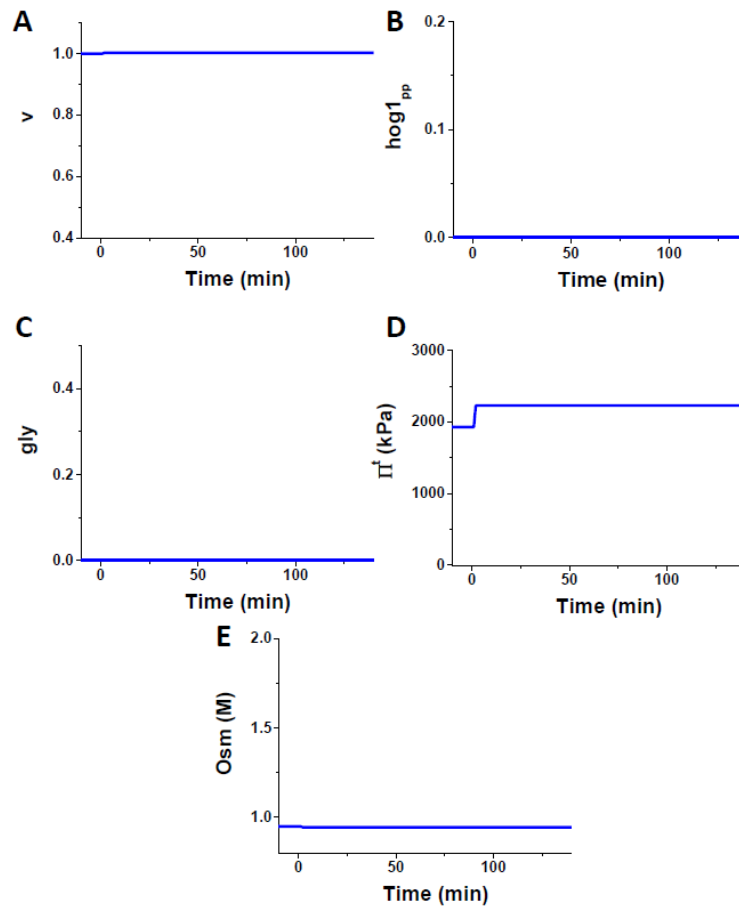


Figure 7.9. The model predictions after the introduction of the modified biophysical part in response to the hypo-osmotic stress 0.05M.

A. The volume of the cell. B. Hog1 phosphorylation. C. Glycerol. D. Turgor pressure. E. The concentration of osmotically active compounds.

### 7.8.3 Modification 2 of the glycerol metabolism module

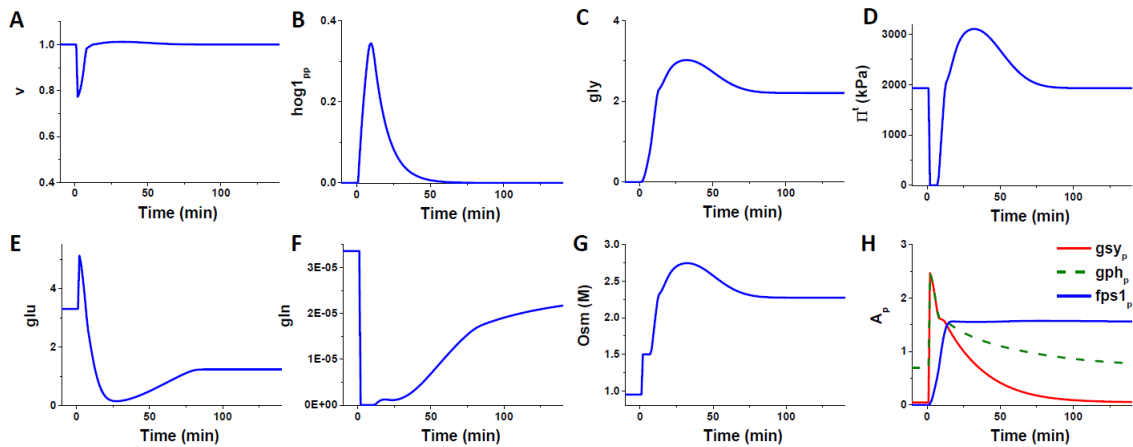


Figure 7.10. The model predictions after the introduction of the modified glycerol metabolism module in response to the strong hyper-osmotic stress 1.5M. A. The volume of the cell. B. Hog1 phosphorylation. C. Glycerol. D. Turgor pressure. E. glucose. F. Glycogen. G. The concentration of osmotically active compounds. H. Phosphorylation of glycogen synthase, glycogen phosphorylase and Fps1.

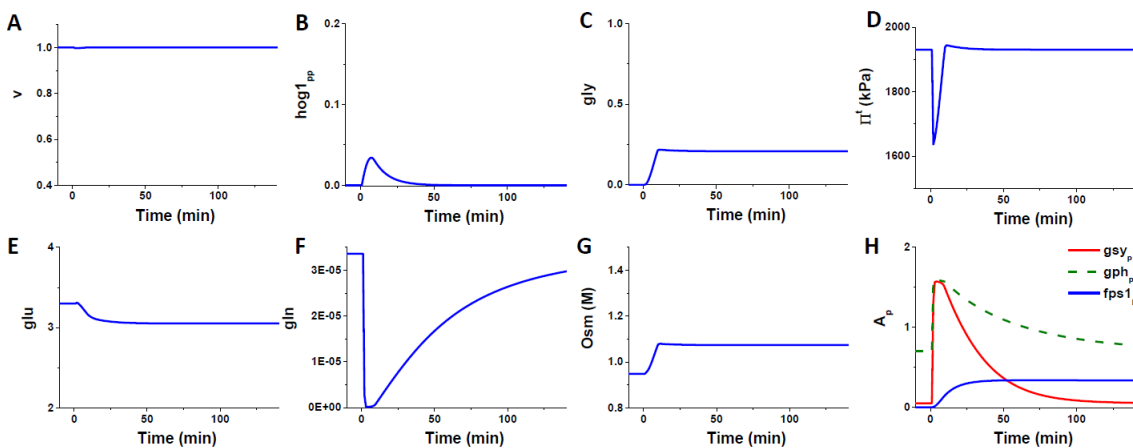


Figure 7.11. The model predictions after the introduction of the modified glycerol metabolism module in response to the mild hyper-osmotic stress 0.3M. A. The volume of the cell. B. Hog1 phosphorylation. C. Glycerol. D. Turgor pressure. E. glucose. F. Glycogen. G. The concentration of osmotically active compounds. H. Phosphorylation of glycogen synthase, glycogen phosphorylase and Fps1.

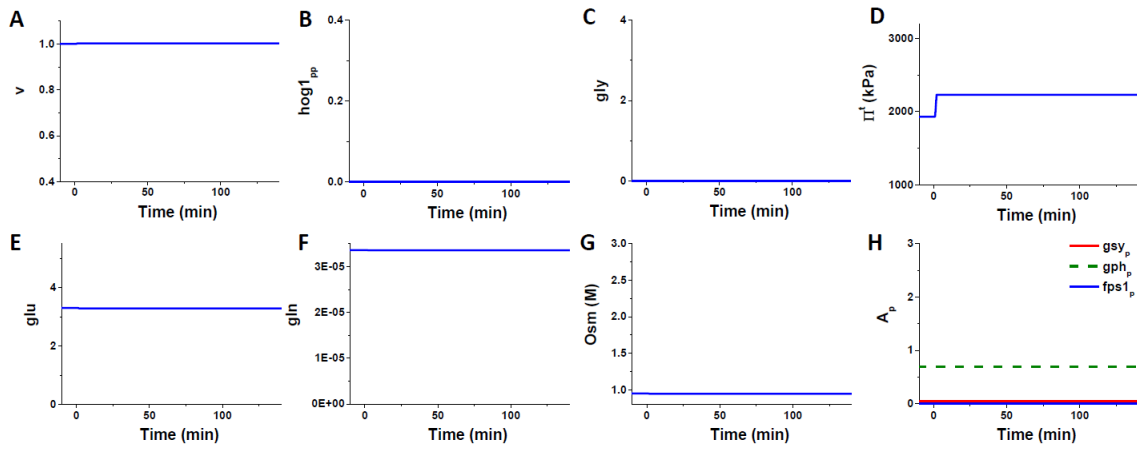


Figure 7.12. The model predictions after the introduction of the modified glycerol metabolism module in response to the hypo-osmotic stress 0.05M. A. The volume of the cell. B. Hog1 phosphorylation. C. Glycerol. D. Turgor pressure. E. glucose. F. Glycogen. G. The concentration of osmotically active compounds. H. Phosphorylation of glycogen synthase, glycogen phosphorylase and Fps1.

#### 7.8.4 Modification 3 of the Hog1 activation module

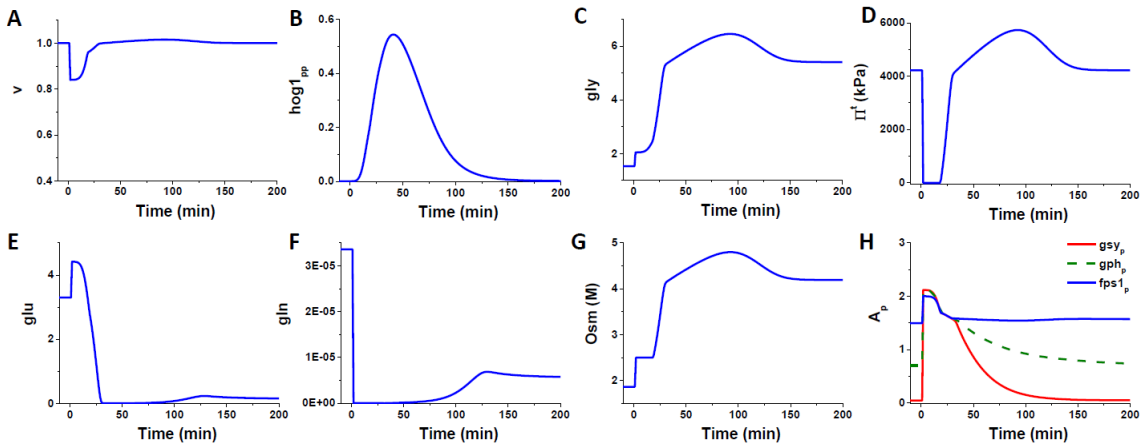


Figure 7.13. The model predictions after the introduction of the modified Hog1 activation module in response to the strong hyper-osmotic stress 2.5M. A. The volume of the cell. B. Hog1 phosphorylation. C. Glycerol. D. Turgor pressure. E. glucose. F. Glycogen. G. The concentration of osmotically active compounds. H. Phosphorylation of glycogen synthase, glycogen phosphorylase and Fps1.

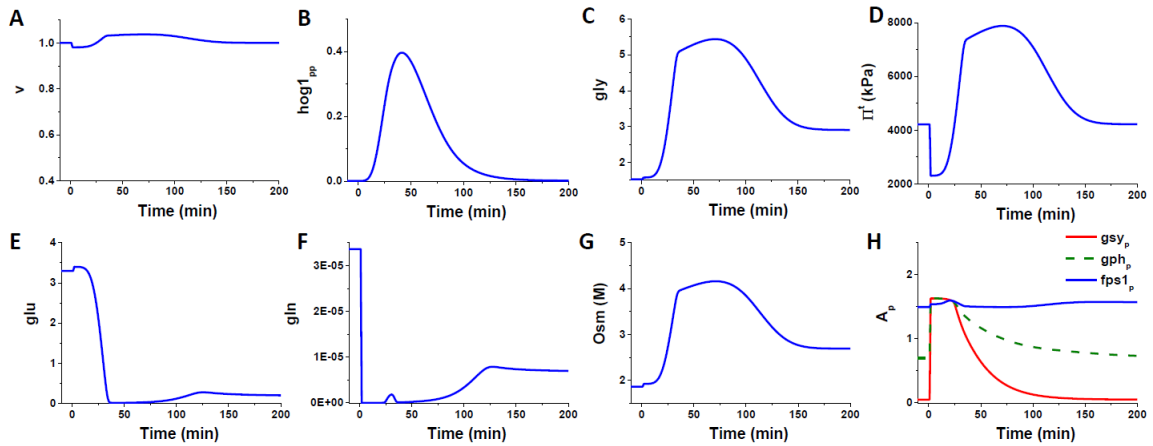


Figure 7.14. The model predictions after the introduction of the modified Hog1 activation module in response to the mild hyper-osmotic stress 1M. A. The volume of the cell. B. Hog1 phosphorylation. C. Glycerol. D. Turgor pressure. E. glucose. F. Glycogen. G. The concentration of osmotically active compounds. H. Phosphorylation of glycogen synthase, glycogen phosphorylase and Fps1.

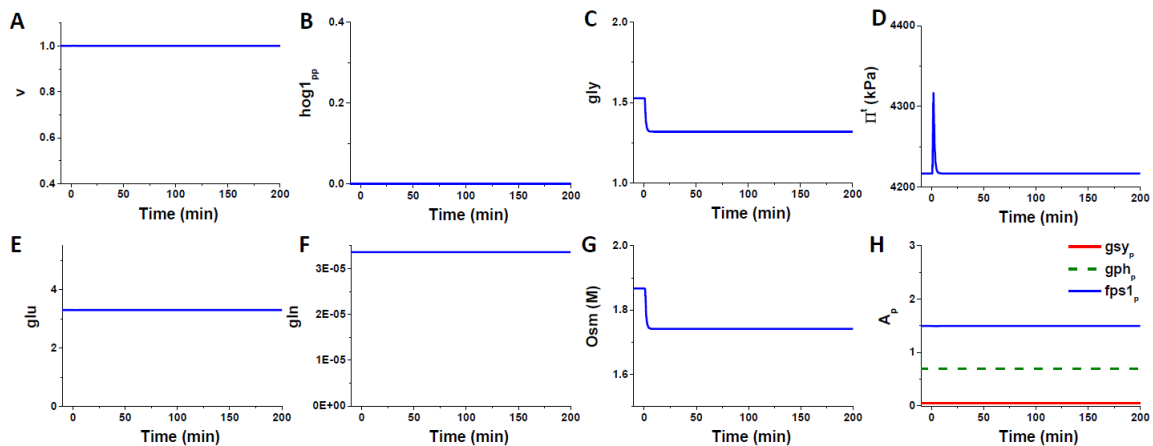


Figure 7.15. The model predictions after the introduction of the modified Hog1 activation module in response to the hypo-osmotic stress 0.05M. A. The volume of the cell. B. Hog1 phosphorylation. C. Glycerol. D. Turgor pressure. E. glucose. F. Glycogen. G. The concentration of osmotically active compounds. H. Phosphorylation of glycogen synthase, glycogen phosphorylase and Fps1.

### 7.8.5 Modification 4 of the receptor activation

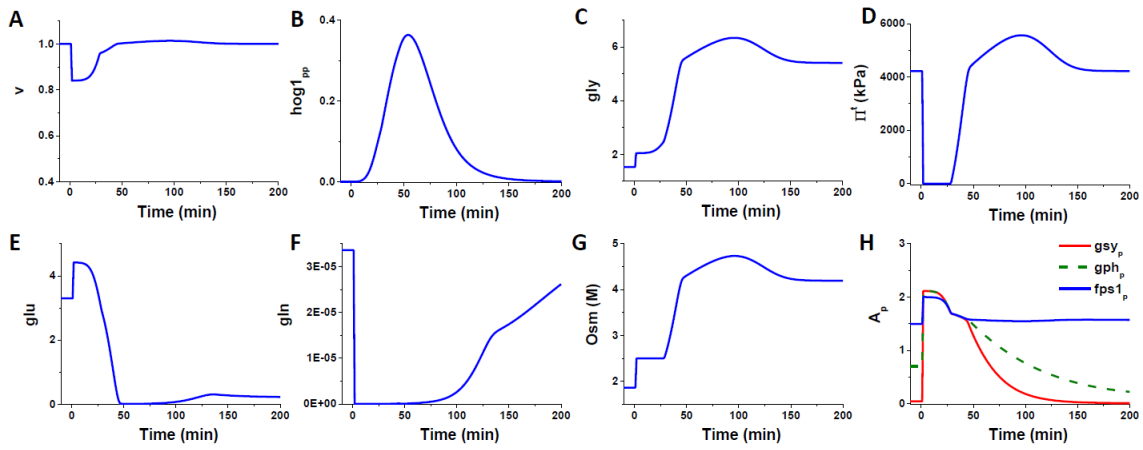


Figure 7.16. The model predictions after the introduction of the modified receptor activation module in response to the strong hyper-osmotic stress 2.5M. A. The volume of the cell. B. Hog1 phosphorylation. C. Glycerol. D. Turgor pressure. E. glucose. F. Glycogen. G. The concentration of osmotically active compounds. H. Phosphorylation of glycogen synthase, glycogen phosphorylase and Fps1.

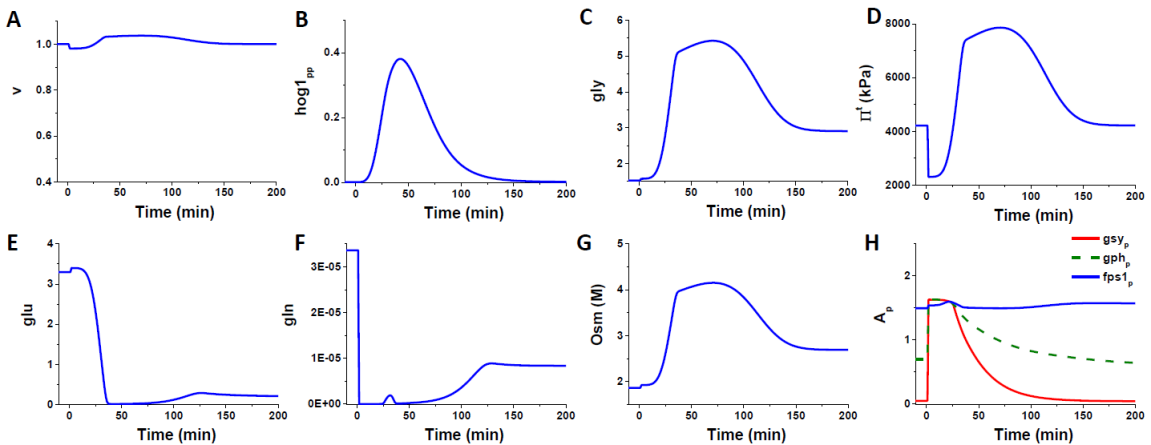


Figure 7.17. The model predictions after the introduction of the modified receptor activation module in response to the mild hyper-osmotic stress 1M. A. The volume of the cell. B. Hog1 phosphorylation. C. Glycerol. D. Turgor pressure. E. glucose. F. Glycogen. G. The concentration of osmotically active compounds. H. Phosphorylation of glycogen synthase, glycogen phosphorylase and Fps1.



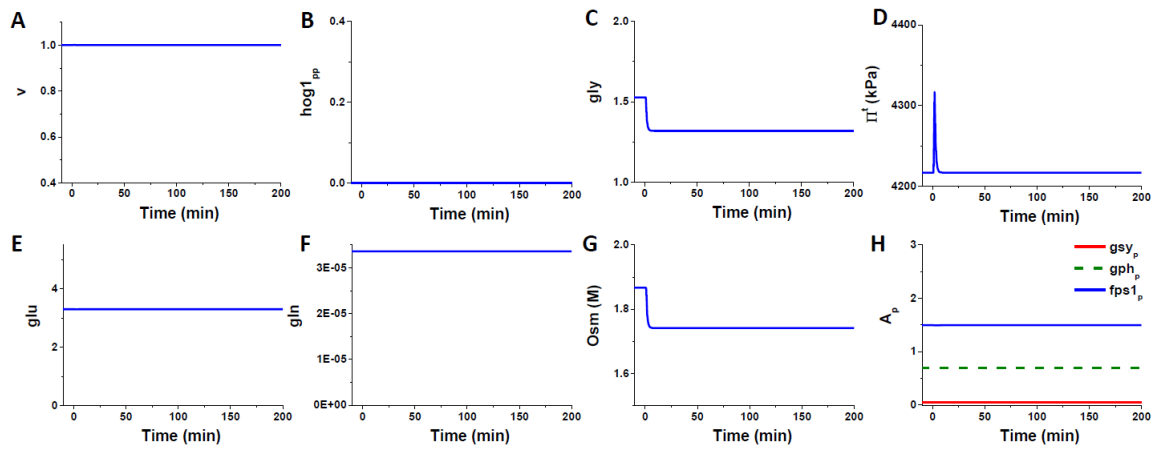


Figure 7.18. The model predictions after the introduction of the modified receptor activation module in response to the hypo-osmotic stress 0.05M. A. The volume of the cell. B. Hog1 phosphorylation. C. Glycerol. D. Turgor pressure. E. glucose. F. Glycogen. G. The concentration of osmotically active compounds. H. Phosphorylation of glycogen synthase, glycogen phosphorylase and Fps1.

## 7.8.6 Other quantitative predictions

Table 7.5. Nominal and optimised parameters.

Par	Nom	O1	O2	O3	O4	O5	O6	O7	O8	O9	O10	O11	O12	O13	O14	O15
f <sub>1</sub>	5.000	2.921	4.339	6.336	3.747	9.589	2.967	3.789	9.566	3.673	9.944	3.733	7.982	6.040	2.872	4.604
b <sub>1</sub>	0.003	0.005	0.003	0.004	0.002	0.004	0.005	0.004	0.002	0.004	0.004	0.005	0.003	0.005	0.005	0.003
f <sub>2</sub> <sup>p</sup>	12.000	17.559	13.947	7.946	17.713	13.427	17.501	16.622	23.892	7.063	10.801	17.349	16.630	14.132	10.954	11.997
b <sub>2</sub> <sup>p</sup>	2.300	2.185	3.091	3.414	1.473	2.572	3.134	3.897	3.711	4.426	3.187	2.558	2.493	2.096	2.697	2.317
f <sub>3</sub> <sup>p</sup>	17.000	21.861	29.022	19.470	26.533	20.270	17.300	23.925	29.924	9.762	26.818	20.680	14.785	17.319	17.097	17.347
ff <sub>1</sub>	0.005	0.008	0.006	0.003	0.004	0.003	0.004	0.003	0.005	0.005	0.007	0.009	0.010	0.006	0.007	0.005
bb <sub>1</sub>	3.200	4.024	6.302	5.650	3.894	6.272	5.830	2.585	3.242	2.865	4.773	4.239	5.196	6.346	4.189	3.164
m <sub>1</sub>	2.000	1.761	1.542	1.707	3.854	3.715	2.710	3.339	1.287	1.061	3.033	2.403	2.130	1.660	3.883	1.895
m <sub>2</sub>	2.000	3.915	3.243	3.336	3.493	1.388	1.534	2.118	3.369	2.132	3.511	1.945	3.245	3.482	3.776	1.787
m <sub>3</sub>	2.000	2.527	2.039	3.968	3.896	3.695	1.063	1.285	2.090	3.884	3.056	2.161	1.658	1.816	2.767	1.892
m <sub>4</sub>	1.000	1.736	1.034	1.345	1.714	0.767	0.764	0.589	1.582	1.469	0.658	1.182	1.984	0.968	1.258	0.854
m <sub>5</sub>	1.000	1.009	1.602	1.405	1.754	1.722	1.611	1.726	1.746	1.756	1.474	1.654	1.920	1.117	1.095	1.450
m <sub>6</sub>	1.000	1.561	1.980	1.005	1.778	1.583	0.813	1.995	0.978	1.924	1.561	1.241	1.129	1.709	1.509	1.146
m <sub>7</sub>	2.000	2.122	1.701	3.651	1.083	3.709	4.000	1.860	3.647	3.247	1.226	3.890	1.315	1.447	3.805	1.698
m <sub>8</sub>	2.000	1.514	3.911	2.552	3.389	2.413	2.129	1.944	2.698	1.815	3.191	1.970	3.029	2.869	3.117	1.910
m <sub>9</sub>	2.000	3.974	2.878	2.032	2.749	3.175	2.417	2.193	2.141	1.757	3.483	2.304	2.022	3.874	3.089	1.703
m <sub>10</sub>	1.000	1.799	0.859	1.863	1.937	1.410	1.558	1.659	1.266	1.808	1.741	0.570	1.490	1.453	1.738	1.118
d <sub>4</sub>	5.000	7.169	3.742	5.373	4.063	7.636	4.903	5.652	4.538	6.475	8.479	9.908	3.967	9.798	9.978	5.016
d <sub>5</sub>	4.600	5.156	2.366	4.607	3.733	4.888	5.942	6.755	5.276	3.418	6.712	4.923	8.108	6.358	3.598	4.584
d <sub>6</sub>	5.400	8.117	4.422	6.447	3.717	9.658	6.713	6.246	8.598	8.999	8.177	5.035	5.945	9.042	8.900	5.376
dd <sub>2</sub>	4.300	4.046	6.755	6.438	6.661	4.605	3.163	5.947	6.286	7.451	5.150	7.320	6.562	5.936	7.168	4.290
dd <sub>3</sub>	1.700	1.865	1.611	2.781	1.901	3.288	1.955	2.491	2.354	1.141	3.235	2.785	2.478	1.531	2.169	1.698
hh <sub>1</sub>	5.400	10.741	9.079	8.641	6.455	4.842	4.703	7.039	8.297	3.906	5.621	5.320	10.329	9.588	10.583	5.379
hh <sub>2</sub>	1.500	2.222	2.293	2.480	1.567	2.306	2.766	2.063	2.655	1.965	0.834	1.957	2.099	2.288	2.142	1.531
hh <sub>3</sub>	5.000	4.077	5.985	5.272	8.243	5.395	7.947	8.760	6.653	8.718	4.776	7.575	3.295	3.920	5.532	4.960
hh <sub>4</sub>	5.000	9.335	9.590	9.956	8.113	8.285	8.006	9.380	8.837	8.614	9.130	9.326	6.925	3.106	9.359	4.678
hh <sub>5</sub>	5.000	6.102	6.826	6.396	7.788	3.475	4.998	5.260	4.786	5.207	2.932	7.412	5.065	2.793	5.450	4.985
p <sub>t</sub>	0.020	0.026	0.022	0.017	0.021	0.019	0.034	0.023	0.017	0.027	0.018	0.029	0.021	0.032	0.027	0.024
p1 <sub>t</sub>	0.005	0.006	0.009	0.009	0.008	0.010	0.004	0.008	0.006	0.005	0.005	0.008	0.010	0.005	0.007	0.005
p2 <sub>t</sub>	0.010	0.015	0.011	0.011	0.008	0.012	0.012	0.007	0.015	0.020	0.006	0.010	0.020	0.015	0.012	0.012
p3 <sub>t</sub>	0.021	0.017	0.036	0.016	0.031	0.020	0.018	0.023	0.013	0.014	0.034	0.011	0.021	0.042	0.014	0.023
p4 <sub>t</sub>	0.100	0.059	0.111	0.157	0.106	0.088	0.066	0.139	0.169	0.142	0.169	0.060	0.183	0.092	0.129	0.097
km <sub>16</sub>	0.600	0.849	0.697	0.729	0.734	1.073	0.628	0.386	0.867	0.506	0.594	0.798	1.188	0.358	1.127	0.564
k <sub>1</sub>	0.005	0.010	0.004	0.003	0.005	0.008	0.007	0.009	0.007	0.003	0.003	0.006	0.004	0.004	0.006	0.005
k <sub>2</sub>	0.100	0.174	0.066	0.097	0.127	0.078	0.114	0.110	0.169	0.178	0.131	0.090	0.098	0.060	0.072	0.109
k <sub>3</sub>	0.200	0.270	0.202	0.320	0.109	0.289	0.289	0.391	0.268	0.166	0.257	0.356	0.338	0.253	0.233	0.197
k <sub>4</sub>	0.020	0.037	0.036	0.027	0.012	0.025	0.014	0.029	0.038	0.019	0.030	0.023	0.018	0.019	0.017	0.021
k <sub>5</sub>	0.030	0.019	0.026	0.035	0.043	0.037	0.059	0.055	0.018	0.058	0.046	0.025	0.041	0.029	0.027	0.035
k <sub>6</sub>	0.003	0.006	0.004	0.005	0.003	0.002	0.005	0.005	0.006	0.004	0.003	0.006	0.003	0.005	0.004	0.003
k <sub>7</sub>	15.000	8.532	29.472	9.203	25.591	8.004	10.013	21.912	17.396	17.462	20.403	29.446	10.794	21.083	21.123	15.165
k <sub>8</sub>	1.000	1.826	1.363	0.855	1.220	1.570	1.572	0.938	1.305	1.224	1.225	1.947	1.077	1.075	1.753	1.011
k <sub>9</sub>	0.740	0.784	1.406	0.516	0.761	1.296	0.662	0.783	0.770	0.951	0.822	1.096	0.691	1.420	1.127	0.741
k <sub>10</sub>	0.005	0.004	0.003	0.006	0.003	0.007	0.010	0.004	0.007	0.009	0.007	0.007	0.004	0.007	0.007	0.005
k <sub>11</sub>	0.006	0.010	0.010	0.005	0.008	0.009	0.004	0.011	0.005	0.008	0.010	0.008	0.009	0.010	0.011	0.006
m <sub>11</sub>	0.600	0.769	0.550	0.588	0.687	0.843	0.335	0.330	0.361	0.940	0.926	0.948	0.762	0.387	0.466	0.636
m <sub>12</sub>	3.400	2.998	2.266	6.541	4.886	6.460	6.472	2.422	5.675	6.530	5.210	5.780	5.758	6.102	6.468	3.406
m <sub>13</sub>	1.000	1.187	1.553	1.465	1.050	1.306	1.272	1.206	1.152	1.016	0.932	1.412	1.305	1.468	1.933	0.927
m <sub>14</sub>	1.000	0.933	0.954	0.667	1.501	0.539	1.220	0.564	0.715	0.804	1.057	0.911	1.658	1.645	1.038	0.908
m <sub>15</sub>	0.100	0.121	0.164	0.167	0.054	0.059	0.145	0.116	0.154	0.151	0.189	0.174	0.084	0.096	0.174	0.117
m <sub>17</sub>	0.100	0.107	0.139	0.174	0.134	0.114	0.178	0.131	0.110	0.077	0.184	0.191	0.085	0.146	0.075	0.093
m <sub>18</sub>	0.200	0.361	0.342	0.276	0.323	0.103	0.208	0.156	0.150	0.379	0.282	0.220	0.149	0.235	0.299	0.217
m <sub>19</sub>	0.200	0.277	0.198	0.325	0.365	0.264	0.101	0.109	0.113	0.126	0.300	0.322	0.148	0.213	0.146	0.248
m <sub>20</sub>	60.000	36.336	94.147	98.262	75.565	109.690	66.611	57.150	89.744	87.036	77.496	67.272	114.820	116.670	76.789	58.295
gsy <sub>p</sub> <sup>0</sup>	0.050	0.028	0.043	0.085	0.082	0.098	0.072	0.071	0.051	0.090	0.099	0.082	0.056	0.100	0.098	0.054
gph <sub>p</sub> <sup>0</sup>	0.700	1.394	1.100	1.373	0.565	0.630	1.049	0.739	0.606	0.752	1.377	0.665	0.460	1.109	1.243	0.695
glu <sub>ext</sub> <sup>0</sup>	3.300	4.173	3.385	4.432	2.465	5.340	2.277	1.820	3.713	2.039	4.291	5.379	1.846	3.836	2.749	3.337
n	1.000	1.183	1.199	1.115	1.978	0.997	1.579	1.868	0.927	1.938	1.991	1.854	0.880	1.583	1.245	1.150
SM	0.085	0.021	0.030	0.016	0.026	0.018	0.020	0.017	0.019	0.018	0.018	0.014	0.019	0.015	0.017	0.020
Osm0	1.866	228.727	1.322	67.710	2.298	1.874	79.690	1.142	1.731	152.527	1.891	203.064	307.929	116.549	67.309	1.960

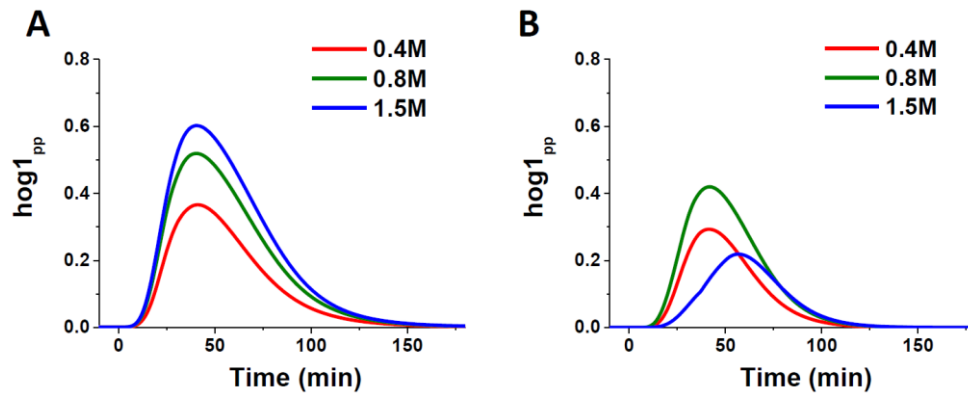


Figure 7.19. The comparison of Hog1 phosphorylation for BG2 and 2001 strains of *C. glabrata*.

A. Model predictions for BG2 strain. B. Model predictions for 2001 strain.

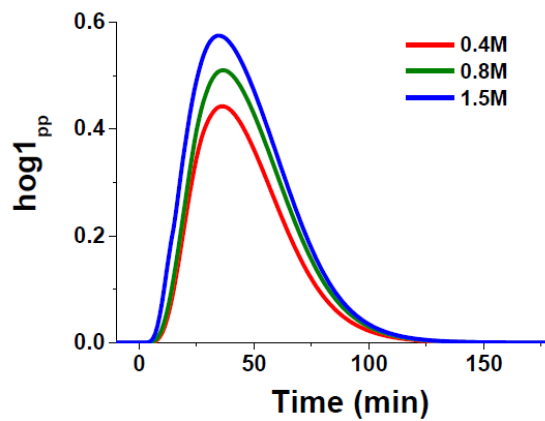


Figure 7.20. The model predictions for the overexpression of Sho1 in 2001 strain of *C. glabrata*.

Phosphorylated Hog1 levels in response to the three NaCl concentrations if the assumption regarding the number of activated receptors, noted as Modification 4, is not correct.

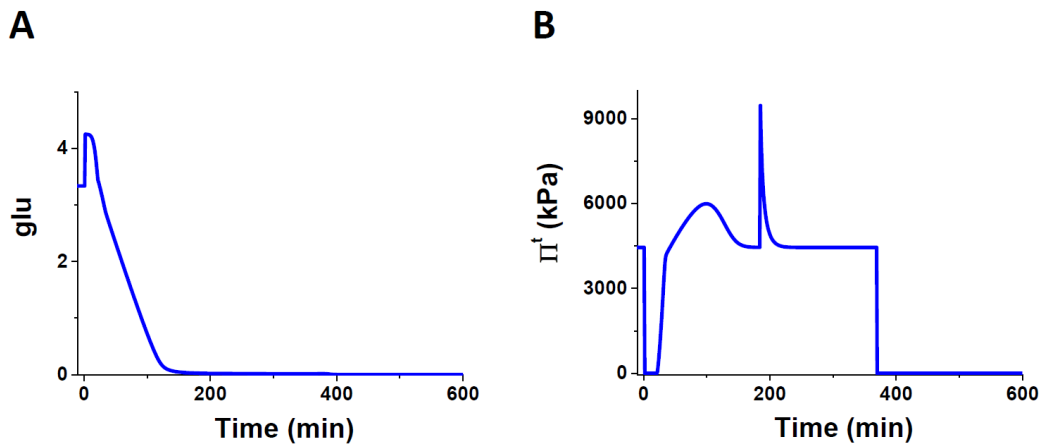


Figure 7.21. Model predictions for the double hyper-and-hypo-osmotic stress. A. Model predictions for the external glucose concentration. B. Model predictions for the turgor pressure.

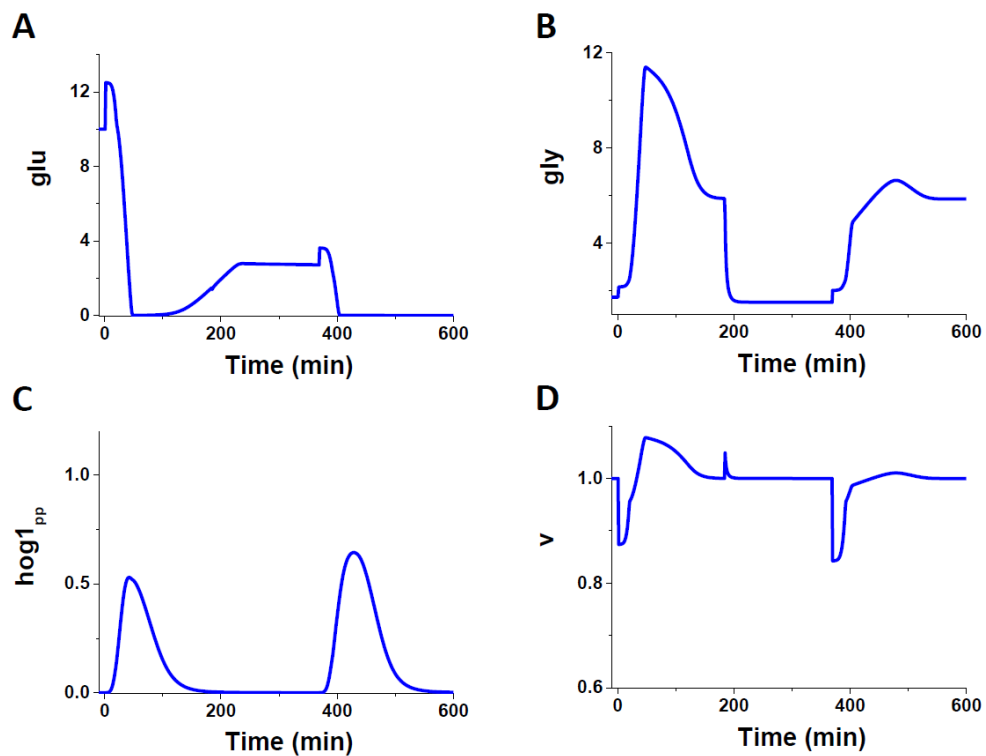


Figure 7.22. Model predictions for the double hyper-and-hypo-osmotic stress when the concentration of extracellular glucose in equilibrium is increased. The increased  $glu_{ext}^0$  (A) leads to the ability of the cell to produce glycerol (B) by Hog1 phosphorylation (C) and restore its volume (D).

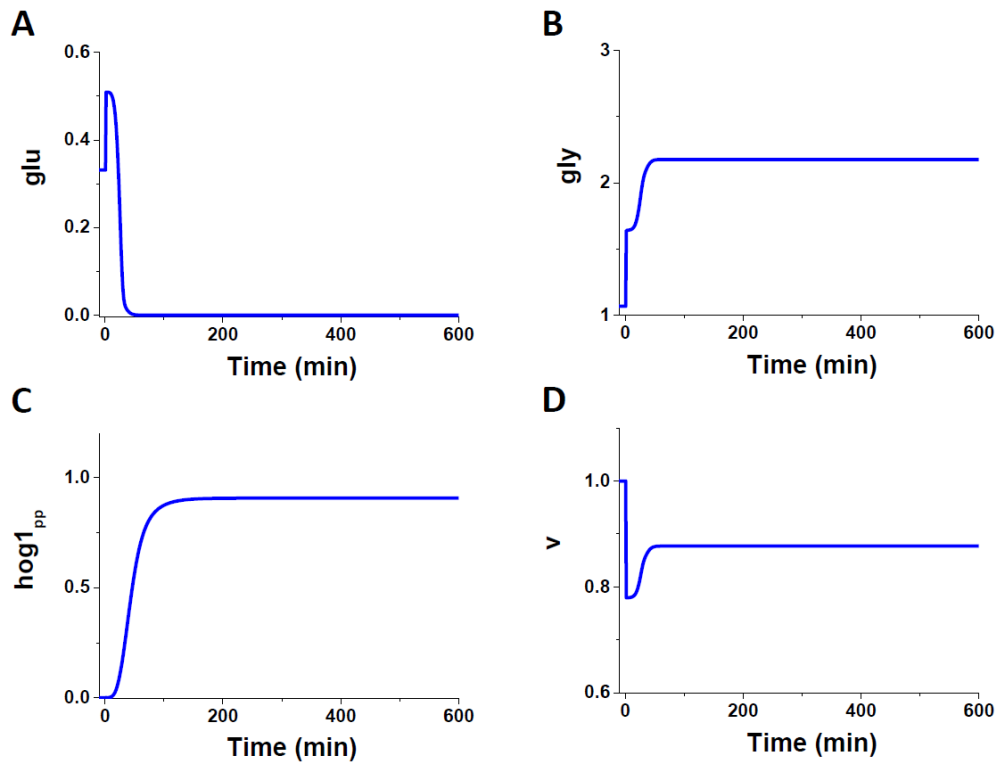


Figure 7.23. Model predictions for the single hyper-osmotic stress when the concentration of extracellular glucose in equilibrium is decreased.

The decreased  $glu_{ext}^0$  (A) leads to the inability of the cell to produce enough glycerol (B) even in the presence of Hog1 phosphorylation (C) and restore its volume (D).


## 7.9 Appendix E

### 7.9.1 The permission to use the experimental data in this thesis

DATE: 16/06/2015

TO: Ildar Sadreev

FROM: Emily Cook

SIGNATURE:  \_\_\_\_\_

RE: PERMISSION FOR USE OF EXPERIMENTAL  
DATA

TITLE OF THE PROJECT: *C. Glabrata* adaptation to osmotic stress

I hereby confirm that I give Ildar Sadreev permission to analyze the data collected during the project, "*C. Glabrata* adaptation to osmotic stress" expressly for the thesis titled "Mathematical Modelling of Inter- and Intracellular Signal Transduction: The Regulatory Role of Multisite Interactions".

I have obtained the experimental data in the experimental laboratories in Biosciences, University of Exeter.

In his thesis, Ildar Sadreev will use the collected data to validate his mathematical model.

## Bibliography

1. Valeyev NV, Bates DG, Umezawa Y, Gizatullina AN, Kotov NV (2010) Systems biology of cell behavior. *Methods Mol Biol* 662: 79-95.
2. Li P, Dada JO, Jameson D, Spasic I, Swainston N, et al. (2010) Systematic integration of experimental data and models in systems biology. *BMC Bioinformatics* 11: 582.
3. Wang YC, Peterson SE, Loring JF (2014) Protein post-translational modifications and regulation of pluripotency in human stem cells. *Cell Res* 24: 143-160.
4. Pollard TD (2010) A guide to simple and informative binding assays. *Mol Biol Cell* 21: 4061-4067.
5. Fiedler D, Braberg H, Mehta M, Chechik G, Cagney G, et al. (2009) Functional organization of the *S. cerevisiae* phosphorylation network. *Cell* 136: 952-963.
6. Klein BG (2013) *Cunningham's Textbook of Veterinary Physiology*. 624 p.
7. Valeyev NV, Heslop-Harrison P, Postlethwaite I, Kotov NV, Bates DG (2008) Multiple calcium binding sites make calmodulin multifunctional. *Mol Biosyst* 4: 66-73.
8. Salazar C, Hofer T (2009) Multisite protein phosphorylation--from molecular mechanisms to kinetic models. *FEBS J* 276: 3177-3198.
9. Hill AV (1910) The possible effects of the aggregation of the molecules of haemoglobin on its dissociation curves. *Journal of Physiology-London* 40: 4-7.
10. Adair GS (1925) The hemoglobin system. IV. The reproduction of the carbon dioxide curves of blood with an artificial mixture of hemoglobin and sodium bicarbonate. *Journal of Biological Chemistry* 63: 515-516.
11. Pauling L (1935) The oxygen equilibrium of hemoglobin and its structural interpretation. *Proceedings of the National Academy of Sciences of the United States of America* 21: 186-191.
12. Klotz IM, Hunston DL (1975) Protein Interactions with Small Molecules - Relationships between Stoichiometric Binding Constants, Site Binding Constants, and Empirical Binding Parameters. *Journal of Biological Chemistry* 250: 3001-3009.
13. Weiss JN (1997) The Hill equation revisited: uses and misuses. *FASEB J* 11: 835-841.
14. Shifman JM, Choi MH, Mihalas S, Mayo SL, Kennedy MB (2006) Ca<sup>2+</sup>/calmodulin-dependent protein kinase II (CaMKII) is activated by calmodulin with two bound calciums. *Proc Natl Acad Sci U S A* 103: 13968-13973.
15. Kung C, Preston RR, Maley ME, Ling KY, Kanabrocki JA, et al. (1992) In vivo *Paramecium* mutants show that calmodulin orchestrates membrane responses to stimuli. *Cell Calcium* 13: 413-425.
16. Hyde JR, Kezunovic N, Urbano FJ, Garcia-Rill E (2013) Spatiotemporal properties of high speed calcium oscillations in the pedunculopontine nucleus. *J Appl Physiol*.
17. Bading H (2013) Nuclear calcium signalling in the regulation of brain function. *Nat Rev Neurosci* 14: 593-608.
18. Semenov I, Xiao S, Pakhomova ON, Pakhomov AG (2013) Recruitment of the intracellular Ca<sup>2+</sup> by ultrashort electric stimuli: The impact of pulse duration. *Cell Calcium* 54: 145-150.
19. Faas GC, Schwaller B, Vergara JL, Mody I (2007) Resolving the fast kinetics of cooperative binding: Ca<sup>2+</sup> buffering by calretinin. *PLoS Biol* 5: e311.
20. Valeyev NV, Bates DG, Heslop-Harrison P, Postlethwaite I, Kotov NV (2008) Elucidating the mechanisms of cooperative calcium-calmodulin interactions: a structural systems biology approach. *BMC Syst Biol* 2: 48.
21. Yap KL, Ames JB, Swindells MB, Ikura M (1999) Diversity of conformational states and changes within the EF-hand protein superfamily. *Proteins-Structure Function and Genetics* 37: 499-507.
22. Kawasaki H, Nakayama S, Kretsinger RH (1998) Classification and evolution of EF-hand proteins. *Biometals* 11: 277-295.
23. Goldbeter A, Koshland DE, Jr. (1981) An amplified sensitivity arising from covalent modification in biological systems. *Proc Natl Acad Sci U S A* 78: 6840-6844.
24. Szomolay B, Shahrezaei V (2012) Bell-shaped and ultrasensitive dose-response in phosphorylation-dephosphorylation cycles: the role of kinase-phosphatase complex formation. *BMC Syst Biol* 6: 26.
25. Bluthgen N, Bruggeman FJ, Legewie S, Herzog H, Westerhoff HV, et al. (2006) Effects of sequestration on signal transduction cascades. *FEBS J* 273: 895-906.

26. Ciliberto A, Capuani F, Tyson JJ (2007) Modeling networks of coupled enzymatic reactions using the total quasi-steady state approximation. *PLoS Comput Biol* 3: e45.
27. Varedi KS, Ventura AC, Merajver SD, Lin XN (2010) Multisite phosphorylation provides an effective and flexible mechanism for switch-like protein degradation. *PLoS One* 5: e14029.
28. Liu X, Bardwell L, Nie Q (2010) A combination of multisite phosphorylation and substrate sequestration produces switchlike responses. *Biophys J* 98: 1396-1407.
29. Xing J, Chen J (2008) The Goldbeter-Koshland switch in the first-order region and its response to dynamic disorder. *PLoS One* 3: e2140.
30. Sadreev, II, Chen MZ, Welsh GI, Umezawa Y, Kotov NV, et al. (2014) A systems model of phosphorylation for inflammatory signaling events. *PLoS One* 9: e110913.
31. Bazanovas AN, Evstifeev AI, Khaiboullina SF, Sadreev, II, Skorinkin AI, et al. (2015) Erythrocyte: A systems model of the control of aggregation and deformability. *Biosystems* 131: 1-8.
32. Magombedze G, Reddy PB, Eda S, Ganusov VV (2013) Cellular and population plasticity of helper CD4(+) T cell responses. *Front Physiol* 4: 206.
33. Hohmann S (2002) Osmotic stress signaling and osmoadaptation in yeasts. *Microbiol Mol Biol Rev* 66: 300-372.
34. Lin J, Buettner R, Yuan YC, Yip R, Horne D, et al. (2009) Molecular dynamics simulations of the conformational changes in signal transducers and activators of transcription, Stat1 and Stat3. *J Mol Graph Model* 28: 347-356.
35. Calo V, Migliavacca M, Bazan V, Macaluso M, Buscemi M, et al. (2003) STAT proteins: from normal control of cellular events to tumorigenesis. *J Cell Physiol* 197: 157-168.
36. Harris ED, Jr. (1990) Rheumatoid arthritis. *Pathophysiology and implications for therapy. N Engl J Med* 322: 1277-1289.
37. Viallard JF, Pellegrin JL, Ranchin V, Schaeveerbecke T, Dehais J, et al. (1999) Th1 (IL-2, interferon-gamma (IFN-gamma)) and Th2 (IL-10, IL-4) cytokine production by peripheral blood mononuclear cells (PBMC) from patients with systemic lupus erythematosus (SLE). *Clin Exp Immunol* 115: 189-195.
38. Haskins K, McDuffie M (1990) Acceleration of diabetes in young NOD mice with a CD4+ islet-specific T cell clone. *Science* 249: 1433-1436.
39. Cope A, Le Friec G, Cardone J, Kemper C (2011) The Th1 life cycle: molecular control of IFN-gamma to IL-10 switching. *Trends Immunol* 32: 278-286.
40. Yamada S, Shiono S, Joo A, Yoshimura A (2003) Control mechanism of JAK/STAT signal transduction pathway. *FEBS Lett* 534: 190-196.
41. Rateitschak K, Karger A, Fitzner B, Lange F, Wolkenhauer O, et al. (2010) Mathematical modelling of interferon-gamma signalling in pancreatic stellate cells reflects and predicts the dynamics of STAT1 pathway activity. *Cell Signal* 22: 97-105.
42. Swameye I, Muller TG, Timmer J, Sandra O, Klingmuller U (2003) Identification of nucleocytoplasmic cycling as a remote sensor in cellular signaling by databased modeling. *Proc Natl Acad Sci U S A* 100: 1028-1033.
43. Blatke MA, Dittrich A, Rohr C, Heiner M, Schaper F, et al. (2013) JAK/STAT signalling--an executable model assembled from molecule-centred modules demonstrating a module-oriented database concept for systems and synthetic biology. *Mol Biosyst* 9: 1290-1307.
44. Yoshimura A, Suzuki M, Sakaguchi R, Hanada T, Yasukawa H (2012) SOCS, Inflammation, and Autoimmunity. *Front Immunol* 3: 20.
45. Roetzer A, Gabaldon T, Schuller C (2011) From *Saccharomyces cerevisiae* to *Candida glabrata* a few easy steps: important adaptations for an opportunistic pathogen. *FEMS Microbiol Lett* 314: 1-9.
46. Kaloriti D, Tillmann A, Cook E, Jacobsen M, You T, et al. (2012) Combinatorial stresses kill pathogenic *Candida* species. *Med Mycol* 50: 699-709.
47. Gennemark P, Nordlander B, Hohmann S, Wedelin D (2006) A simple mathematical model of adaptation to high osmolarity in yeast. *In Silico Biol* 6: 193-214.
48. Klipp E, Nordlander B, Kruger R, Gennemark P, Hohmann S (2005) Integrative model of the response of yeast to osmotic shock. *Nat Biotechnol* 23: 975-982.
49. Zi Z, Liebermeister W, Klipp E (2010) A quantitative study of the Hog1 MAPK response to fluctuating osmotic stress in *Saccharomyces cerevisiae*. *PLoS One* 5: e9522.
50. Mettetal JT, Muzzey D, Gomez-Urbe C, van Oudenaarden A (2008) The frequency dependence of osmo-adaptation in *Saccharomyces cerevisiae*. *Science* 319: 482-484.
51. Parmar JH, Bhartiya S, Venkatesh KV (2009) A model-based study delineating the roles of the two signaling branches of *Saccharomyces cerevisiae*, Sho1 and Sln1, during adaptation to osmotic stress. *Phys Biol* 6: 036019.



52. Hao N, Behar M, Parnell SC, Torres MP, Borchers CH, et al. (2007) A systems-biology analysis of feedback inhibition in the Sho1 osmotic-stress-response pathway. *Curr Biol* 17: 659-667.
53. Huang CY, Ferrell JE, Jr. (1996) Ultrasensitivity in the mitogen-activated protein kinase cascade. *Proc Natl Acad Sci U S A* 93: 10078-10083.
54. Qiao L, Nachbar RB, Kevrekidis IG, Shvartsman SY (2007) Bistability and oscillations in the Huang-Ferrell model of MAPK signaling. *PLoS Comput Biol* 3: 1819-1826.
55. Wang X, Hao N, Dohlman HG, Elston TC (2006) Bistability, stochasticity, and oscillations in the mitogen-activated protein kinase cascade. *Biophys J* 90: 1961-1978.
56. Angeli D, Ferrell JE, Jr., Sontag ED (2004) Detection of multistability, bifurcations, and hysteresis in a large class of biological positive-feedback systems. *Proc Natl Acad Sci U S A* 101: 1822-1827.
57. Markevich NI, Hoek JB, Kholodenko BN (2004) Signaling switches and bistability arising from multisite phosphorylation in protein kinase cascades. *J Cell Biol* 164: 353-359.
58. Swain PS, Siggia ED (2002) The role of proofreading in signal transduction specificity. *Biophys J* 82: 2928-2933.
59. Thattai M, van Oudenaarden A (2002) Attenuation of noise in ultrasensitive signaling cascades. *Biophys J* 82: 2943-2950.
60. Purich DL (2010) *Enzyme kinetics catalysis & control : a reference of theory and best-practice methods*. San Diego, Calif. Oxford: Elsevier Academic ; Elsevier Science distributor ,. pp. p.
61. Wright MR (2004) *Introduction to chemical kinetics*. Chichester: Wiley,. pp. 256 p.
62. Briggs GE, Haldane JB (1925) A Note on the Kinetics of Enzyme Action. *Biochem J* 19: 338-339.
63. Hoefflich KP, Ikura M (2002) Calmodulin in action: diversity in target recognition and activation mechanisms. *Cell* 108: 739-742.
64. Kissinger CR, Parge HE, Knighton DR, Lewis CT, Pelletier LA, et al. (1995) Crystal-Structures of Human Calcineurin and the Human Fkbp12-Fk506-Calcineurin Complex. *Nature* 378: 641-644.
65. Maki M, Maemoto Y, Osako Y, Shibata H (2012) Evolutionary and physical linkage between calpains and penta-EF-hand Ca<sup>2+</sup>-binding proteins. *Febs Journal* 279: 1414-1421.
66. Chillakuri CR, Sheppard D, Lea SM, Handford PA (2012) Notch receptor-ligand binding and activation: insights from molecular studies. *Semin Cell Dev Biol* 23: 421-428.
67. Grabarek Z (2011) Insights into modulation of calcium signaling by magnesium in calmodulin, troponin C and related EF-hand proteins. *Biochimica Et Biophysica Acta-Molecular Cell Research* 1813: 913-921.
68. Canepari M, Maffei M, Longa E, Geeves M, Bottinelli R (2012) Actomyosin kinetics of pure fast and slow rat myosin isoforms studied by in vitro motility assay approach. *Experimental Physiology* 97: 873-881.
69. Oz S, Benmocha A, Sasson Y, Sachyani D, Almagor L, et al. (2013) Competitive and Non-competitive Regulation of Calcium-dependent Inactivation in Ca<sub>v</sub>1.2 L-type Ca<sup>2+</sup> Channels by Calmodulin and Ca<sup>2+</sup>-binding Protein 1. *Journal of Biological Chemistry* 288: 12680-12691.
70. Wei XY, Pan S, Lang WH, Kim HY, Schneider T, et al. (1995) Molecular Determinants of Cardiac Ca<sup>2+</sup> Channel Pharmacology - Subunit Requirement for the High-Affinity and Allosteric Regulation of Dihydropyridine Binding. *Journal of Biological Chemistry* 270: 27106-27111.
71. McCarron JG, Chalmers S, Olson ML, Girkin JM (2012) Subplasma Membrane Ca<sup>2+</sup> Signals. *Jubmb Life* 64: 573-585.
72. Kotov NV, Bates DG, Gizatullina AN, Gilaziev B, Khairullin RN, et al. (2011) Computational modelling elucidates the mechanism of ciliary regulation in health and disease. *BMC Syst Biol* 5: 143.
73. Berridge MJ, Lipp P, Bootman MD (2000) The versatility and universality of calcium signalling. *Nat Rev Mol Cell Biol* 1: 11-21.
74. Berridge MJ, Bootman MD, Lipp P (1998) Calcium--a life and death signal. *Nature* 395: 645-648.
75. Gargus JJ (2009) Genetic calcium signaling abnormalities in the central nervous system: seizures, migraine, and autism. *Ann N Y Acad Sci* 1151: 133-156.
76. Talavera D, Robertson DL, Lovell SC (2011) Characterization of protein-protein interaction interfaces from a single species. *PLoS One* 6: e21053.

77. Fuchs F, Grabarek Z (2011) The Ca/Mg Sites of Troponin C Can Modulate Crossbridge-Mediated Thin Filament Activation in Rat Cardiac Myofibrils. *Biophysical Journal* 100: 112-113.
78. Pearson DS, Swartz DR, Geeves MA (2008) Fast pressure jumps can perturb calcium and magnesium binding to troponin C F29W. *Biochemistry* 47: 12146-12158.
79. Guo Q, Shen Y, Lee YS, Gibbs CS, Mrksich M, et al. (2005) Structural basis for the interaction of Bordetella pertussis adenylyl cyclase toxin with calmodulin. *Embo J* 24: 3190-3201.
80. Robison J C, RJ (2004) Calcium/Calmodulin-Dependent Protein Kinases. In: WJ Lennarz ML, editor. *Encyclopedia of Biological Chemistry*: Elsevier Inc. pp. 281-286.
81. Bhattacharya S, Bunick CG, Chazin WJ (2004) Target selectivity in EF-hand calcium binding proteins. *Biochim Biophys Acta* 1742: 69-79.
82. Nelson MR, Thulin E, Fagan PA, Forsen S, Chazin WJ (2002) The EF-hand domain: a globally cooperative structural unit. *Protein Sci* 11: 198-205.
83. Schumacher MA, Rivard AF, Bachinger HP, Adelman JP (2001) Structure of the gating domain of a Ca<sup>2+</sup>-activated K<sup>+</sup> channel complexed with Ca<sup>2+</sup>/calmodulin. *Nature* 410: 1120-1124.
84. Rodney GG, Moore CP, Williams BY, Zhang JZ, Krol J, et al. (2001) Calcium binding to calmodulin leads to an N-terminal shift in its binding site on the ryanodine Receptor. *J Biol Chem* 276: 2069-2074.
85. Yap KL, Ames JB, Swindells MB, Ikura M (1999) Diversity of conformational states and changes within the EF-hand protein superfamily. *Proteins* 37: 499-507.
86. Valeyev NV, Heslop-Harrison P, Postlethwaite I, Gizatullina AN, Kotov NV, et al. (2009) Crosstalk between G-protein and Ca<sup>2+</sup> pathways switches intracellular cAMP levels. *Mol Biosyst* 5: 43-51.
87. Mann MD (1997) *The Nervous System In Action*.
88. Stein RB, Bobet J, Oguztoreli MN, Fryer M (1988) The kinetics relating calcium and force in skeletal muscle. *Biophys J* 54: 705-717.
89. Pearson DS, Holtermann G, Ellison P, Cremo C, Geeves MA (2002) A novel pressure-jump apparatus for the microvolume analysis of protein-ligand and protein-protein interactions: its application to nucleotide binding to skeletal-muscle and smooth-muscle myosin subfragment-1. *Biochem J* 366: 643-651.
90. Toseland CP, Geeves MA (2014) Rapid reaction kinetic techniques. *EXS* 105: 49-65.
91. Adair GS (1925) The hemoglobin system. VI. The oxygen dissociation curve of hemoglobin. *J Biol Chem* 63: 529-545.
92. Klotz IM, Hunston DL (1975) Protein interactions with small molecules. Relationships between stoichiometric binding constants, site binding constants, and empirical binding parameters. *J Biol Chem* 250: 3001-3009.
93. Faas GC, Raghavachari S, Lisman JE, Mody I (2011) Calmodulin as a direct detector of Ca<sup>2+</sup> signals. *Nat Neurosci* 14: 301-304.
94. Andre I, Kesvatera T, Jonsson B, Akerfeldt KS, Linse S (2004) The role of electrostatic interactions in calmodulin-peptide complex formation. *Biophys J* 87: 1929-1938.
95. Andre I, Kesvatera T, Jonsson B, Linse S (2006) Salt enhances calmodulin-target interaction. *Biophys J* 90: 2903-2910.
96. Zhang M, Tanaka T, Ikura M (1995) Calcium-induced conformational transition revealed by the solution structure of apo calmodulin. *Nat Struct Biol* 2: 758-767.
97. Chattopadhyaya R, Meador WE, Means AR, Quioco FA (1992) Calmodulin structure refined at 1.7 Å resolution. *J Mol Biol* 228: 1177-1192.
98. Aloy P, Russell RB (2006) Structural systems biology: modelling protein interactions. *Nat Rev Mol Cell Biol* 7: 188-197.
99. Vetter SW, Leclerc E (2003) Novel aspects of calmodulin target recognition and activation. *Eur J Biochem* 270: 404-414.
100. Nelson MR, Chazin WJ (1998) An interaction-based analysis of calcium-induced conformational changes in Ca<sup>2+</sup> sensor proteins. *Protein Sci* 7: 270-282.
101. Yang W, Lee HW, Hellinga H, Yang JJ (2002) Structural analysis, identification, and design of calcium-binding sites in proteins. *Proteins* 47: 344-356.
102. Friedberg F (1988) Calcium Binding Protein Families: The 'E-F Hand' Family. *Biochem Educ* 16: 35-36.
103. Minowa O, Yagi K (1984) Calcium binding to tryptic fragments of calmodulin. *J Biochem* 96: 1175-1182.
104. Linse S, Helmersson A, Forsen S (1991) Calcium binding to calmodulin and its globular domains. *J Biol Chem* 266: 8050-8054.

105. Cimperman P, Baranauskiene L, Jachimoviciute S, Jachno J, Torresan J, et al. (2008) A quantitative model of thermal stabilization and destabilization of proteins by ligands. *Biophys J* 95: 3222-3231.
106. Almagor H, Levitzki A (1990) Analytical determination of receptor-ligand dissociation constants of two populations of receptors from displacement curves. *Proc Natl Acad Sci U S A* 87: 6482-6486.
107. Kragh-Hansen U (1983) Graphical analysis of competitive binding of comparable concentrations of ligand, inhibitor and protein. Ligand binding to serum albumin. *Biochem Pharmacol* 32: 2679-2681.
108. Stefan MI, Edelstein SJ, Le Novere N (2008) An allosteric model of calmodulin explains differential activation of PP2B and CaMKII. *Proc Natl Acad Sci U S A* 105: 10768-10773.
109. Rusnak F, Mertz P (2000) Calcineurin: form and function. *Physiol Rev* 80: 1483-1521.
110. Lu HE, MacGillavry HD, Frost NA, Blanpied TA (2014) Multiple spatial and kinetic subpopulations of CaMKII in spines and dendrites as resolved by single-molecule tracking PALM. *J Neurosci* 34: 7600-7610.
111. Lee SJ, Escobedo-Lozoya Y, Szatmari EM, Yasuda R (2009) Activation of CaMKII in single dendritic spines during long-term potentiation. *Nature* 458: 299-304.
112. Nishiyama M, Kimura Y, Nishiyama Y, Terazima M (2009) Pressure-induced changes in the structure and function of the kinesin-microtubule complex. *Biophys J* 96: 1142-1150.
113. Shaikh TR, Barnard D, Meng X, Wagenknecht T (2009) Implementation of a flash-photolysis system for time-resolved cryo-electron microscopy. *J Struct Biol* 165: 184-189.
114. Frieden C, Hoeltzli SD, Ropson IJ (1993) NMR and protein folding: equilibrium and stopped-flow studies. *Protein Sci* 2: 2007-2014.
115. Nagerl UV, Novo D, Mody I, Vergara JL (2000) Binding kinetics of calbindin-D(28k) determined by flash photolysis of caged Ca(2+). *Biophys J* 79: 3009-3018.
116. Gunawardena J (2007) Distributivity and processivity in multisite phosphorylation can be distinguished through steady-state invariants. *Biophys J* 93: 3828-3834.
117. Quinn KV, Giblin JP, Tinker A (2004) Multisite phosphorylation mechanism for protein kinase A activation of the smooth muscle ATP-sensitive K+ channel. *Circ Res* 94: 1359-1366.
118. Countaway JL, McQuilkin P, Girones N, Davis RJ (1990) Multisite phosphorylation of the epidermal growth factor receptor. Use of site-directed mutagenesis to examine the role of serine/threonine phosphorylation. *J Biol Chem* 265: 3407-3416.
119. Zhang H, Berezov A, Wang Q, Zhang G, Drebin J, et al. (2007) ErbB receptors: from oncogenes to targeted cancer therapies. *J Clin Invest* 117: 2051-2058.
120. Dushek O, van der Merwe PA, Shahrezaei V (2011) Ultrasensitivity in multisite phosphorylation of membrane-anchored proteins. *Biophys J* 100: 1189-1197.
121. Guy CS, Vignali DA (2009) Organization of proximal signal initiation at the TCR:CD3 complex. *Immunol Rev* 232: 7-21.
122. Johnson P, Cross JL (2009) Tyrosine phosphorylation in immune cells: direct and indirect effects on toll-like receptor-induced proinflammatory cytokine production. *Crit Rev Immunol* 29: 347-367.
123. Decker T, Kovarik P (2000) Serine phosphorylation of STATs. *Oncogene* 19: 2628-2637.
124. Rawlings JS, Rosler KM, Harrison DA (2004) The JAK/STAT signaling pathway. *J Cell Sci* 117: 1281-1283.
125. Johnston JA, Bacon CM, Finbloom DS, Rees RC, Kaplan D, et al. (1995) Tyrosine phosphorylation and activation of STAT5, STAT3, and Janus kinases by interleukins 2 and 15. *Proc Natl Acad Sci U S A* 92: 8705-8709.
126. Kaymaz BT, Selvi N, Gokbulut AA, Aktan C, Gunduz C, et al. (2013) Suppression of STAT5A and STAT5B chronic myeloid leukemia cells via siRNA and antisense-oligonucleotide applications with the induction of apoptosis. *Am J Blood Res* 3: 58-70.
127. Shuai K, Liu B (2003) Regulation of JAK-STAT signalling in the immune system. *Nat Rev Immunol* 3: 900-911.
128. Lovato P, Brender C, Agnholt J, Kelsen J, Kaltoft K, et al. (2003) Constitutive STAT3 activation in intestinal T cells from patients with Crohn's disease. *J Biol Chem* 278: 16777-16781.
129. Coskun M, Salem M, Pedersen J, Nielsen OH (2013) Involvement of JAK/STAT signaling in the pathogenesis of inflammatory bowel disease. *Pharmacol Res* 76: 1-8.
130. Atsumi T, Ishihara K, Kamimura D, Ikushima H, Ohtani T, et al. (2002) A point mutation of Tyr-759 in interleukin 6 family cytokine receptor subunit gp130 causes autoimmune arthritis. *J Exp Med* 196: 979-990.

131. Ogura H, Murakami M, Okuyama Y, Tsuruoka M, Kitabayashi C, et al. (2008) Interleukin-17 promotes autoimmunity by triggering a positive-feedback loop via interleukin-6 induction. *Immunity* 29: 628-636.
132. Grivennikov SI, Karin M (2010) Dangerous liaisons: STAT3 and NF-kappaB collaboration and crosstalk in cancer. *Cytokine Growth Factor Rev* 21: 11-19.
133. Cherian TS, Kariuki SN, Franek BS, Buyon JP, Clancy RM, et al. (2012) Brief Report: IRF5 systemic lupus erythematosus risk haplotype is associated with asymptomatic serologic autoimmunity and progression to clinical autoimmunity in mothers of children with neonatal lupus. *Arthritis Rheum* 64: 3383-3387.
134. Cheng TF, Brzostek S, Ando O, Van Scoy S, Kumar KP, et al. (2006) Differential activation of IFN regulatory factor (IRF)-3 and IRF-5 transcription factors during viral infection. *J Immunol* 176: 7462-7470.
135. Chang Foreman HC, Van Scoy S, Cheng TF, Reich NC (2012) Activation of interferon regulatory factor 5 by site specific phosphorylation. *PLoS One* 7: e33098.
136. Egwuagu CE (2009) STAT3 in CD4+ T helper cell differentiation and inflammatory diseases. *Cytokine* 47: 149-156.
137. Paun A, Bankoti R, Joshi T, Pitha PM, Stager S (2011) Critical role of IRF-5 in the development of T helper 1 responses to *Leishmania donovani* infection. *PLoS Pathog* 7: e1001246.
138. Zheng SG (2013) Regulatory T cells vs Th17: differentiation of Th17 versus Treg, are the mutually exclusive? *Am J Clin Exp Immunol* 2: 94-106.
139. Afzali B, Lombardi G, Lechler RI, Lord GM (2007) The role of T helper 17 (Th17) and regulatory T cells (Treg) in human organ transplantation and autoimmune disease. *Clin Exp Immunol* 148: 32-46.
140. Zhu J, Yamane H, Paul WE (2010) Differentiation of effector CD4 T cell populations (\*). *Annu Rev Immunol* 28: 445-489.
141. Bishop JJ, Popel AS, Intaglietta M, Johnson PC (2001) Rheological effects of red blood cell aggregation in the venous network: a review of recent studies. *Biorheology* 38: 263-274.
142. Cicco G, Pirrelli A (1999) Red blood cell (RBC) deformability, RBC aggregability and tissue oxygenation in hypertension. *Clin Hemorheol Microcirc* 21: 169-177.
143. Das B, Bishop JJ, Kim S, Meiselman HJ, Johnson PC, et al. (2007) Red blood cell velocity profiles in skeletal muscle venules at low flow rates are described by the Casson model. *Clin Hemorheol Microcirc* 36: 217-233.
144. Kim S, Popel AS, Intaglietta M, Johnson PC (2005) Aggregate formation of erythrocytes in postcapillary venules. *Am J Physiol Heart Circ Physiol* 288: H584-590.
145. Meiselman HJ (2009) Red blood cell aggregation: 45 years being curious. *Biorheology* 46: 1-19.
146. Cokelet GR, Goldsmith HL (1991) Decreased hydrodynamic resistance in the two-phase flow of blood through small vertical tubes at low flow rates. *Circ Res* 68: 1-17.
147. Goldsmith HL, Bell DN, Spain S, McIntosh FA (1999) Effect of red blood cells and their aggregates on platelets and white cells in flowing blood. *Biorheology* 36: 461-468.
148. Alonso C, Pries AR, Gaehtgens P (1993) Time-dependent rheological behavior of blood at low shear in narrow vertical tubes. *Am J Physiol* 265: H553-561.
149. Suzuki Y, Tateishi N, Soutani M, Maeda N (1996) Flow behavior of erythrocytes in microvessels and glass capillaries: effects of erythrocyte deformation and erythrocyte aggregation. *Int J Microcirc Clin Exp* 16: 187-194.
150. Baskurt OK, Meiselman HJ (2007) Hemodynamic effects of red blood cell aggregation. *Indian J Exp Biol* 45: 25-31.
151. Tateishi N, Suzuki Y, Shirai M, Cicha I, Maeda N (2002) Reduced oxygen release from erythrocytes by the acceleration-induced flow shift, observed in an oxygen-permeable narrow tube. *J Biomech* 35: 1241-1251.
152. Goldbeter A, Koshland DE, Jr. (1984) Ultrasensitivity in biochemical systems controlled by covalent modification. Interplay between zero-order and multistep effects. *J Biol Chem* 259: 14441-14447.
153. Gunawardena J (2005) Multisite protein phosphorylation makes a good threshold but can be a poor switch. *Proc Natl Acad Sci U S A* 102: 14617-14622.
154. Chan C, Liu X, Wang L, Bardwell L, Nie Q, et al. (2012) Protein scaffolds can enhance the bistability of multisite phosphorylation systems. *PLoS Comput Biol* 8: e1002551.
155. Salazar C, Hofer T (2007) Versatile regulation of multisite protein phosphorylation by the order of phosphate processing and protein-protein interactions. *FEBS J* 274: 1046-1061.

156. Kapuy O, Barik D, Sananes MR, Tyson JJ, Novak B (2009) Bistability by multiple phosphorylation of regulatory proteins. *Prog Biophys Mol Biol* 100: 47-56.
157. Wang L, Nie Q, Enciso G (2010) Nonessential sites improve phosphorylation switch. *Biophys J* 99: L41-43.
158. Thingnes J, Lavelle TJ, Gjuvslund AB, Omholt SW, Hovig E (2012) Towards a quantitative understanding of the MITF-PIAS3-STAT3 connection. *BMC Syst Biol* 6: 11.
159. Casanovas G, Banerji A, d'Alessio F, Muckenthaler MU, Legewie S (2014) A multi-scale model of hepcidin promoter regulation reveals factors controlling systemic iron homeostasis. *PLoS Comput Biol* 10: e1003421.
160. Selvarajoo K (2006) Discovering differential activation machinery of the Toll-like receptor 4 signaling pathways in MyD88 knockouts. *FEBS Lett* 580: 1457-1464.
161. Rapoport TA, Heinrich R, Rapoport SM (1976) The regulatory principles of glycolysis in erythrocytes in vivo and in vitro. A minimal comprehensive model describing steady states, quasi-steady states and time-dependent processes. *Biochem J* 154: 449-469.
162. Ataulakhanov FI, Vitvitsky VM, Zhabotinsky AM, Pichugin AV, Platonova OV, et al. (1981) The regulation of glycolysis in human erythrocytes. The dependence of the glycolytic flux on the ATP concentration. *Eur J Biochem* 115: 359-365.
163. Joshi A, Palsson BO (1989) Metabolic dynamics in the human red cell. Part I--A comprehensive kinetic model. *J Theor Biol* 141: 515-528.
164. Krausgruber T, Blazek K, Smallie T, Alzabin S, Lockstone H, et al. (2011) IRF5 promotes inflammatory macrophage polarization and TH1-TH17 responses. *Nat Immunol* 12: 231-238.
165. Floss DM, Mrotzek S, Klocker T, Schroder J, Grotzinger J, et al. (2013) Identification of canonical tyrosine-dependent and non-canonical tyrosine-independent STAT3 activation sites in the intracellular domain of the interleukin 23 receptor. *J Biol Chem* 288: 19386-19400.
166. Takaoka A, Yanai H, Kondo S, Duncan G, Negishi H, et al. (2005) Integral role of IRF-5 in the gene induction programme activated by Toll-like receptors. *Nature* 434: 243-249.
167. Minton K (2011) Macrophages: a transcription factor to call their own. *Nat Rev Immunol* 11: 74.
168. Kusaba H, Ghosh P, Derin R, Buchholz M, Sasaki C, et al. (2005) Interleukin-12-induced interferon-gamma production by human peripheral blood T cells is regulated by mammalian target of rapamycin (mTOR). *J Biol Chem* 280: 1037-1043.
169. Kleinewietfeld M, Hafler DA (2013) The plasticity of human Treg and Th17 cells and its role in autoimmunity. *Semin Immunol* 25: 305-312.
170. Shi G, Cox CA, Vistica BP, Tan C, Wawrousek EF, et al. (2008) Phenotype switching by inflammation-inducing polarized Th17 cells, but not by Th1 cells. *J Immunol* 181: 7205-7213.
171. Catlett-Falcone R, Landowski TH, Oshiro MM, Turkson J, Levitzki A, et al. (1999) Constitutive activation of Stat3 signaling confers resistance to apoptosis in human U266 myeloma cells. *Immunity* 10: 105-115.
172. Kuhn DJ, Smith DM, Pross S, Whiteside TL, Dou QP (2003) Overexpression of interleukin-2 receptor alpha in a human squamous cell carcinoma of the head and neck cell line is associated with increased proliferation, drug resistance, and transforming ability. *J Cell Biochem* 89: 824-836.
173. Voit EO, Martens HA, Omholt SW (2015) 150 years of the mass action law. *PLoS Comput Biol* 11: e1004012.
174. Ferrell JE, Jr., Machleder EM (1998) The biochemical basis of an all-or-none cell fate switch in *Xenopus* oocytes. *Science* 280: 895-898.
175. Mutalik VK, Venkatesh KV (2005) Quantification of the glycogen cascade system: the ultrasensitive responses of liver glycogen synthase and muscle phosphorylase are due to distinctive regulatory designs. *Theor Biol Med Model* 2: 19.
176. Palani S, Sarkar CA (2011) Synthetic conversion of a graded receptor signal into a tunable, reversible switch. *Mol Syst Biol* 7: 480.
177. Lechner MG, Megiel C, Church CH, Angell TE, Russell SM, et al. (2012) Survival signals and targets for therapy in breast implant-associated ALK--anaplastic large cell lymphoma. *Clin Cancer Res* 18: 4549-4559.
178. Tai WT, Cheng AL, Shiau CW, Liu CY, Ko CH, et al. (2012) Dovitinib induces apoptosis and overcomes sorafenib resistance in hepatocellular carcinoma through SHP-1-mediated inhibition of STAT3. *Mol Cancer Ther* 11: 452-463.
179. Balkhi MY, Fitzgerald KA, Pitha PM (2010) IKKalpha negatively regulates IRF-5 function in a MyD88-TRAF6 pathway. *Cell Signal* 22: 117-127.

180. Hochrainer K, Racchumi G, Anrather J (2013) Site-specific phosphorylation of the p65 protein subunit mediates selective gene expression by differential NF-kappaB and RNA polymerase II promoter recruitment. *J Biol Chem* 288: 285-293.
181. Macian F (2005) NFAT proteins: key regulators of T-cell development and function. *Nat Rev Immunol* 5: 472-484.
182. Borghans JA, de Boer RJ, Segel LA (1996) Extending the quasi-steady state approximation by changing variables. *Bull Math Biol* 58: 43-63.
183. Nelson GA, Andrews ML, Karnovsky MJ (1983) Control of erythrocyte shape by calmodulin. *J Cell Biol* 96: 730-735.
184. de Oliveira S, Silva-Herdade AS, Saldanha C (2008) Modulation of erythrocyte deformability by PKC activity. *Clin Hemorheol Microcirc* 39: 363-373.
185. Alberts B (2002) *Molecular biology of the cell*. New York: Garland Science. xxxiv, 1548 p.
186. Dhananjanyulu V, Sagar PV, Kumar G, Viswanathan GA (2012) Noise propagation in two-step series MAPK cascade. *PLoS One* 7: e35958.
187. Murray JW, Edmonds BT, Liu G, Condeelis J (1996) Bundling of actin filaments by elongation factor 1 alpha inhibits polymerization at filament ends. *J Cell Biol* 135: 1309-1321.
188. Ryazanov AG, Ward MD, Mendola CE, Pavur KS, Dorovkov MV, et al. (1997) Identification of a new class of protein kinases represented by eukaryotic elongation factor-2 kinase. *Proc Natl Acad Sci U S A* 94: 4884-4889.
189. Thomson M, Gunawardena J (2009) Unlimited multistability in multisite phosphorylation systems. *Nature* 460: 274-277.
190. Stone RC, Feng D, Deng J, Singh S, Yang L, et al. (2012) Interferon regulatory factor 5 activation in monocytes of systemic lupus erythematosus patients is triggered by circulating autoantigens independent of type I interferons. *Arthritis Rheum* 64: 788-798.
191. Sadzak I, Schiff M, Gattermeier I, Glinitzer R, Sauer I, et al. (2008) Recruitment of Stat1 to chromatin is required for interferon-induced serine phosphorylation of Stat1 transactivation domain. *Proc Natl Acad Sci U S A* 105: 8944-8949.
192. Sakaguchi M, Oka M, Iwasaki T, Fukami Y, Nishigori C (2012) Role and regulation of STAT3 phosphorylation at Ser727 in melanocytes and melanoma cells. *J Invest Dermatol* 132: 1877-1885.
193. Niemand C, Nimmegern A, Haan S, Fischer P, Schaper F, et al. (2003) Activation of STAT3 by IL-6 and IL-10 in primary human macrophages is differentially modulated by suppressor of cytokine signaling 3. *J Immunol* 170: 3263-3272.
194. Schuringa JJ, Wierenga AT, Kruijer W, Vellenga E (2000) Constitutive Stat3, Tyr705, and Ser727 phosphorylation in acute myeloid leukemia cells caused by the autocrine secretion of interleukin-6. *Blood* 95: 3765-3770.
195. Liu YP, Tan YN, Wang ZL, Zeng L, Lu ZX, et al. (2008) Phosphorylation and nuclear translocation of STAT3 regulated by the Epstein-Barr virus latent membrane protein 1 in nasopharyngeal carcinoma. *Int J Mol Med* 21: 153-162.
196. Aggarwal BB, Kunnumakkara AB, Harikumar KB, Gupta SR, Tharakan ST, et al. (2009) Signal transducer and activator of transcription-3, inflammation, and cancer: how intimate is the relationship? *Ann N Y Acad Sci* 1171: 59-76.
197. Darnell JE, Jr. (1997) STATs and gene regulation. *Science* 277: 1630-1635.
198. Au-Yeung N, Mandhana R, Horvath CM (2013) Transcriptional regulation by STAT1 and STAT2 in the interferon JAK-STAT pathway. *JAKSTAT* 2: e23931.
199. Barry SP, Townsend PA, Latchman DS, Stephanou A (2007) Role of the JAK-STAT pathway in myocardial injury. *Trends Mol Med* 13: 82-89.
200. Mitchell TJ, John S (2005) Signal transducer and activator of transcription (STAT) signalling and T-cell lymphomas. *Immunology* 114: 301-312.
201. Husby J, Todd AK, Haider SM, Zinzalla G, Thurston DE, et al. (2012) Molecular dynamics studies of the STAT3 homodimer:DNA complex: relationships between STAT3 mutations and protein-DNA recognition. *J Chem Inf Model* 52: 1179-1192.
202. Kershaw NJ, Murphy JM, Liao NP, Varghese LN, Laktyushin A, et al. (2013) SOCS3 binds specific receptor-JAK complexes to control cytokine signaling by direct kinase inhibition. *Nat Struct Mol Biol* 20: 469-476.
203. Lubberts E, van den Berg WB (2003) Cytokines in the pathogenesis of rheumatoid arthritis and collagen-induced arthritis. *Adv Exp Med Biol* 520: 194-202.
204. Chomar P, Vannier E, Dechanet J, Rissoan MC, Banchereau J, et al. (1995) Balance of IL-1 receptor antagonist/IL-1 beta in rheumatoid synovium and its regulation by IL-4 and IL-10. *J Immunol* 154: 1432-1439.

205. Sule S, Rosen A, Petri M, Akhter E, Andrade F (2011) Abnormal production of pro- and anti-inflammatory cytokines by lupus monocytes in response to apoptotic cells. *PLoS One* 6: e17495.
206. Sivalingam SP, Thumboo J, Vasoo S, Thio ST, Tse C, et al. (2007) In vivo pro- and anti-inflammatory cytokines in normal and patients with rheumatoid arthritis. *Ann Acad Med Singapore* 36: 96-99.
207. Dean GS, Tyrrell-Price J, Crawley E, Isenberg DA (2000) Cytokines and systemic lupus erythematosus. *Ann Rheum Dis* 59: 243-251.
208. Russell MA, Cooper AC, Dhayal S, Morgan NG (2013) Differential effects of interleukin-13 and interleukin-6 on Jak/STAT signaling and cell viability in pancreatic beta-cells. *Islets* 5: 95-105.
209. Kaminski A, Welters HJ, Kaminski ER, Morgan NG (2010) Human and rodent pancreatic beta-cells express IL-4 receptors and IL-4 protects against beta-cell apoptosis by activation of the PI3K and JAK/STAT pathways. *Biosci Rep* 30: 169-175.
210. Nelson EA, Sharma SV, Settleman J, Frank DA (2011) A chemical biology approach to developing STAT inhibitors: molecular strategies for accelerating clinical translation. *Oncotarget* 2: 518-524.
211. Hayakawa F, Sugimoto K, Harada Y, Hashimoto N, Ohi N, et al. (2013) A novel STAT inhibitor, OPB-31121, has a significant antitumor effect on leukemia with STAT-addictive oncokines. *Blood Cancer J* 3: e166.
212. Herr F, Lemoine R, Gouilleux F, Meley D, Kazma I, et al. (2014) IL-2 phosphorylates STAT5 to drive IFN-gamma production and activation of human dendritic cells. *J Immunol* 192: 5660-5670.
213. Stumhofer JS, Silver JS, Laurence A, Porrett PM, Harris TH, et al. (2007) Interleukins 27 and 6 induce STAT3-mediated T cell production of interleukin 10. *Nat Immunol* 8: 1363-1371.
214. Aaronson DS, Horvath CM (2002) A road map for those who don't know JAK-STAT. *Science* 296: 1653-1655.
215. Jiao H, Berrada K, Yang W, Tabrizi M, Plataniias LC, et al. (1996) Direct association with and dephosphorylation of Jak2 kinase by the SH2-domain-containing protein tyrosine phosphatase SHP-1. *Mol Cell Biol* 16: 6985-6992.
216. Collison LW, Delgoffe GM, Guy CS, Vignali KM, Chaturvedi V, et al. (2012) The composition and signaling of the IL-35 receptor are unconventional. *Nat Immunol* 13: 290-299.
217. Delgoffe GM, Vignali DA (2013) STAT heterodimers in immunity: A mixed message or a unique signal? *JAKSTAT* 2: e23060.
218. Fung MM, Rohwer F, McGuire KL (2003) IL-2 activation of a PI3K-dependent STAT3 serine phosphorylation pathway in primary human T cells. *Cell Signal* 15: 625-636.
219. Liu CY, Tseng LM, Su JC, Chang KC, Chu PY, et al. (2013) Novel sorafenib analogues induce apoptosis through SHP-1 dependent STAT3 inactivation in human breast cancer cells. *Breast Cancer Res* 15: R63.
220. Chen Y, Wen R, Yang S, Schuman J, Zhang EE, et al. (2003) Identification of Shp-2 as a Stat5A phosphatase. *J Biol Chem* 278: 16520-16527.
221. Valev NV, Hundhausen C, Umezawa Y, Kotov NV, Williams G, et al. (2010) A systems model for immune cell interactions unravels the mechanism of inflammation in human skin. *PLoS Comput Biol* 6: e1001024.
222. Delpire E, Gagnon KB (2008) SPAK and OSR1: STE20 kinases involved in the regulation of ion homeostasis and volume control in mammalian cells. *Biochem J* 409: 321-331.
223. Karsten CM, Kohl J (2010) The complement receptor CD46 tips the scales in T(H)1 self-control. *Nat Immunol* 11: 775-777.
224. Guo L, Junttila IS, Paul WE (2012) Cytokine-induced cytokine production by conventional and innate lymphoid cells. *Trends Immunol* 33: 598-606.
225. Strengell M, Matikainen S, Siren J, Lehtonen A, Foster D, et al. (2003) IL-21 in synergy with IL-15 or IL-18 enhances IFN-gamma production in human NK and T cells. *J Immunol* 170: 5464-5469.
226. Kasahara T, Hooks JJ, Dougherty SF, Oppenheim JJ (1983) Interleukin 2-mediated immune interferon (IFN-gamma) production by human T cells and T cell subsets. *J Immunol* 130: 1784-1789.
227. Niedbala W, Wei XQ, Cai B, Hueber AJ, Leung BP, et al. (2007) IL-35 is a novel cytokine with therapeutic effects against collagen-induced arthritis through the expansion of regulatory T cells and suppression of Th17 cells. *Eur J Immunol* 37: 3021-3029.

228. Scheeren FA, Diehl SA, Smit LA, Beaumont T, Naspetti M, et al. (2008) IL-21 is expressed in Hodgkin lymphoma and activates STAT5: evidence that activated STAT5 is required for Hodgkin lymphomagenesis. *Blood* 111: 4706-4715.
229. Gilmour KC, Pine R, Reich NC (1995) Interleukin 2 activates STAT5 transcription factor (mammary gland factor) and specific gene expression in T lymphocytes. *Proc Natl Acad Sci U S A* 92: 10772-10776.
230. Wurster AL, Tanaka T, Grusby MJ (2000) The biology of Stat4 and Stat6. *Oncogene* 19: 2577-2584.
231. Shi M, Lin TH, Appell KC, Berg LJ (2008) Janus-kinase-3-dependent signals induce chromatin remodeling at the *Irfng* locus during T helper 1 cell differentiation. *Immunity* 28: 763-773.
232. Gonsky R, Deem RL, Bream J, Young HA, Targan SR (2004) Enhancer role of STAT5 in CD2 activation of IFN-gamma gene expression. *J Immunol* 173: 6241-6247.
233. Tsuji-Takayama K, Suzuki M, Yamamoto M, Harashima A, Okochi A, et al. (2008) The production of IL-10 by human regulatory T cells is enhanced by IL-2 through a STAT5-responsive intronic enhancer in the IL-10 locus. *J Immunol* 181: 3897-3905.
234. Stewart CA, Metheny H, Iida N, Smith L, Hanson M, et al. (2013) Interferon-dependent IL-10 production by Tregs limits tumor Th17 inflammation. *J Clin Invest* 123: 4859-4874.
235. Saraiva M, O'Garra A (2010) The regulation of IL-10 production by immune cells. *Nat Rev Immunol* 10: 170-181.
236. Sanz E, Hofer MJ, Unzeta M, Campbell IL (2008) Minimal role for STAT1 in interleukin-6 signaling and actions in the murine brain. *Glia* 56: 190-199.
237. Saraiva M, Christensen JR, Veldhoen M, Murphy TL, Murphy KM, et al. (2009) Interleukin-10 production by Th1 cells requires interleukin-12-induced STAT4 transcription factor and ERK MAP kinase activation by high antigen dose. *Immunity* 31: 209-219.
238. Hibbert L, Pflanz S, De Waal Malefyt R, Kastelein RA (2003) IL-27 and IFN-alpha signal via Stat1 and Stat3 and induce T-Bet and IL-12Rbeta2 in naive T cells. *J Interferon Cytokine Res* 23: 513-522.
239. Li X, Leung S, Qureshi S, Darnell JE, Jr., Stark GR (1996) Formation of STAT1-STAT2 heterodimers and their role in the activation of IRF-1 gene transcription by interferon-alpha. *J Biol Chem* 271: 5790-5794.
240. Wang WB, Levy DE, Lee CK (2011) STAT3 negatively regulates type I IFN-mediated antiviral response. *J Immunol* 187: 2578-2585.
241. Higashi T, Tsukada J, Yoshida Y, Mizobe T, Mouri F, et al. (2005) Constitutive tyrosine and serine phosphorylation of STAT4 in T-cells transformed with HTLV-I. *Genes Cells* 10: 1153-1162.
242. Tanabe Y, Nishibori T, Su L, Arduini RM, Baker DP, et al. (2005) Cutting edge: role of STAT1, STAT3, and STAT5 in IFN-alpha beta responses in T lymphocytes. *J Immunol* 174: 609-613.
243. Gupta S, Jiang M, Pernis AB (1999) IFN-alpha activates Stat6 and leads to the formation of Stat2:Stat6 complexes in B cells. *J Immunol* 163: 3834-3841.
244. Cardone J, Le Friec G, Vantourout P, Roberts A, Fuchs A, et al. (2010) Complement regulator CD46 temporally regulates cytokine production by conventional and unconventional T cells. *Nat Immunol* 11: 862-871.
245. Ho HH, Ivashkiv LB (2006) Role of STAT3 in type I interferon responses. Negative regulation of STAT1-dependent inflammatory gene activation. *J Biol Chem* 281: 14111-14118.
246. Lucas M, Zhang X, Prasanna V, Mosser DM (2005) ERK activation following macrophage Fc-gammaR ligation leads to chromatin modifications at the IL-10 locus. *J Immunol* 175: 469-477.
247. Sarkar S, Han J, Sinsimer KS, Liao B, Foster RL, et al. (2011) RNA-binding protein AUF1 regulates lipopolysaccharide-induced IL10 expression by activating I-kappaB kinase complex in monocytes. *Mol Cell Biol* 31: 602-615.
248. Ma CS, Chew GY, Simpson N, Priyadarshi A, Wong M, et al. (2008) Deficiency of Th17 cells in hyper IgE syndrome due to mutations in STAT3. *J Exp Med* 205: 1551-1557.
249. Yang Y, Ramelot TA, Ni S, McCarrick RM, Kennedy MA (2013) Measurement of rate constants for homodimer subunit exchange using double electron-electron resonance and paramagnetic relaxation enhancements. *J Biomol NMR* 55: 47-58.
250. Forsberg G, Hernell O, Melgar S, Israelsson A, Hammarstrom S, et al. (2002) Paradoxical coexpression of proinflammatory and down-regulatory cytokines in intestinal T cells in childhood celiac disease. *Gastroenterology* 123: 667-678.
251. Chu Y, Jayaraman A, Hahn J (2007) Parameter sensitivity analysis of IL-6 signalling pathways. *IET Syst Biol* 1: 342-352.



252. Saltelli A, Ratto M, Tarantola S, Campolongo F (2005) Sensitivity analysis for chemical models. *Chem Rev* 105: 2811-2828.
253. McCarthy DJ, Smyth GK (2009) Testing significance relative to a fold-change threshold is a TREAT. *Bioinformatics* 25: 765-771.
254. Dalman MR, Deeter A, Nimishakavi G, Duan ZH (2012) Fold change and p-value cutoffs significantly alter microarray interpretations. *BMC Bioinformatics* 13 Suppl 2: S11.
255. Marino S, Hogue IB, Ray CJ, Kirschner DE (2008) A methodology for performing global uncertainty and sensitivity analysis in systems biology. *J Theor Biol* 254: 178-196.
256. Saltelli AT, S.; Chan, K.P.S. (1999) A quantitative model-independent method for global sensitivity analysis of model output. *Technometrics* 41: 39-56.
257. Schmidt H, Jirstrand M (2006) Systems Biology Toolbox for MATLAB: a computational platform for research in systems biology. *Bioinformatics* 22: 514-515.
258. Tanaka RJ, Ono M, Harrington HA (2011) Skin barrier homeostasis in atopic dermatitis: feedback regulation of kallikrein activity. *PLoS One* 6: e19895.
259. Pollard KM, Cauvi DM, Toomey CB, Morris KV, Kono DH (2013) Interferon-gamma and systemic autoimmunity. *Discov Med* 16: 123-131.
260. Moore KW, de Waal Malefyt R, Coffman RL, O'Garra A (2001) Interleukin-10 and the interleukin-10 receptor. *Annu Rev Immunol* 19: 683-765.
261. Hedrich CM, Rauen T, Apostolidis SA, Grammatikos AP, Rodriguez Rodriguez N, et al. (2014) Stat3 promotes IL-10 expression in lupus T cells through trans-activation and chromatin remodeling. *Proc Natl Acad Sci U S A* 111: 13457-13462.
262. Malek TR, Castro I (2010) Interleukin-2 receptor signaling: at the interface between tolerance and immunity. *Immunity* 33: 153-165.
263. Kimura D, Miyakoda M, Honma K, Shibata Y, Yuda M, et al. (2010) Production of IFN-gamma by CD4(+) T cells in response to malaria antigens is IL-2 dependent. *Int Immunol* 22: 941-952.
264. Bream JH, Hodge DL, Gonsky R, Spolski R, Leonard WJ, et al. (2004) A distal region in the interferon-gamma gene is a site of epigenetic remodeling and transcriptional regulation by interleukin-2. *J Biol Chem* 279: 41249-41257.
265. Chen J, Yu WM, Bunting KD, Qu CK (2004) A negative role of SHP-2 tyrosine phosphatase in growth factor-dependent hematopoietic cell survival. *Oncogene* 23: 3659-3669.
266. Jin JO, Han X, Yu Q (2013) Interleukin-6 induces the generation of IL-10-producing Tr1 cells and suppresses autoimmune tissue inflammation. *J Autoimmun* 40: 28-44.
267. Denson LA, Held MA, Menon RK, Frank SJ, Parlow AF, et al. (2003) Interleukin-6 inhibits hepatic growth hormone signaling via upregulation of Cis and Socs-3. *Am J Physiol Gastrointest Liver Physiol* 284: G646-654.
268. Anderson CF, Oukka M, Kuchroo VJ, Sacks D (2007) CD4(+)CD25(-)Foxp3(-) Th1 cells are the source of IL-10-mediated immune suppression in chronic cutaneous leishmaniasis. *J Exp Med* 204: 285-297.
269. Moore KW, Vieira P, Fiorentino DF, Trounstein ML, Khan TA, et al. (1990) Homology of cytokine synthesis inhibitory factor (IL-10) to the Epstein-Barr virus gene BCRF1. *Science* 248: 1230-1234.
270. Furqan M, Akinleye A, Mukhi N, Mittal V, Chen Y, et al. (2013) STAT inhibitors for cancer therapy. *J Hematol Oncol* 6: 90.
271. Boehm F, Martin M, Kesselring R, Schiechl G, Geissler EK, et al. (2012) Deletion of Foxp3+ regulatory T cells in genetically targeted mice supports development of intestinal inflammation. *BMC Gastroenterol* 12: 97.
272. Fletcher S, Drewry JA, Shahani VM, Page BD, Gunning PT (2009) Molecular disruption of oncogenic signal transducer and activator of transcription 3 (STAT3) protein. *Biochem Cell Biol* 87: 825-833.
273. Scoles DR, Nguyen VD, Qin Y, Sun CX, Morrison H, et al. (2002) Neurofibromatosis 2 (NF2) tumor suppressor schwannomin and its interacting protein HRS regulate STAT signaling. *Hum Mol Genet* 11: 3179-3189.
274. Demartis A, Bernassola F, Savino R, Melino G, Ciliberto G (1996) Interleukin 6 receptor superantagonists are potent inducers of human multiple myeloma cell death. *Cancer Res* 56: 4213-4218.
275. Sporeno E, Savino R, Ciapponi L, Paonessa G, Cabibbo A, et al. (1996) Human interleukin-6 receptor super-antagonists with high potency and wide spectrum on multiple myeloma cells. *Blood* 87: 4510-4519.
276. Leung S, Liu X, Fang L, Chen X, Guo T, et al. (2010) The cytokine milieu in the interplay of pathogenic Th1/Th17 cells and regulatory T cells in autoimmune disease. *Cell Mol Immunol* 7: 182-189.

277. Clerici M, Shearer GM (1993) A TH1-->TH2 switch is a critical step in the etiology of HIV infection. *Immunol Today* 14: 107-111.
278. Lane N, Robins RA, Corne J, Fairclough L (2010) Regulation in chronic obstructive pulmonary disease: the role of regulatory T-cells and Th17 cells. *Clin Sci (Lond)* 119: 75-86.
279. Fidel PL, Jr., Cutright JL, Tait L, Sobel JD (1996) A murine model of *Candida glabrata* vaginitis. *J Infect Dis* 173: 425-431.
280. Culakova H, Dzugasova V, Valencikova R, Gbelska Y, Subik J (2015) Stress response and expression of fluconazole resistance associated genes in the pathogenic yeast *Candida glabrata* deleted in the CgPDR16 gene. *Microbiol Res* 174: 17-23.
281. Fidel PL, Jr., Vazquez JA, Sobel JD (1999) *Candida glabrata*: review of epidemiology, pathogenesis, and clinical disease with comparison to *C. albicans*. *Clin Microbiol Rev* 12: 80-96.
282. Demiraslan H, Alabay S, Kilic AU, Borlu M, Doganay M (2013) Cutaneous candidiasis caused by *Candida glabrata* in a HIV/AIDS patient. *Int J STD AIDS* 24: 753-755.
283. Hajjeh RA, Sofair AN, Harrison LH, Lyon GM, Arthington-Skaggs BA, et al. (2004) Incidence of bloodstream infections due to *Candida* species and in vitro susceptibilities of isolates collected from 1998 to 2000 in a population-based active surveillance program. *J Clin Microbiol* 42: 1519-1527.
284. Silva S, Negri M, Henriques M, Oliveira R, Williams DW, et al. (2012) *Candida glabrata*, *Candida parapsilosis* and *Candida tropicalis*: biology, epidemiology, pathogenicity and antifungal resistance. *FEMS Microbiol Rev* 36: 288-305.
285. Krcmery V, Barnes AJ (2002) Non-*albicans* *Candida* spp. causing fungaemia: pathogenicity and antifungal resistance. *J Hosp Infect* 50: 243-260.
286. Shim JH, Seo NS, Roh SA, Kim JW, Cha H, et al. (2007) Improved bread-baking process using *Saccharomyces cerevisiae* displayed with engineered cyclodextrin glucanotransferase. *J Agric Food Chem* 55: 4735-4740.
287. Izawa S, Ikeda K, Miki T, Wakai Y, Inoue Y (2010) Vacuolar morphology of *Saccharomyces cerevisiae* during the process of wine making and Japanese sake brewing. *Appl Microbiol Biotechnol* 88: 277-282.
288. Saito H (2010) Regulation of cross-talk in yeast MAPK signaling pathways. *Curr Opin Microbiol* 13: 677-683.
289. Reiser V, Raitt DC, Saito H (2003) Yeast osmosensor Sln1 and plant cytokinin receptor Cre1 respond to changes in turgor pressure. *J Cell Biol* 161: 1035-1040.
290. Gustin MC, Albertyn J, Alexander M, Davenport K (1998) MAP kinase pathways in the yeast *Saccharomyces cerevisiae*. *Microbiol Mol Biol Rev* 62: 1264-1300.
291. O'Rourke SM, Herskowitz I (1998) The Hog1 MAPK prevents cross talk between the HOG and pheromone response MAPK pathways in *Saccharomyces cerevisiae*. *Genes Dev* 12: 2874-2886.
292. Saito H, Posas F (2012) Response to hyperosmotic stress. *Genetics* 192: 289-318.
293. Gregori C, Schuller C, Roetzer A, Schwarzmuller T, Ammerer G, et al. (2007) The high-osmolarity glycerol response pathway in the human fungal pathogen *Candida glabrata* strain ATCC 2001 lacks a signaling branch that operates in baker's yeast. *Eukaryot Cell* 6: 1635-1645.
294. Cheetham J, MacCallum DM, Doris KS, da Silva Dantas A, Scorfield S, et al. (2011) MAPKKK-independent regulation of the Hog1 stress-activated protein kinase in *Candida albicans*. *J Biol Chem* 286: 42002-42016.
295. English JG, Shellhammer JP, Malahe M, McCarter PC, Elston TC, et al. (2015) MAPK feedback encodes a switch and timer for tunable stress adaptation in yeast. *Sci Signal* 8: ra5.
296. Young C, Mapes J, Hanneman J, Al-Zarban S, Ota I (2002) Role of Ptc2 type 2C Ser/Thr phosphatase in yeast high-osmolarity glycerol pathway inactivation. *Eukaryot Cell* 1: 1032-1040.
297. Jacoby T, Flanagan H, Faykin A, Seto AG, Mattison C, et al. (1997) Two protein-tyrosine phosphatases inactivate the osmotic stress response pathway in yeast by targeting the mitogen-activated protein kinase, Hog1. *J Biol Chem* 272: 17749-17755.
298. Diner P, Veide Vilg J, Kjellen J, Migdal I, Andersson T, et al. (2011) Design, synthesis, and characterization of a highly effective Hog1 inhibitor: a powerful tool for analyzing MAP kinase signaling in yeast. *PLoS One* 6: e20012.
299. Alepuz PM, de Nadal E, Zapater M, Ammerer G, Posas F (2003) Osmostress-induced transcription by Hot1 depends on a Hog1-mediated recruitment of the RNA Pol II. *EMBO J* 22: 2433-2442.

300. Reed RH, Chudek JA, Foster R, Gadd GM (1987) Osmotic significance of glycerol accumulation in exponentially growing yeasts. *Appl Environ Microbiol* 53: 2119-2123.
301. Soveral G, Prista C, Moura TF, Loureiro-Dias MC (2010) Yeast water channels: an overview of orthodox aquaporins. *Biol Cell* 103: 35-54.
302. Lee J, Reiter W, Dohnal I, Gregori C, Beese-Sims S, et al. (2013) MAPK Hog1 closes the *S. cerevisiae* glycerol channel Fps1 by phosphorylating and displacing its positive regulators. *Genes Dev* 27: 2590-2601.
303. Rep M, Reiser V, Gartner U, Thevelein JM, Hohmann S, et al. (1999) Osmotic stress-induced gene expression in *Saccharomyces cerevisiae* requires Msn1p and the novel nuclear factor Hot1p. *Mol Cell Biol* 19: 5474-5485.
304. Remize F, Roustan JL, Sablayrolles JM, Barre P, Dequin S (1999) Glycerol overproduction by engineered *saccharomyces cerevisiae* wine yeast strains leads to substantial changes in By-product formation and to a stimulation of fermentation rate in stationary phase. *Appl Environ Microbiol* 65: 143-149.
305. Cirillo VP (1962) Mechanism of glucose transport across the yeast cell membrane. *J Bacteriol* 84: 485-491.
306. Teusink B, Diderich JA, Westerhoff HV, van Dam K, Walsh MC (1998) Intracellular glucose concentration in derepressed yeast cells consuming glucose is high enough to reduce the glucose transport rate by 50%. *J Bacteriol* 180: 556-562.
307. Berg JM, Tymoczko JL, Stryer L, Stryer L (2002) *Biochemistry*. New York: W.H. Freeman. xxxviii, 974, 972 p. p.
308. Kristiansen M, Andersen B, Iversen LF, Westergaard N (2004) Identification, synthesis, and characterization of new glycogen phosphorylase inhibitors binding to the allosteric AMP site. *J Med Chem* 47: 3537-3545.
309. Lawrence JC, Jr., Roach PJ (1997) New insights into the role and mechanism of glycogen synthase activation by insulin. *Diabetes* 46: 541-547.
310. Fang X, Yu SX, Lu Y, Bast RC, Jr., Woodgett JR, et al. (2000) Phosphorylation and inactivation of glycogen synthase kinase 3 by protein kinase A. *Proc Natl Acad Sci U S A* 97: 11960-11965.
311. Johnson LN (1992) Glycogen phosphorylase: control by phosphorylation and allosteric effectors. *FASEB J* 6: 2274-2282.
312. Alczuk Sde S, Bonfim-Mendonca Pde S, Rocha-Brischiliari SC, Shinobu-Mesquita CS, Martins HP, et al. (2015) EFFECT OF HIGHLY ACTIVE ANTIRETROVIRAL THERAPY ON VAGINAL *Candida* spp. ISOLATION IN HIV-INFECTED COMPARED TO HIV-UNINFECTED WOMEN. *Rev Inst Med Trop Sao Paulo* 57: 169-174.
313. Posteraro B, Tumbarello M, La Sorda M, Spanu T, Trecarichi EM, et al. (2006) Azole resistance of *Candida glabrata* in a case of recurrent fungemia. *J Clin Microbiol* 44: 3046-3047.
314. Pappas PG, Rex JH (1999) Therapeutic Approach to *Candida* Sepsis. *Curr Infect Dis Rep* 1: 245-252.
315. Petelenz-Kurdziel E, Eriksson E, Smedh M, Beck C, Hohmann S, et al. (2011) Quantification of cell volume changes upon hyperosmotic stress in *Saccharomyces cerevisiae*. *Integr Biol (Camb)* 3: 1120-1126.
316. Babazadeh R, Adiels CB, Smedh M, Petelenz-Kurdziel E, Goksor M, et al. (2013) Osmostress-induced cell volume loss delays yeast Hog1 signaling by limiting diffusion processes and by Hog1-specific effects. *PLoS One* 8: e80901.
317. Beese SE, Negishi T, Levin DE (2009) Identification of positive regulators of the yeast fps1 glycerol channel. *PLoS Genet* 5: e1000738.
318. Nobel PS (1969) The Boyle-Van't Hoff relation. *J Theor Biol* 23: 375-379.
319. Levin RL, Ushiyama M, Cravalho EG (1979) Water permeability of yeast cells at sub-zero temperatures. *J Membr Biol* 46: 91-124.
320. Stenson JD, Hartley P, Wang C, Thomas CR (2011) Determining the mechanical properties of yeast cell walls. *Biotechnol Prog* 27: 505-512.
321. Farkas I, Gergely P (1989) Activation/dephosphorylation of muscle glycogen synthase phosphorylated by phosphorylase kinase. *Int J Biochem* 21: 631-634.
322. Saltiel AR, Pessin JE (2007) *Mechanisms of insulin action*. Austin, Tex. New York, N.Y.: Landes Bioscience ; Springer Science+Business Media. 214 p. p.
323. Luyten K, Albertyn J, Skibbe WF, Prior BA, Ramos J, et al. (1995) Fps1, a yeast member of the MIP family of channel proteins, is a facilitator for glycerol uptake and efflux and is inactive under osmotic stress. *EMBO J* 14: 1360-1371.
324. McClean MN, Mody A, Broach JR, Ramanathan S (2007) Cross-talk and decision making in MAP kinase pathways. *Nat Genet* 39: 409-414.

325. Toh TH, Kayingo G, van der Merwe MJ, Kilian SG, Hallsworth JE, et al. (2001) Implications of FPS1 deletion and membrane ergosterol content for glycerol efflux from *Saccharomyces cerevisiae*. *FEMS Yeast Res* 1: 205-211.
326. Dickinson JR, Schweizer M (2004) The metabolism and molecular physiology of *Saccharomyces cerevisiae*. Boca Raton: CRC Press. xiv, 459 p. p.
327. Evans CM, Jenner RG (2013) Transcription factor interplay in T helper cell differentiation. *Brief Funct Genomics* 12: 499-511.
328. Tanaka RJ, Okano H, Kimura H (2006) Mathematical description of gene regulatory units. *Biophys J* 91: 1235-1247.
329. Tanaka RJ, Kimura H (2008) Mathematical classification of regulatory logics for compound environmental changes. *J Theor Biol* 251: 363-379.
330. Gilbert SF (2000) *Developmental biology*. Sunderland, Mass.: Sinauer Associates. xviii, 749 p. p.
331. Freeman W H LH, Berk A, Zipursky S L, Matsudaira P, Baltimore D, and Darnell J. (2000) *Molecular Cell Biology*, 4th edition. Section 2.3 Chemical Equilibrium. ISBN-10: 0-7167-3136-3.
332. Goutelle S, Maurin M, Rougier F, Barbaut X, Bourguignon L, et al. (2008) The Hill equation: a review of its capabilities in pharmacological modelling. *Fundam Clin Pharmacol* 22: 633-648.
333. Stefan MI, Le Novere N (2013) Cooperative binding. *PLoS Comput Biol* 9: e1003106.
334. Cornish-Bowden A (1995) *Fundamentals of enzyme kinetics*. London: Portland. xiii, 343p. p.
335. Michaelis L, Menten ML (1913) The kinetics of the inversion effect. *Biochemische Zeitschrift* 49: 333-369.